Project funded by the European Commission under the 6th (EC) RTD Framework Programme (2002- 2006) within the framework of the specific research and technological development programme “Integrating and strengthening the European Research Area”

Project UpWind

Contract No.:
019945 (SES6)

“Integrated Wind Turbine Design”

MATERIAL MODEL INCORPORATING LOSS OF STRENGTH AND STIFFNESS DUE TO FATIGUE

Preliminary results from FE model implementation

AUTHOR:	T. P. Philippidis
AFFILIATION:	University of Patras, Dept. of Mech. Engng & Aeronautics, Section of Applied Mechanics
ADDRESS:	P. O. Box 1401, Panepistimioupolis Rio, GR 265 04, Greece
TEL.:	+30 2610 969450, 997235
EMAIL:	philippidis@mech.upatras.gr
FURTHER AUTHORS:	E. N. Eliopoulos, A. A. Antoniou, V. A. Passipoularidis
REVIEWER:	
APPROVER:	

Document Information

DOCUMENT TYPE	Deliverable
DOCUMENT NAME:	Material Model Incorporating Loss of Strength and Stiffness due to Fatigue
REVISION:	0
REV.DATE:	
CLASSIFICATION:	R3: Restricted to WP3 members + PL
STATUS:	S3: Draft for comments

Abstract: Work described in this technical report was performed in the frame of Task 3.3 “Damage Tolerant Design Concept” of Work-Package WP3 “Rotor Structure and Materials” of the UPWIND project. Static tests to failure of OB prismatic coupons are simulated using FEM. A detailed stress analysis is performed, investigating each ply separately. Material non-linear behaviour, failure criteria and progressive damage scenarios are implemented in a thick shell element to predict damage onset and propagation, failure loads and failure patterns. In-plane elastic properties of the OB UD material are presented with the corresponding experimental data and curve fit equations used to model material performance. Damage initiation and propagation conditions are discussed and the results are compared with experimental data. Furthermore, life prediction of composite laminates under cyclic loading is considered. The FADAS (FAtigue DAmage Simulator) methodology based on a ply-to-laminate approach is presented, in which the fatigue load applied on a laminate is conveyed to a plane stress field at each ply, inducing damage progression and stress redistribution which in their turn affect the laminate strength and stiffness. The methodology proposed, implements on one hand simple phenomenological models to describe strength and stiffness loss of each ply due to fatigue loading and on the other hand an adequate failure criterion (Puck), to predict damage progression caused by different failure modes. The model is capable of predicting strength and stiffness of the laminate after arbitrary, constant amplitude or variable amplitude biaxial fatigue loading, once the properties of the constitutive ply are defined. In this report, model implementation into FE thick shell formulation is evaluated by comparing preliminary theoretical predictions with constant amplitude fatigue data from multidirectional Glass/Epoxy laminates.

Contents

STATUS, CONFIDENTIALITY AND ACCESSIBILITY										
Status				**Confidentiality**				**Accessibility**		
S0	Approved/Released			**R0**	General public			Private web site		
S1	Reviewed			**R1**	Restricted to project members			Public web site		
S2	Pending for review			**R2**	Restricted to European. Commission			Paper copy		
S3	Draft for commends	**X**		**R3**	Restricted to WP members + PL	**X**				
S4	Under preparation			**R4**	Restricted to Task members +WPL+PL					

PL: *Project leader* **WPL:** *Work package leader* **TL:** *Task leader*

1. Introduction

The objective is to formulate and develop a shell-based finite element (FE) numerical methodology for life prediction, as well as residual strength and stiffness of wind turbine rotor blades made of fibre reinforced plastics (FRP), subjected to irregular cyclic loads. Development of such a numerical tool for predicting the mechanical response of the rotor blade is a complicated problem consisting of several major tasks: (i) non-linear stress analysis of the multilayer structure, (ii) failure prediction of the building layer under static or cyclic loads by giving the option of using a number of different new generation failure criteria not always available in commercial codes, (iii) modelling of both, progressive property degradation due to fatigue and sudden property change due to failure and finally, (iv) formulation of "overall structural failure" condition, resulting in prediction of remaining life, residual strength and stiffness. The algorithm for fatigue damage simulation (FADAS) as well as the set of new failure criteria that will be part of the proposed FE-shell formulation is implemented in ANSYS FE package.

Fatigue Damage Simulator (FADAS)

The concept of modelling damage development in multilayer laminates under quasi-static loads has been discussed theoretically to some extent the last decade. However, very limited research results are only available from modelling damage accumulation as a result of cycling. One of the reasons for the lack of work in this field, besides the considerable inherent difficulties associated with the multitude of failure mechanisms and their interaction, is the huge effort required to create comprehensive material property databases with test results from static, cyclic and residual strength experiments under multi-axial loading conditions. The proposed simulation procedure was based on OPTIDAT database.

The numerical simulation tool, FADAS, is composed of the following modules.

(i) Non-linear stress analysis. Material non-linearity was taken into account to model adequately the highly non-linear in-plane shear response and the usually moderate non-linearity observed under compression in the transverse direction of a FRP UD layer. A 3D shell formulation was used, featuring 1st order shear theory kinematics (Mindlin formulation) so as to model efficiently up to moderately thick composite laminates.
(ii) Failure prediction under static loads. While there are too many theories predicting failure of an orthotropic ply under complex 3D states of stress, some of them being already implemented in commercial FE packages, there are considerably less predictive schemes for laminate failure, none of which being available with FE codes. In these theoretical schemes, of paramount importance is the discrimination between the various failure modes encountered in FRP composites and the resulting material property degradation allowing post-FPF analyses. Several such failure criteria sets, e.g. Puck, were implemented in the finite element routine of ANSYS.
(iii) Life prediction under cyclic loads. Theoretical attempts for engineering models to predict life of laminated composite structures under cyclic complex states of stress are difficult to find in the literature and therefore, no commercial FE packages exist implementing such theory. Appropriate residual strength and stiffness theories were implemented in the FE code so as to formulate life prediction procedures under cyclic loading. The algorithm takes into account that at the start of cyclic loading the strength of the material is greater than the maximum cyclic stress at each point of the structure. Increasing the number of cycles leads to non-uniform material property degradation, i.e. depending on the stress state of each point and of course the number of cycles. At a certain number of cycles, after continuous stiffness degradation and stress redistributions, failure begins at points where residual strength drops to the level of the applied stress.
(iv) Rules for strength and stiffness degradation. Considering a certain point at the structural component, as failure occurs in a ply of the laminate, the stiffness tensor of that ply is modified

using fit to purpose rules (sudden damage), depending on the mode of failure. On the other hand, under cyclic loading, both stiffness and strength tensors are gradually modified, with the number of cycles, so as to model progressive damage development. This is accomplished by using appropriate criteria (progressive damage rules). All above mentioned degradation rules were derived by analyzing data of OPTIDAT database.

Preliminary model verification concerning static strength and CA fatigue is performed by using data from OPTIDAT.

1.1 Static Loading

State-of-the-art design calculations for rotor blades, according to International Standards as well as widely accepted practices on mechanics of composites, consider FRP materials as linear up to failure and are in essence of “safe life” type in the sense no damage is allowed in the structure under the extreme static or fatigue loading cases. Damage in only one layer, either matrix cracking or fibre breakage is considered as the design limit condition. This corresponds to what is better known as state of “First Ply Failure” (FPF) for composites. However fibre reinforced composites accumulate damage, resisting in total failure through stress redistribution mechanisms.

However, after that load level, usually the composite laminates, depending also on the stacking sequence, exhibit substantial load bearing capacity up to ultimate failure, “Last Ply Failure” (LPF), which remains unexploited. Germanischer Lloyd since its 2004 edition and the latest DNV standard (DNV-OS-J102), have adopted the implementation of stress cases in which limited material damage, mainly in the form of matrix cracks that run parallel to the fibres, is still acceptable. Although not requested by design regulations at present, to correctly implement such type of analyses in blade design one needs to fully characterize material elastic properties, highly non-linear in some aspects, use failure criteria accounting for the various failure modes encountered in FRP composites and utilize the appropriate stiffness and strength degradation scenarios.

Numerous anisotropic failure criteria have been proposed up to now for FRP composites to assess damage initiation. They can be broadly distinguished to *macroscopic* such as the quadratic form of failure tensor polynomial, better known as Tsai-Wu criterion [1] and those that discriminate between different failure modes, a concept introduced by Z. Hashin [2]. He has first presented a phenomenological failure criterion with separate equations to describe different modes of damage. Theoretical base for this assumption was Mohr hypothesis for brittle materials that fracture is exclusively created by stresses applied on the fracture plane. Puck et al. [3] have established a more generalized set of criteria, providing a number of user defined parameters enhancing modelling flexibility. Comparison between several failure criteria and a large discussion on their efficiency in correctly predicting failure, took place in the ‘World Wide Failure Exercise’ [4].

After failure onset, progressive damage scenarios due to strength and stiffness degradation, are of vital importance in predicting ultimate load at final rupture, LPF. Chang et al [5] proposed a progressive damage analysis implementing a failure criterion that distinguishes between different failure modes. An analytical expression was used to model the non-linear shear stress-strain behaviour. An abrupt elastic degradation rule was used, reducing the mechanical properties, depending on the predicted failure mode. Lin et al [6] have suggested a linear degradation rule only for the transverse, to the fibre direction, elastic modulus. Puck et al [7], [8] have introduced an efficient albeit more complex progressive damage rule for the transverse elastic and shear modulus respectively, as well as for Poisson ratios.

A detailed investigation of failure predictions using the Puck criteria is presented in this report suggesting best practice rules for this type of Glass/Epoxy system. Non-linear material behaviour, failure criteria and progressive damage scenarios are implemented in the

commercial finite element code ANSYS v.9.0, in a shell element (SHELL 181), but can be also easily transferred to any other FE platform, prompting for damage tolerant design of wind turbine rotor blades. A layer by layer stress analysis is carried out in a variety of laminated coupons of different stacking sequences that are statically loaded to failure. Either tensile or compressive tests are performed and detailed experimental data in the form of stress-strain curves are compared with FEM results. The agreement between the two sets of data is remarkably good.

1.2 Cyclic Loading

Life prediction of composite laminates subjected to cyclic loading has been a major research issue during the past decades. The complexity and variety of damage mechanisms developing and interacting with each other inside a composite structure during fatigue loading prevented the development of life prediction schemes based on the good understanding and modelling of micromechanical damage occurring inside the lamina, such as transverse matrix cracking, random fibre breakage or matrix-fibre debonding or at laminate level, such as delaminations and local buckling. Instead of that, extensive testing is been performed each time, to characterize typical composite lay-ups in order to define, in a purely phenomenological laminate level approach, their performance under different fatigue loading conditions.

In order to achieve applicable engineering models able to predict mechanical properties of structural composite laminates, such as strength, stiffness or life, while as little experimental effort as possible is required, several theories have been proposed. Some of them try to link damage parameters in the micro or meso scale to useful engineering properties of a multidirectional laminate. For example, Talreja [9] characterizes the damage state of the composite through a vector set, each component representing a specific cracking mode, related theoretically to strength and stiffness properties. Daniel in [10] suggests that fatigue life can be expressed as a function of the number of cycles required for matrix crack saturation. Varna et al. [11] propose as characteristic property the crack opening displacement parameter, along with computational methodologies for its determination, related with stiffness degradation through their model. In the same spirit, Song and Otani [12] or Charewitz et al. [13] link fatigue life or residual strength components with the density of various failure events in the laminate after fatigue. Looking macroscopically the constituents of the laminate, Reifsneider et al. [14]-[16] developed the Critical Element Model which distinguishes between critical (causing overall failure) and sub-critical (undergoing strength and stiffness degradation) elements inside the composite. They propose strength and stiffness degradation (as several other researches do), as convenient quantities for the description of damage. Shokrieh and Lessard [17]-[18] developed their Generalized Material Property Degradation Model, which considers the 3D stress state developing in each ply during fatigue while using again strength and stiffness degradation to model stress redistribution and modification of the failure tensor components that ultimately lead to macroscopic failure of the composite.

While models linking damage events in the micro-scale (e.g. crack density) to mechanical properties of composites might in the future become applicable for structural design, semi phenomenological models as the latter ones, can offer a reasonable tool for design of composite structures, once the experimental effort for complete, mechanical characterization of the basic ply in terms of static strength, fatigue life and elastic behaviour has been spent. Despite this considerable experimental cost, they turn out to be more economical compared to the characterization of specific lay-ups, if one considers their general applicability once a basic ply has been fully characterized. More so, since in contemporary large scale composite structures, such as Wind Turbine Rotor Blades, that are made of multidirectional laminates composed of a basic prepreg or UD layer and which undergo dynamic loading, such methodologies have the advantage of modelling the direct consequences of damage and local failures in ply level (such as stiffness and strength loss). This ‘progressive damage’ approach makes possible the prediction and assessment of damage events, helping to distinguish between ‘catastrophic’ and ‘non-catastrophic’ failures, thus helping e.g. implement Last Ply Failure (LPF) instead of First Ply Failure (FPF) structural design tools, leading ultimately to full

use of the composite material and justification -or reconsideration- of the severe safety factors applied today in design.

In this report, a plate theory model for life prediction of multidirectional laminates based on an extensive database for a RIM Glass/Epoxy composite is developed. Simple phenomenological stiffness and strength degradation models are implemented in an effort to minimize the experimental cost required for material characterization. State of the art formulations for the Constant Life Diagram (CLD) are adopted, while the failure criterion of Puck [3], [7]-[8] is implemented.

2. Material Performance

2.1 Mechanical Properties

Mechanical properties are obtained through a series of coupon tests. A standard specimen geometry is adopted for all tests either static or fatigue for the unidirectional material [19]. It is of rectangular shape with nominal dimensions of 145mm long, 25mm wide and 35mm gauge length between tabs. Number of layers, hence thickness, varies depending on the property under investigation. Unidirectional coupons loaded in the fibre direction are nominally 3.52mm thick having 4 layers through the thickness while those loaded transversely to the fibres are 6.16mm composed of 7 layers. The corresponding specimen for multidirectional material lay up, composed of layers at 0, +45 and -45 degrees, is 150mm long, 25mm wide and there is a 40mm gauge length between tabs. Nominal thickness is considered to be 6.57mm [19]. For shear modulus and strength evaluation, ISO 14129 standard coupon is used. Strain measurements are conducted on both coupon faces, in the middle of the gauge length and an average is considered as the experimentally obtained value.

However as previously stated, FRP composites with organic matrix, exhibit highly non-linear stress-strain behaviour, especially in shear and compression transversely to the fibres, Figs.1, 2, while they perform linearly in tension and compression parallel to the fibres, see Fig.3.

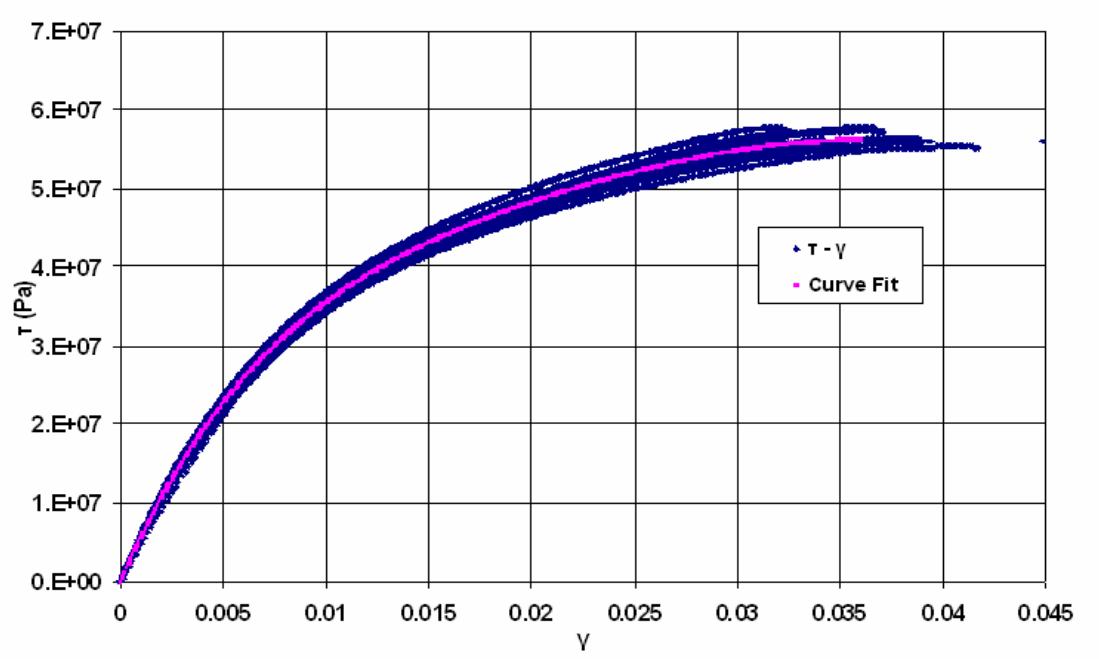

Fig. 1: In-plane shear stress-strain behaviour of OB UD Glass/Epoxy.

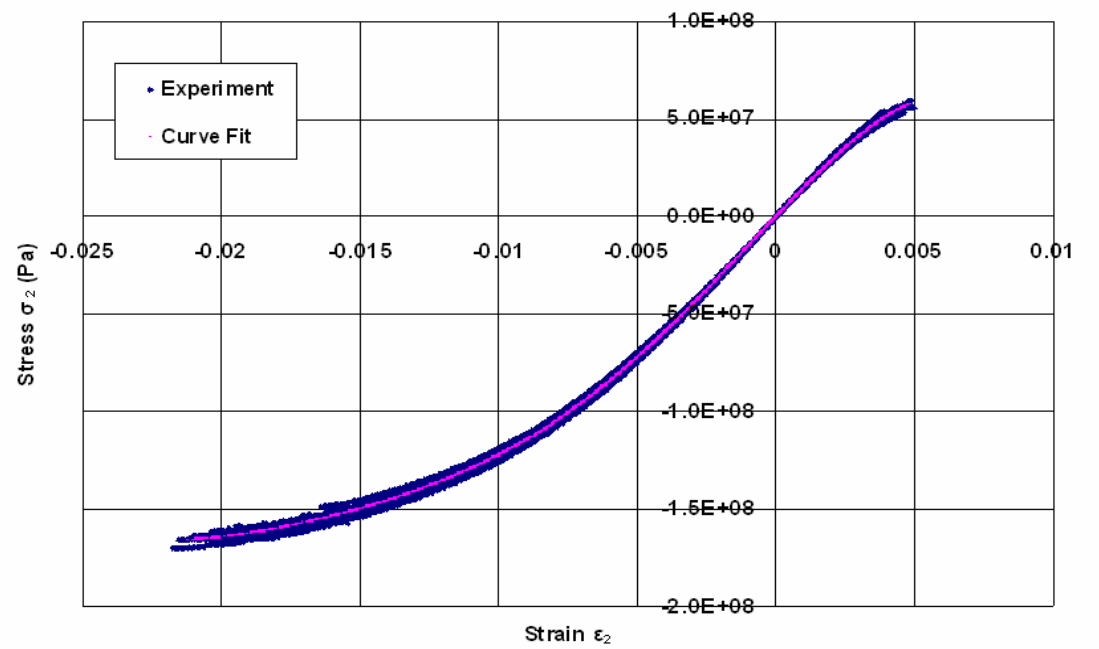

Fig. 2: Tension-compression in the transverse to the fibre direction for OB UD Glass/Epoxy

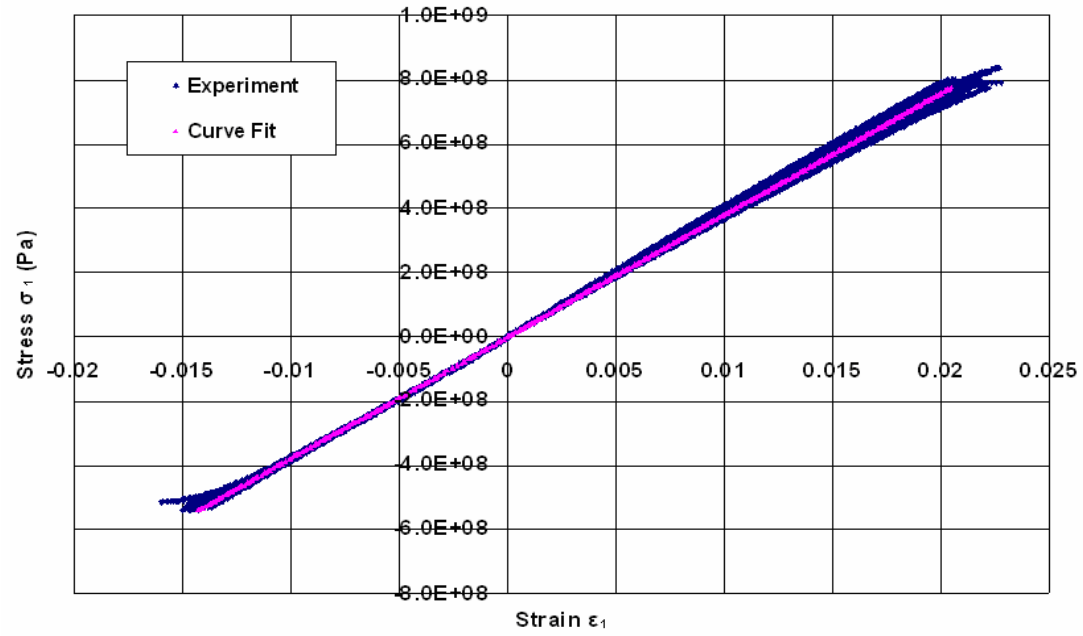

Fig. 3: Tension-compression parallel to the fibres for OB UD Glass/Epoxy

Major Poisson ratio obtained from tensile experiments in UD material parallel to the fibres can be described with a linear regression function; see Fig. 4 and Table 1.

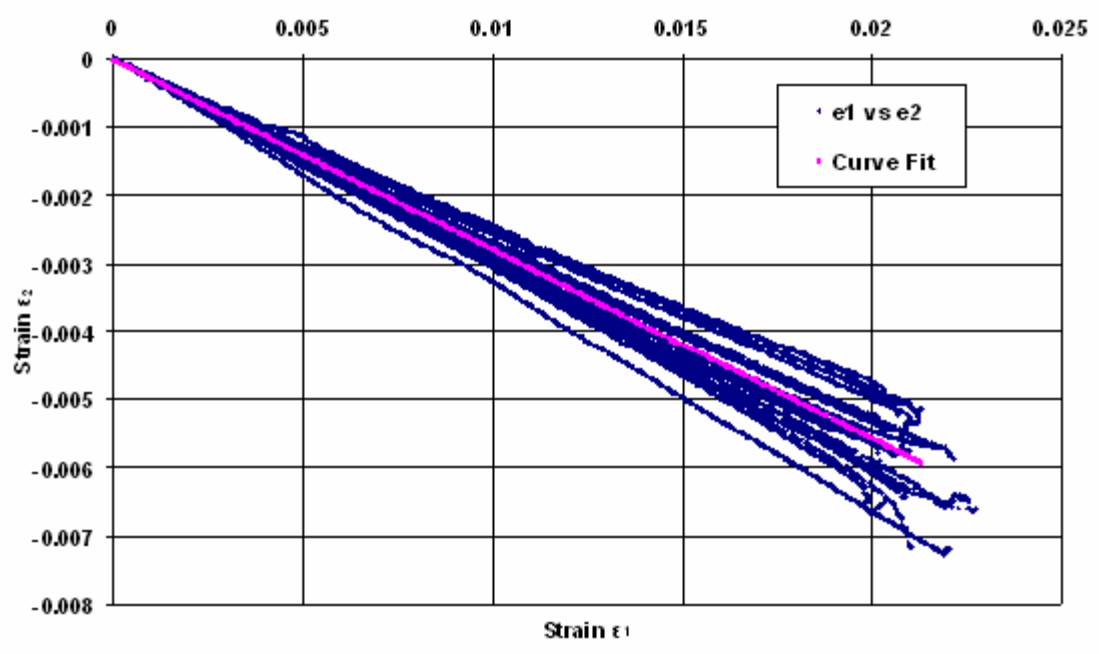

Fig. 4: Major Poisson ratio of OB UD Glass/Epoxy

Provided the $\sigma_i = f(\varepsilon_i)$ curve fit equation is defined from the experimental data, the tangential modulus of elasticity is computed at every load step by:

$$E_i = \frac{\partial \sigma_i}{\partial \varepsilon_i} \quad \text{and} \quad G_{12} = \frac{\partial \tau}{\partial \gamma} \tag{1}$$

In the fibre direction, the material is considered to remain linear until final fracture either in tension or compression. The respective elastic modulus and major Poisson ratio are taken equal to:

$$\begin{aligned} E_1 &= 37.95 \text{ GPa} \\ \nu_{12} &= 0.2778 \end{aligned} \tag{2}$$

The non-linear behavior of the OB UD material is accurately described using a more elegant analytic expression of the Ramberg-Osgood type [20], introduced by Richard and Blacklock [21]. The general form of the equation, expressed either with respect to stress or strain, is given by:

$$\sigma = \frac{E_o \varepsilon}{\left[1 + \left(\frac{E_o \varepsilon}{\sigma_o}\right)^n\right]^{\frac{1}{n}}} \quad \text{or} \quad \varepsilon = \frac{\sigma}{E_o \left[1 - \left(\frac{\sigma}{\sigma_o}\right)^n\right]^{\frac{1}{n}}} \tag{3}$$

Tangential Young modulus is given by:

$$E_t = \frac{d\sigma}{d\varepsilon} = \frac{E_o}{\left[1+\left(\frac{E_o\varepsilon}{\sigma_o}\right)^n\right]^{\frac{1}{n}+1}} = E_o\left[1-\left(\frac{\sigma}{\sigma_o}\right)^n\right]^{\frac{1}{n}+1} \quad (4)$$

The corresponding relation for the shear modulus is:

$$G_{12_t} = \frac{d\tau}{d\gamma} = \frac{G_{12_o}}{\left[1+\left(\frac{G_{12_o}\gamma}{\tau_o}\right)^{n_s}\right]^{\frac{1}{n_s}+1}} = G_{12_o}\left[1-\left(\frac{\tau}{\tau_o}\right)^{n_s}\right]^{\frac{1}{n_s}+1} \quad (5)$$

Further, parameters for the transverse to the fiber behavior are different for tension and compression. Comparison of the theoretical curves and the experimental data, along with the values of the respective parameters are presented in Figs. 5 to 8.

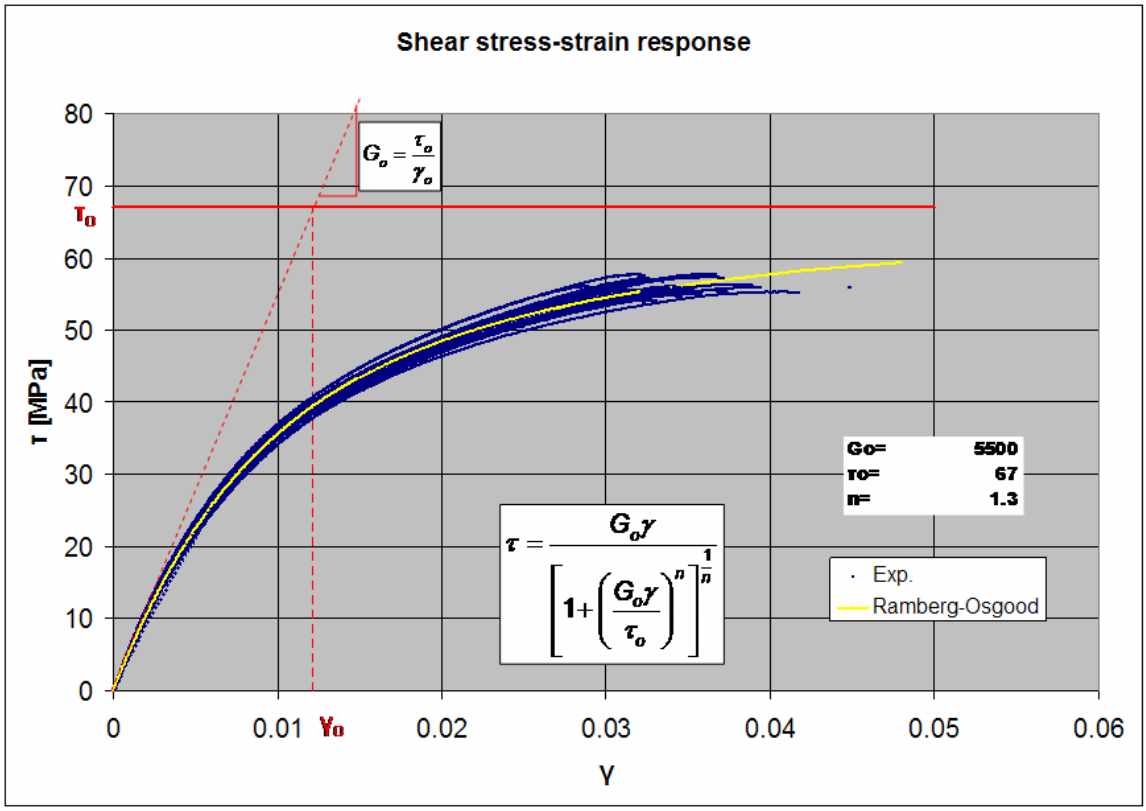

Fig. 5: In-plane shear stress-strain behaviour of OB UD Glass/Epoxy.

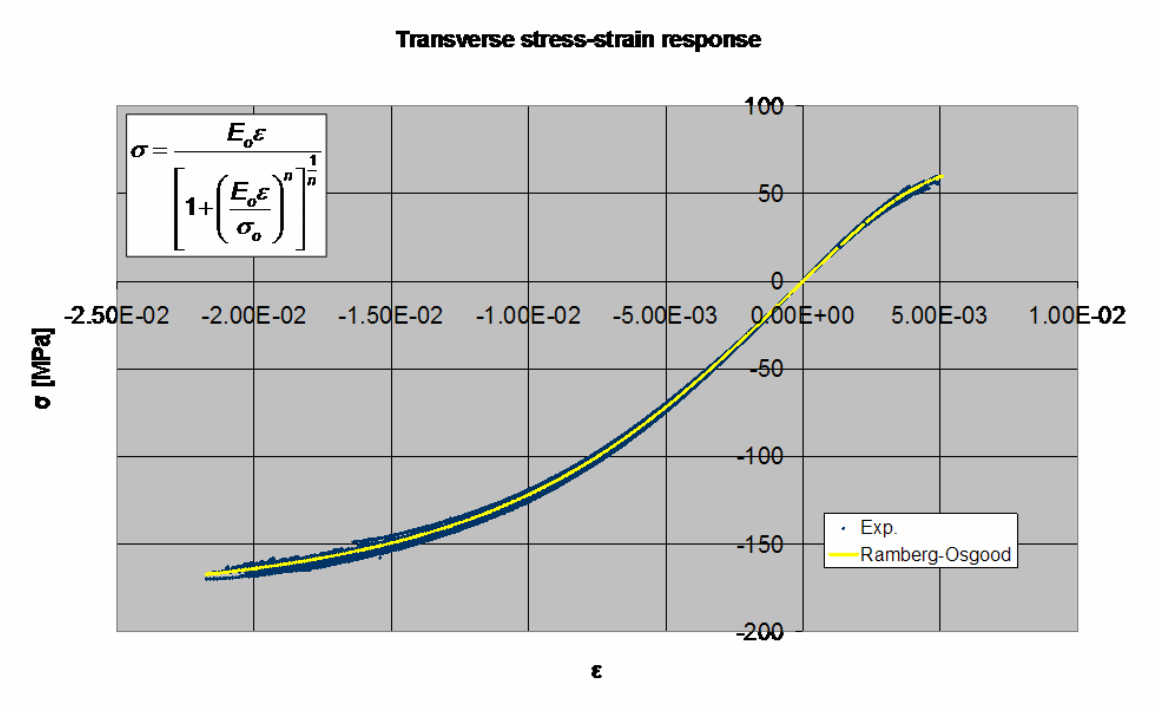

Fig. 6: Tension-compression in the transverse to the fibre direction for OB UD Glass/Epoxy

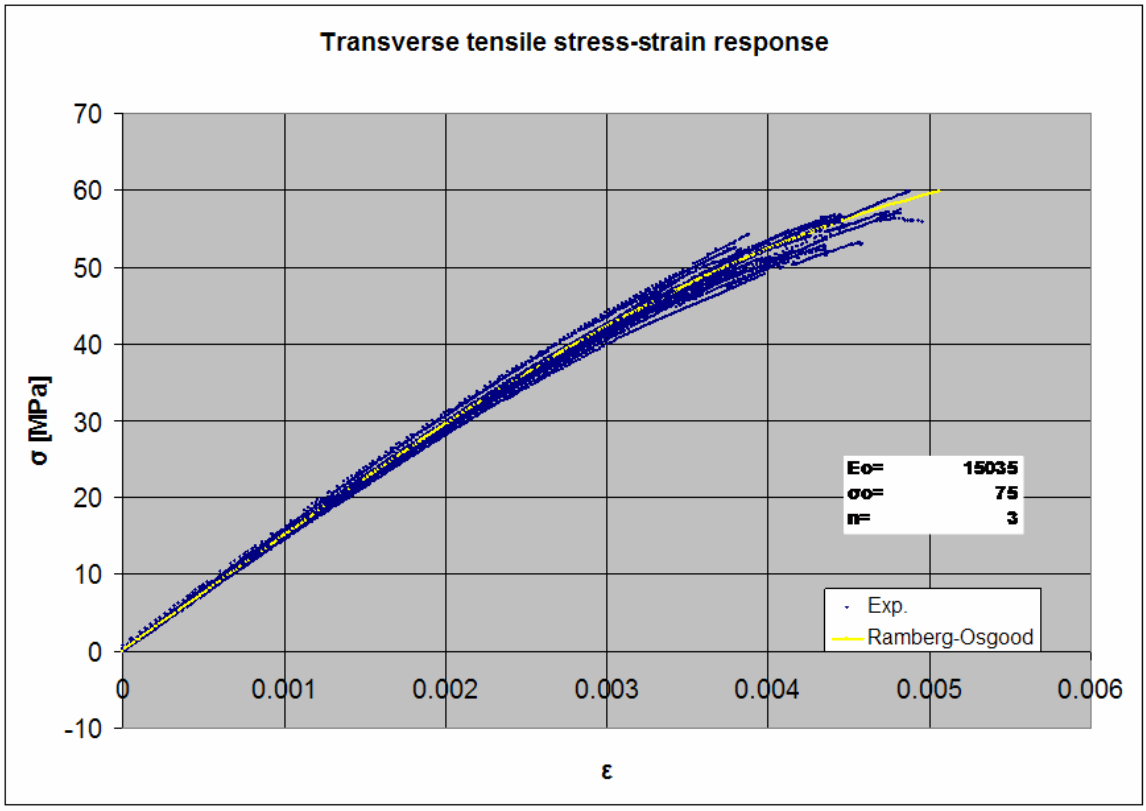

Fig. 7: Tension in the transverse to the fibre direction for OB UD Glass/Epoxy

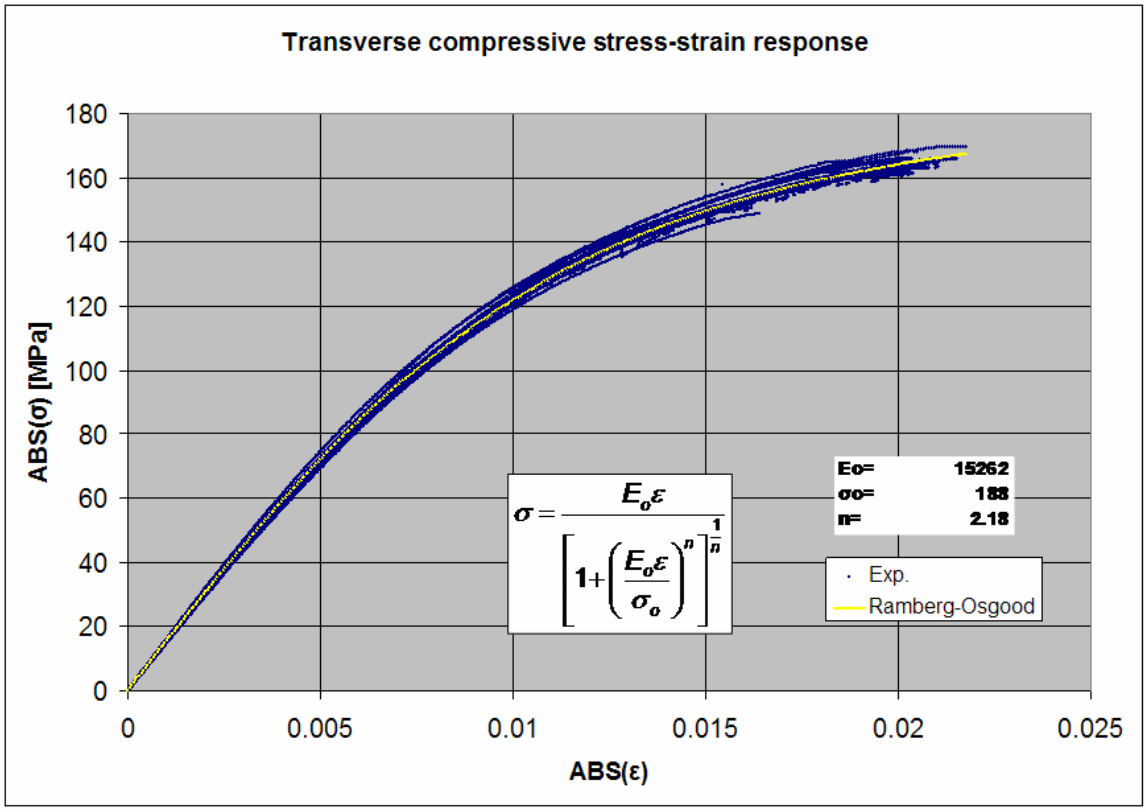

Fig. 8: Compression in the transverse to the fibre direction for OB UD Glass/Epoxy

2.2 Stiffness Degradation

In-plane stiffness of the lamina is degrading due to several reasons, e.g. sudden stiffness degradation due to some kind of failure occurrence or progressive stiffness reduction due to fatigue. In general, the latter is non linear and various formulations have been proposed in literature to describe it. Herein it is assumed to depend only on the fatigue life fraction, i.e. the fraction of the fatigue cycles versus the nominal fatigue life at the current stress level.

An example of how stiffness degradation is estimated from the experimental data is shown below in Figs.9-12 for OB UD cycled at the fiber direction under R=-1.

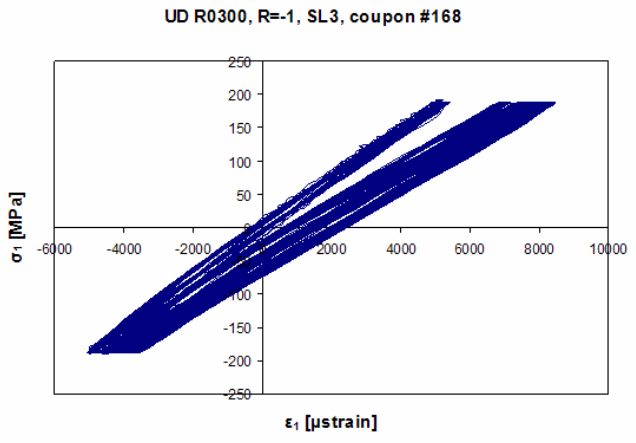

Fig. 9: Stress-strain loops of OB UD under CA fatigue

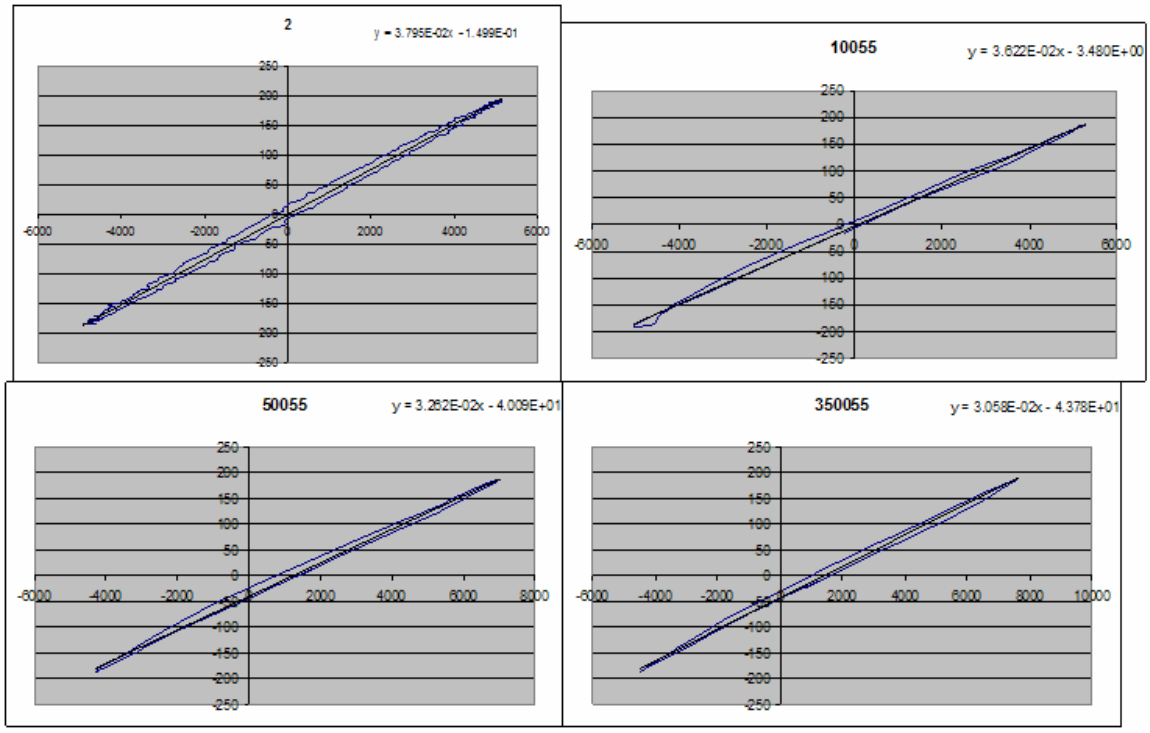

Fig. 10: Modulus determination by curve fitting discrete cycles (2, 10,055, 50,055, 350,055)

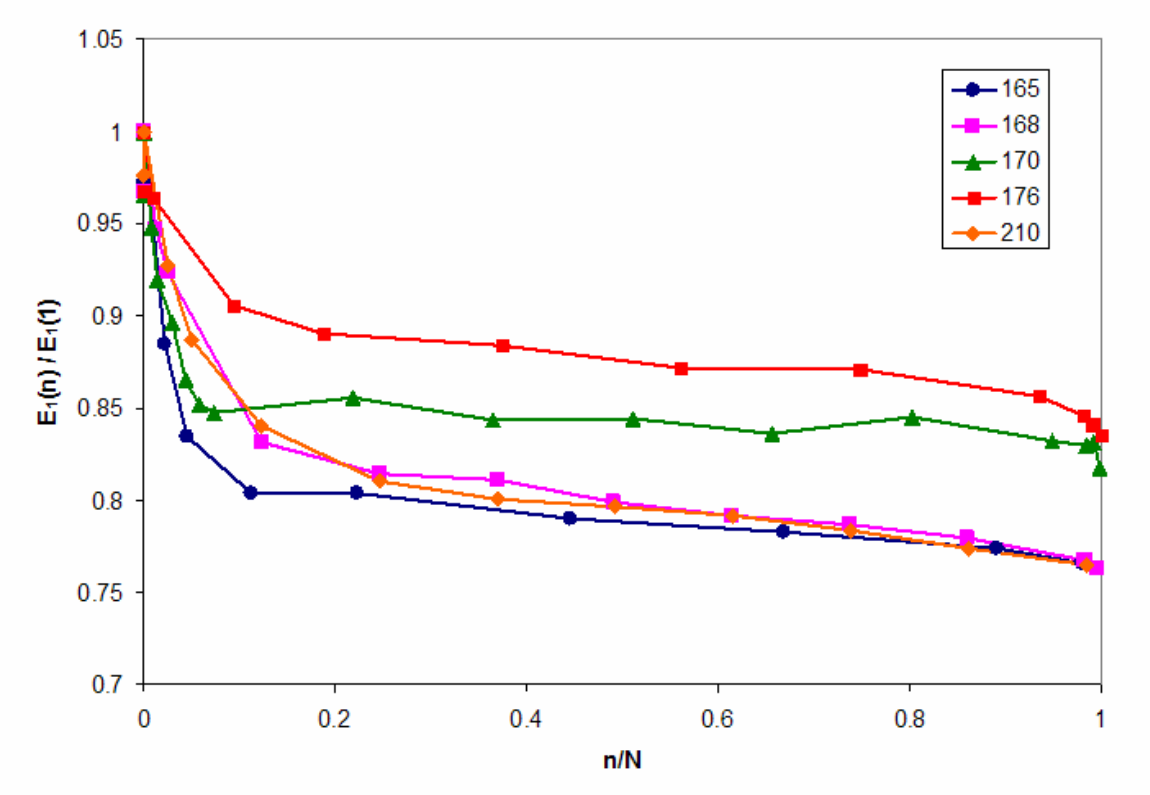

Fig. 11: Modulus degradation with life spent from different coupons

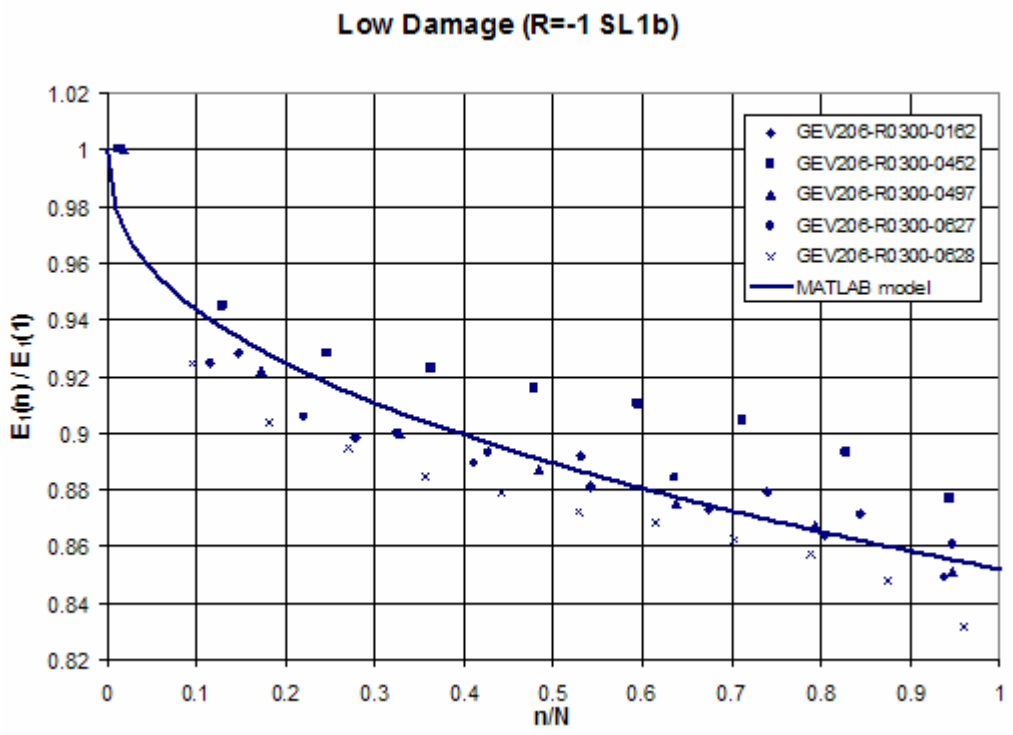

Fig. 12: Modulus degradation model for UD in the fiber direction (low damage case)

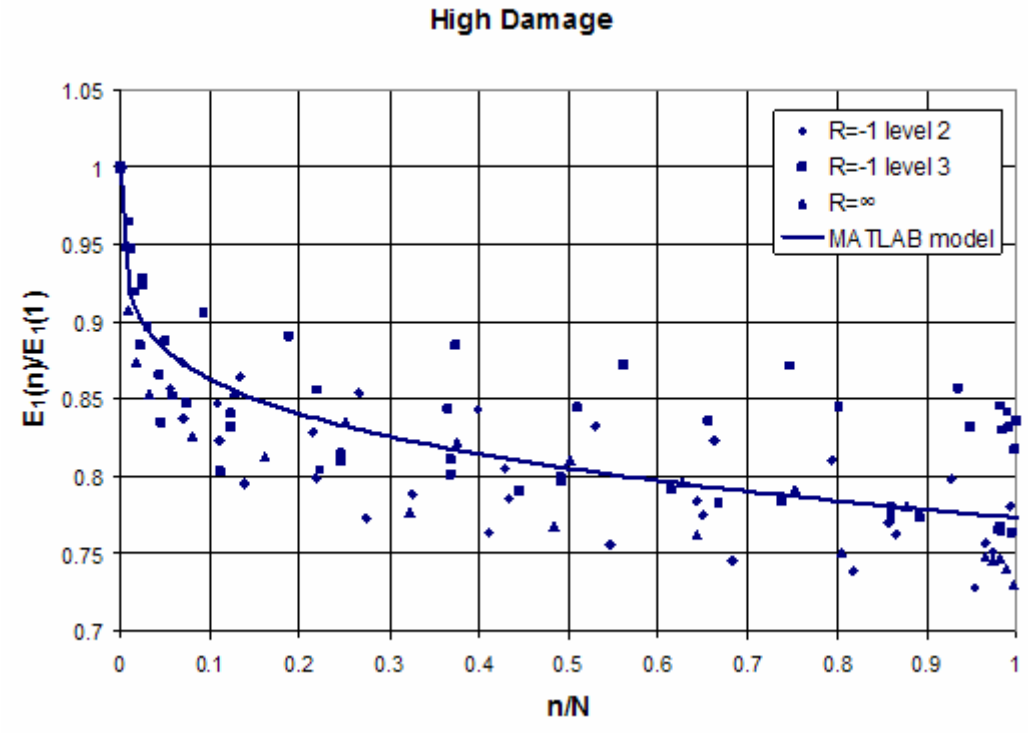

Fig. 13: Modulus degradation model for UD in the fiber direction (severe damage case)

Regression models plotted in Figs. 12, 13 are given by the following equation:

$$\frac{E_1(n)}{E_1(1)} = 1-(1-a)\left(\frac{n}{N}\right)^b \qquad (6)$$

With a=0.8519, b=0.4191 for the low damage model and a=0.7733, b=0.2182 for the high damage model respectively. As it is seen, E_1 modulus degradation is implicitly dependent on R and σ_{max} values since the allowable number of cycles, N, is determined from the CLD data.

Stiffness degradation models for the Young modulus transverse to the fibres and the in-plane shear modulus are shown in Figs.14 to 16.

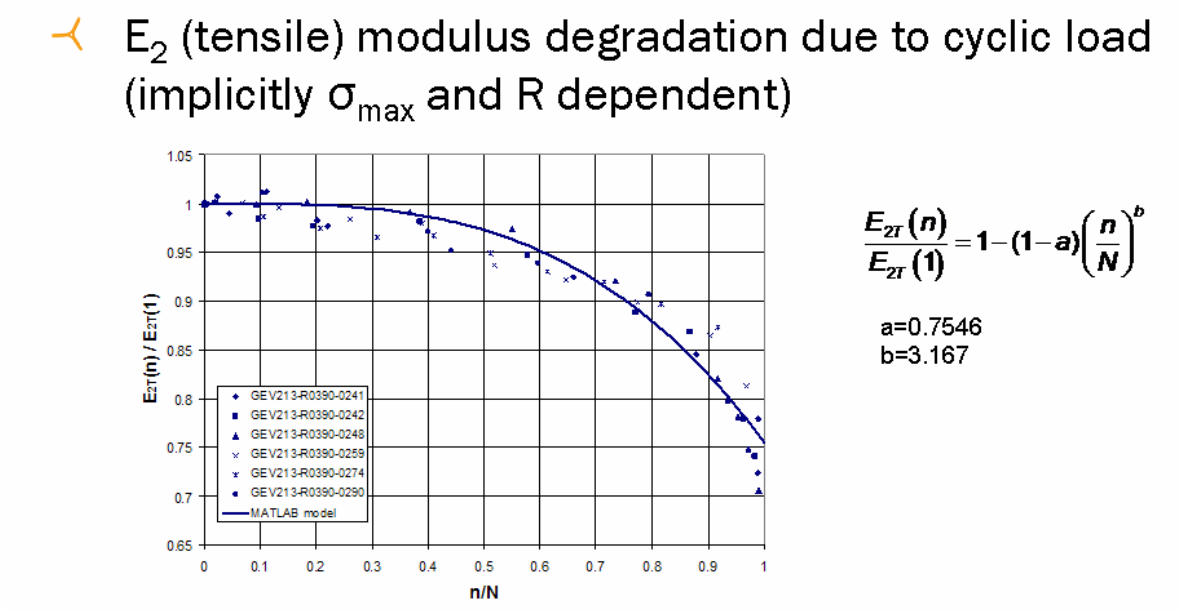

Fig. 14: Modulus degradation model for UD transverse to the fiber direction (T-T, T-C fatigue)

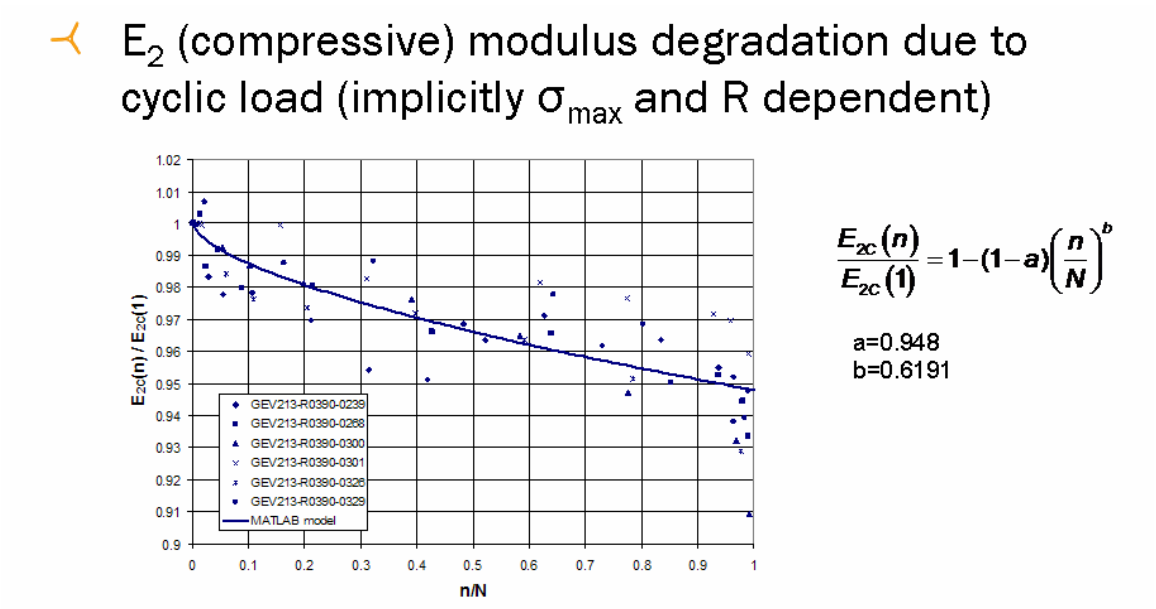

Fig. 15: Modulus degradation model for UD transverse to the fiber direction (C-C fatigue)

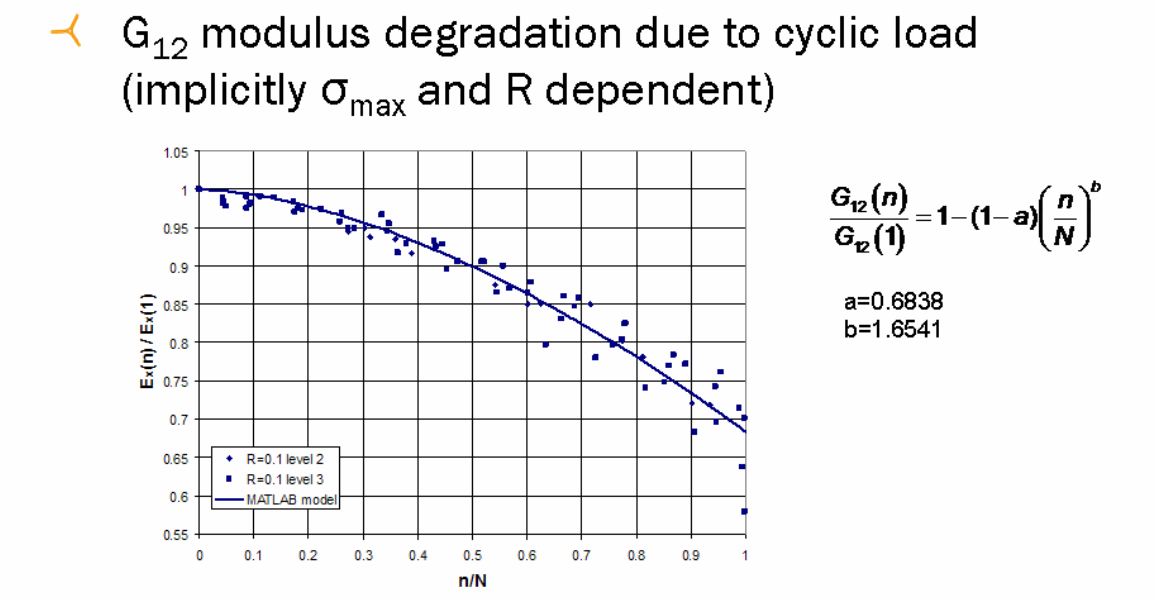

Fig. 16: In-plane shear modulus degradation model for UD Gl/Ep

Besides the progressive stiffness degradation due to fatigue, sudden stiffness degradation also occurs as a result of some kind of macroscopic failure in the lamina level or due to loading-unloading-reloading (L-U-R) cycles of the composite. The former is considered in one of the next sections of this report, in conjunction with the failure criterion used and the associated failure modes predicted. The latter type of stiffness degradation, although probably due to micro-cracking of the lamina, possibly in the interface region with the fibers, and individual fiber breaks is considered as a constitutive tensor property of the lamina. It is derived by means of dedicated experiments performed in the frame of OPTIMAT BLADES, [22], [23]; an example is presented in Fig.17. It is expected to affect theoretical predictions, especially in cases of VA loading. Considering a slightly greater unloading modulus, allows the consideration of residual strains as well.

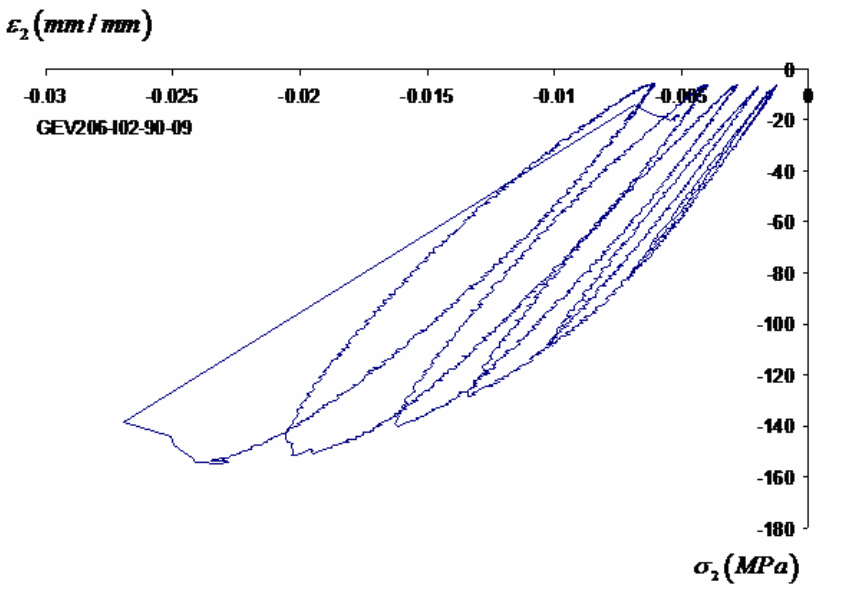

Fig. 17: Stress-strain curve of GEV206-I02-90 specimen tested in static L-U-R compression [22]

In-plane, sudden stiffness degradation models for the basic Gl/Ep lamina due to Loading-Unloading- Reloading cycles are presented in Figs. 18-22.

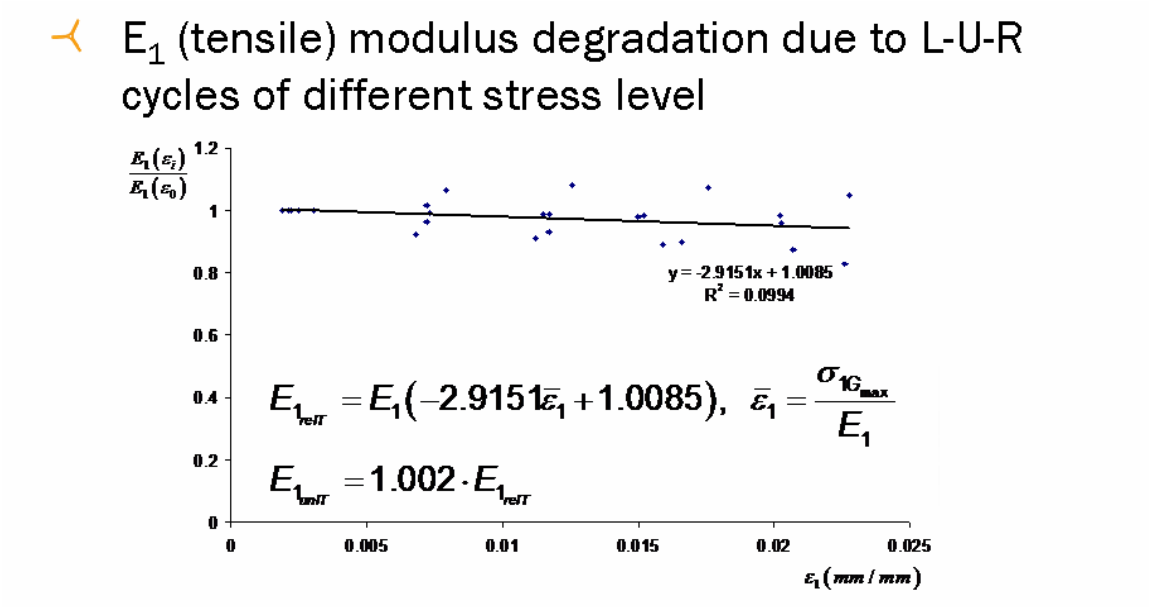

Fig. 18: Tensile E_1 modulus degradation due to static L-U-R cycles [22]

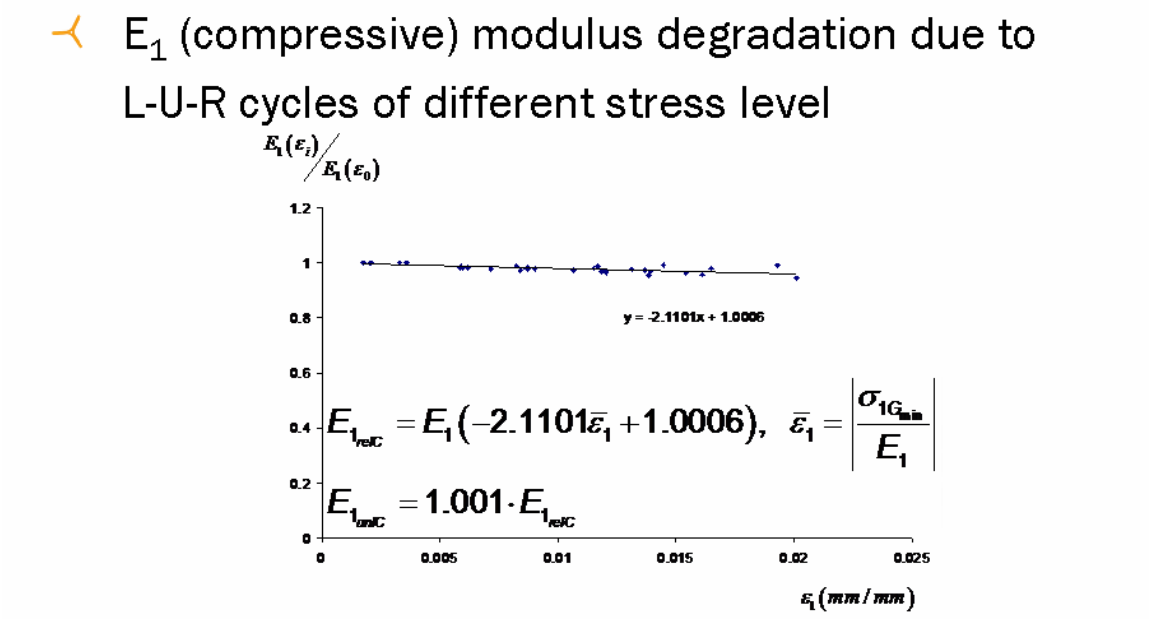

Fig. 19: Compressive E_1 modulus degradation due to static L-U-R cycles [22]

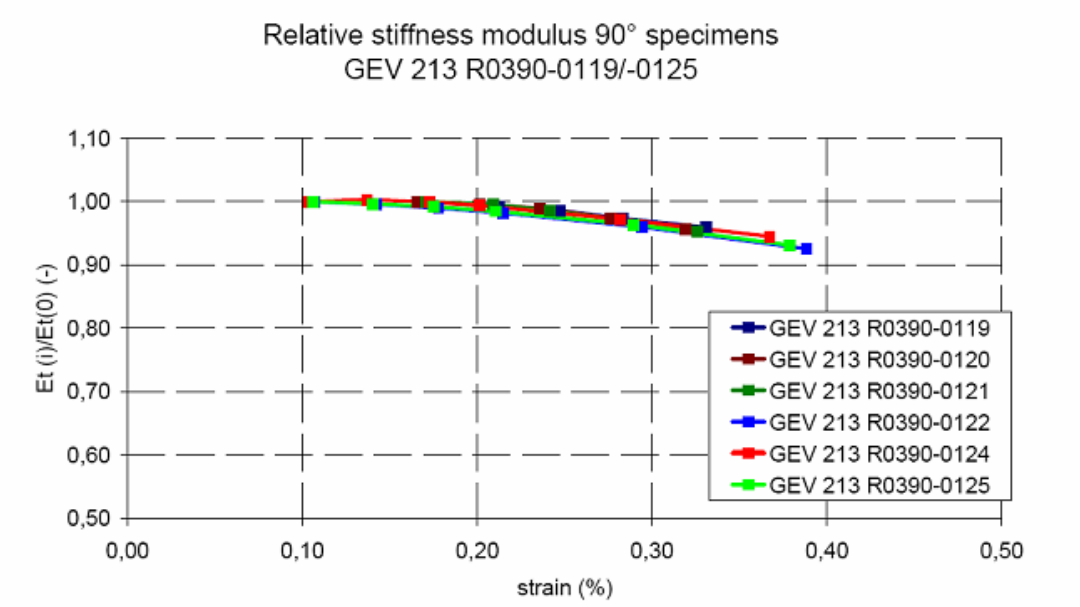

$$E_{2_{relT}} = E_{2oT}\left(-2.083 \cdot 10^{-9}\sigma_{2Gmax} + 1.04\right) \text{ in } [Pa]$$

$$E_{2_{unlT}} = 1.002 \cdot E_{2_{relT}}$$

Fig. 20: Tensile E_2 modulus degradation due to static L-U-R cycles [23]

- E_2 (compressive) modulus degradation due to L-U-R cycles of different stress level

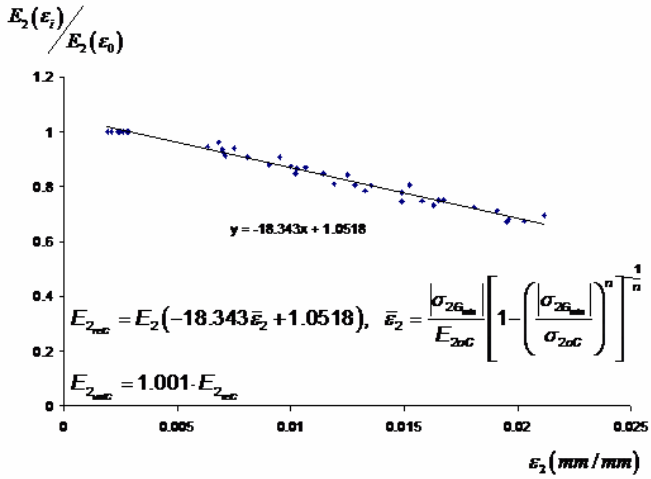

Fig. 21: Compressive E_2 modulus degradation due to static L-U-R cycles [23]

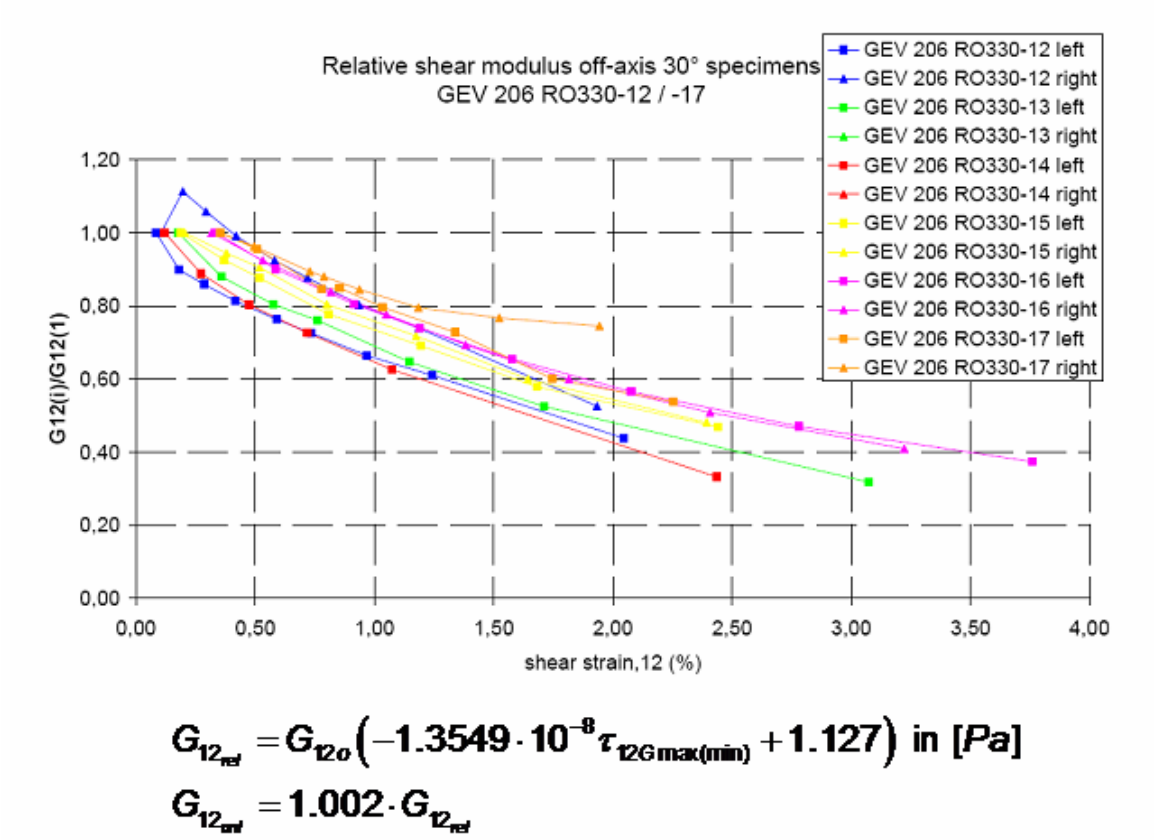

Fig. 22: Shear modulus, G_{12}, degradation due to static L-U-R cycles [23]

2.3 Strength Degradation

Static strength degradation or residual strength after fatigue in composites has been a research issue for quite some time. A variety of models have been developed, most of them non linear, including one or more parameters. As demonstrated in [24], the complexity of the model does not necessarily pay back in accuracy of the predictions. Therefore, the models used herein to describe the phenomenon are two: For the modelling of tensile residual strength along the principal material directions, under T-T ot T-C cyclic loading, as well as in shear, the linear degradation model proposed by Broutman & Sahu [25] is chosen. It is the simplest one available and it requires no residual strength testing, while at the same time it has been proven to produce always safe residual strength predictions under various stress conditions and lay-ups [26].

It is described respectively by the following equations:

$$X_{Tr} = X_T - \left(X_T - \sigma_{1max}\right)\left(\frac{n}{N_1}\right)$$

$$Y_{Tr} = Y_T - \left(Y_T - \sigma_{2max}\right)\left(\frac{n}{N_2}\right) \qquad (7)$$

$$S_r = S - \left(S - \sigma_{6max}\right)\left(\frac{n}{N_6}\right)$$

X_{Tr} and Y_{Tr} is the residual strength parallel and transversely to the fibers respectively, while S_r is the residual shear strength. σ_{1max}, σ_{2max} and σ_{6max} are the maximum cyclic stresses acting at the on-axis direction, transversely to the fibers and in shear, n is the number of fatigue cycles applied and N_i, i=1,2,6, the corresponding fatigue life at the specific stress level. Even though eq.(7) seems to be dependent only on the stress level, it also depends on the stress ratio through the fatigue life N, obtained for a specific stress ratio through the CLD used. The model can be implemented once the static strength and fatigue behavior at arbitrary R-ratios and stress levels are known.

Compressive strength in both on-axis and transverse directions has been shown not to degrade significantly due to fatigue [27]. When modeling compressive residual strength under C-C or T-C cyclic loading, a degradation equation simulating constant strength throughout the life with a sudden drop near failure of the following form is implemented:

$$X_{Cr} = X_C - \left(X_C - \sigma_{1max}\right)\left(\frac{n}{N_1}\right)^k$$

$$Y_{Cr} = Y_C - \left(Y_C - \sigma_{2max}\right)\left(\frac{n}{N_2}\right)^k \quad (8)$$

The exponent k is attributed a value of 50 to simulate the above mentioned behavior.

Derivation of above models was based on experimental data processing performed in [24]. A summary of experimental evidence is presented in Figs. 23 to 28 where the models used are denoted by BR or LM in Fig.28. A general remark from the experimental data is that residual strength in both principal material directions is not affected when cyclic stress of the opposite sign is applied, i.e. tensile strength is not reduced under purely compressive cycles and vice versa.

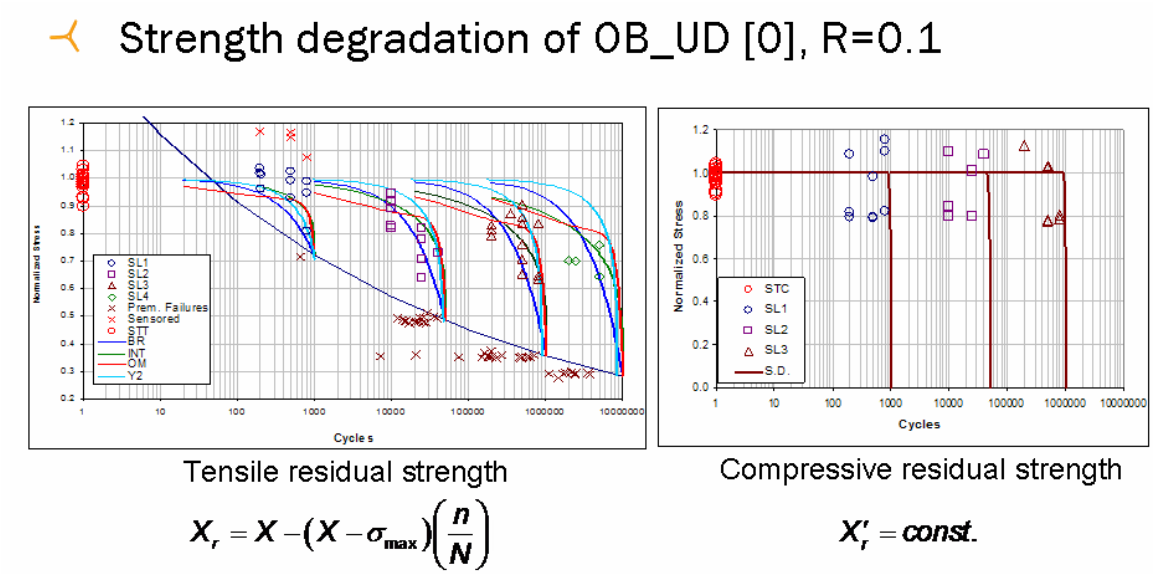

Fig. 23: Strength degradation of OB UD along the fibre direction under T-T CA cyclic loading

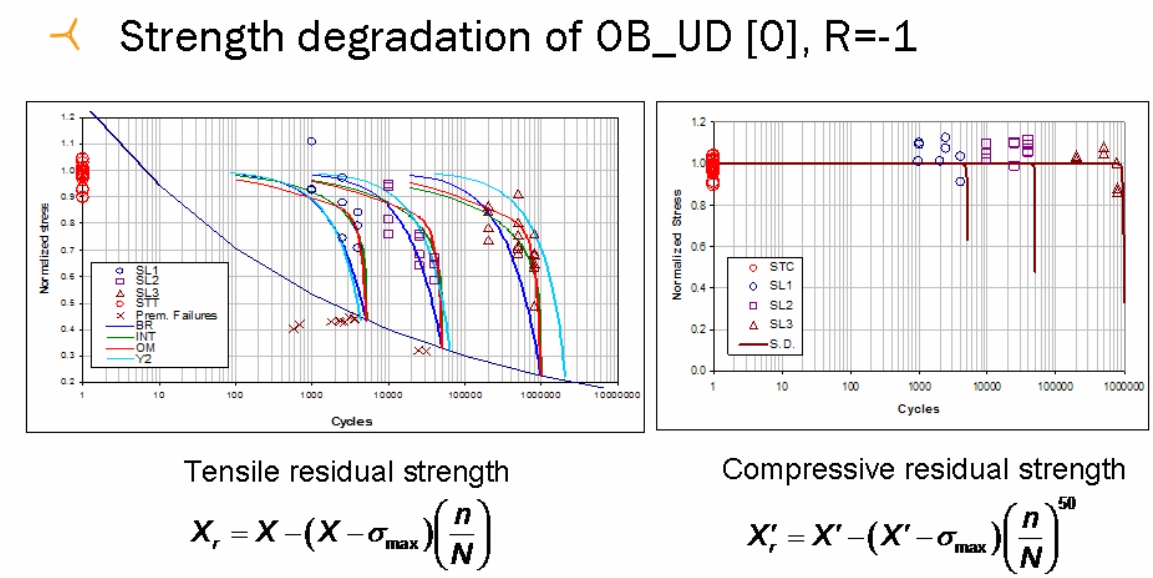

Fig. 24: Strength degradation of OB UD along the fibre direction under T-C CA cyclic loading

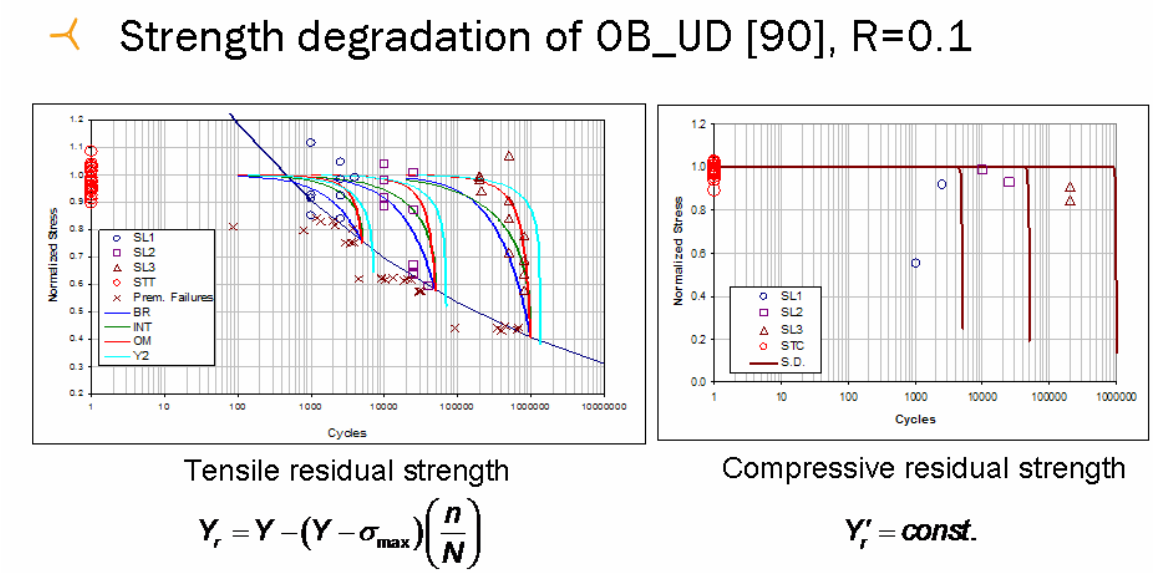

Fig. 25: Strength degradation of OB UD transversely to the fibre under T-T CA cyclic loading

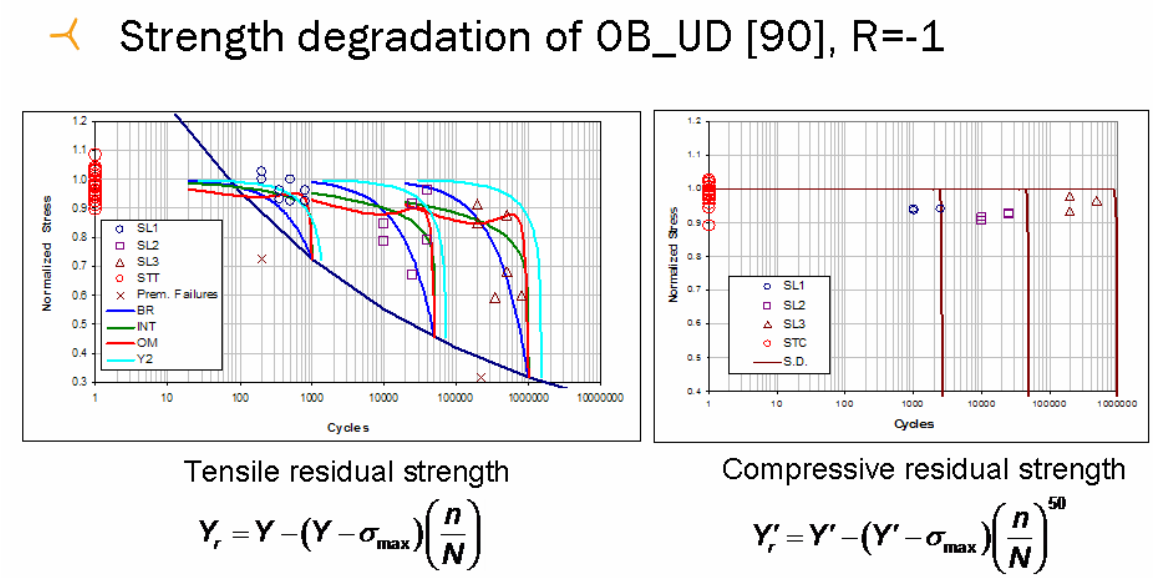

Fig. 26: Strength degradation of OB UD transversely to the fibre under T-C CA cyclic loading

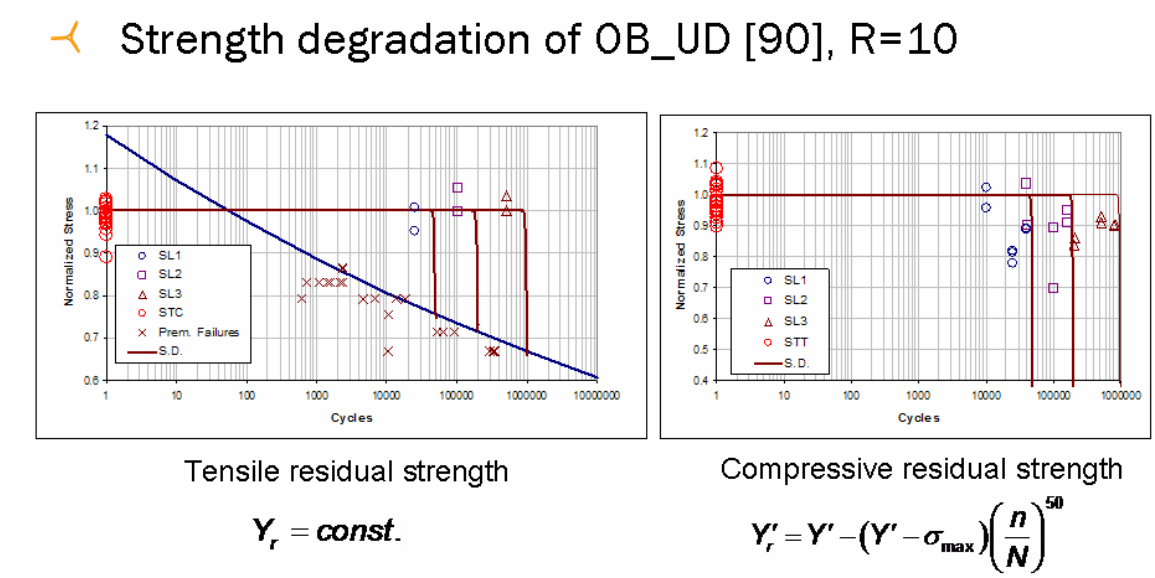

Fig. 27: Strength degradation of OB UD transversely to the fibre under C-C CA cyclic loading

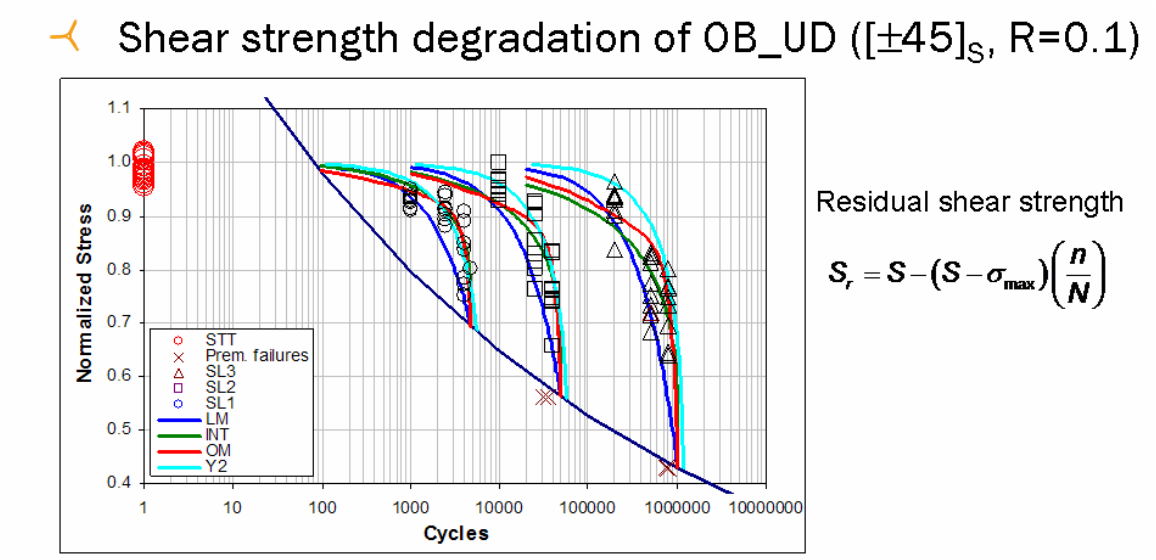

Fig. 28: In-plane shear strength degradation of OB UD under CA cyclic loading

3. Failure Onset

Material damage initiates and propagates as the load increases. Puck failure criterion is implemented to assess the magnitude of damage and to distinguish between different failure modes [3], [8].

Fiber failure effort or stress exposure factor, $f_{E(FF)}$, in tension (T) or compression (C) is estimated using the following conditions:

$$f^{T}_{E(FF)} = \frac{1}{X_T}\left[\sigma_1 + \left(\frac{E_1}{E_{f1}}\nu_{f12}m_{\sigma f} - \nu_{12}\right)\sigma_2\right] \le 1 \tag{9}$$

$$f^{C}_{E(FF)} = \frac{1}{X_C}\left|\sigma_1 + \left(\frac{E_1}{E_{f1}}\nu_{f12}m_{\sigma f} - \nu_{12}\right)\sigma_2\right| + \left(10\varepsilon_6\right)^2 \le 1 \tag{10}$$

σ_1 is the stress in the fibres direction and X_T, X_C are the ultimate tensile (UTS) and compressive (UCS) stresses of the unidirectional layer, see Table 1. It is noted that UCS is taken from tests using coupons of ISO geometry [28], since the standard coupon geometry previously mentioned, suffered from buckling. The value of the failure criterion for the fibres is referred to as $f_{E(FF)}$. E_{f1} and ν_{f1} is the elastic modulus and the Poisson ratio of the fibres. The term $m_{\sigma f}$ accounts for a stress magnification effect caused by the different moduli between fibres and matrix which leads to an uneven distribution of the stress σ_2 from a micromechanical point of view: in the fibres it is slightly higher than the matrix. For glass-fibre FRP, a value of $m_{\sigma f}\approx 1.3$ is suggested by Puck [3]. Term $(10\varepsilon_6)^2$ is a purely empirical factor accounting for shear contribution in fibre micro-buckling under compressive loads.

Table 1 Strength values (in MPa) for the reference OB UD Glass\Epoxy ply

X_T	X_C	Y_T	Y_C	S
776.497	686.0	54.0	167.0	80.0

Matrix failure effort transverse to the fibers due to tensile stresses, $\sigma_2>0$:

$$f^{A}_{E(IFF)} = \sqrt{\left(\frac{\sigma_6}{S}\right)^2 + \left(1 - p^{(+)}_{\perp\parallel}\frac{Y_T}{S}\right)^2\left(\frac{\sigma_2}{Y_T}\right)^2} + p^{(+)}_{\perp\parallel}\frac{\sigma_2}{S} + \left|\frac{\sigma_1}{\sigma_{1D}}\right|^6 \le 1 \tag{11}$$

This type of failure is denoted as mode A, see Fig.29, and results to cracks that open transversely to the applied load, parallel to the fibers. In the failure condition, σ_6 is the shear stress developed in the (1-2) principal plane of the layer. S is the in-plane shear strength, σ_2 is the normal stress transverse to the fibers and Y_T its respective ultimate, see Table 1. Shear strength derived from ISO 14129 tests is 56 MPa. For numerical simulation purposes and optimum reproduction of the stress strain curve and failure load of the ISO $[\pm 45]_s$ coupon, S is selected equal to 80 MPa, a value close to the strength value measured from the V-notched beam experiments [28].

The term σ_1/σ_{1D} accounts for matrix damage due to single fiber breakage before σ_1 reaches its ultimate X_T. For simplification, it is proposed by Puck [3] to set the ratio value equal to 0.9 of the

fibre failure effort. It is raised at high powers, e.g. 6 for brittle resins, so it affects the rupture condition only at high values of σ_1. The exponent of the term σ_1/σ_{1D} is an empirical parameter. Factor $p^{(+)}_{\perp\parallel}$ represents the slope of the failure locus (σ_2, σ_6) at $\sigma_2=0^+$. It is obtained with a fitting procedure on experimental data with positive normal stress ($\sigma_2 \geq 0$). Puck et al. [8] give guidelines for the determination of this parameter and some typical values for FRP materials. Specifically for Glass/Epoxy material a value equal to 0.3 was proposed.

Matrix failure effort transverse to the fibers when compressive stresses are developed, $\sigma_2 \leq 0$ and $|\sigma_2 / \sigma_6| \leq R^A_{\perp\perp} / |\sigma_{6c}|$:

$$f^B_{E(IFF)} = \frac{1}{S}\left(\sqrt{\left(\sigma_6^2\right) + \left(p^{(-)}_{\perp\parallel}\sigma_2\right)^2} + p^{(-)}_{\perp\parallel}\sigma_2\right) + \left|\frac{\sigma_1}{\sigma_{1D}}\right|^6 \leq 1 \qquad (12)$$

In that case cracks are formed parallel to the fibres, relatively closed when compared to those of mode A. The failure mode is denoted as B and the shear stresses σ_6 for failure onset are increased along with the magnitude of the compressive normal stress σ_2, see Fig.29. The parameter $p^{(-)}_{\perp\parallel}$ represents the slope of the failure locus (σ_2, σ_6) at $\sigma_2=0^-$. It is derived from experimental data with negative normal stress ($\sigma_2 \leq 0$). Puck et al [8] suggest again some typical values for FRP materials; 0.25 for Glass/Epoxy. Parameter $R^A_{\perp\perp}$ stands for the ultimate transverse shear strength and it is defined analytically by Puck et al. [8].

Further increase of the compressive transverse stress σ_2 leads to an explosive matrix failure type that is called mode C, $\sigma_2 \leq 0$ and $|\sigma_6 / \sigma_2| \leq |\sigma_{6c}| / R^A_{\perp\perp}$, see Fig.29:

$$f^C_{E(IFF)} = \left[\left(\frac{\sigma_6}{2\left(1+p^{(-)}_{\perp\perp}\right)S}\right)^2 + \left(\frac{\sigma_2}{Y_C}\right)^2\right]\left(\frac{Y_C}{\left(-\sigma_2\right)}\right) + \left|\frac{\sigma_1}{\sigma_{1D}}\right|^6 \leq 1 \qquad (13)$$

Damage occurs in a plane that is not perpendicular to the one defined by the in-plane stresses. The parameter $p^{(-)}_{\perp\perp}$ represents the inclination of the failure locus (σ_2, σ_4) at $\sigma_2=0$. Since it is very difficult to perform such kind of experiments, Puck et al. [8] suggested an empirical formula to estimate the slope. The term Y_C stands for the ultimate compressive stress transverse to the fibers direction. The value of the matrix failure criterion is referred to as stress exposure factor $f_{E(IFF)}$.

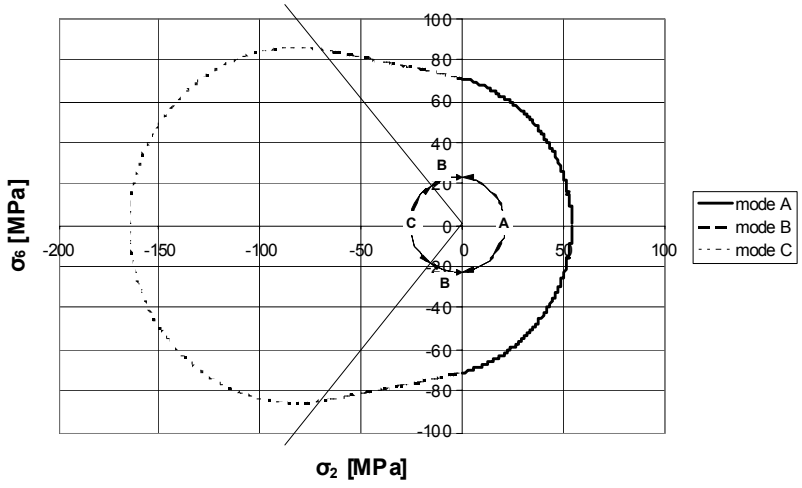

Fig. 29: Failure locus in the (σ_2, σ_6) stress space, predicted with Puck failure criterion.

4. Damage Propagation

Sudden stiffness degradation follows failure onset. Depending on the damage mode, different stiffness reduction policies are implemented. Since failure mode A results in matrix cracks that tend to open, it is assumed that load bearing capacity normal to the crack is reduced along with the ability of shear load transfer. Hence, transverse Young modulus, E_2, and shear modulus, G_{12}, are degrading simultaneously. The degradation factor is chosen equal for both properties. In damage mode B matrix cracks developed during loading tend to close due to compressive stresses. However, a certain sliding movement of the crack faces relative to each other is expected to occur. A degradation factor is applied only in shear modulus value. In 'explosive' mode C transverse Young modulus, E_2, and shear modulus, G_{12}, are set to zero (multiplied by 1.0E-6).

A "progressive" stiffness degradation model is adopted, according to which the degradation factor is given by [7]:

$$\eta = \frac{1-\eta_r}{1+c(f_{E(IFF)}-1)^{\xi}} + \eta_r \qquad (14)$$

where c, ξ and η_r are model parameters defined by means of basic tests. The term η_r represents the remaining value of the specific stiffness property after damage accumulation reaches its saturation level. A value of η_r equal to zero is proposed herein for all failure modes. Puck et al. [7] have originally suggested typical values of c≈4 and ξ≈2, for FRP composites, see Fig. 30, using the concept of secant modulus of elasticity for the numerical calculations. However, they recommended that this set of values has to be defined for any new material system. In this work, tangential modulus of elasticity is implemented instead. The parameters are tuned so as to achieve optimal stress-strain prediction for a matrix dominated multidirectional material system under tension (MD60). Thus, the parameters as implemented in the FEM model are equal to c=20000 and ξ=8, assuming more abrupt stiffness degradation, see Fig. 30.

Predicted stress-strain curves from a FEM simulation of a multidirectional coupon implementing the two different c, ξ sets are presented in Fig. 31. Material model with the set values proposed in [7] demonstrates much stiffer behaviour (red line) than the experiment.

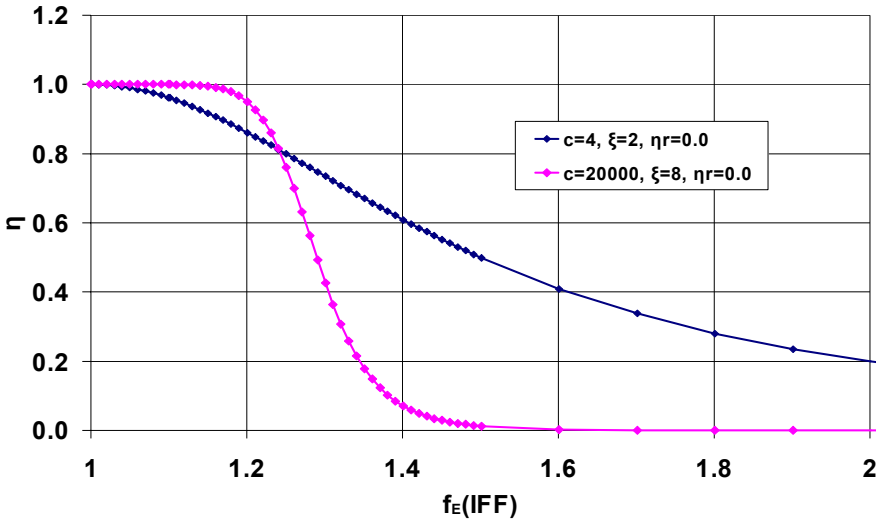

Fig. 30: Degradation factor η vs. matrix failure effort $f_{E(IFF)}$

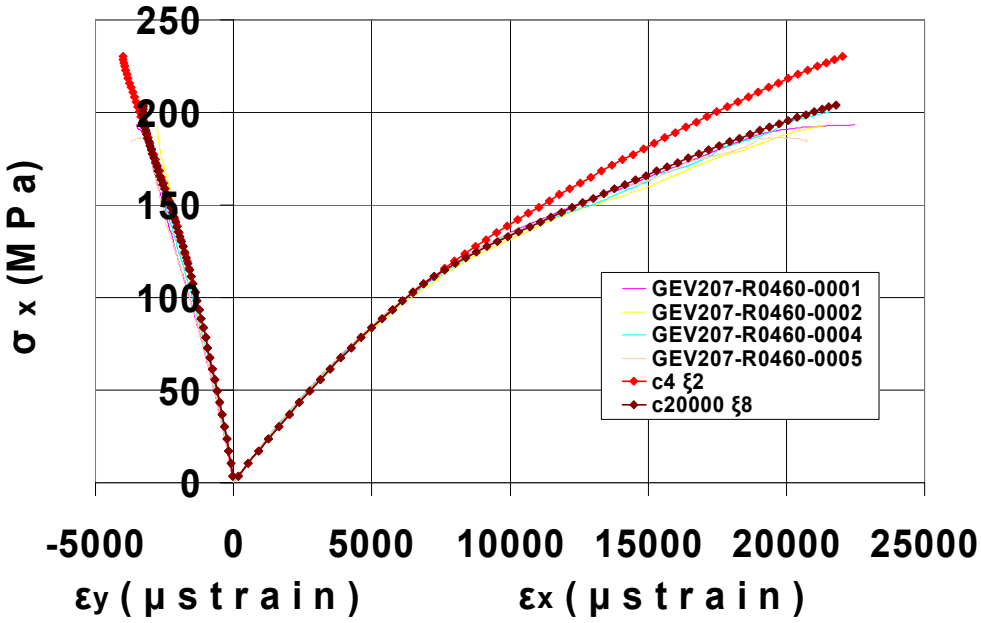

Fig. 31: Stress-strain experimental data & FEM predictions for a multidirectional laminate

The calculation of the degradation factor η is directly related to the failure effort $f_{E(IFF)}$ for matrix cracking. If no failure is observed ($f_{E(IFF)}$<1) then η=1 and the solution continues to the next load step multiplying the stiffness values by 1. Otherwise, if $f_{E(IFF)}$≥1 the layer has reached its crack onset point. Depending on the failure mode, the values of the corresponding elasticity moduli, obtained from the material non-linear response, are multiplied by the degradation factor η, eq.(14), and the solution continues to the next load step. The difference ($f_{E(IFF)}$-1) increases with load, resulting in reduced η values and so it can be considered as a representative parameter of matrix crack accumulation.

When fibre breakage ($f_{E(FF)}$≥1) occurs, either in tension or compression, all stiffness moduli are set to zero (multiplied by 1.0E-06) simultaneously.

Stiffness degradation strategy is summarized in Table 2, below. (It is assumed that calculations take place at the i^{th} loading increment).

Table 2 Stiffness degradation rules

Failure Mode	
FF(T) or FF(C)	$E_1^{(i+1)} = 1.0E-06 \cdot E_1^{(Failure)}$ $E_2^{(i+1)} = 1.0E-06 \cdot E_2^{(Failure)}$ $G_{12}^{(i+1)} = 1.0E-06 \cdot G_{12}^{(Failure)}$ $\nu_{12}^{(i+1)} = 1.0E-06 \cdot \nu_{12}^{(Failure)}$

IFF(A)	$\eta = \frac{1-\eta_r}{1+c(f_{E(IFF)}-1)^{\xi}} + \eta_r,\ c = 2.0E+04,\ \xi = 8,\ \eta_r = 0$
	IF $\eta(i) \le \eta(i\text{-}1)$ THEN
	$\eta = \eta(i)$
	ELSE
	$\eta = \eta(i\text{-}1)$
	$E_2^{(i+1)} = \eta E_{2(NL)}^{(i)}$
	$G_{12}^{(i+1)} = \eta G_{12(NL)}^{(i)}$

IFF(B)	Same conditions for η $G_{12}^{(i+1)} = \eta G_{12(NL)}^{(i)}$
IFF(C)	$E_2^{(i+1)} = 1.0E-06 \cdot E_2^{(Failure)}$ $G_{12}^{(i+1)} = 1.0E-06 \cdot G_{12}^{(Failure)}$

5. Fatigue Damage Considerations

The FADAS methodology developed for life prediction, considers a basic orthotropic UD lamina to be the constitutive element of the multidirectional (MD) plate. Application of the model requires in-plane mechanical properties of the ply, i.e. on-axis, transversely to the fibre and in shear to be experimentally derived. In more detail, the static strength vector (5x1) as well as S-N curves parallel, transversely to the fibre and in shear, at some stress ratios R must be obtained. The R-ratios used in this work are R=0.1, -1 and 10 which apart from being proposed by certification bodies [29] cover a minimum range of fatigue conditions, both in tension and compression.

The elastic behaviour is assumed non-linear, as already presented in a previous section. Elasticity is subject to a gradual degradation due to the fatigue loading, which is accounted for through simple models included in the algorithm. Adequate formulations for degradation of tensile, compressive and shear static strength due to fatigue, both in tension and compression, are also taken into account, as a physically interpreted damage accumulation metric. Finally, the parameters of the Failure Criterion of Puck are tuned in order to model the post-failure elastic response of severely damaged plies.

Once all properties and constitutive behaviour are implemented, the algorithm proceeds by using a Reissner-Mindlin shell FEM formulation for the current external load segment (peak-trough pair) and calculates strains and stresses at the principal coordinate system of each ply. With stresses known, the Failure Criterion is applied. If failure occurs, one must distinguish between the catastrophic case leading to fracture of the entire laminate and non-catastrophic leading to an updated strength and stiffness matrix of the failed layer. Once failure events are accounted for, the algorithm progresses with calculation of the gradual strength and stiffness degradation due to fatigue: The stress amplitude and R-ratio of each stress component is defined and the corresponding fatigue life is derived using appropriate CLD (Constant Life Diagram) data. The algorithm progresses at reasonable speed either by single segments, which is necessary for VA fatigue, or by blocks of cycles, which accelerates the procedure during CA fatigue modelling. A flowchart of the algorithm is shown in Fig. 32.

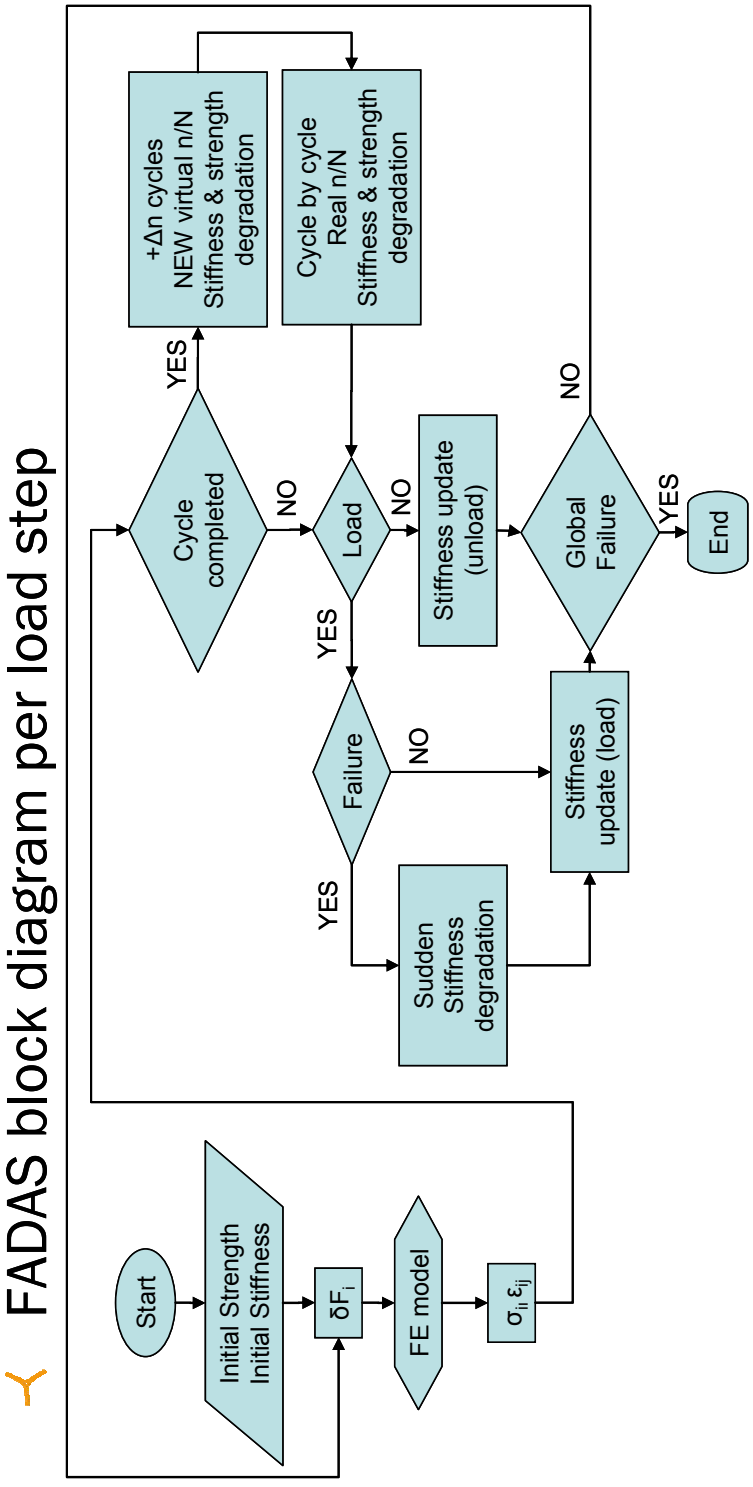

Fig. 32: Flowchart of the FADAS algorithm.

6. Model Implementation in FEM

Four different FEM models were implemented so as to account for differences in coupon geometry and lay-up:

a) Unidirectional coupon having fibres parallel to the loading axis (752 elements, 4 layers).
b) Unidirectional coupon with fibres transversely to the loading direction (752 elements, 7 layers).
c) Multidirectional coupon (752 elements, 14 layers), see Fig. 33.
d) [±45] coupon (1728 elements, 4 layers).

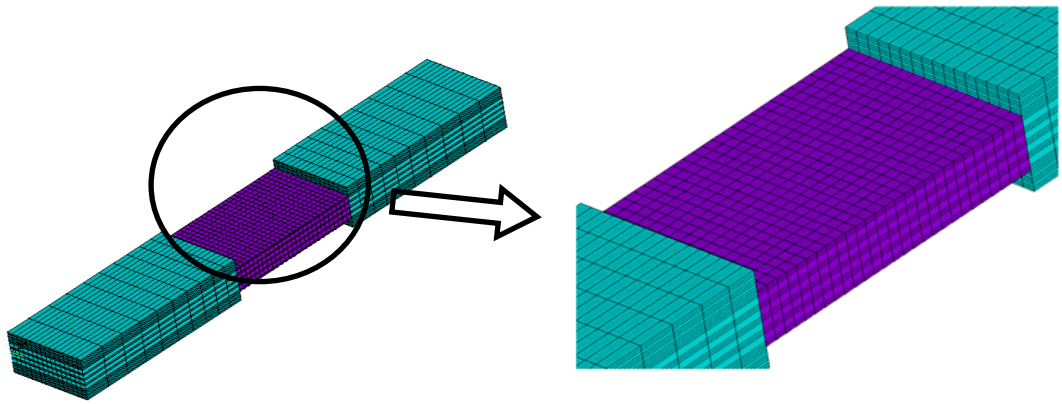

Fig. 33 FEM model of a simulated prismatic test coupon

In all specimens, node displacements along X-axis are all constrained in left tab region while coupon movement along Y -axis is limited through node constraints in the centreline (longitudinal coupon axis), allowing Poisson 'breathing'. Displacement is incrementally applied on the other tab area, see Fig. 34, for which Y-axis displacement is also constrained along the centreline. Load-step resolution is specified so as to accurately simulate material non-linearity and to avoid numerical convergence problems.

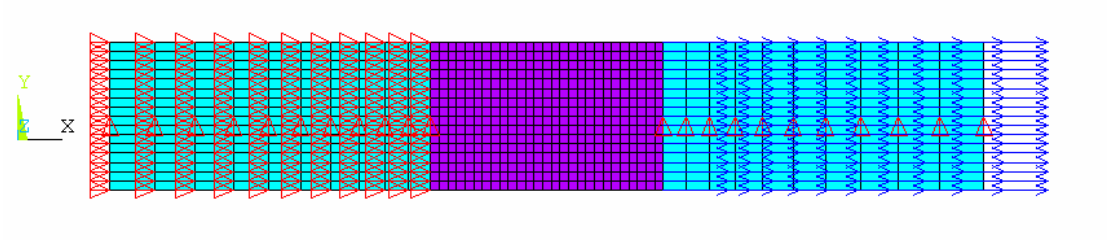

Fig. 34 Simulated boundary conditions

Analysis is performed with ANSYS commercial FEM code. A 3-D shell element (SHELL181) implementing first order shear deformation theory (Mindlin-Reissner) was used. A user defined constitutive model was implemented in a FORTRAN routine, compatible with the specific element. Material non-linear behaviour, failure criteria and progressive damage scenarios are incorporated in this routine which is compiled with ANSYS core code, resulting in a new ANSYS executable file. Using this procedure saves a lot of time when running the FEM code instead of programming the progressive damage concept with the APDL-ANSYS programming language. For the static simulation results presented in the next section the most time consuming model

has 1728 elements, 11118 d.o.f and needs up to ten minutes to be solved while using APDL based routines would need over 24 hours of computational time in the same processor.
For the case of fatigue simulation, with the same SHELL181 formulation, 768 elements are used to model the OB MD coupon, 14 plies per element and 3 integration points per ply. The calculations are performed per load step at each integration point. For a Pentium 4, 3.2 GHz, 2 GB RAM processor, CPU time counted was 10 sec per load step and 720 sec per 1000 cycles block.

To simulate an S-N curve for MD coupons, on-axis under reverse loading (R=-1), with 4 different stress levels, time counted was as follows:

- SL1:150 load steps, 200 cycles block. Time: 1500+288=1788sec=0.5h
- SL1b:200 load steps, 500 cycles block. Time: 2000+1080=3080sec=0.9h
- SL2:300 load steps, 5000 cycles block. Time: 3000+18000=21000sec=5.8h
- SL3:250 load steps, 100000 cycles block. Time: 2500+288000=290500sec=80.7h

Total time was 87.9h=3.66 days.

6.1 Predictions vs. Experimental data; Monotonic Static Loading

6.1.1 Tension of Gl/Ep $[\pm 45]_s$ coupon

Material response in shear stress is highly non-linear. To validate numerical model effectiveness in predicting such a performance, an ISO $[\pm 45]_s$ coupon, used for the material shear modulus determination, is modelled under tensile loading. The FEM calculations seem to agree with experimental strain measurements in the axial (loading) and transverse directions, Fig.35, following the curve slope reduction and also correctly predicting coupon strength, see Table 3.

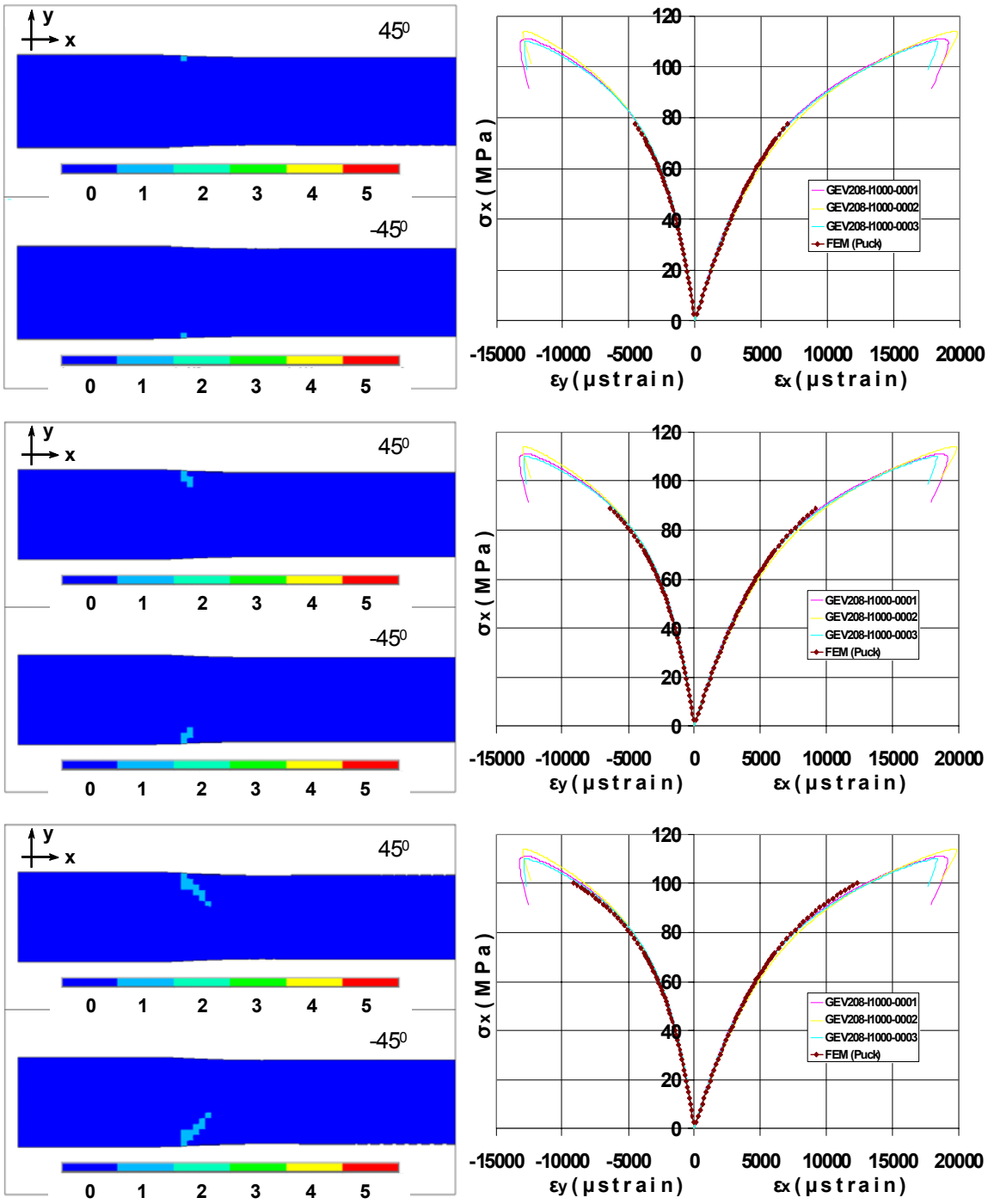

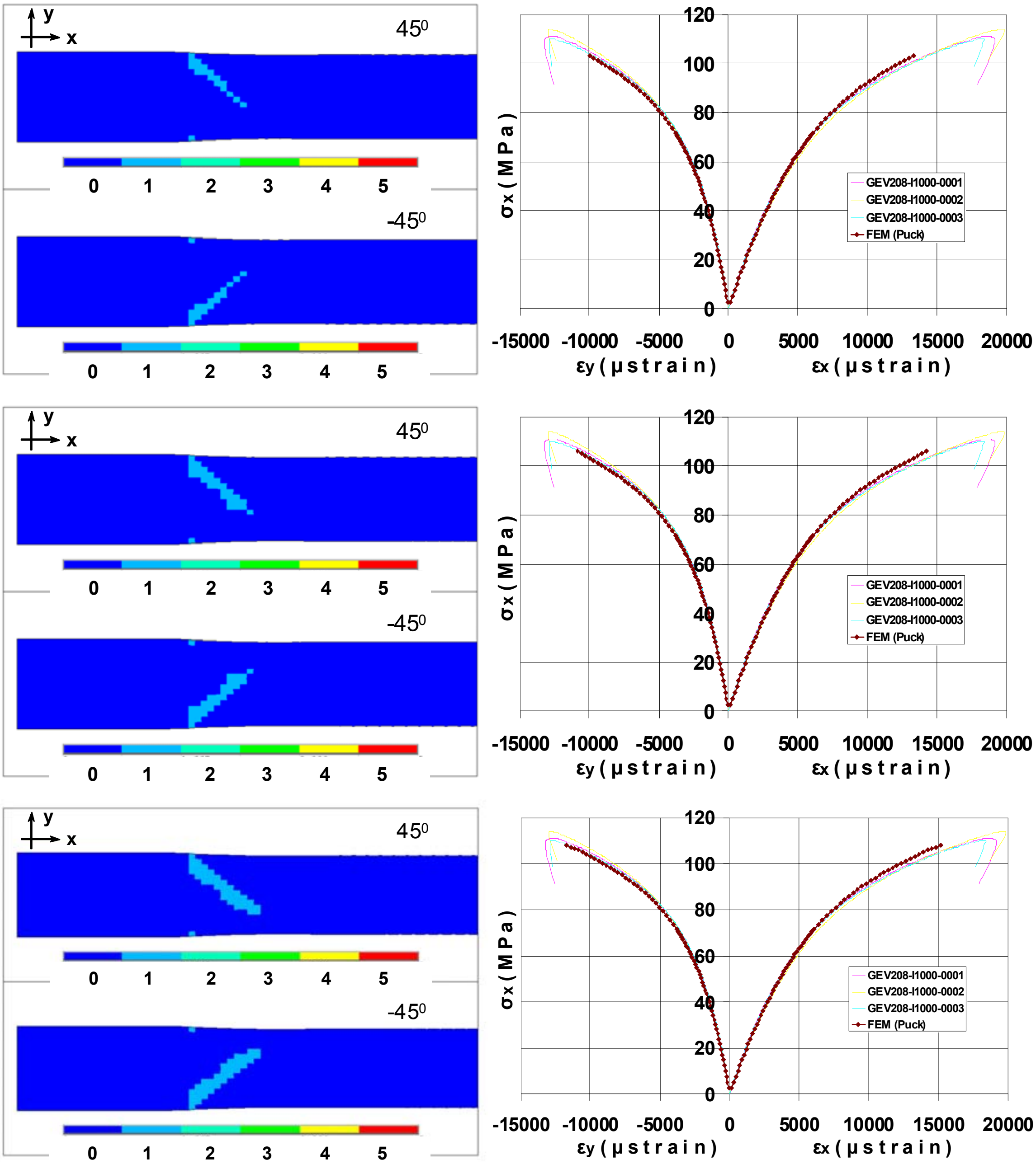

y
x
45⁰
-45⁰
0 1 2 3 4 5
σx (MPa)
εy (μstrain)
εx (μstrain)
GEV208-I1000-0001
GEV208-I1000-0002
GEV208-I1000-0003
FEM (Puck)

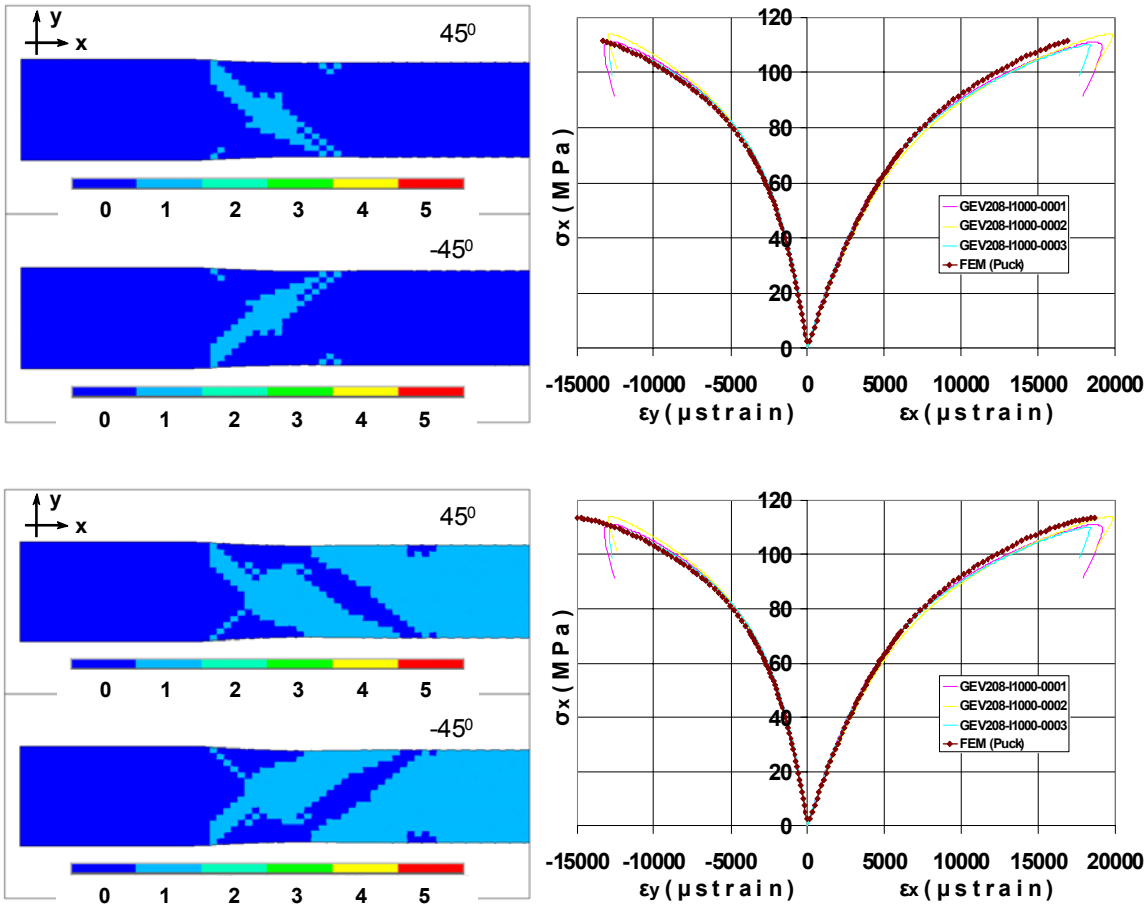

Fig. 35: Damage in the 1st and 2nd layer and stress-strain evolution of a $[\pm 45]_s$ coupon under tension

Predicted damage propagation map for the first two layers is presented in Fig. 35 with load evolution. Failure initiates next to the tabs region at 70% of the failure load. Catastrophic separation is considered to occur when cracks parallel to the fibres direction are bridged trough the specimen width, in all plies, Fig. 35.

Area indicated with colour number 0 corresponds to intact material while region designated with colour number 1 highlights the damaged material failed under mode IFF(A). Numbers 2 to 5 correspond respectively to IFF(B), IFF(C), FF(T) and FF(C). The prediction is fairly close to the observed experimental failure mode shown in Fig. 36.

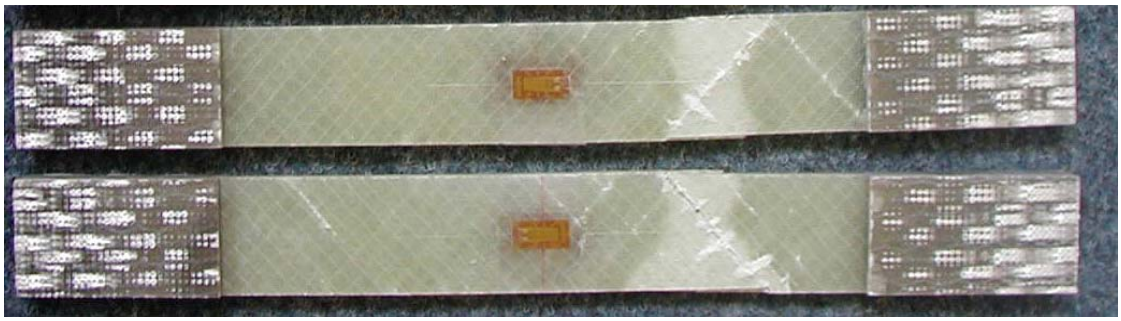

Fig. 36: Upper & Lower faces of a $[\pm 45]_s$ coupon failed under tensile loading

Table 3 Experimental and numerical strength values for $[\pm 45]_s$ coupon under tension

	Exp.	**FEM**	**Difference %**
MPa	112.14	113.505	-1.22

6.1.2 Tension of GI\Ep $[90]_7$ coupon (transverse to the fibres)

Tensile loading is applied in the direction transverse to the fibres where matrix performance dominates. Material demonstrates fairly non-linear behaviour, see Fig.2. The FEM results for the 7 layer coupon are in excellent agreement with the experimental data, Fig. 37, while the failure load is satisfactorily predicted, Table 4.

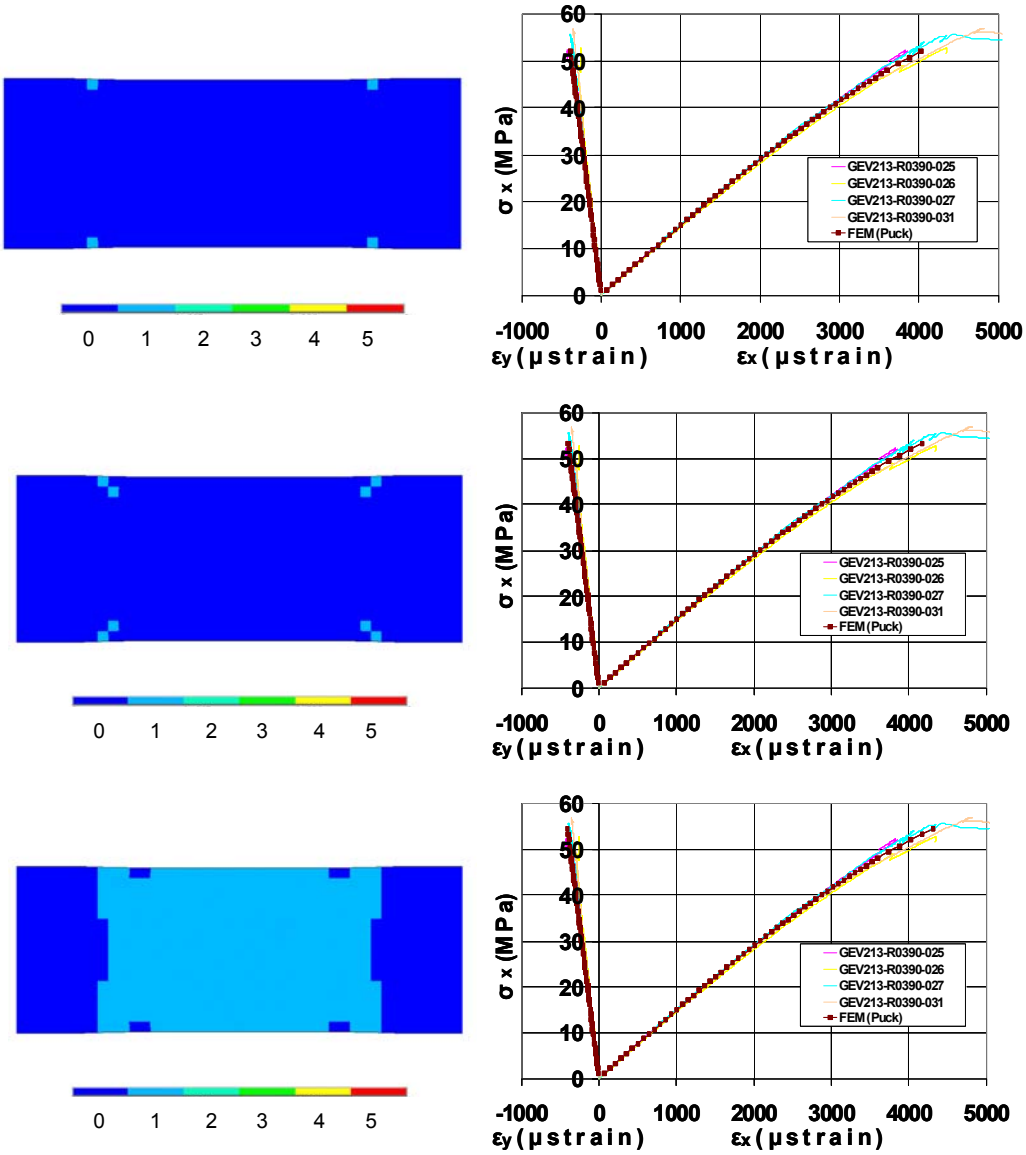

Fig. 37: Stress-Strain behaviour of a $[90]_7$ coupon in tension.

Table 4 Experimental and numerical strength values for $[90]_7$ coupon under tension

	Exp.	FEM	%
MPa	53.952	54.53	-1.07

Failure initiates near the tabs region with rupture occurring abruptly, in a sense of a 'Sudden Death' manner, Fig. 37. The appearance of the crack leads suddenly to a catastrophic failure of type A that is indicated by the region corresponding to number 1. Intact area is pointed out with number 0.

Although the 'Sudden Death' model matches well with the specimen experimental behaviour, the damage pattern shown in Fig. 37 is not accurate as it can be seen by comparison with the photos of the failed coupon, Fig.38. This is due to the resolution of loading steps in the numerical calculations and the sudden failure occurrence for this type of geometry and loading. Failure maps of Fig.38 could be improved by increasing substantially the number of load steps, increasing in parallel CPU time. This was not judged necessary since ultimate stress prediction was satisfactory. In addition, an excellent verification of the failure mode A, i.e. a matrix crack initiating and propagating near the tabs region transverse to the load axis, predicted by the FEM model is provided by the lateral view of the failed coupon in Fig.38.

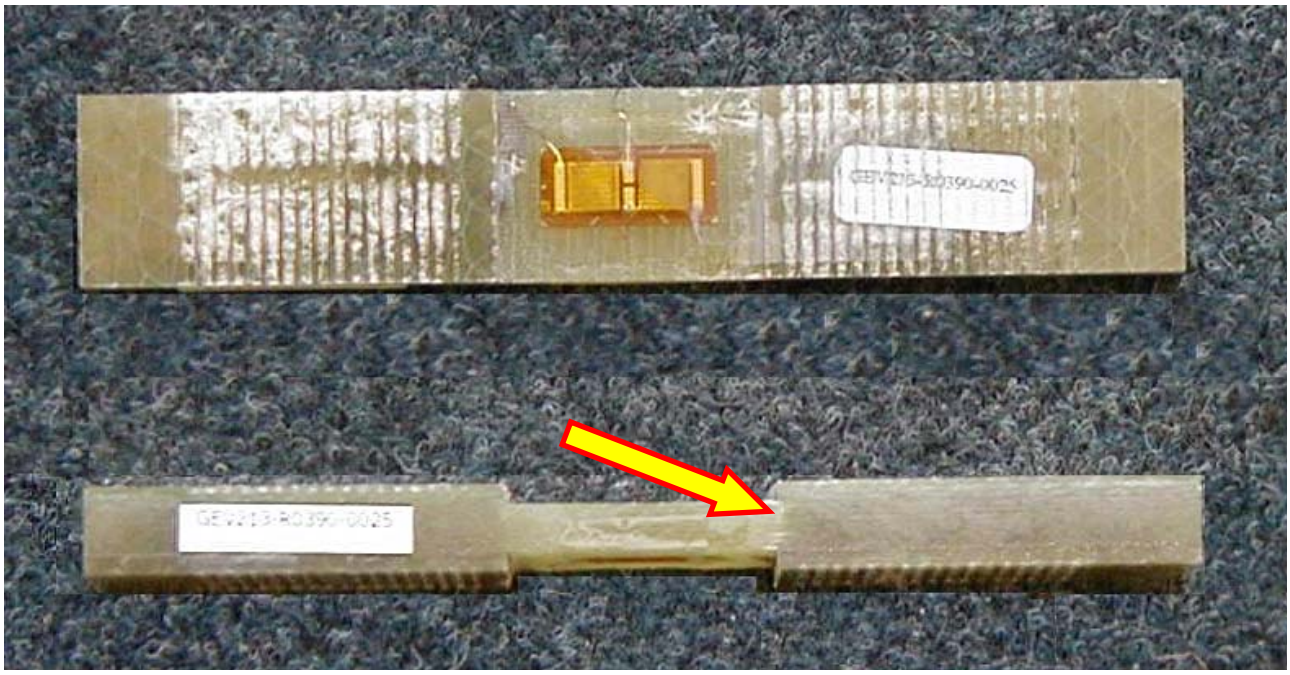

Fig. 38: Front & Lateral side of a failed $[90]_7$ coupon in tension.

6.1.3 Compression of GI\Ep $[90]_7$ coupon (transverse to the fibres)

Compressive loading is applied in a 7 layer coupon in the direction transverse to the fibres. FEM model predictions for the material non-linear behaviour are in excellent agreement with the experimental data, Fig. 39, while a satisfactory prediction for the ultimate compressive stress is obtained, Table 5.

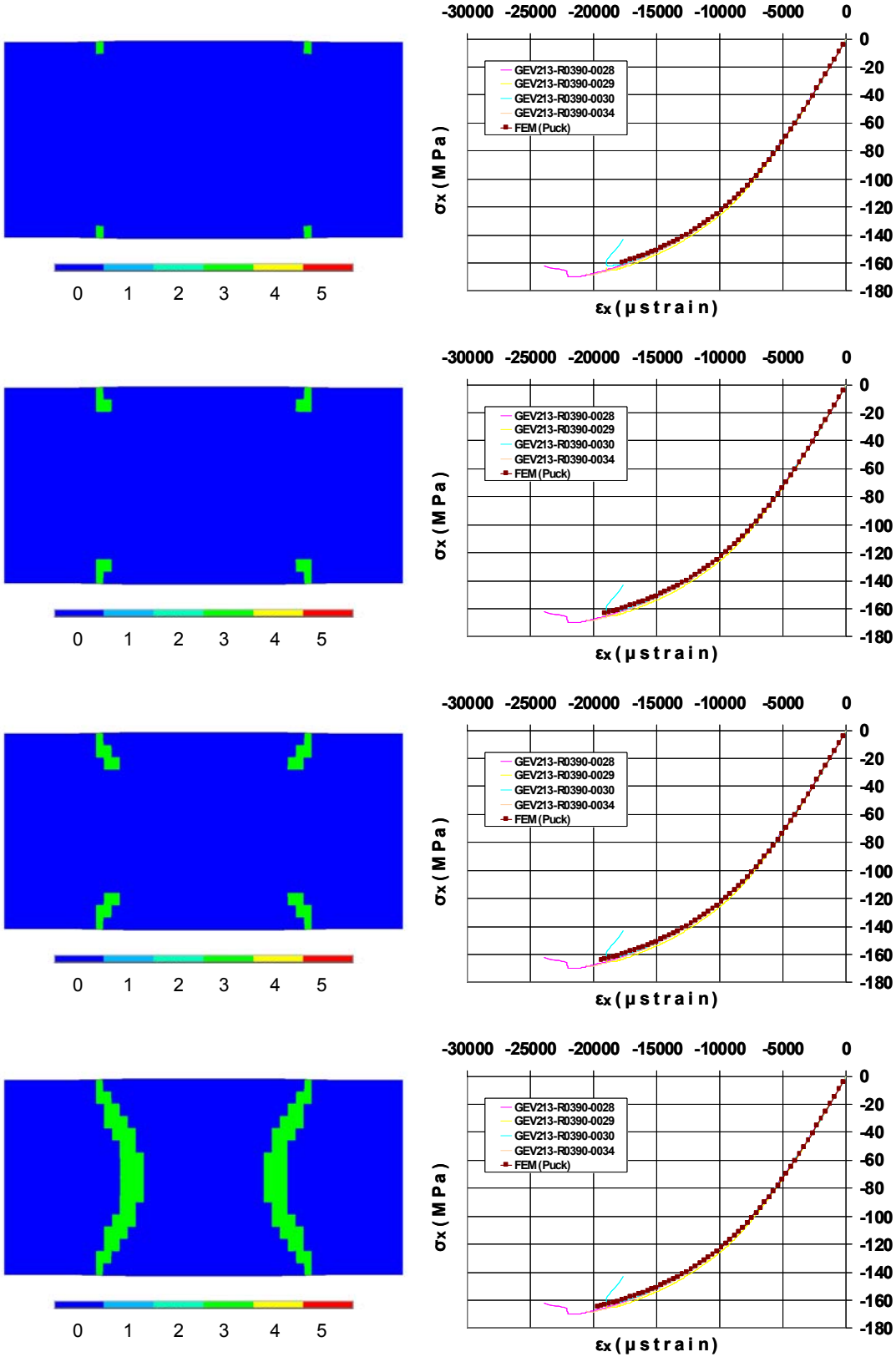

Fig. 39: Stress-Strain behaviour of a $[90]_7$ coupon in compression.

Table 5 Experimental and numerical strength values for $[90]_7$ coupon under compression

	Exp.	**FEM**	**%**
MPa	165.019	164.28	0.447

Failure initiates near the tabs region with final rupture occurring abruptly, in a sense of a 'Sudden Death' manner, Fig. 39. The appearance of the crack leads suddenly to a catastrophic failure of type C that is indicated by the region corresponding to number 3. Intact area is pointed out with number 0.

The model rupture, shown in Fig. 39, matches well with the specimen experimental pattern as it can be seen by comparison with the photos of the failed coupon, Fig. 40. An excellent verification of the failure mode C, i.e. an oblique matrix crack with respect to the compressive load direction, near the tabs area, predicted by the FEM model is provided by the lateral view of the failed coupon in Fig. 40.

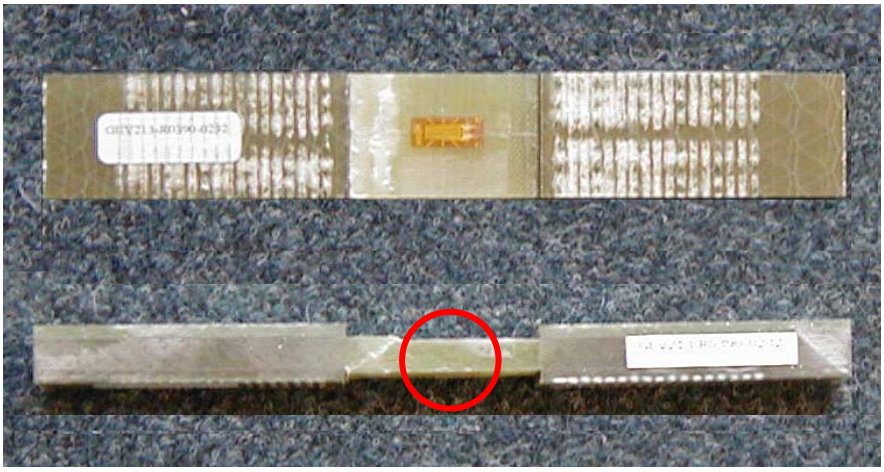

Fig. 40: Front & Lateral side of a failed $[90]_7$ coupon in compression.

6.1.4 Tension of Gl\Ep $[60]_7$ coupon

A seven UD layer coupon, cut at 60 degrees, is simulated under tensile loading. Axial and transverse strains measured on the specimen faces compare moderately well with FEM model results, Fig. 41, that behave modestly stiffer. Specimen strength is calculated with fine precision, see Table 6, and failure mechanism is in a very good agreement with the experiment, however the predicted failure pattern can not be directly compared with the tested coupon, see Fig. 42.

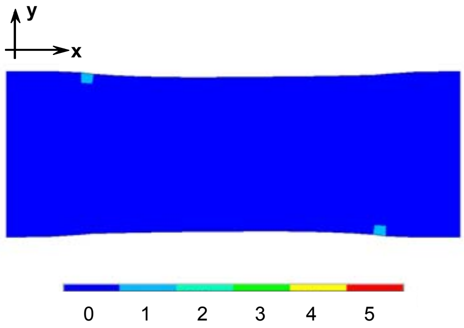
y
x
0 1 2 3 4 5

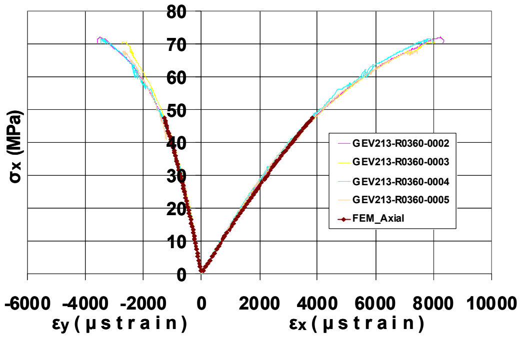
σx (MPa)
0 10 20 30 40 50 60 70 80
-6000 -4000 -2000 0 2000 4000 6000 8000 10000
εy (μstrain)
εx (μstrain)
GEV213-R0360-0002
GEV213-R0360-0003
GEV213-R0360-0004
GEV213-R0360-0005
FEM_Axial

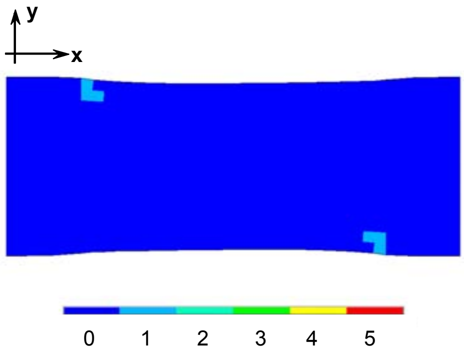
y
x
0 1 2 3 4 5

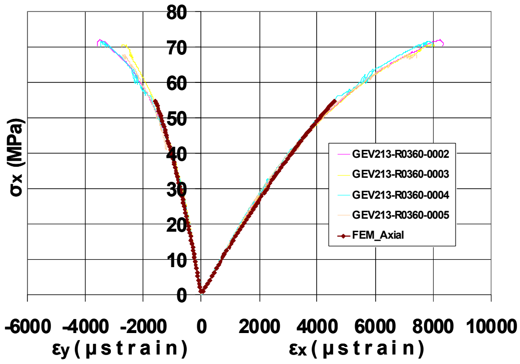
σx (MPa)
0 10 20 30 40 50 60 70 80
-6000 -4000 -2000 0 2000 4000 6000 8000 10000
εy (μstrain)
εx (μstrain)
GEV213-R0360-0002
GEV213-R0360-0003
GEV213-R0360-0004
GEV213-R0360-0005
FEM_Axial

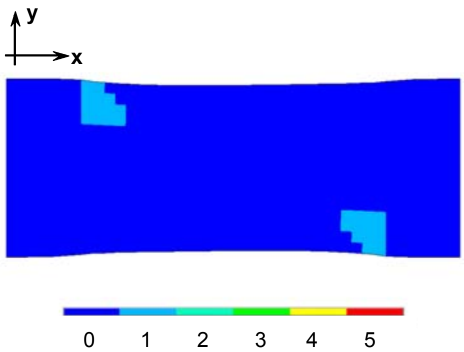
y
x
0 1 2 3 4 5

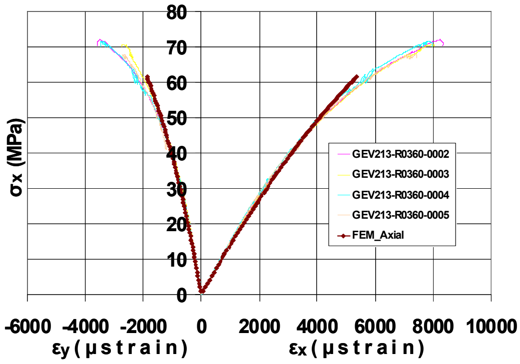
σx (MPa)
0 10 20 30 40 50 60 70 80
-6000 -4000 -2000 0 2000 4000 6000 8000 10000
εy (μstrain)
εx (μstrain)
GEV213-R0360-0002
GEV213-R0360-0003
GEV213-R0360-0004
GEV213-R0360-0005
FEM_Axial

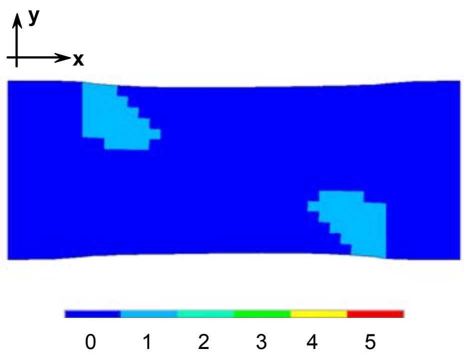
y
x
0 1 2 3 4 5

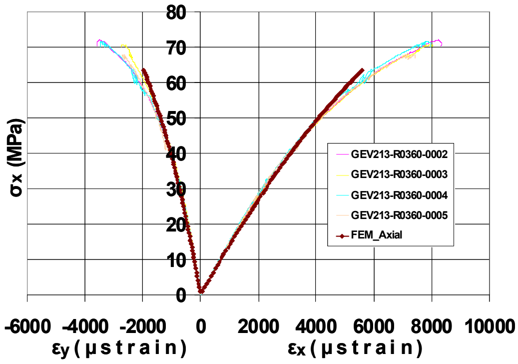
σx (MPa)
0 10 20 30 40 50 60 70 80
-6000 -4000 -2000 0 2000 4000 6000 8000 10000
εy (μstrain)
εx (μstrain)
GEV213-R0360-0002
GEV213-R0360-0003
GEV213-R0360-0004
GEV213-R0360-0005
FEM_Axial

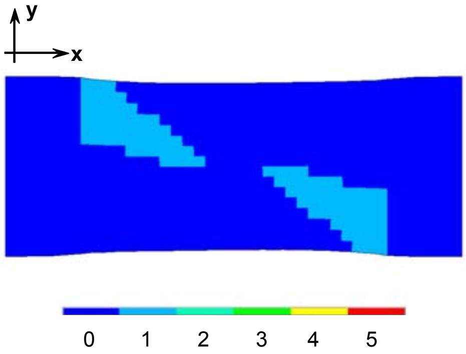
y
x
0 1 2 3 4 5

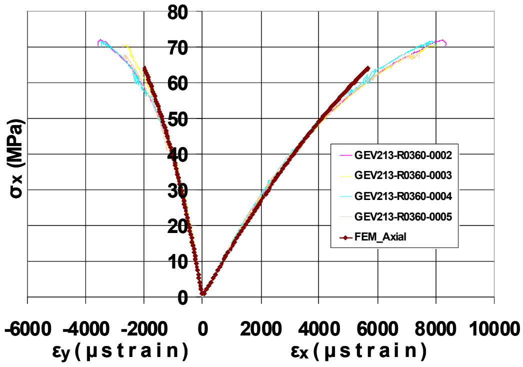
σx (MPa)
εy (μstrain)
εx (μstrain)
GEV213-R0360-0002
GEV213-R0360-0003
GEV213-R0360-0004
GEV213-R0360-0005
FEM_Axial

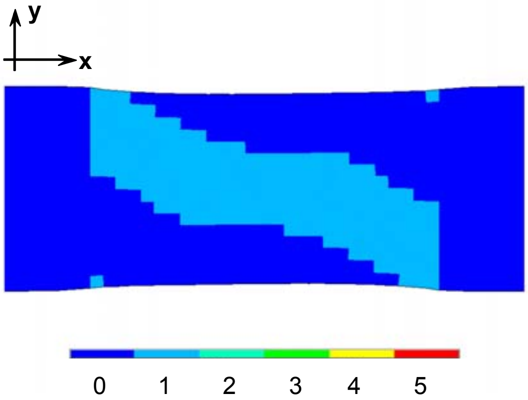
y
x
0 1 2 3 4 5

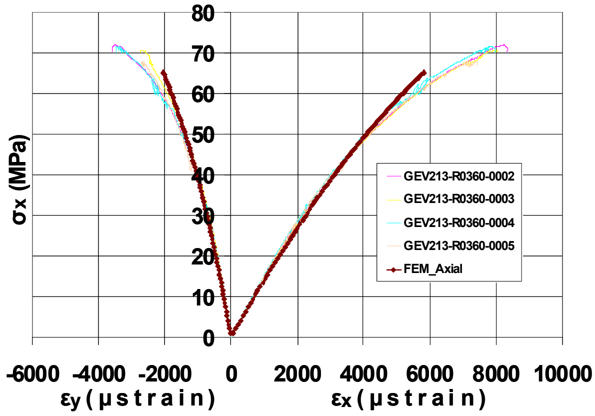
σx (MPa)
εy (μstrain)
εx (μstrain)
GEV213-R0360-0002
GEV213-R0360-0003
GEV213-R0360-0004
GEV213-R0360-0005
FEM_Axial

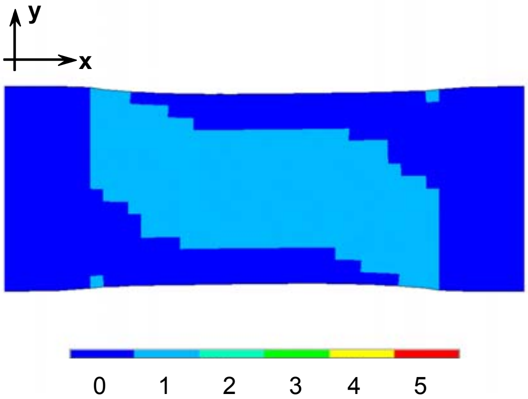
y
x
0 1 2 3 4 5

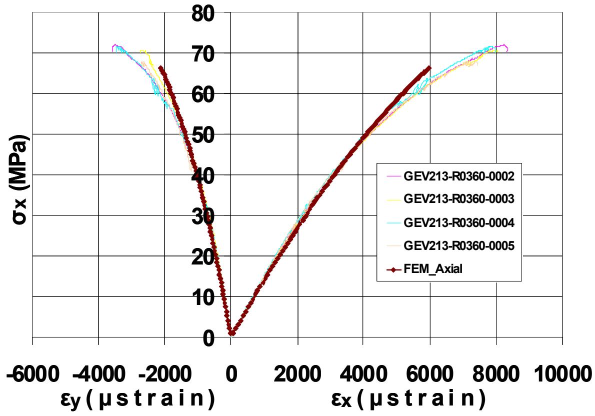
σx (MPa)
εy (μstrain)
εx (μstrain)
GEV213-R0360-0002
GEV213-R0360-0003
GEV213-R0360-0004
GEV213-R0360-0005
FEM_Axial

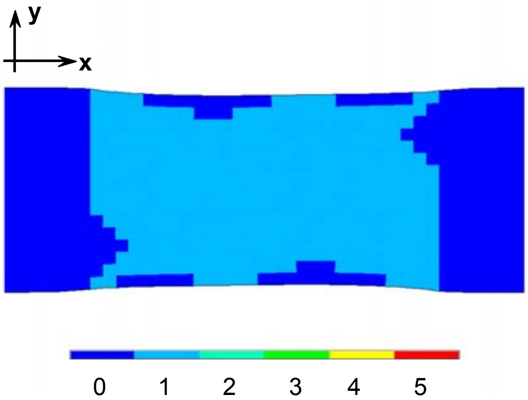
y
x
0 1 2 3 4 5

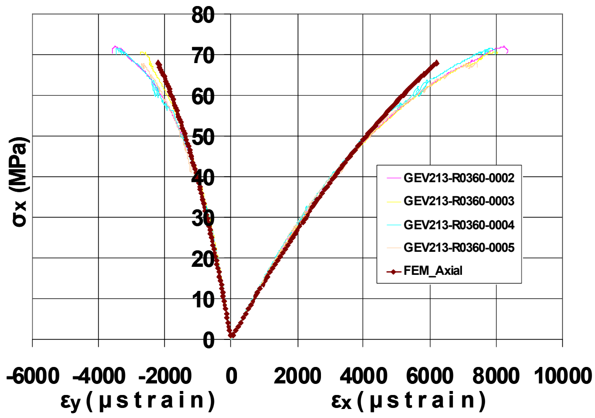
σx (MPa)
εy (μstrain)
εx (μstrain)
GEV213-R0360-0002
GEV213-R0360-0003
GEV213-R0360-0004
GEV213-R0360-0005
FEM_Axial

Fig. 41: Stress-Strain behavior of a $[60]_7$ coupon in tension

Table 6 Experimental and numerical strength values for $[60]_7$ coupon under tension

	Exp.	**FEM**	**%**
MPa	72.23	68.045	5.79

First Ply Failure occurs at 70% of the calculated failure load. The numerical model predicts damage introduction and propagation transverse to the fibres direction, in the form of Mode A corresponding to number 1. Intact area is pointed out with number 0. The specimen is considered to be failed, see Fig. 41, when tensile matrix cracks are bridged among its width, in a direction parallel to the fibres. The numerical model rupture type coincides with the experimental since the coupon fail due to tensile matrix cracks as can be seen from both front and lateral view of the tested specimen in Fig. 42, although the failure patterns do not compare satisfactorily.

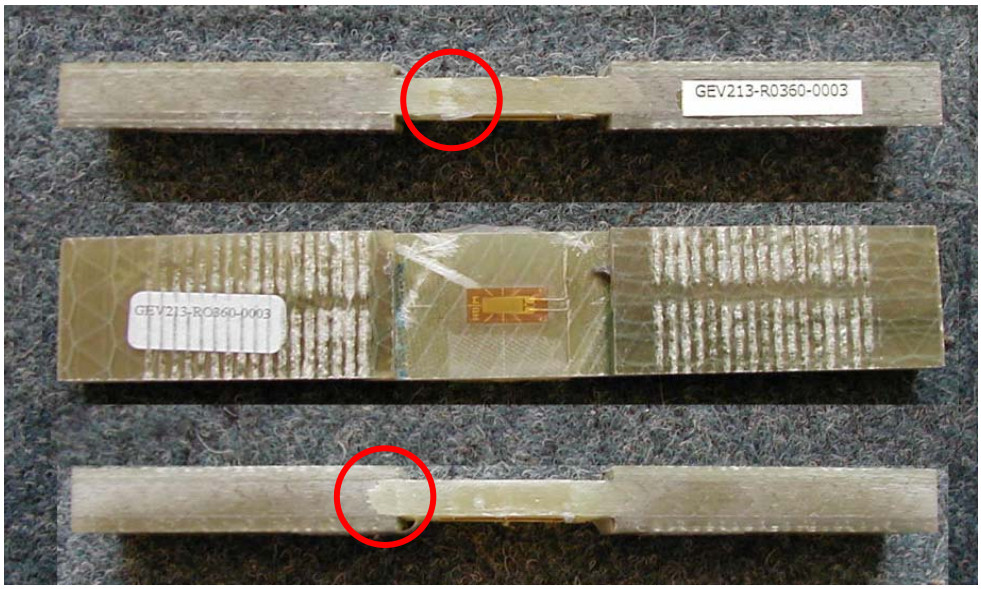

Fig. 42: Front & Lateral side of a failed $[60]_7$ coupon in tension

6.1.5 Compression of Gl\Ep $[60]_7$ coupon

A seven UD layer coupon, cut at 60 degrees, is simulated under compressive loading. The FEM model appears more compliant than the experiment, overestimating the failure strain, see Fig. 43, and the strength value prediction is rather conservative, see Table 7. The failure mechanism is in a very good agreement with the experiment, with the predicted failure pattern being comparable with the tested coupon.

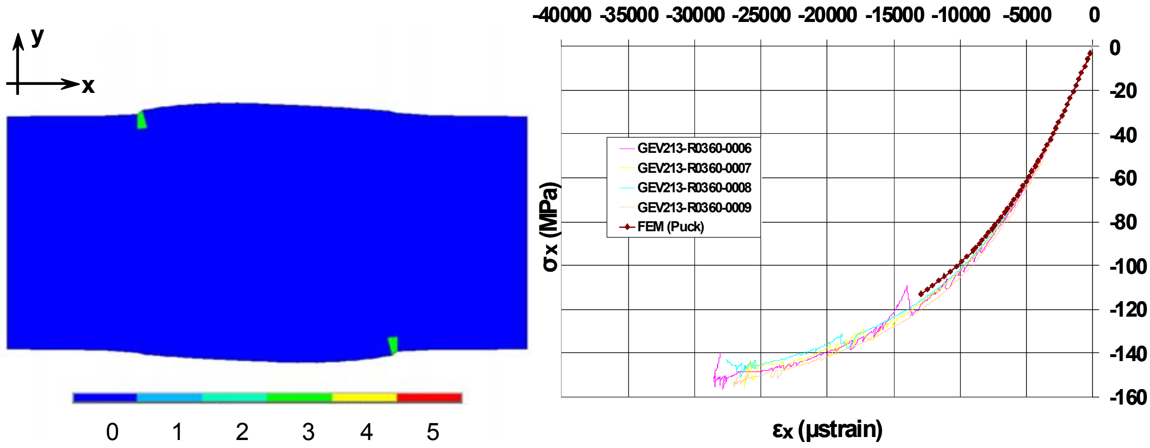
y
x
0 1 2 3 4 5
-40000 -35000 -30000 -25000 -20000 -15000 -10000 -5000 0
0 -20 -40 -60 -80 -100 -120 -140 -160
σx (MPa)
GEV213-R0360-0006
GEV213-R0360-0007
GEV213-R0360-0008
GEV213-R0360-0009
FEM (Puck)
εx (μstrain)

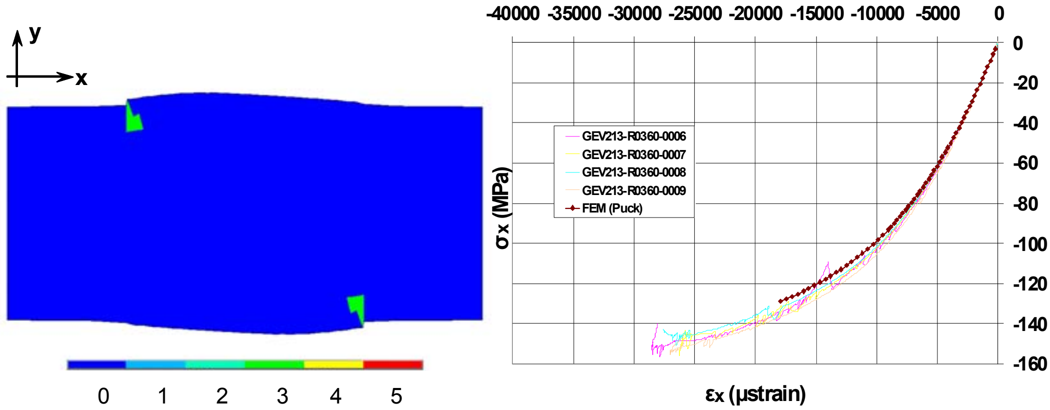
y
x
0 1 2 3 4 5
-40000 -35000 -30000 -25000 -20000 -15000 -10000 -5000 0
0 -20 -40 -60 -80 -100 -120 -140 -160
σx (MPa)
GEV213-R0360-0006
GEV213-R0360-0007
GEV213-R0360-0008
GEV213-R0360-0009
FEM (Puck)
εx (μstrain)

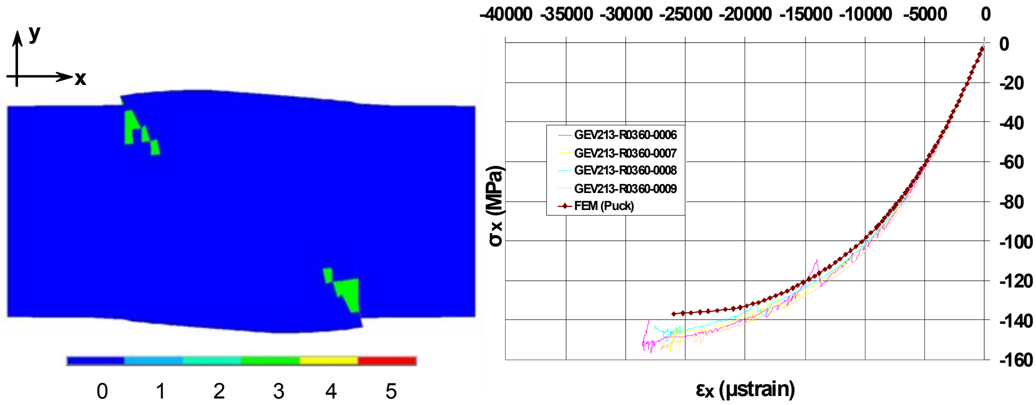
y
x
0 1 2 3 4 5
-40000 -35000 -30000 -25000 -20000 -15000 -10000 -5000 0
0 -20 -40 -60 -80 -100 -120 -140 -160
σx (MPa)
GEV213-R0360-0006
GEV213-R0360-0007
GEV213-R0360-0008
GEV213-R0360-0009
FEM (Puck)
εx (μstrain)

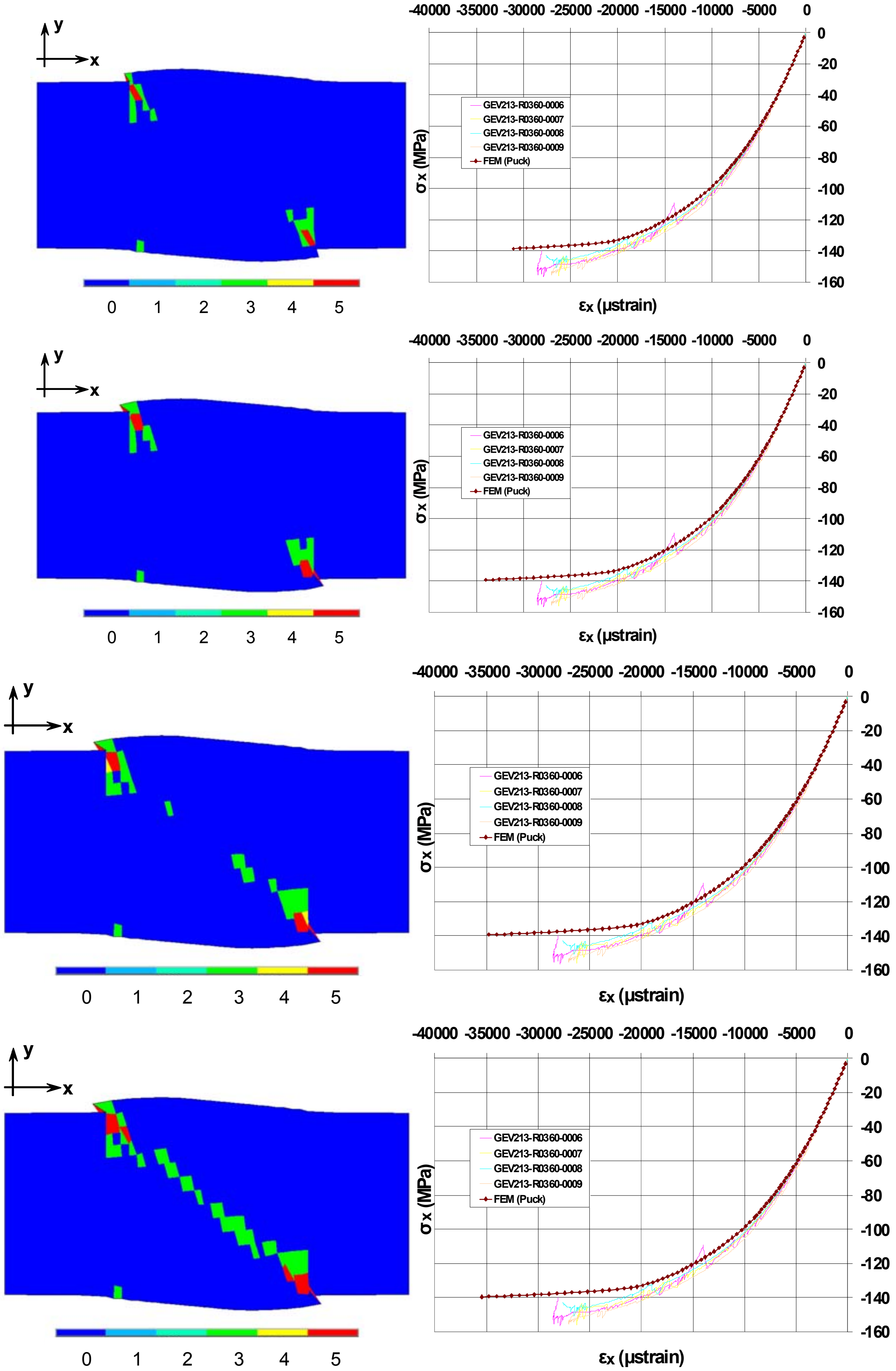
y
x
0 1 2 3 4 5
-40000 -35000 -30000 -25000 -20000 -15000 -10000 -5000 0
0 -20 -40 -60 -80 -100 -120 -140 -160
σx (MPa)
εx (µstrain)
GEV213-R0360-0006
GEV213-R0360-0007
GEV213-R0360-0008
GEV213-R0360-0009
FEM (Puck)

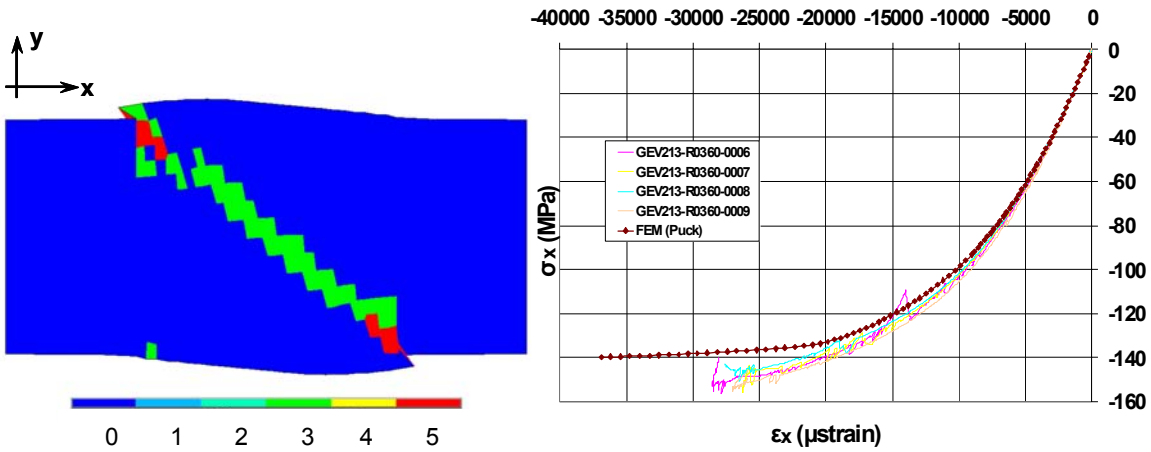

Fig. 43 Stress-Strain behaviour of a $[60]_7$ coupon in compression

Table 7 Experimental and numerical strength values for $[60]_7$ coupon under compression

	Exp.	**FEM**	**%**
MPa	-154.41	-139.95	9.36

First Ply Failure occurs at 80% of the calculated failure load. The numerical model predicts damage introduction and propagation transverse to the fibres direction, in the form of the "explosive" Mode C, corresponding to number 3. Intact area is pointed out with number 0. Fibre kinking, designated with number 5, is emerged due to high calculated shear deformation in the early failed elements. When compressive matrix cracks are bridged among the specimen width, it is considered to be failed, see Fig. 43. In the tested coupon, compressive matrix damage is extended transverse to the fibres direction, see Fig. 44. The predicted failure mode coincides with the experimental since the coupon fails due to explosive matrix cracks as can be seen from a lateral view of the tested specimen in Fig. 44.

Figure 44: Front & Lateral side of a failed $[60]_7$ coupon in compression

6.1.6 Tension of Gl/Ep $[0]_4$ coupon

A tensile test along the fibres is simulated for the 4 layer UD coupon. Axial and transverse strains on the specimen faces measured in the test compare well with FEM results, Fig. 45. Material stress-strain performance, strength, see Table 8, and failure mechanism are in a very good agreement with the experiment.

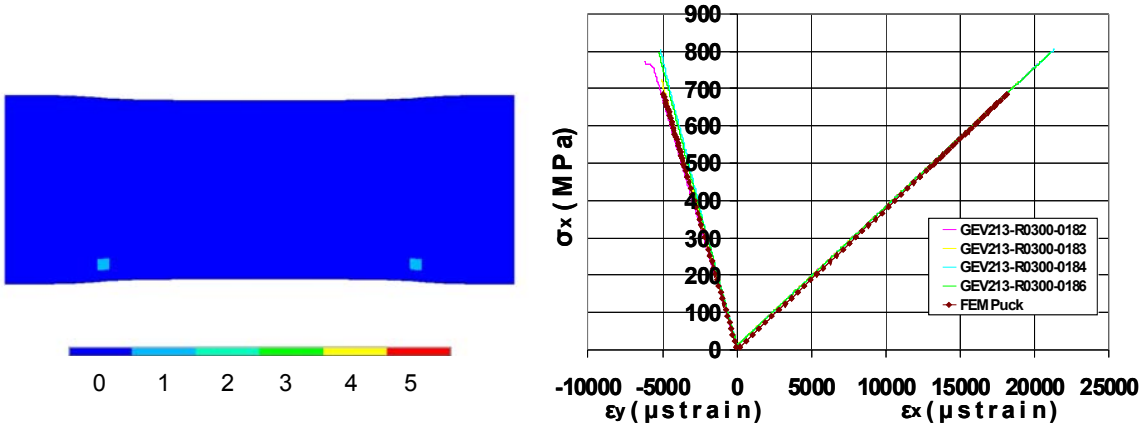

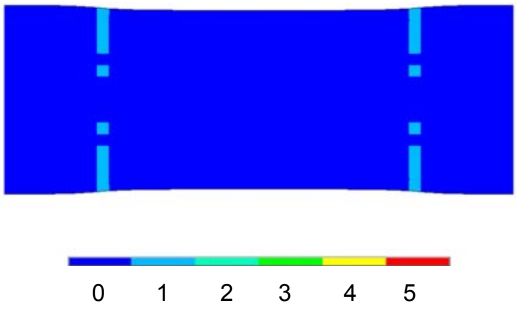
0
1
2
3
4
5

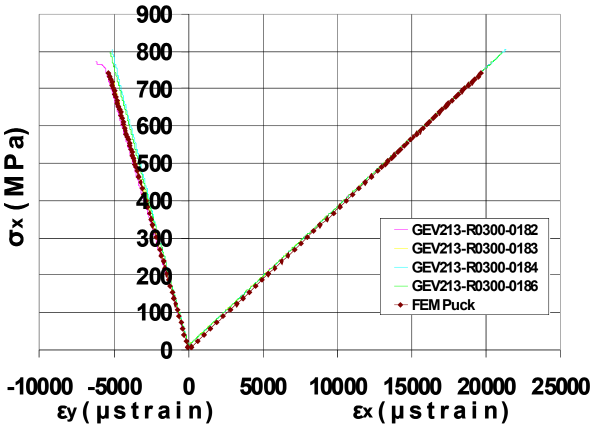
σx (M P a)
εy (μ s t r a i n)
εx (μ s t r a i n)
GEV213-R0300-0182
GEV213-R0300-0183
GEV213-R0300-0184
GEV213-R0300-0186
FEM Puck

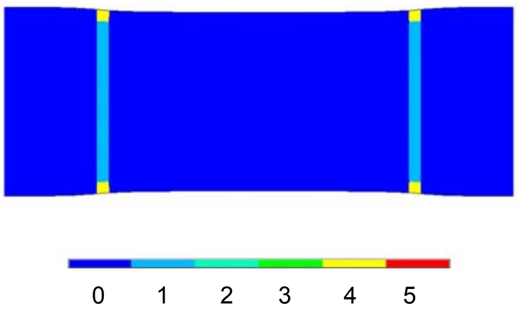
0
1
2
3
4
5

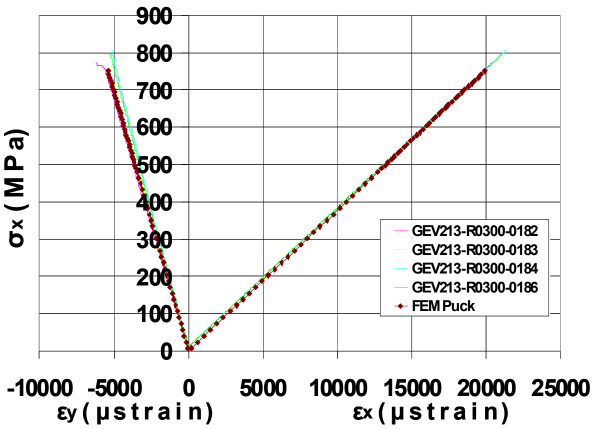
σx (M P a)
εy (μ s t r a i n)
εx (μ s t r a i n)
GEV213-R0300-0182
GEV213-R0300-0183
GEV213-R0300-0184
GEV213-R0300-0186
FEM Puck

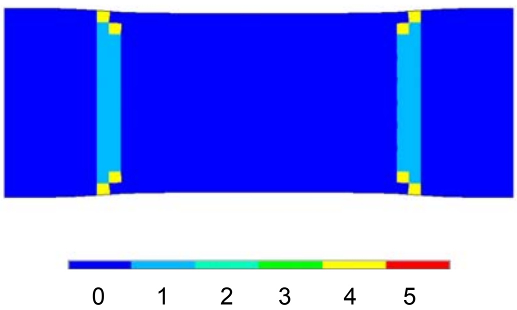
0
1
2
3
4
5

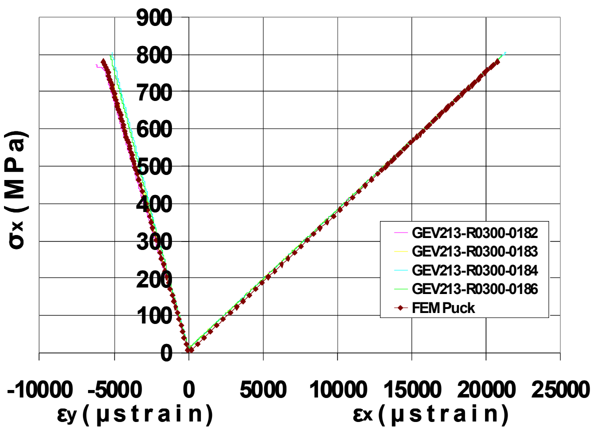
σx (M P a)
εy (μ s t r a i n)
εx (μ s t r a i n)
GEV213-R0300-0182
GEV213-R0300-0183
GEV213-R0300-0184
GEV213-R0300-0186
FEM Puck

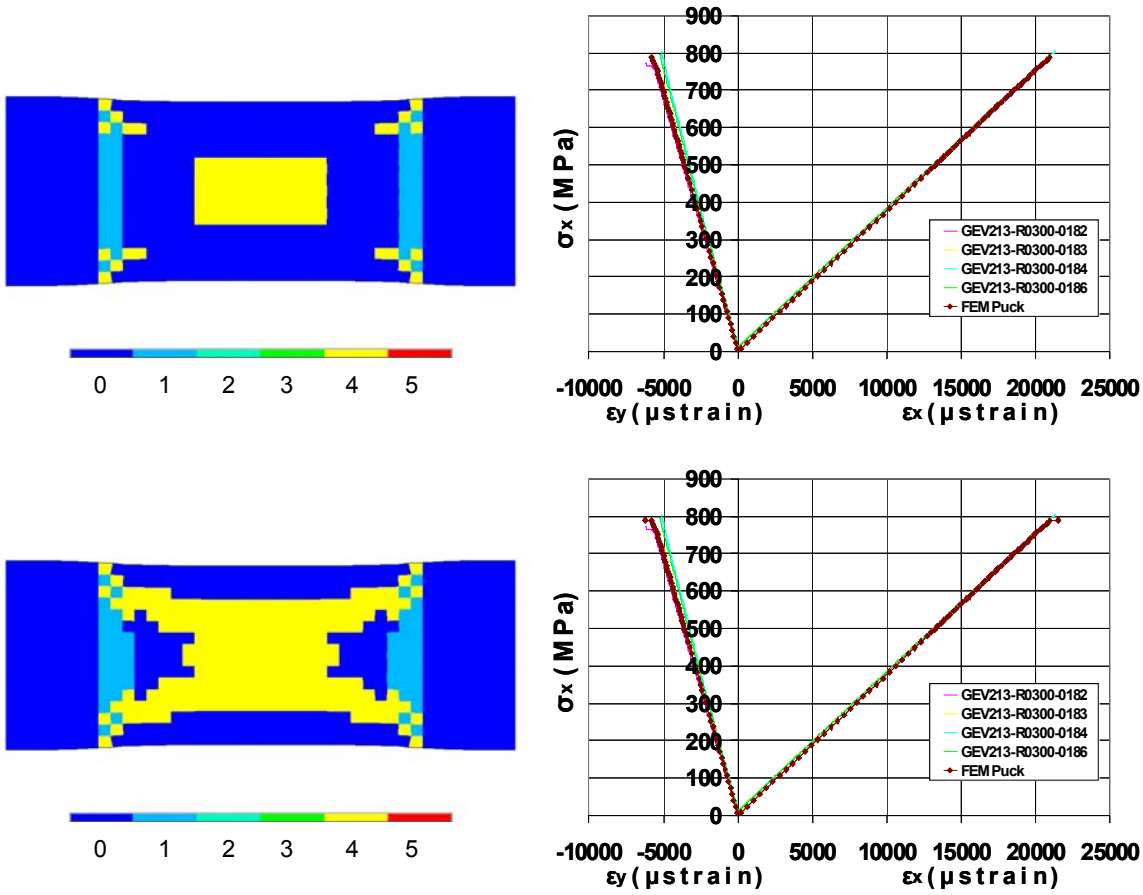

Fig. 45: Stress-Strain behavior of a $[0]_4$ coupon in tension.

Table 8: Experimental and numerical strength values for $[0]_4$ coupon under tension

	Exp.	**FEM**	**%**
MPa	776.497	789.545	-1.68

Damage initiates in the form of tensile matrix cracks of mode A indicated with number 1, promoting fibre breakage near tabs region where also stress concentration exists imposed by the boundary conditions. Fibre rupture under tensile loading, designated with number 4, propagates along specimen length, leading to final rupture. This failure mechanism presented in Fig. 46, is comparable with the fibre “splitting” observed in the experimental procedure. Intact area is pointed out with number 0.

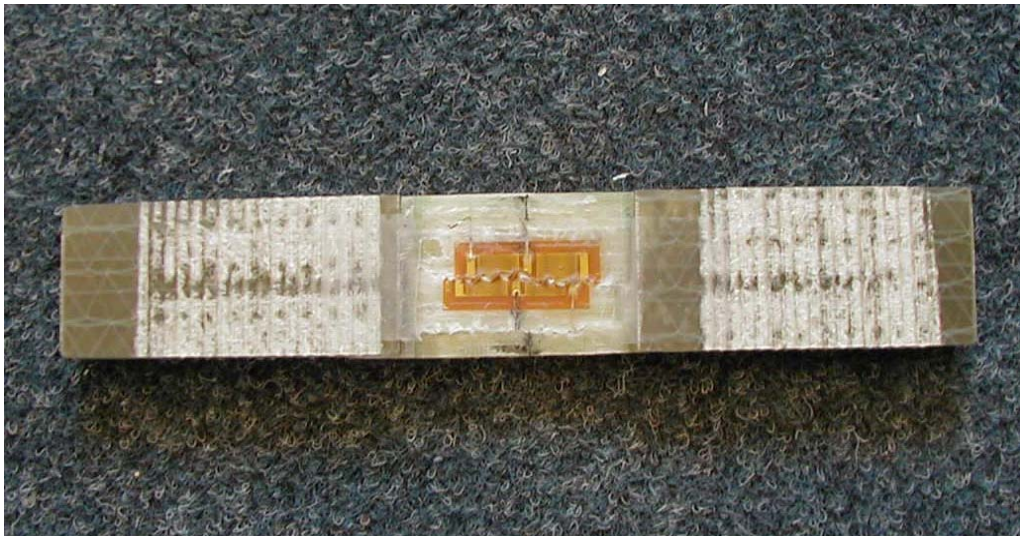

Fig. 46: Failed $[0]_4$ coupon in tension

6.1.7 Compression of Gl/Ep $[0]_4$ coupon

A compressive test along the fibres is simulated for the 4 layer UD coupon. Ultimate compressive strength obtained from ISO coupon is implemented for the numerical calculations as previously stated. Axial strains measured on the specimen faces compare well with the FEM results, Fig. 47. As expected, the predicted material strength, see Table 9, failure strain and failure pattern, see Fig. 48, are not in agreement with the experiment.

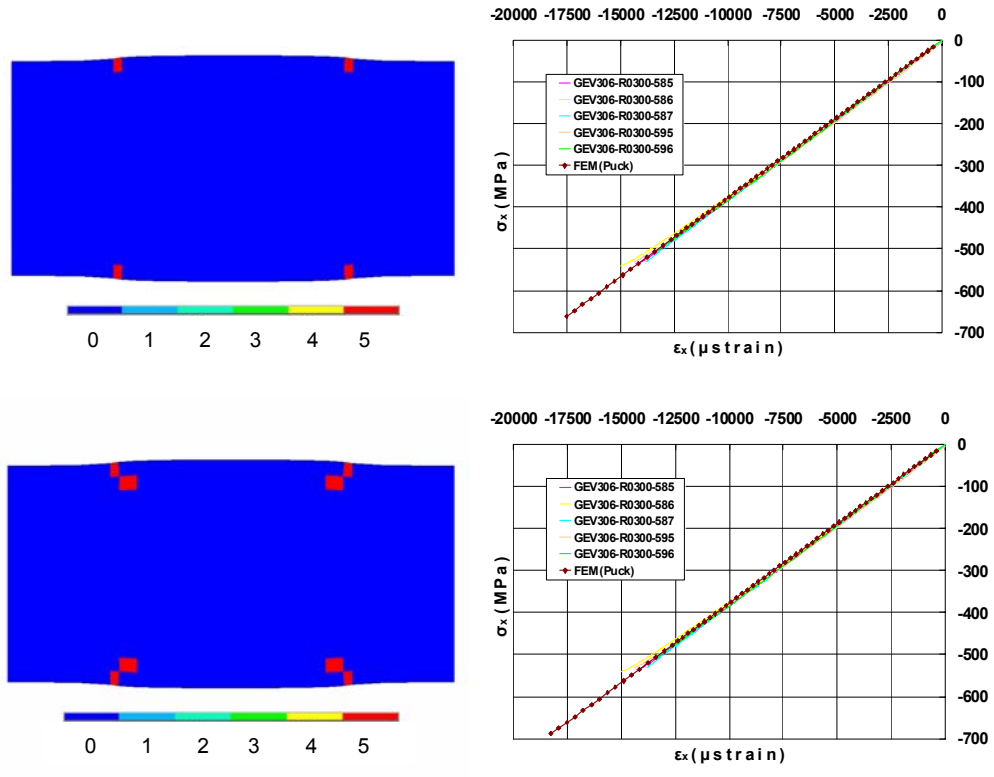

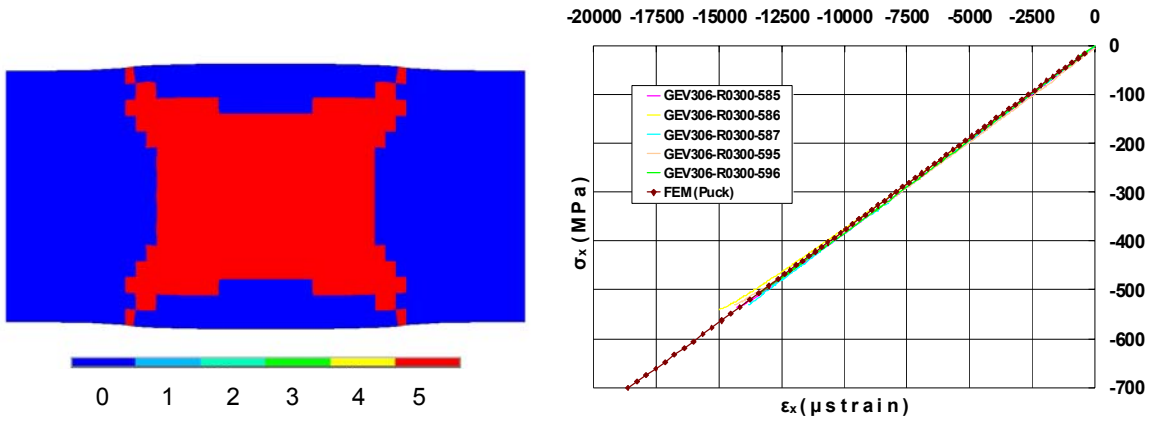

Fig. 47: Stress-Strain behaviour of a $[0]_4$ coupon in compression

Table 9: Experimental and numerical strength values for $[0]_4$ coupon under compression

	Exp.	**FEM**	**%**
MPa	-525.91	-688.34	-30.88

Fig. 48: Failed $[0]_4$ coupon in compression

6.1.8 Tension of MD coupon along the fibres of the [0] layer

The multidirectional coupon (MD) is composed of layers of UD [0] and stitched bi-directional [±45] fabric. Simulation accounts for further evaluation of the progressive damage concept under complex stress states. Predicted damage evolution and a comparison between numerical and test results is presented in Fig. 49.

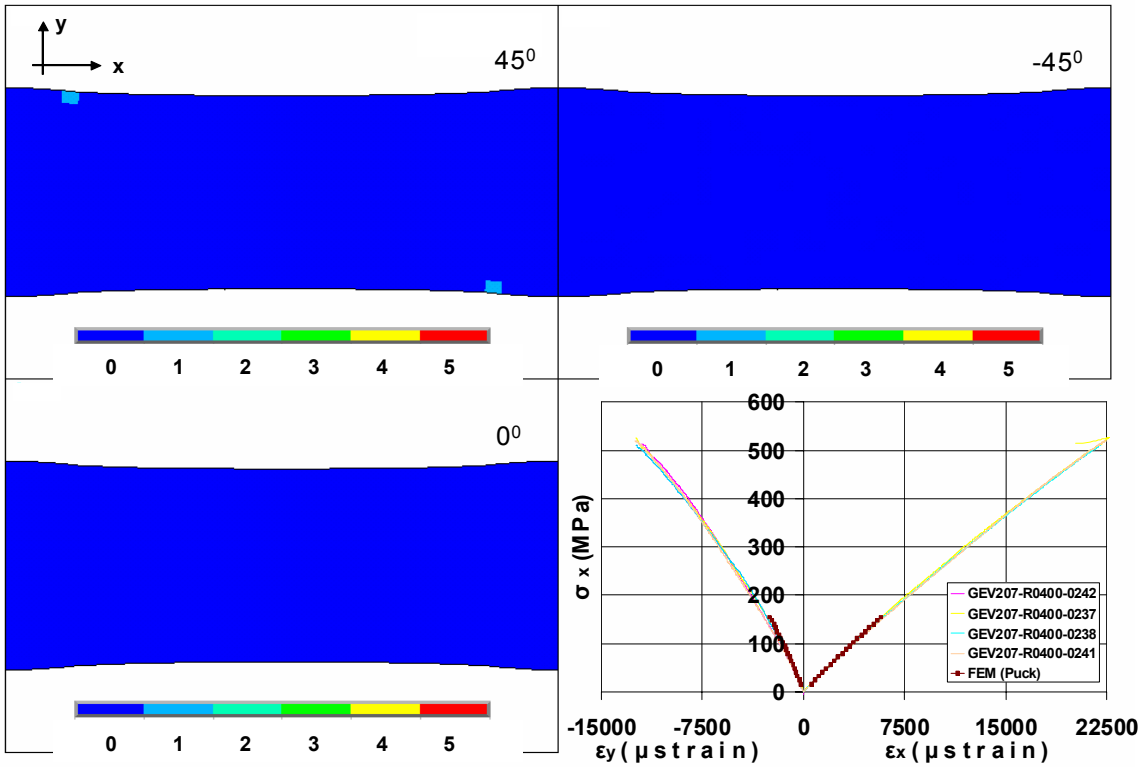
y
x
45⁰
-45⁰
0⁰
0 1 2 3 4 5
σ x (MPa)
600
500
400
300
200
100
0
-15000 -7500 0 7500 15000 22500
εy (μstrain)
εx (μstrain)
GEV207-R0400-0242
GEV207-R0400-0237
GEV207-R0400-0238
GEV207-R0400-0241
FEM (Puck)

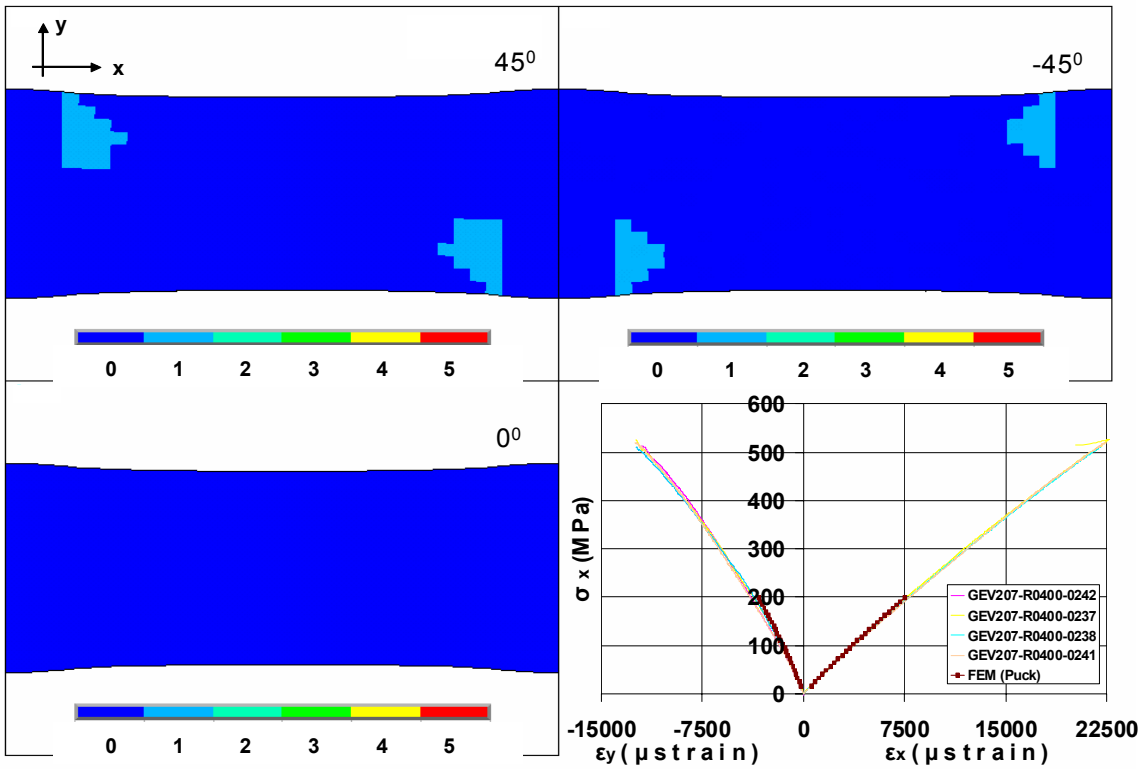
y
x
45⁰
-45⁰
0⁰
0 1 2 3 4 5
σ x (MPa)
600
500
400
300
200
100
0
-15000 -7500 0 7500 15000 22500
εy (μstrain)
εx (μstrain)
GEV207-R0400-0242
GEV207-R0400-0237
GEV207-R0400-0238
GEV207-R0400-0241
FEM (Puck)

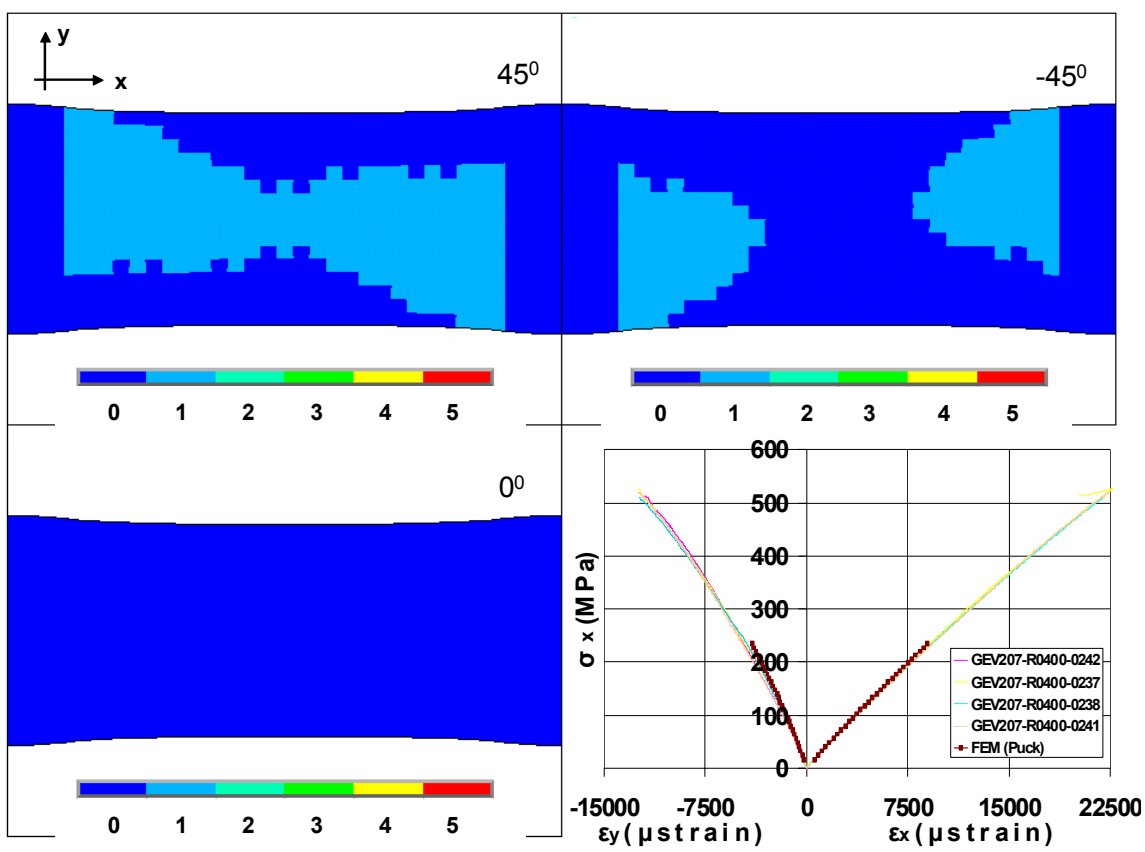
y
x
45⁰
-45⁰
0⁰
0 1 2 3 4 5
600
500
400
300
200
100
0
σ x (MPa)
-15000 -7500 0 7500 15000 22500
εy(μstrain)
εx(μstrain)
GEV207-R0400-0242
GEV207-R0400-0237
GEV207-R0400-0238
GEV207-R0400-0241
FEM (Puck)

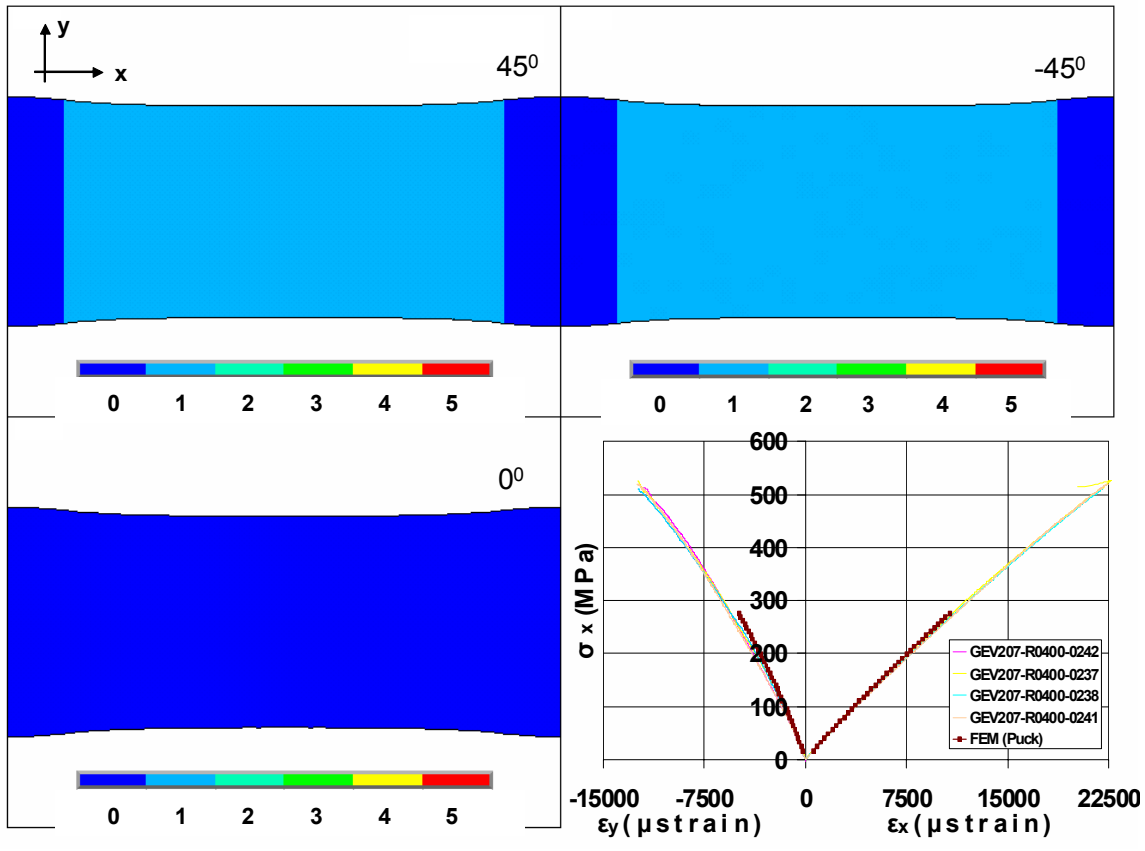
y
x
45⁰
-45⁰
0⁰
0 1 2 3 4 5
600
500
400
300
200
100
0
σ x (MPa)
-15000 -7500 0 7500 15000 22500
εy(μstrain)
εx(μstrain)
GEV207-R0400-0242
GEV207-R0400-0237
GEV207-R0400-0238
GEV207-R0400-0241
FEM (Puck)

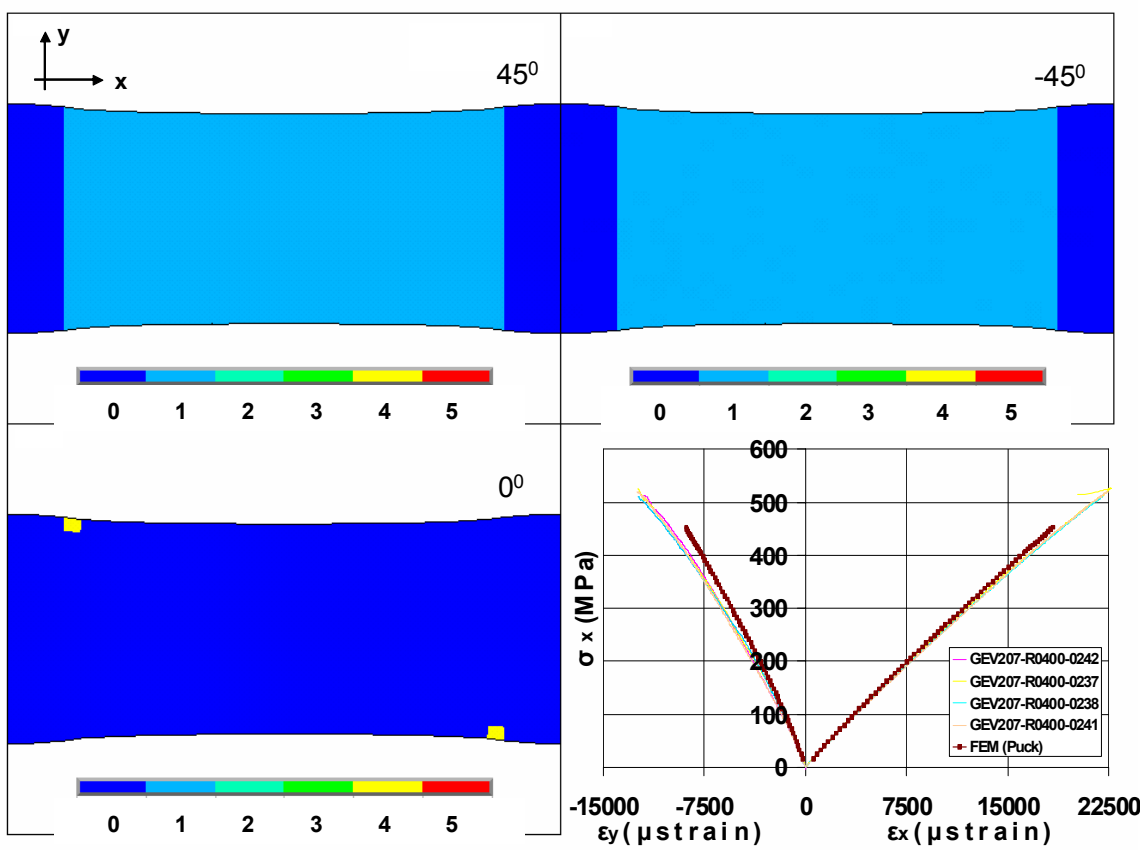
y
x
45⁰
-45⁰
0⁰
0 1 2 3 4 5
600
500
400
300
200
100
0
σ x (MPa)
-15000 -7500 0 7500 15000 22500
εy(μstrain)
εx(μstrain)
GEV207-R0400-0242
GEV207-R0400-0237
GEV207-R0400-0238
GEV207-R0400-0241
FEM (Puck)

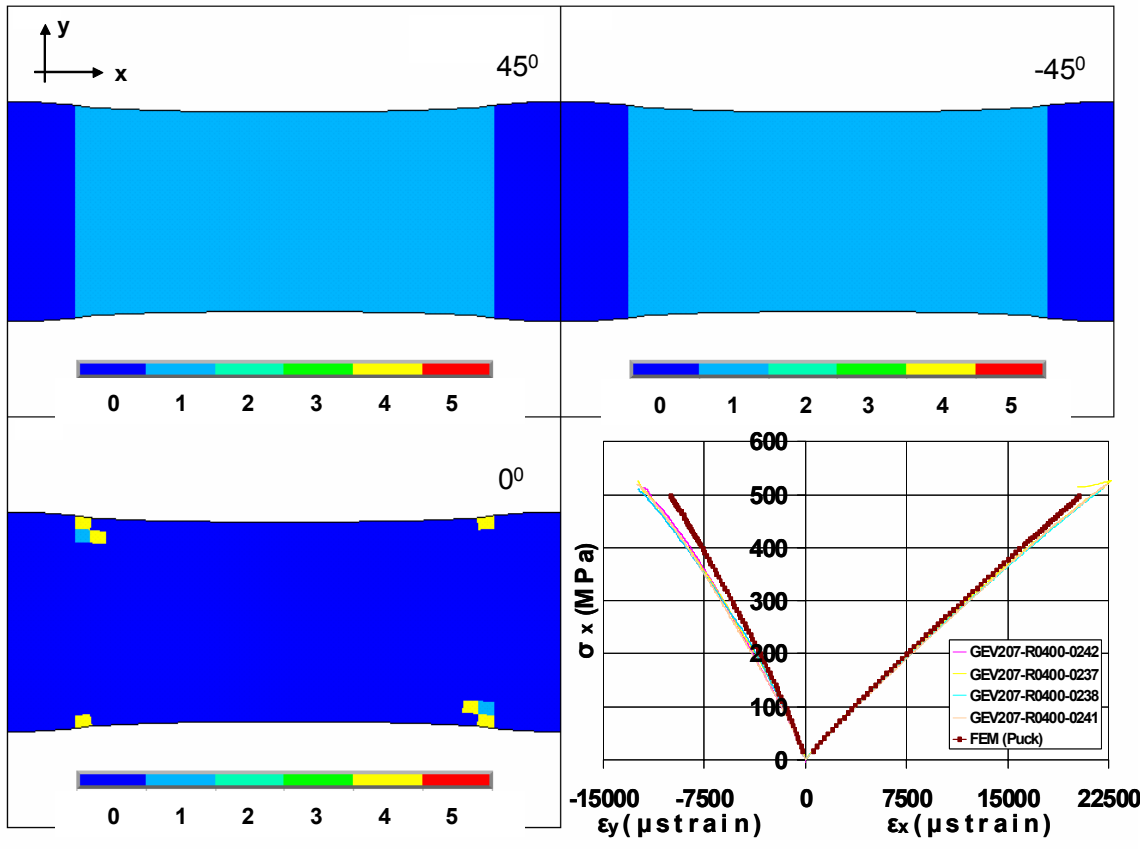
y
x
45⁰
-45⁰
0⁰
0 1 2 3 4 5
600
500
400
300
200
100
0
σ x (MPa)
-15000 -7500 0 7500 15000 22500
εy(μstrain)
εx(μstrain)
GEV207-R0400-0242
GEV207-R0400-0237
GEV207-R0400-0238
GEV207-R0400-0241
FEM (Puck)

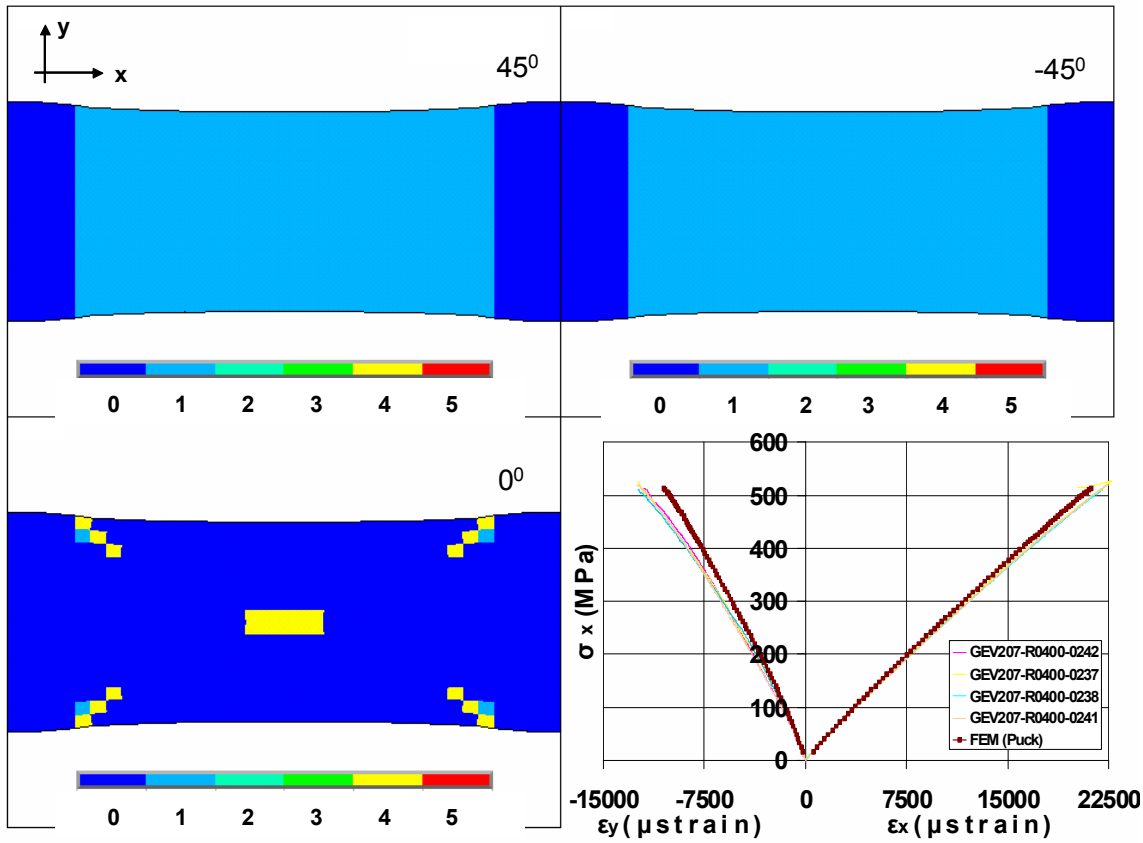
y
x
45⁰
-45⁰
0⁰
0 1 2 3 4 5
σ x (MPa)
600
500
400
300
200
100
0
-15000 -7500 0 7500 15000 22500
εy(μstrain)
εx(μstrain)
GEV207-R0400-0242
GEV207-R0400-0237
GEV207-R0400-0238
GEV207-R0400-0241
FEM (Puck)

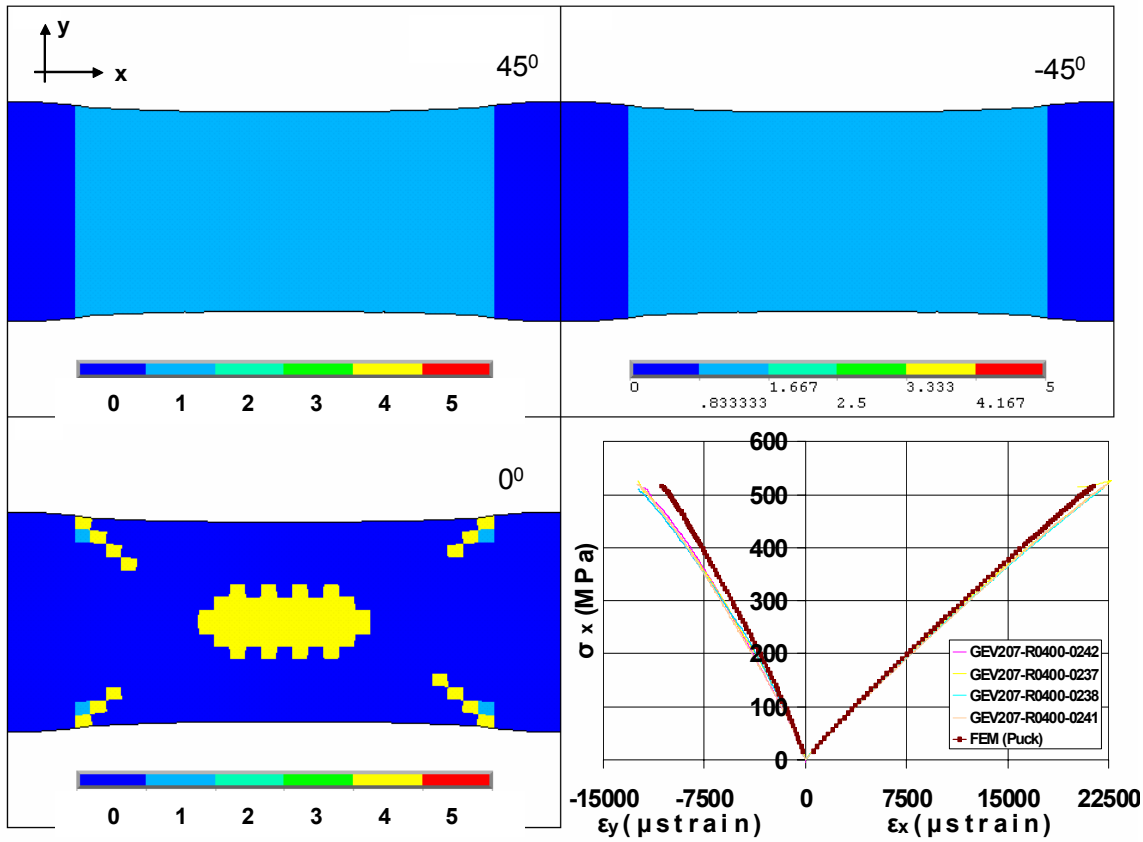
y
x
45⁰
-45⁰
0⁰
0 1 2 3 4 5
0 .833333 1.667 2.5 3.333 4.167 5
σ x (MPa)
600
500
400
300
200
100
0
-15000 -7500 0 7500 15000 22500
εy(μstrain)
εx(μstrain)
GEV207-R0400-0242
GEV207-R0400-0237
GEV207-R0400-0238
GEV207-R0400-0241
FEM (Puck)

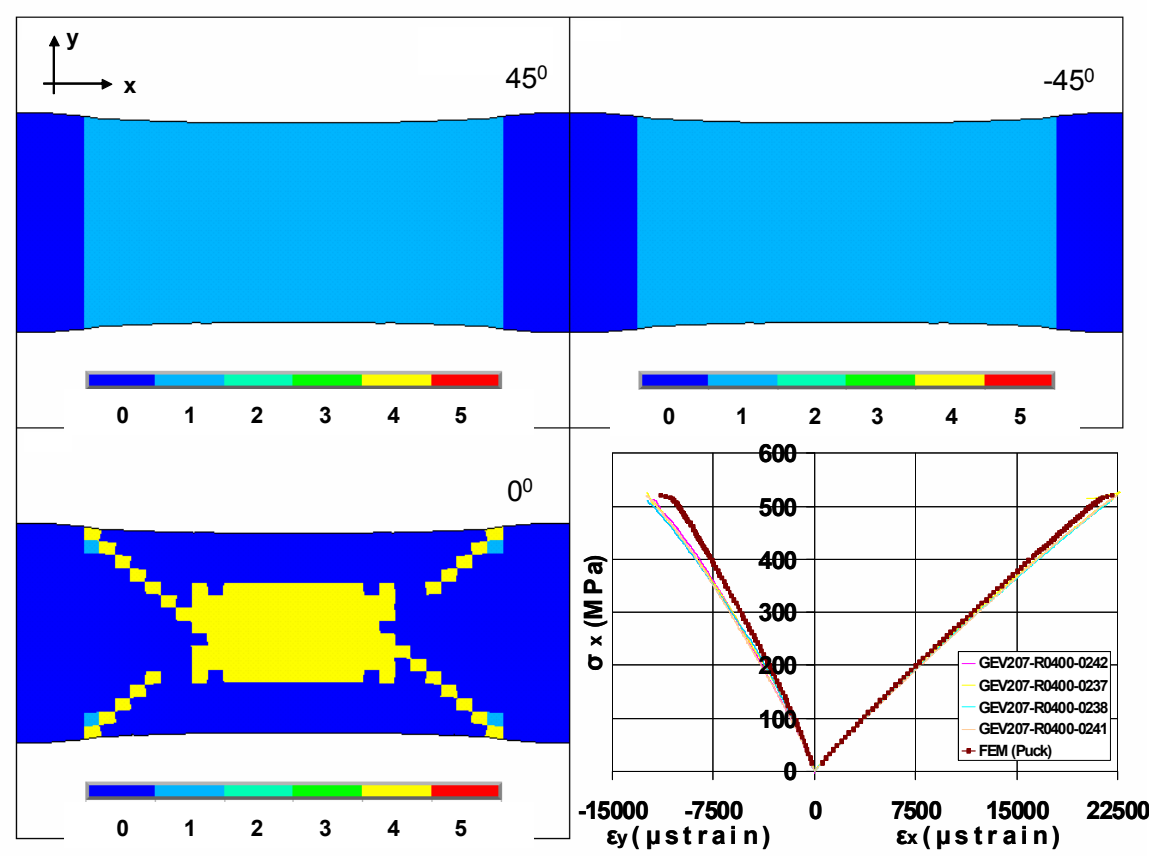

Fig. 49: Stress-Strain behaviour of the MD coupon in tension.

Table 10: Experimental and numerical strength values for MD coupon under tension

	Exp.	**FEM**	**%**
MPa	519.81	520.391	-0.11

The FEM model predicts satisfactorily the material stress-strain curve and the coupon strength, see Table 10, although it behaves a little stiffer than the tested material in the transverse to the load direction. Failure in the form of tensile matrix cracks initiates and propagates in the [±45] layers at almost 30% of the load carrying capacity. Fibre breakage in the unidirectional [0] layers is predicted to start near the tabs region due to stress concentration at 85% of the strength. Sectional weakness leads to further fibre failure till the final rupture. All [0] layers fail simultaneously with the same failure modes approximately.

The simulation model predicts satisfactorily the presence of extended damage on the upper [45] layer, Fig. 49 and additionally the “splitting” rupture of the UD [0] layers as can be observed by a lateral view of the failed coupon, see Fig. 50. Ultrasonic C-scan tests could enhance further assessment.

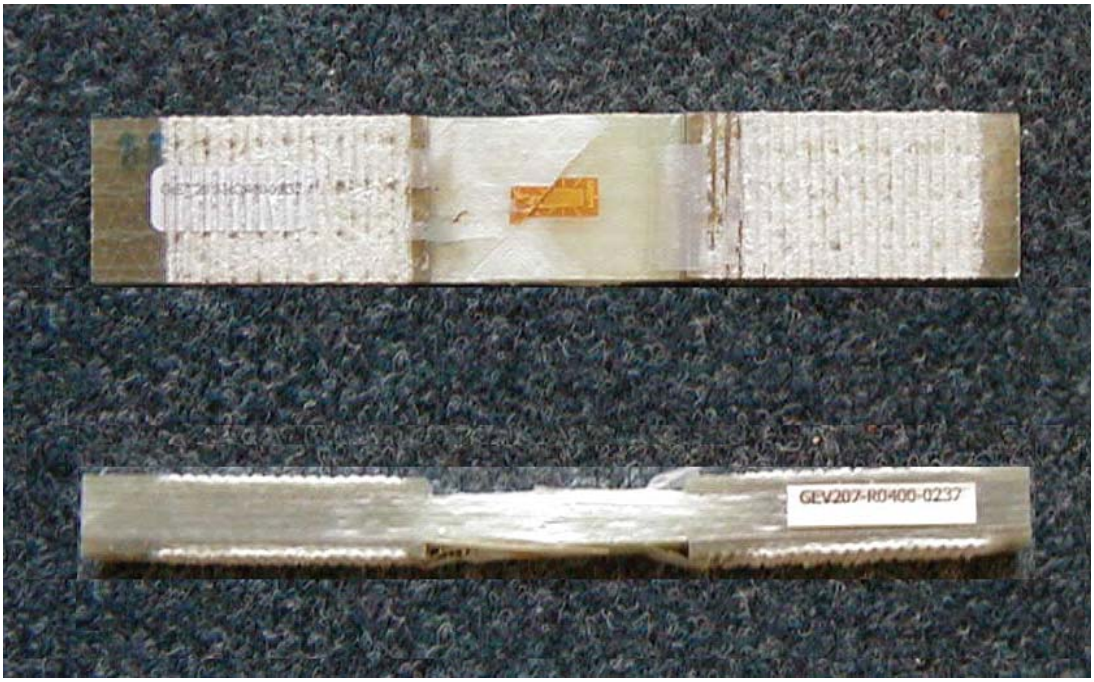

Fig. 50: Failed MD coupon in tension.

6.1.9 Compression of the MD coupon along the fibres of the [0] layer

The multidirectional (MD) coupon is simulated under compressive loading. Material stress-strain behaviour, coupon strength, see Table 11, and damage mechanisms are in a very good agreement with the experiment. Predicted damage and stress-strain progress are presented in Fig. 51.

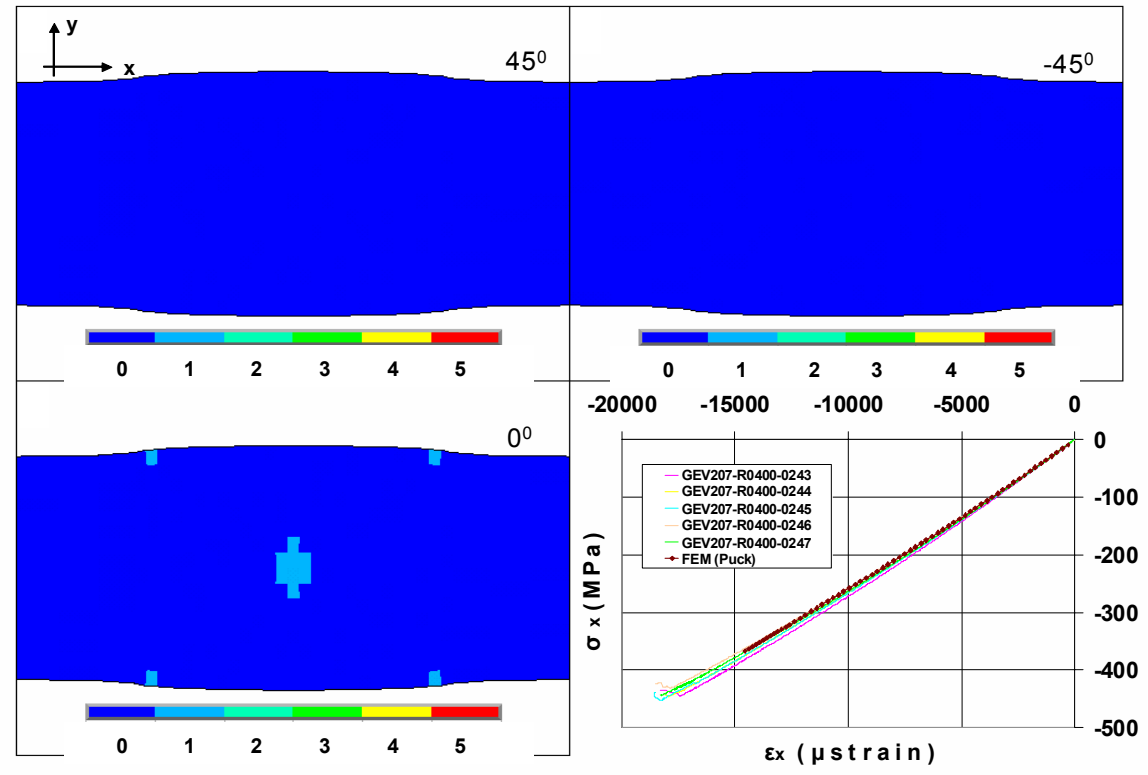

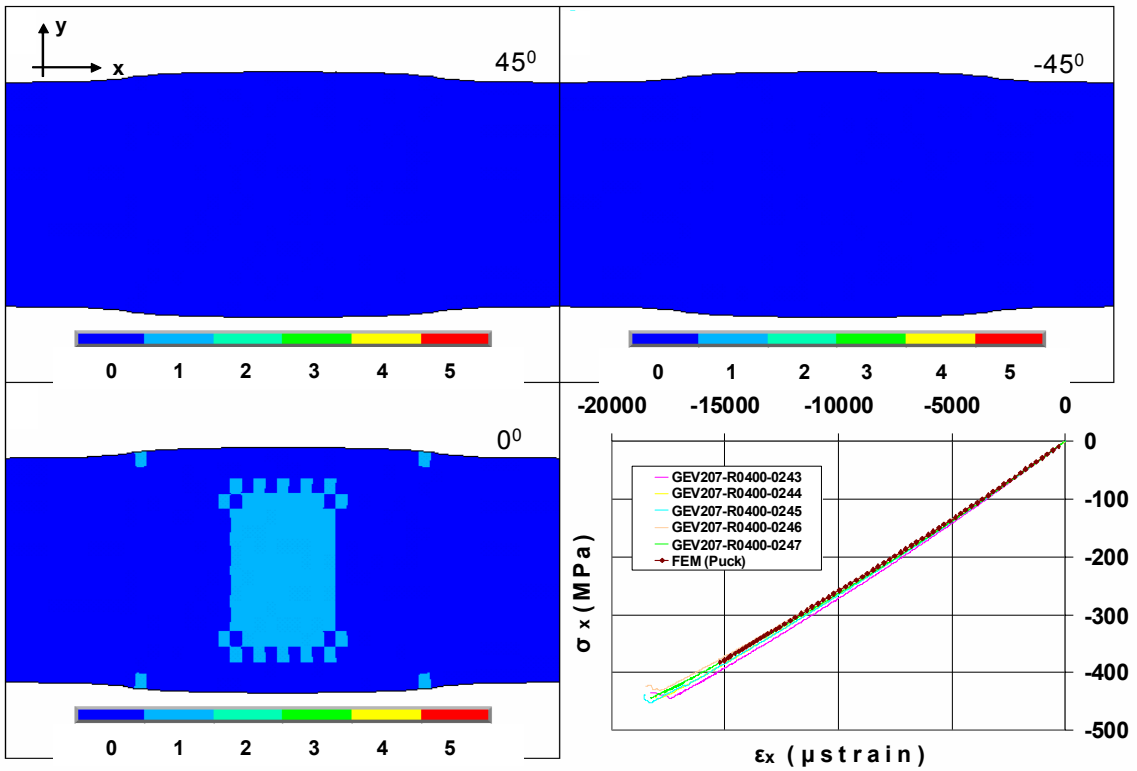
y
x
45⁰
-45⁰
0⁰
0 1 2 3 4 5
-20000 -15000 -10000 -5000 0
0 -100 -200 -300 -400 -500
GEV207-R0400-0243
GEV207-R0400-0244
GEV207-R0400-0245
GEV207-R0400-0246
GEV207-R0400-0247
FEM (Puck)
σ x (MPa)
εx (μstrain)

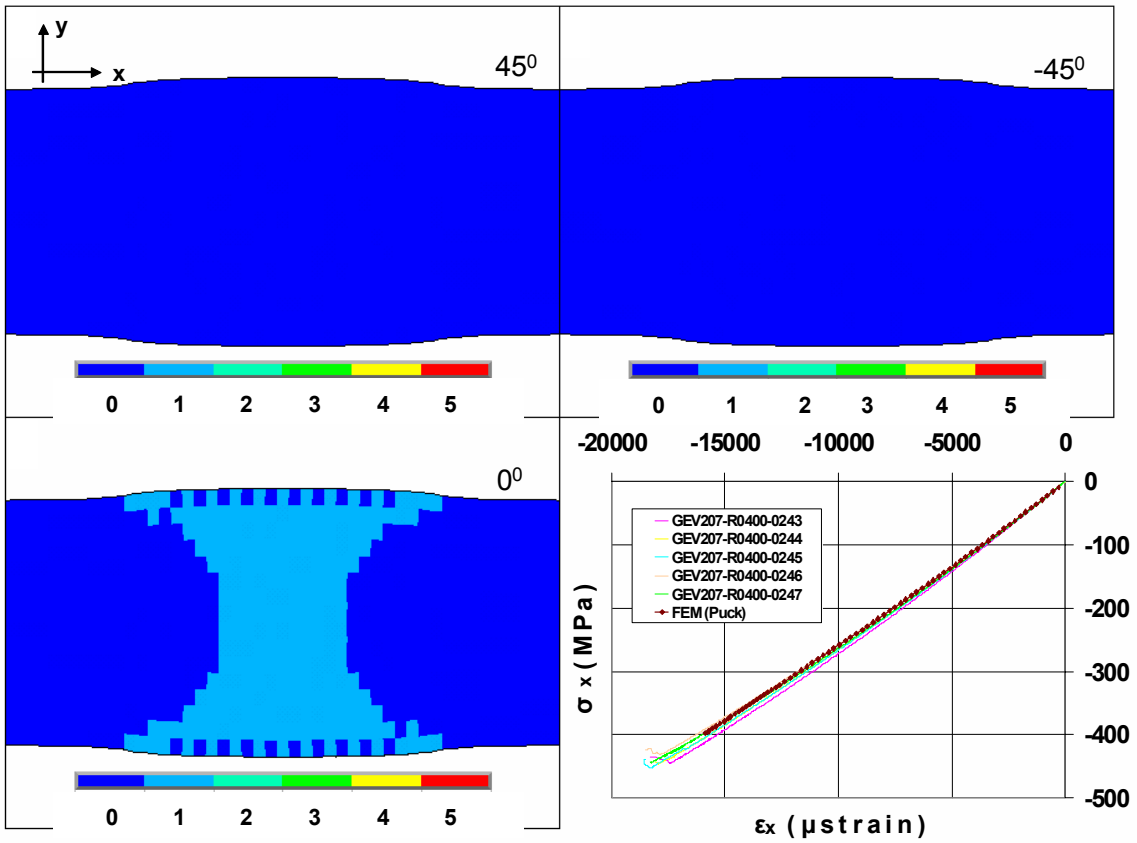
y
x
45⁰
-45⁰
0⁰
0 1 2 3 4 5
-20000 -15000 -10000 -5000 0
0 -100 -200 -300 -400 -500
GEV207-R0400-0243
GEV207-R0400-0244
GEV207-R0400-0245
GEV207-R0400-0246
GEV207-R0400-0247
FEM (Puck)
σ x (MPa)
εx (μstrain)

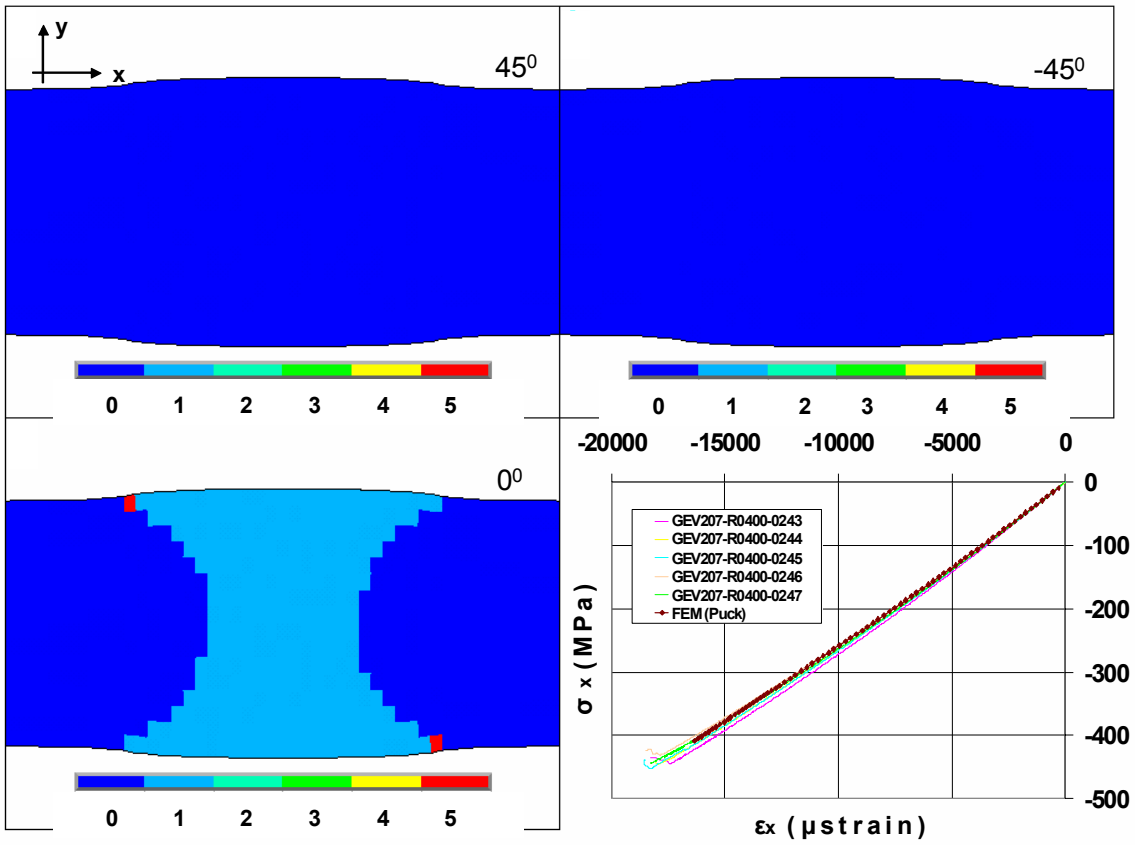
y
x
45⁰
-45⁰
0 1 2 3 4 5
0 1 2 3 4 5
0⁰
0 1 2 3 4 5
-20000 -15000 -10000 -5000 0
0
-100
-200
-300
-400
-500
σ x (MPa)
εx (μstrain)
GEV207-R0400-0243
GEV207-R0400-0244
GEV207-R0400-0245
GEV207-R0400-0246
GEV207-R0400-0247
FEM (Puck)

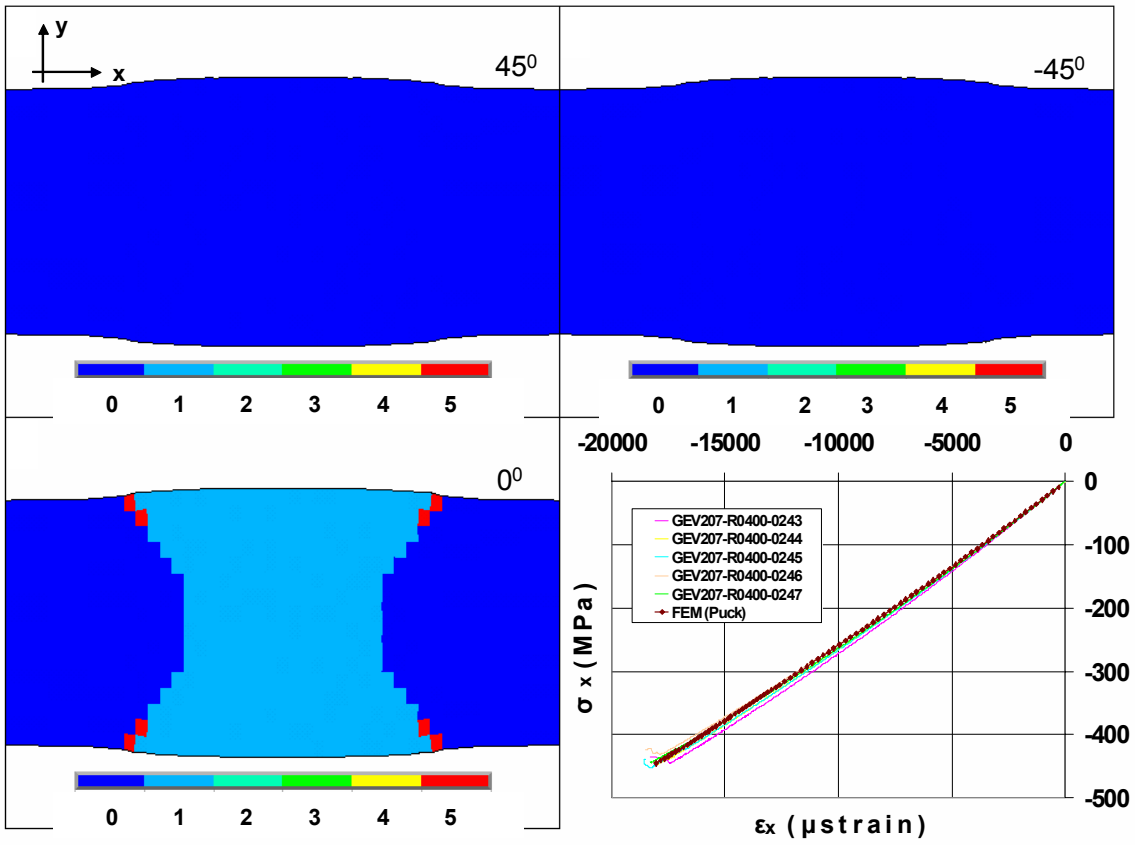
y
x
45⁰
-45⁰
0 1 2 3 4 5
0 1 2 3 4 5
0⁰
0 1 2 3 4 5
-20000 -15000 -10000 -5000 0
0
-100
-200
-300
-400
-500
σ x (MPa)
εx (μstrain)
GEV207-R0400-0243
GEV207-R0400-0244
GEV207-R0400-0245
GEV207-R0400-0246
GEV207-R0400-0247
FEM (Puck)

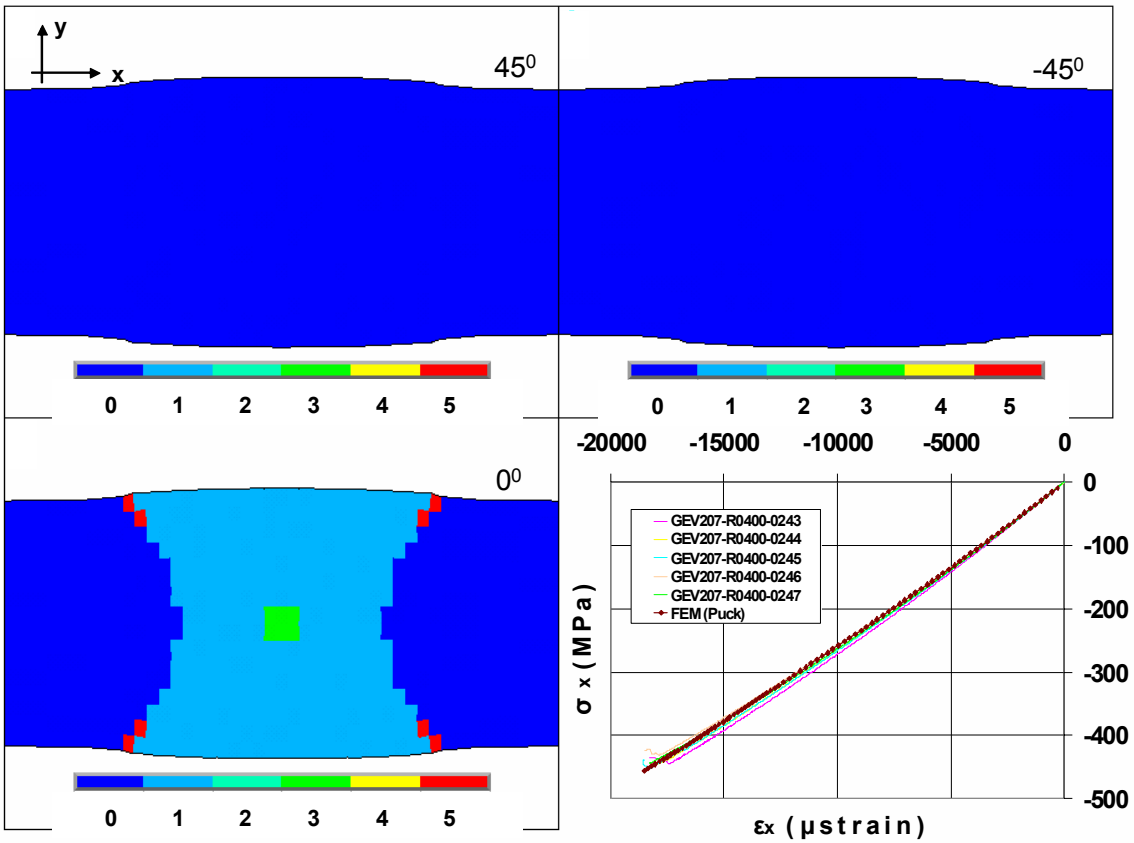
y
x
45⁰
-45⁰
0 1 2 3 4 5
0 1 2 3 4 5
0⁰
0 1 2 3 4 5
-20000 -15000 -10000 -5000 0
0
-100
-200
-300
-400
-500
σ x (MPa)
εx (μstrain)
GEV207-R0400-0243
GEV207-R0400-0244
GEV207-R0400-0245
GEV207-R0400-0246
GEV207-R0400-0247
FEM (Puck)

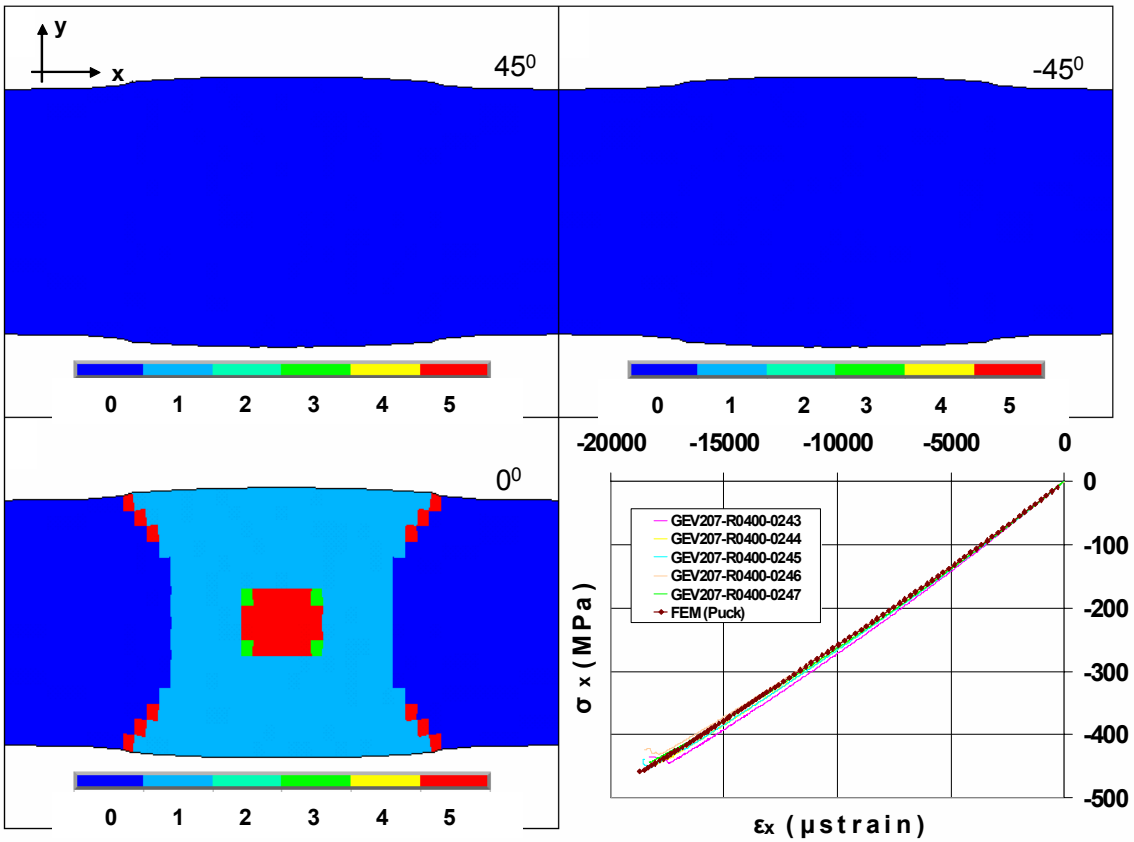
y
x
45⁰
-45⁰
0 1 2 3 4 5
0 1 2 3 4 5
0⁰
0 1 2 3 4 5
-20000 -15000 -10000 -5000 0
0
-100
-200
-300
-400
-500
σ x (MPa)
εx (μstrain)
GEV207-R0400-0243
GEV207-R0400-0244
GEV207-R0400-0245
GEV207-R0400-0246
GEV207-R0400-0247
FEM (Puck)

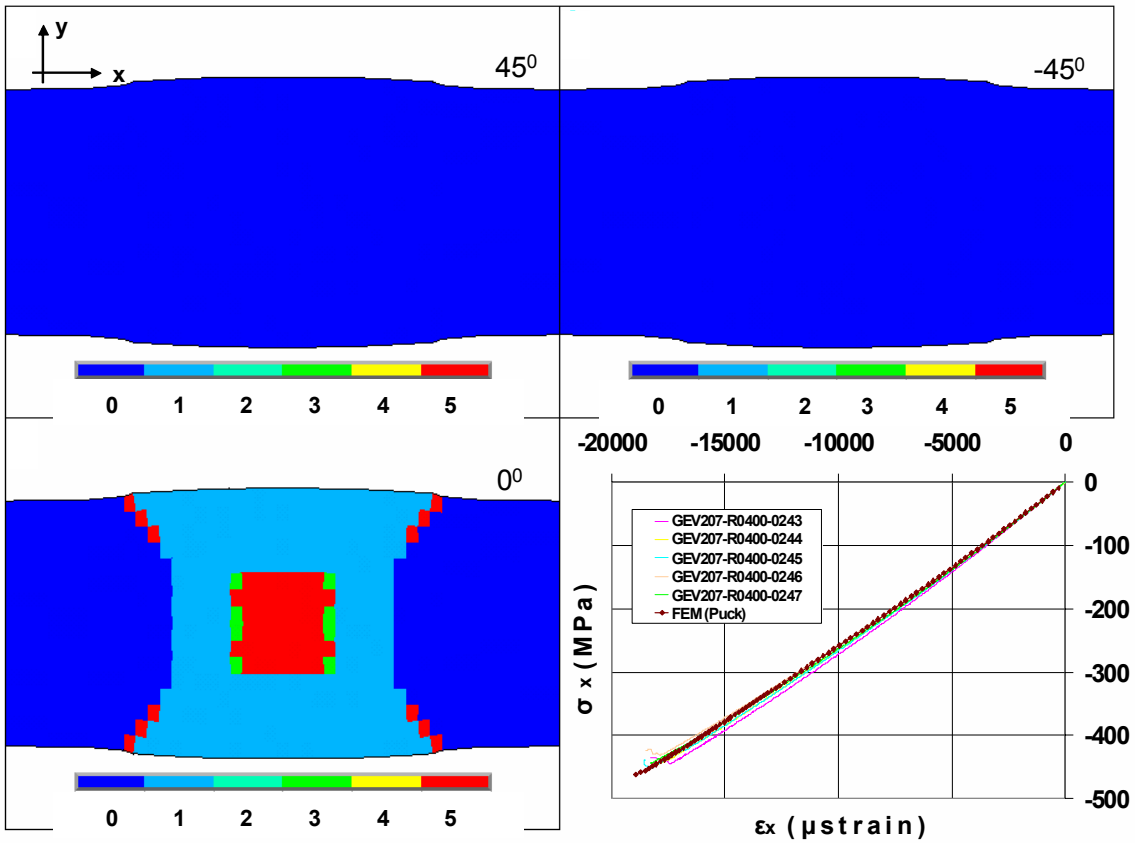
y
x
45⁰
-45⁰
0 1 2 3 4 5
0 1 2 3 4 5
-20000 -15000 -10000 -5000 0
0⁰
0 1 2 3 4 5
GEV207-R0400-0243
GEV207-R0400-0244
GEV207-R0400-0245
GEV207-R0400-0246
GEV207-R0400-0247
FEM (Puck)
σ x (MPa)
0 -100 -200 -300 -400 -500
εx (μstrain)

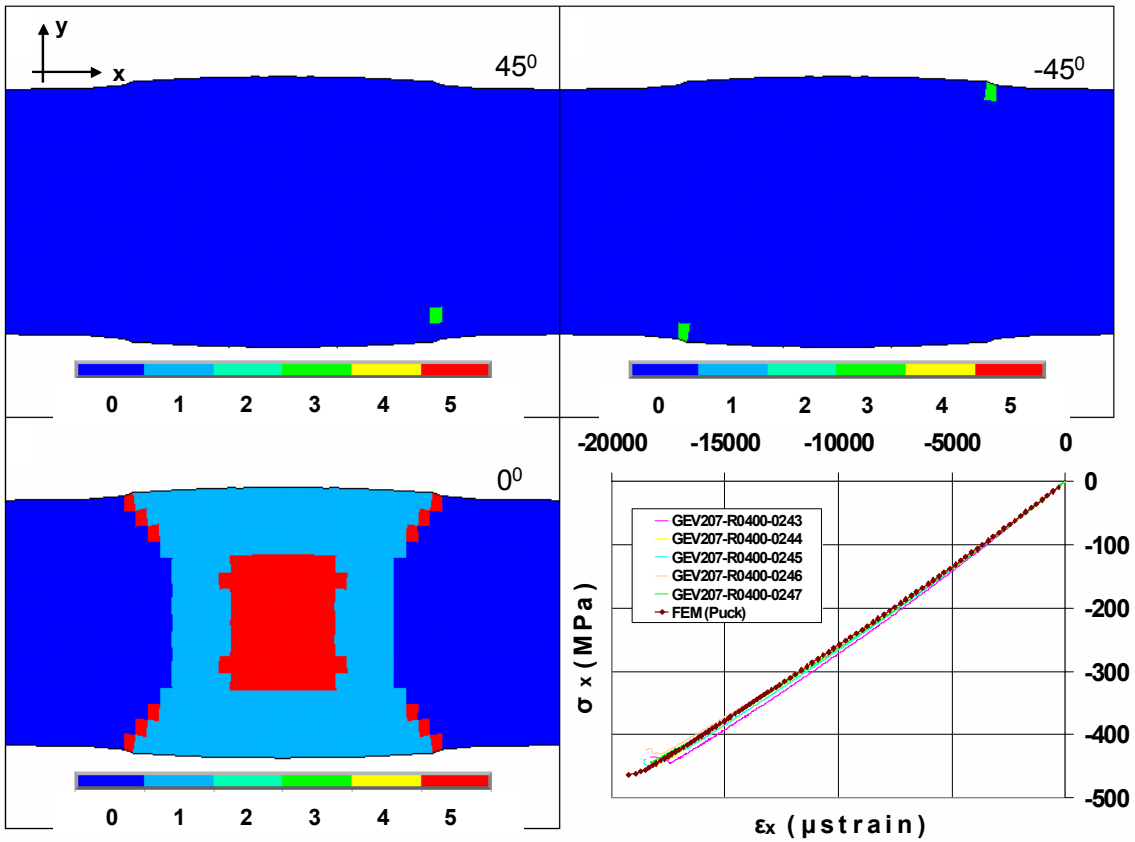
y
x
45⁰
-45⁰
0 1 2 3 4 5
0 1 2 3 4 5
-20000 -15000 -10000 -5000 0
0⁰
0 1 2 3 4 5
GEV207-R0400-0243
GEV207-R0400-0244
GEV207-R0400-0245
GEV207-R0400-0246
GEV207-R0400-0247
FEM (Puck)
σ x (MPa)
0 -100 -200 -300 -400 -500
εx (μstrain)

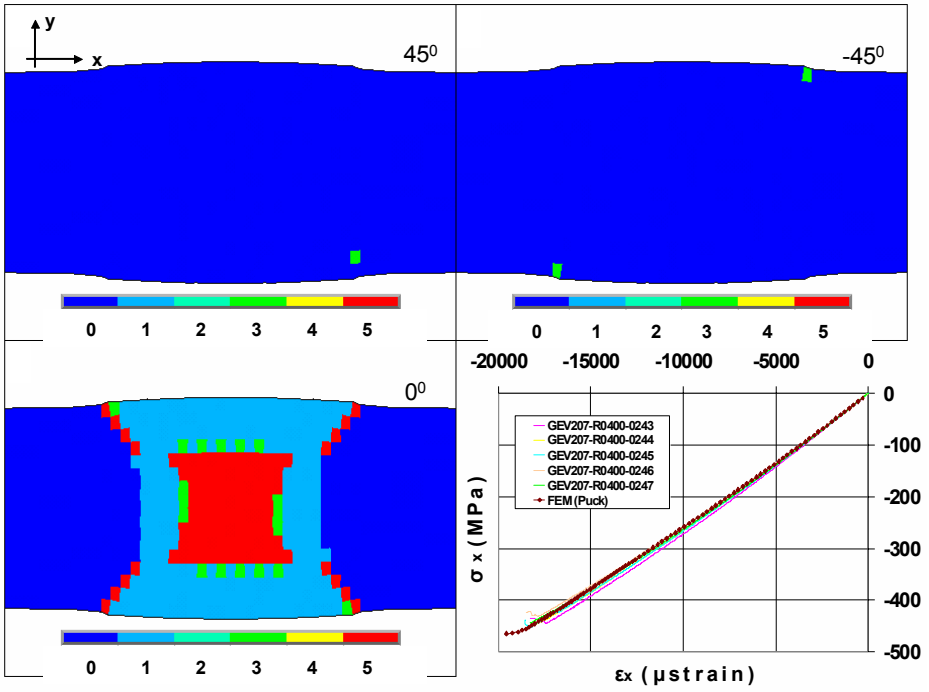

Fig. 51: Stress-Strain behavior of an MD coupon in tension.

Table 11. Experimental and numerical strength values for MD coupon under compression

	Exp.	**FEM**	**%**
MPa	-443.71	-463.15	-4.38

Damage initiates at 80% of the predicted ultimate compressive strength in the form of tensile matrix cracking (mode A), indicated with number 1, and propagates in the [0] layers along coupon width. Stress concentration near tabs area enhances fibre rupture pointed out with number 5. Except the extended damage in the middle of the coupon caused from fibre kinking in the UD [0] layer, a direct comparison cannot be done between the simulated and the experimental failure mode, Fig. 52, but ultrasonic C-scan tests could enhance further assessment.

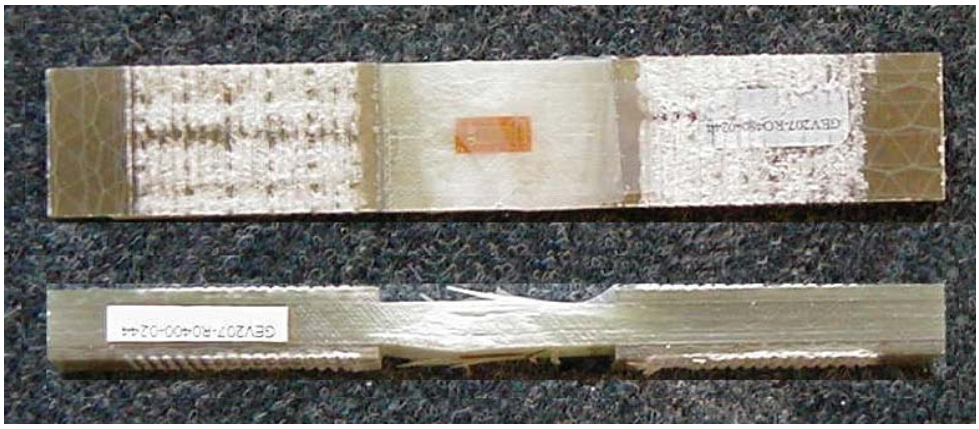

Fig. 52: Failed MD coupon in compression

6.1.10 Tension of MD coupon off-axis loaded at 10^0

To facilitate complex stress states in principal material coordinates of UD 0^0 layers, multidirectional specimens are cut in various off-axis angles with respect to the MD [0] ply and are loaded either in tension or compression. The MD [10] coupon is cut at 10^0 and it is therefore composed of [55], [-35] and [10] layers. It is a highly anisotropic lay-up, unbalanced and non-symmetric leading to severe structural couplings. FEM results are in good agreement with the experimental data, Fig.53. The numerical model predicts satisfactorily the ultimate tensile stress, see Table 12.

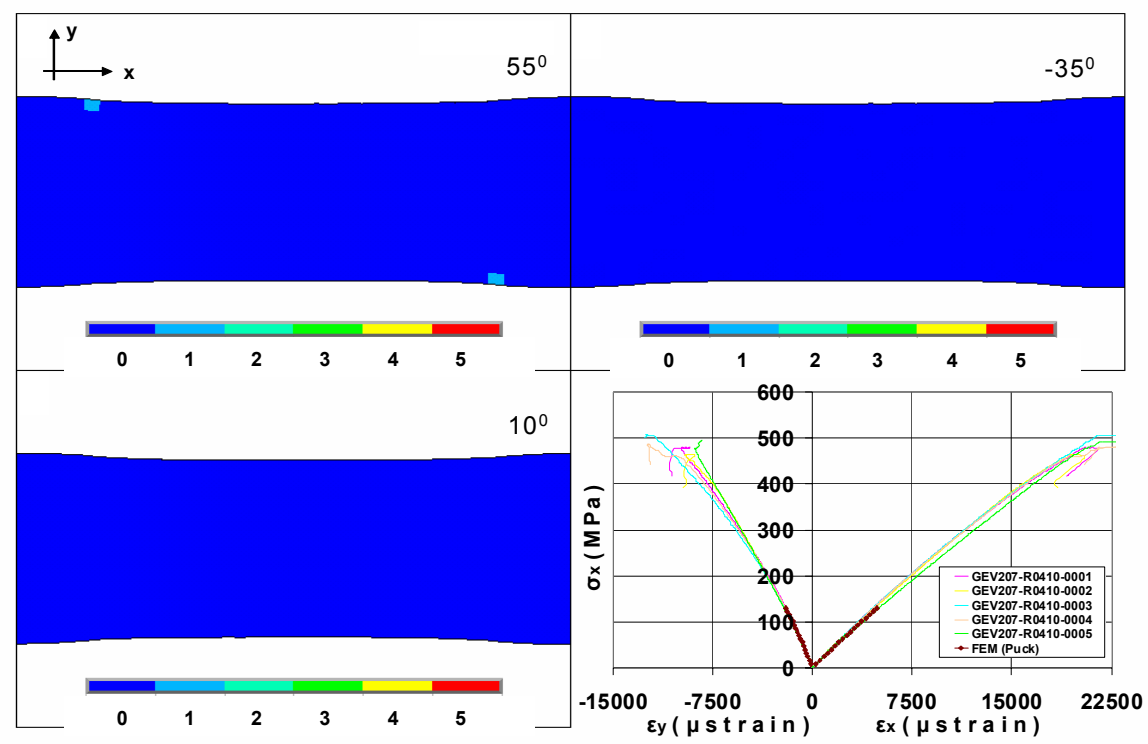

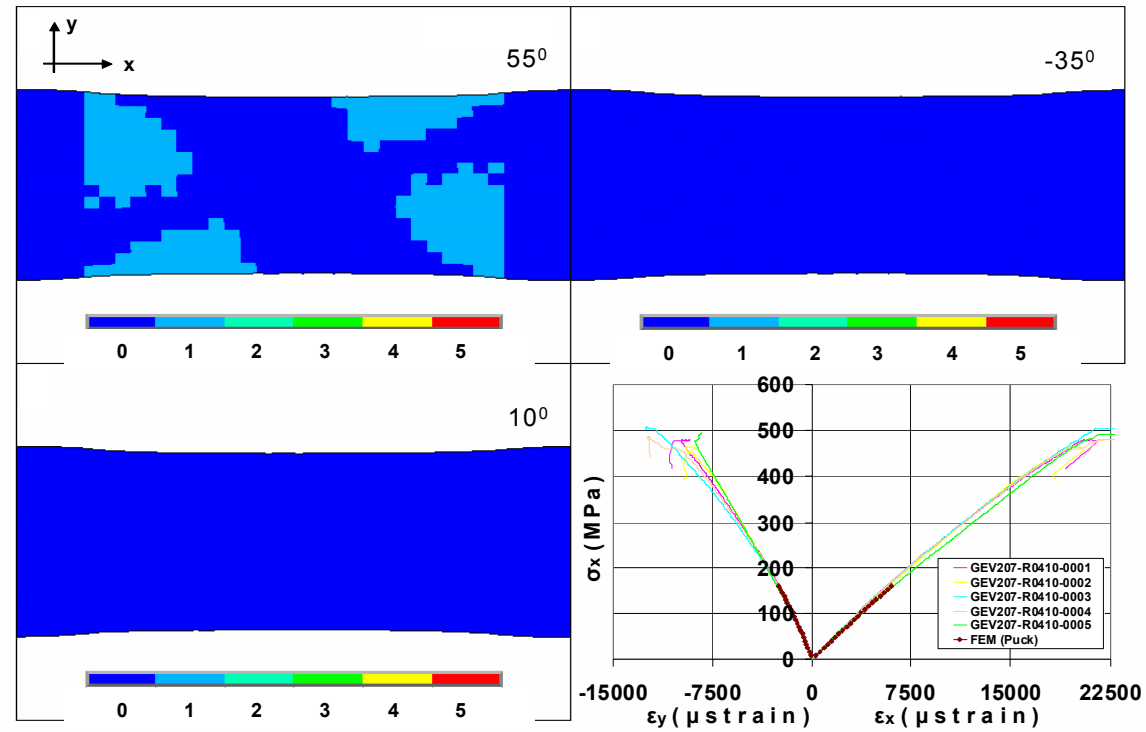
y
x
55⁰
-35⁰
10⁰
0 1 2 3 4 5
600
500
400
300
200
100
0
σx (MPa)
-15000 -7500 0 7500 15000 22500
εy (μstrain) εx (μstrain)
GEV207-R0410-0001
GEV207-R0410-0002
GEV207-R0410-0003
GEV207-R0410-0004
GEV207-R0410-0005
FEM (Puck)

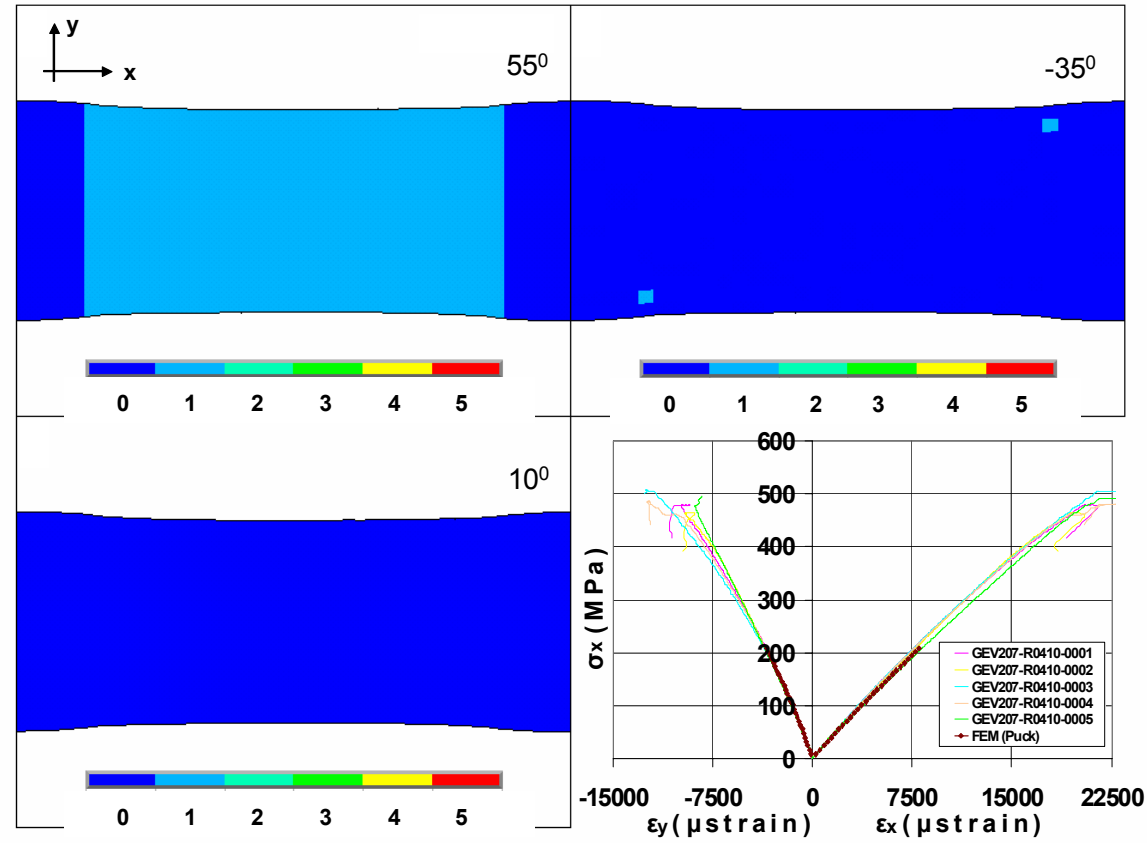
y
x
55⁰
-35⁰
10⁰
0 1 2 3 4 5
600
500
400
300
200
100
0
σx (MPa)
-15000 -7500 0 7500 15000 22500
εy (μstrain) εx (μstrain)
GEV207-R0410-0001
GEV207-R0410-0002
GEV207-R0410-0003
GEV207-R0410-0004
GEV207-R0410-0005
FEM (Puck)

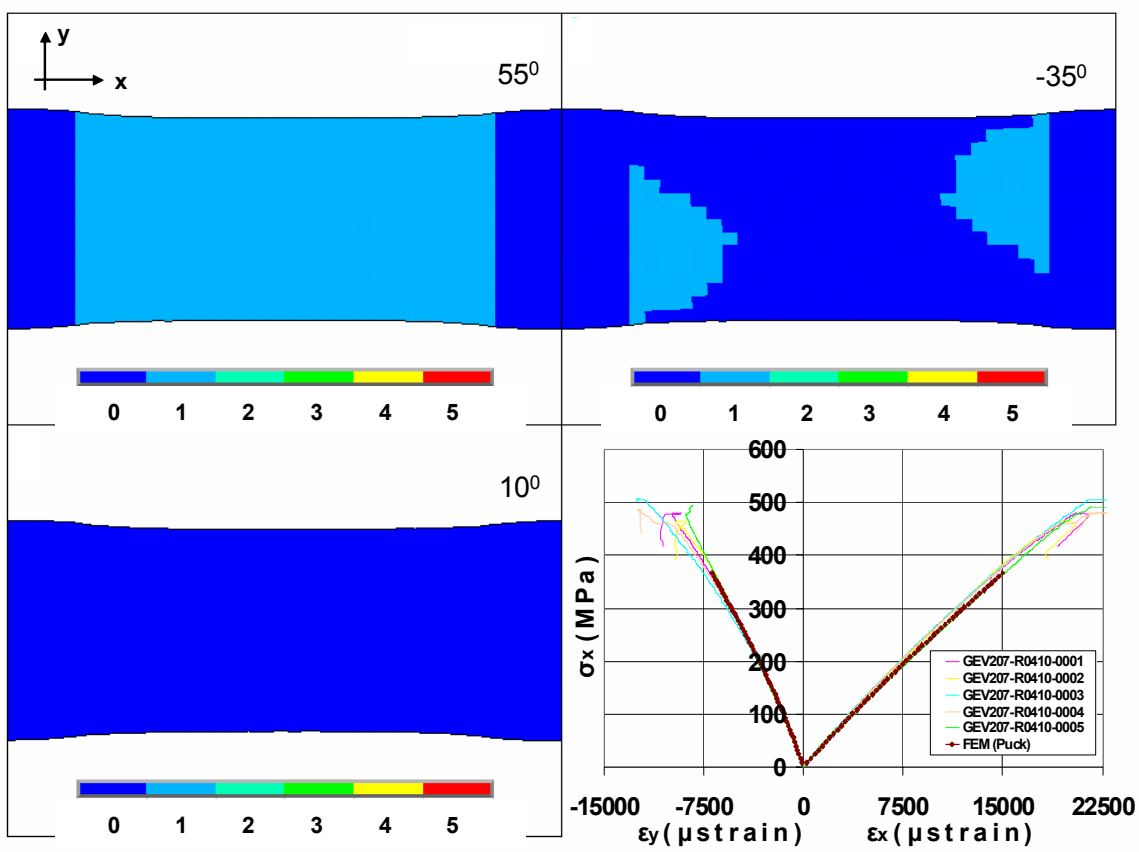
y
x
55⁰
-35⁰
10⁰
0 1 2 3 4 5
600
500
400
300
200
100
0
σx (MPa)
-15000 -7500 0 7500 15000 22500
εy (μstrain)
εx (μstrain)
GEV207-R0410-0001
GEV207-R0410-0002
GEV207-R0410-0003
GEV207-R0410-0004
GEV207-R0410-0005
FEM (Puck)

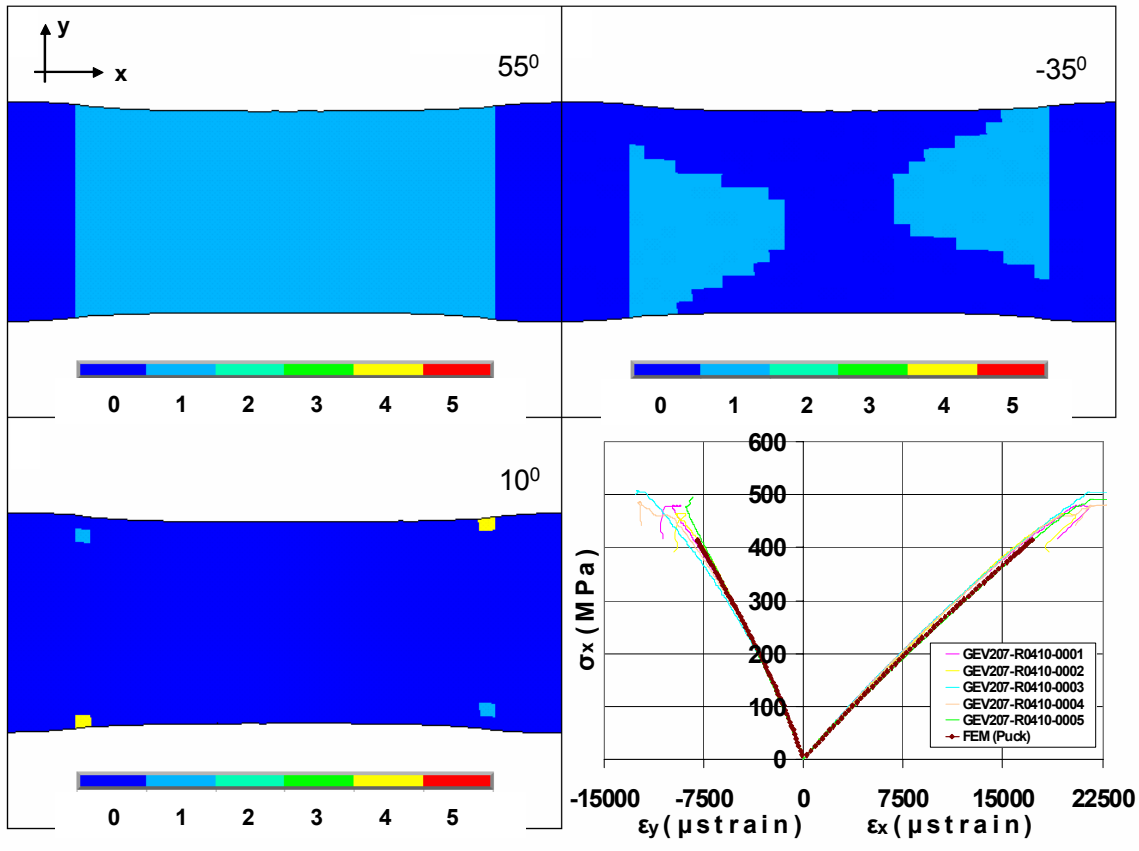
y
x
55⁰
-35⁰
10⁰
0 1 2 3 4 5
600
500
400
300
200
100
0
σx (MPa)
-15000 -7500 0 7500 15000 22500
εy (μstrain)
εx (μstrain)
GEV207-R0410-0001
GEV207-R0410-0002
GEV207-R0410-0003
GEV207-R0410-0004
GEV207-R0410-0005
FEM (Puck)

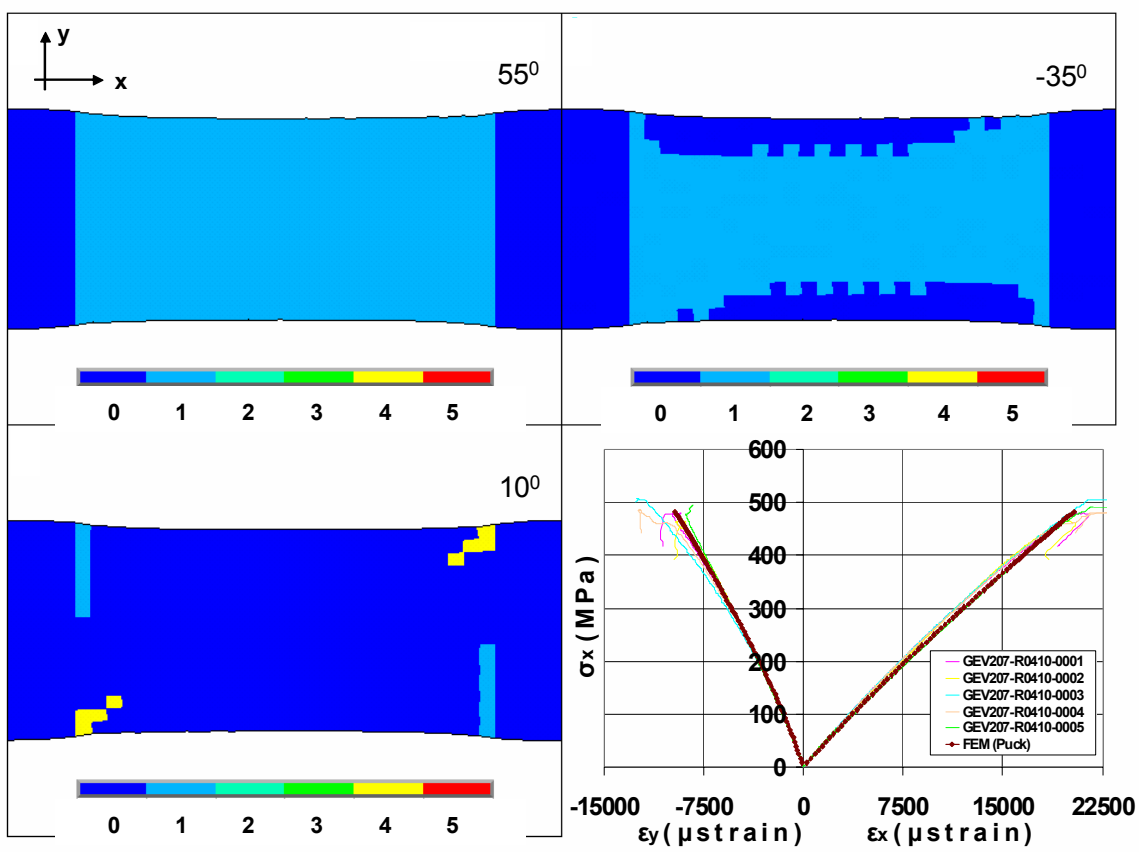
y
x
55⁰
-35⁰
10⁰
0 1 2 3 4 5
σx (MPa)
600
500
400
300
200
100
0
-15000 -7500 0 7500 15000 22500
εy (μstrain) εx (μstrain)
GEV207-R0410-0001
GEV207-R0410-0002
GEV207-R0410-0003
GEV207-R0410-0004
GEV207-R0410-0005
FEM (Puck)

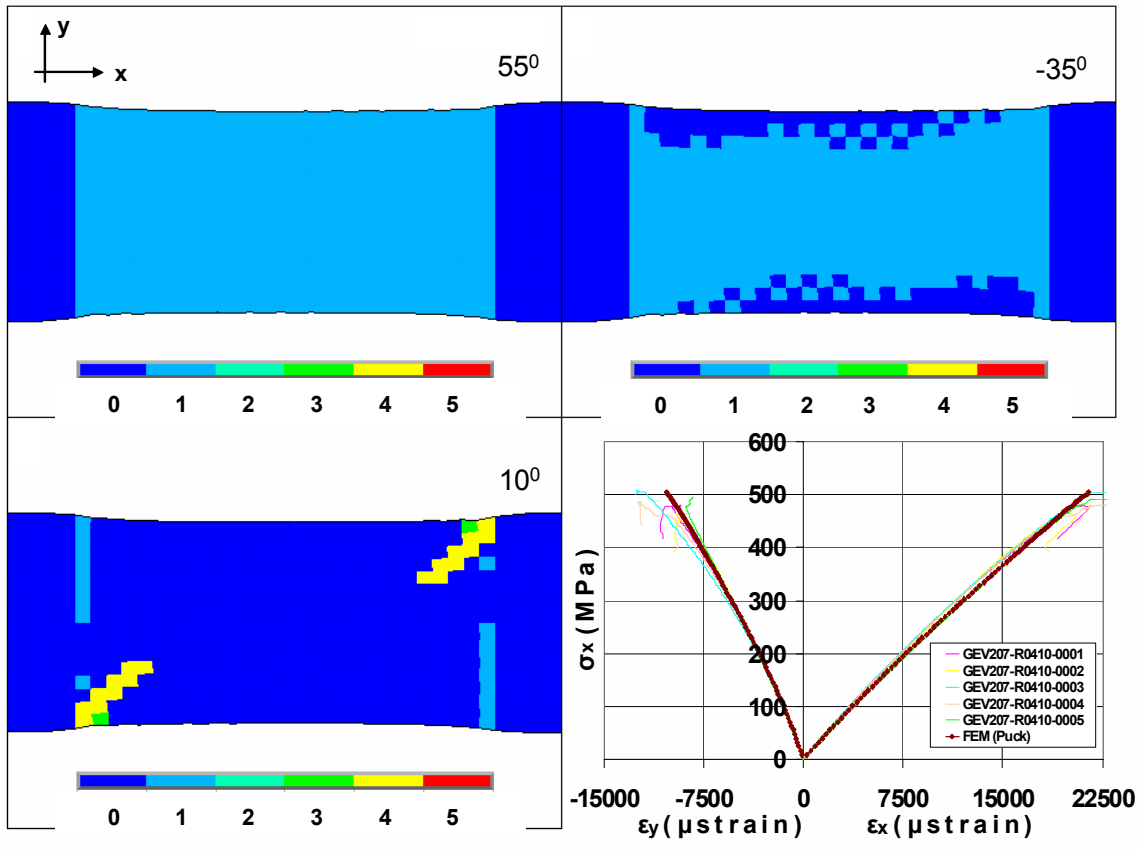
y
x
55⁰
-35⁰
10⁰
0 1 2 3 4 5
σx (MPa)
600
500
400
300
200
100
0
-15000 -7500 0 7500 15000 22500
εy (μstrain) εx (μstrain)
GEV207-R0410-0001
GEV207-R0410-0002
GEV207-R0410-0003
GEV207-R0410-0004
GEV207-R0410-0005
FEM (Puck)

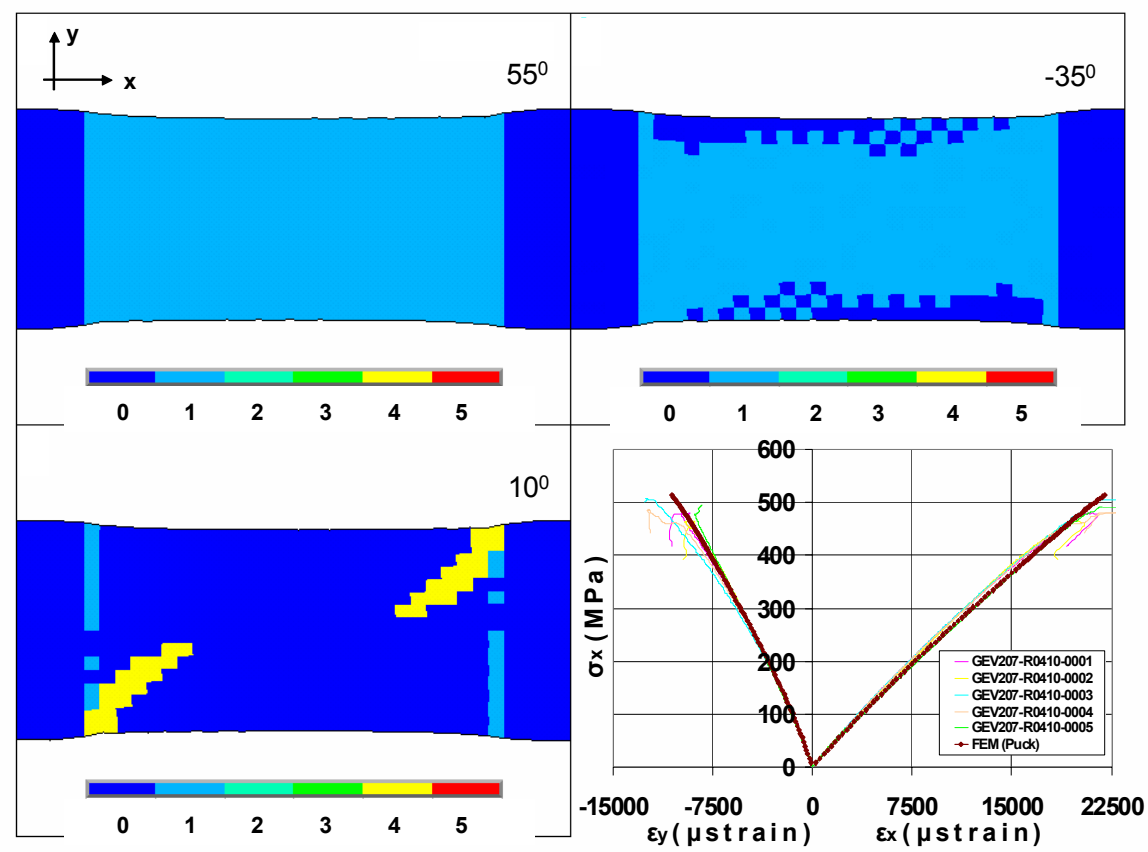
y
x
55⁰
-35⁰
10⁰
0 1 2 3 4 5
σx (MPa)
600
500
400
300
200
100
0
-15000 -7500 0 7500 15000 22500
εy (μstrain) εx (μstrain)
GEV207-R0410-0001
GEV207-R0410-0002
GEV207-R0410-0003
GEV207-R0410-0004
GEV207-R0410-0005
FEM (Puck)

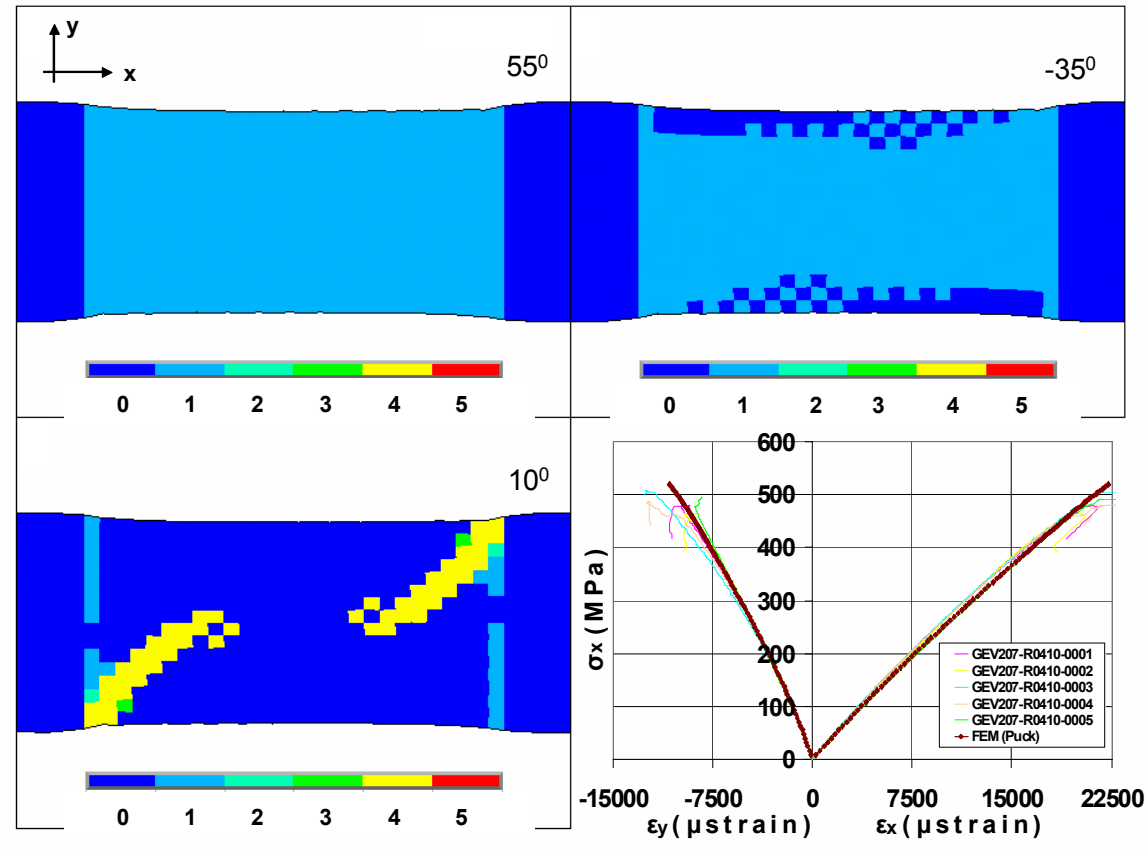
y
x
55⁰
-35⁰
10⁰
0 1 2 3 4 5
σx (MPa)
600
500
400
300
200
100
0
-15000 -7500 0 7500 15000 22500
εy (μstrain) εx (μstrain)
GEV207-R0410-0001
GEV207-R0410-0002
GEV207-R0410-0003
GEV207-R0410-0004
GEV207-R0410-0005
FEM (Puck)

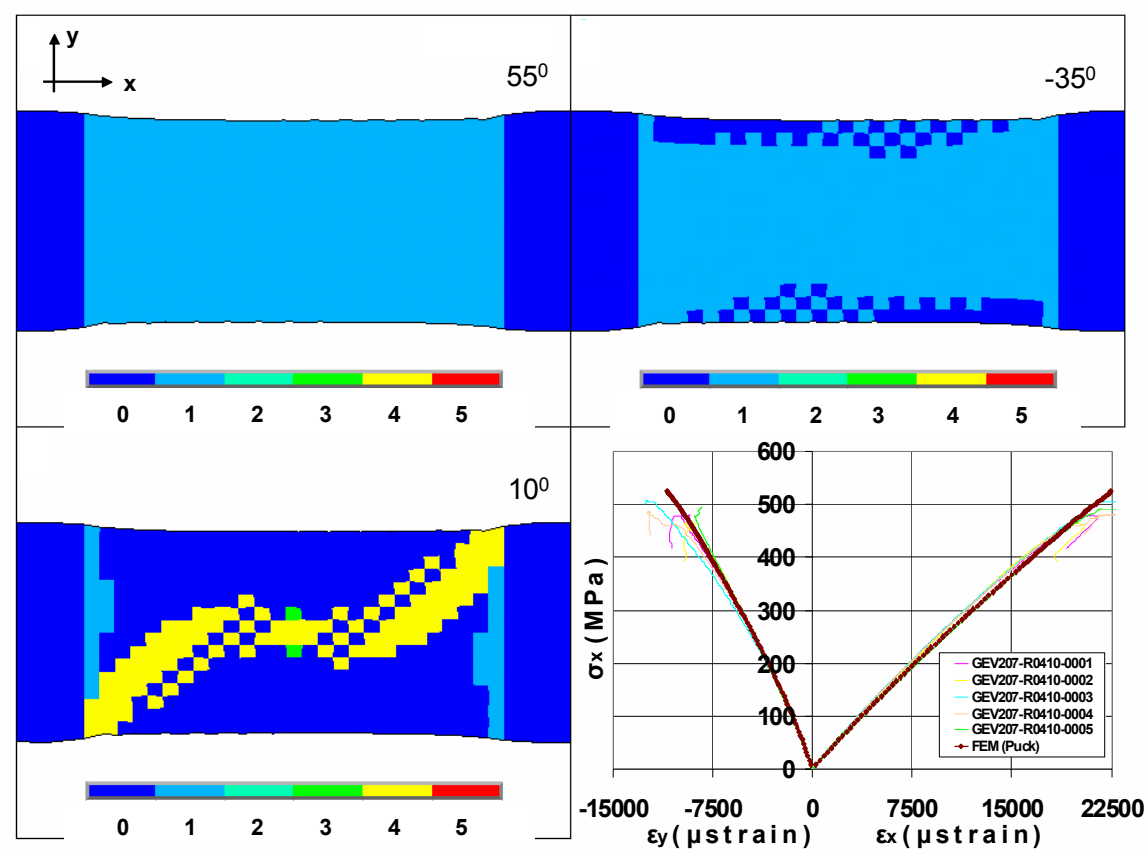

Fig. 53: Stress-Strain behavior of an MD [10] coupon in tension.

Table 12: Experimental and numerical strength values for MD coupon @ 10 degrees under tension

	Exp.	**FEM**	**%**
MPa	486.75	524.95	-7.85

Damage initiates at 25% of the calculated ultimate tensile strength and propagates in the [55] plies as tensile matrix cracks of type A, indicated with number 1, subsequently with the [-35] plies, also in the form of tensile matrix cracks. Well after first ply failure load, catastrophic fiber fracture occurs in the [10] plies, indicated with number 4. Examining the tested coupons, Fig.54, extended damage under and near the tabs region is noticed. This appearance is due to matrix cracking in the upper layers and fiber breakage beneath in UD [10] layers. The FEM model predicts fairly well the location of the final failure; see Fig.53, since no damage is calculated under the tabs region.

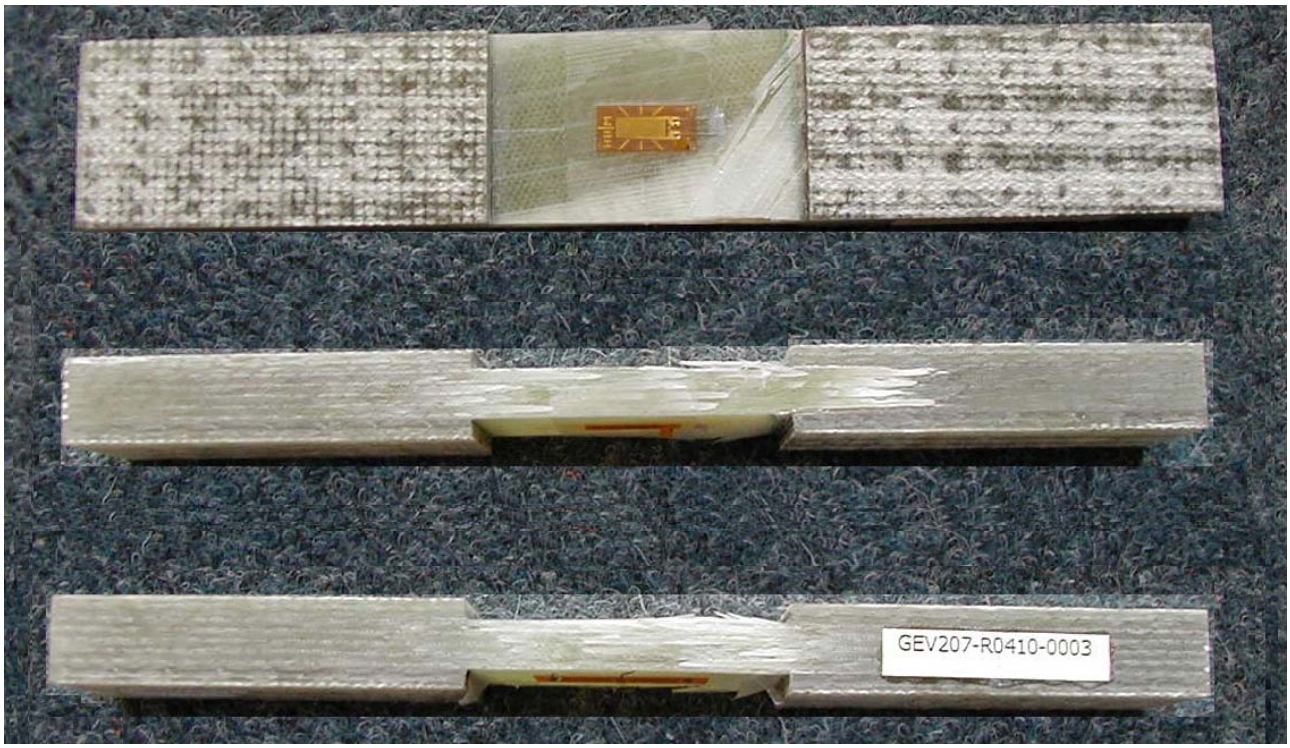

Fig. 54: Failed MD coupon loaded off-axis in tension at 10^o

6.1.11 Compression of MD coupon off-axis loaded at 10^o

MD coupon @ 10^o is simulated under compression. FEM results are in good agreement with the experimental data. The numerical model performs less stiff than the experiment, Fig.55, predicting non-conservative ultimate compressive stress, see Table 13.

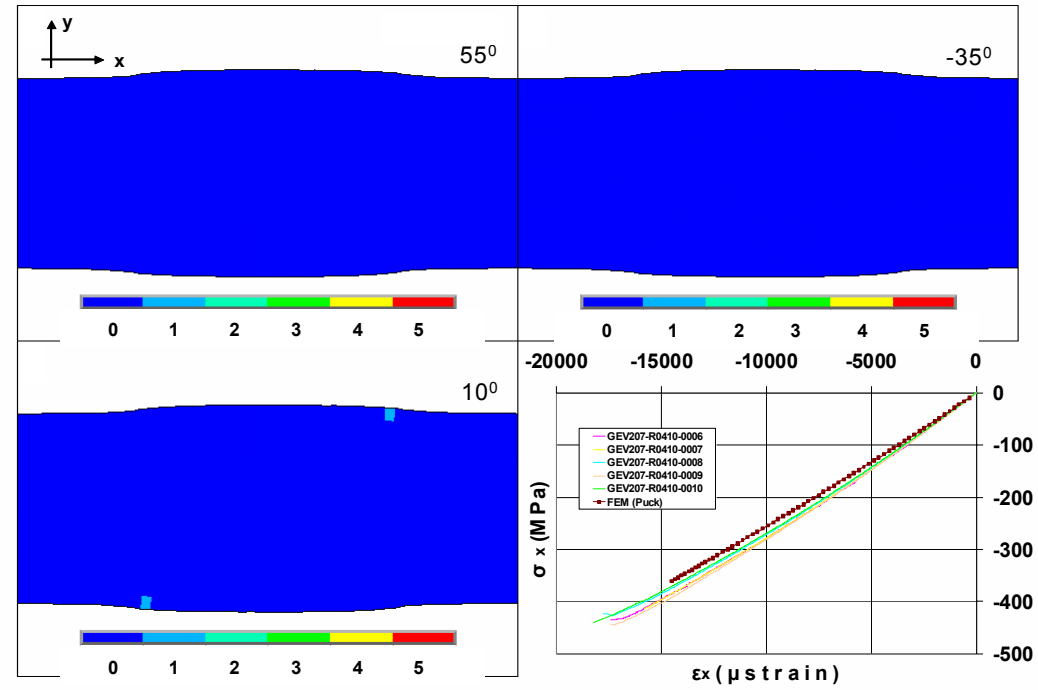

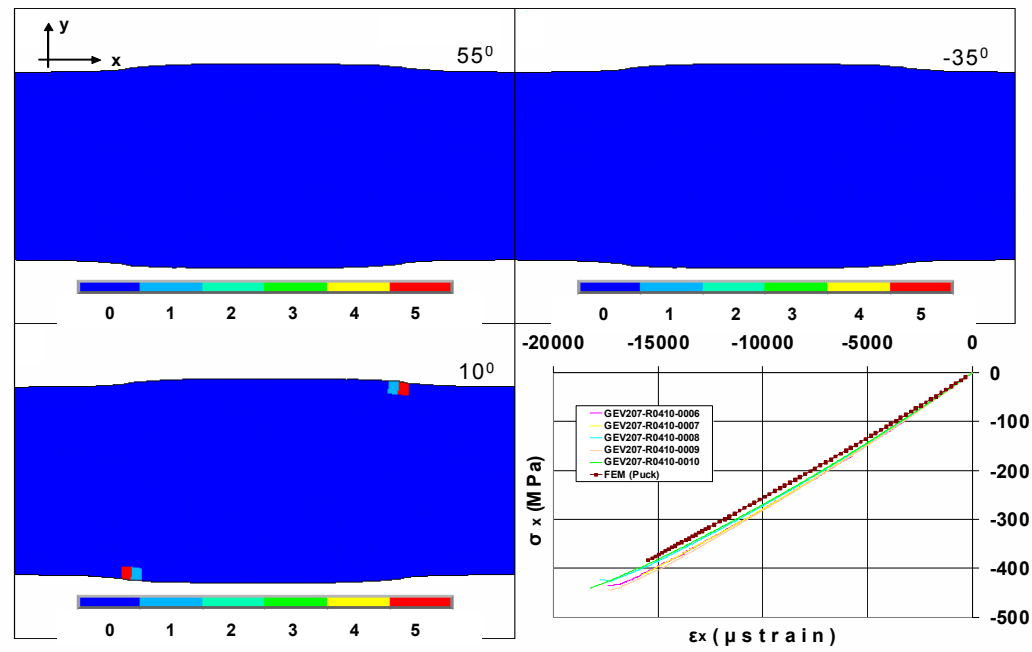
y
x
55⁰
-35⁰
10⁰
0 1 2 3 4 5
-20000 -15000 -10000 -5000 0
0 -100 -200 -300 -400 -500
σ x (MPa)
εx (μstrain)
GEV207-R0410-0006
GEV207-R0410-0007
GEV207-R0410-0008
GEV207-R0410-0009
GEV207-R0410-0010
FEM (Puck)

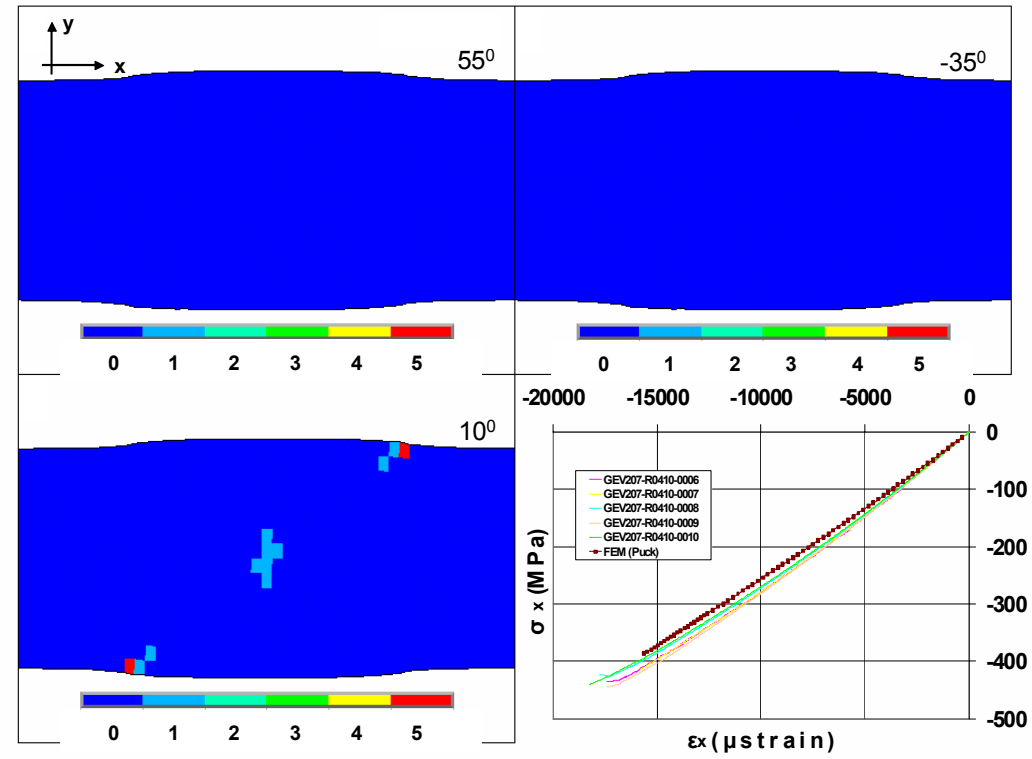
y
x
55⁰
-35⁰
10⁰
0 1 2 3 4 5
-20000 -15000 -10000 -5000 0
0 -100 -200 -300 -400 -500
σ x (MPa)
εx (μstrain)
GEV207-R0410-0006
GEV207-R0410-0007
GEV207-R0410-0008
GEV207-R0410-0009
GEV207-R0410-0010
FEM (Puck)

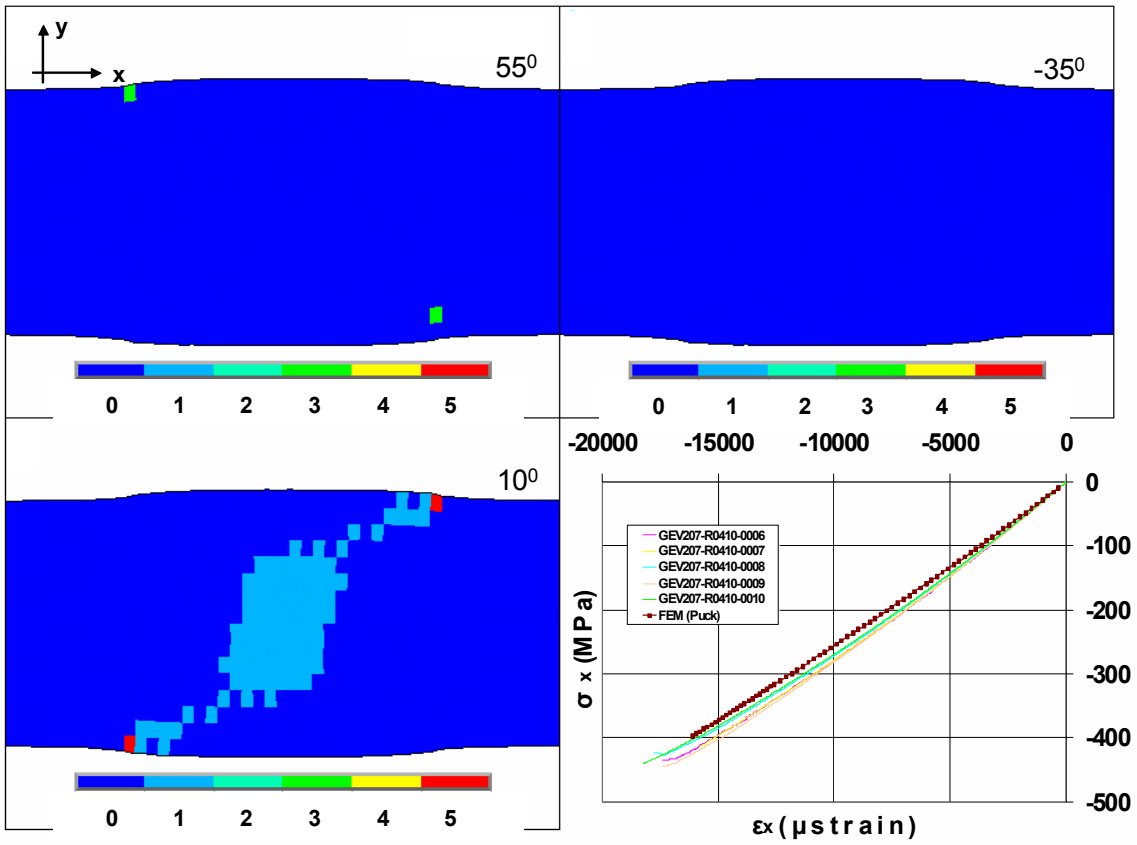
y
x
55⁰
-35⁰
0 1 2 3 4 5
0 1 2 3 4 5
-20000 -15000 -10000 -5000 0
10⁰
0 1 2 3 4 5
GEV207-R0410-0006
GEV207-R0410-0007
GEV207-R0410-0008
GEV207-R0410-0009
GEV207-R0410-0010
FEM (Puck)
σ x (MPa)
0 -100 -200 -300 -400 -500
εx (μstrain)

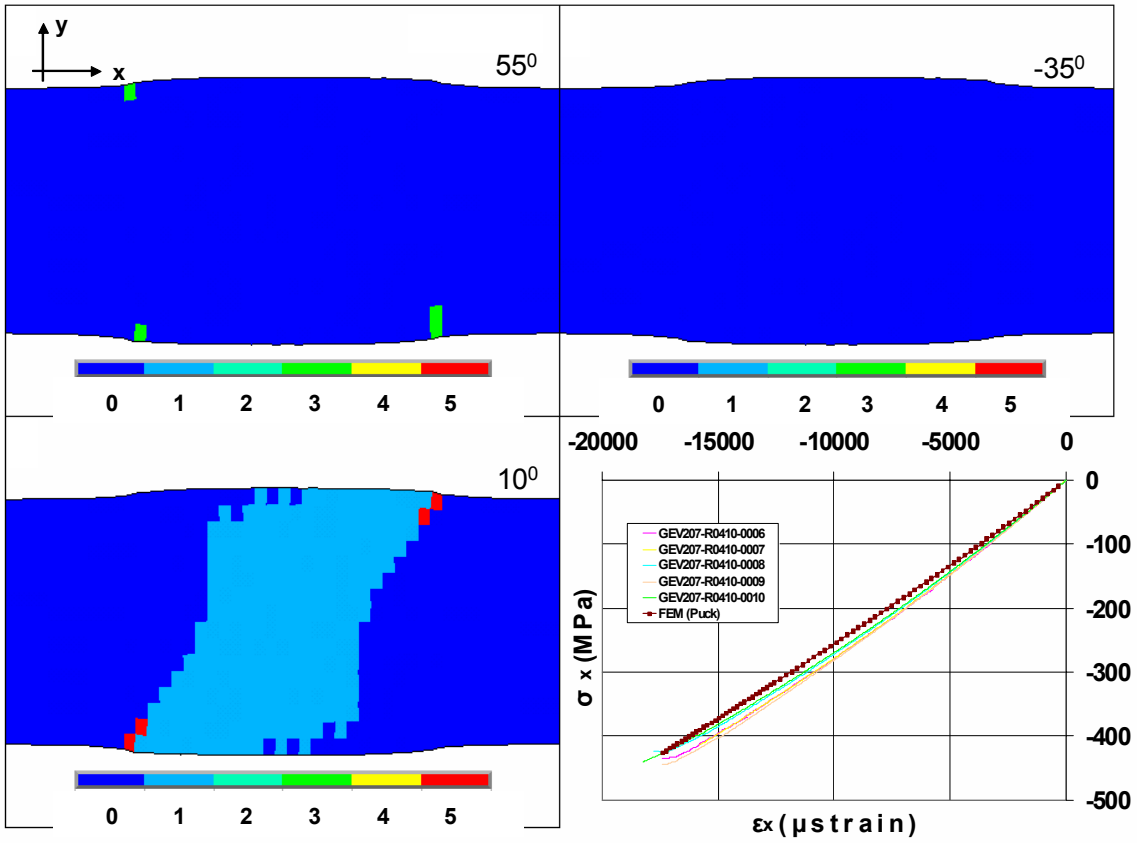
y
x
55⁰
-35⁰
0 1 2 3 4 5
0 1 2 3 4 5
-20000 -15000 -10000 -5000 0
10⁰
0 1 2 3 4 5
GEV207-R0410-0006
GEV207-R0410-0007
GEV207-R0410-0008
GEV207-R0410-0009
GEV207-R0410-0010
FEM (Puck)
σ x (MPa)
0 -100 -200 -300 -400 -500
εx (μstrain)

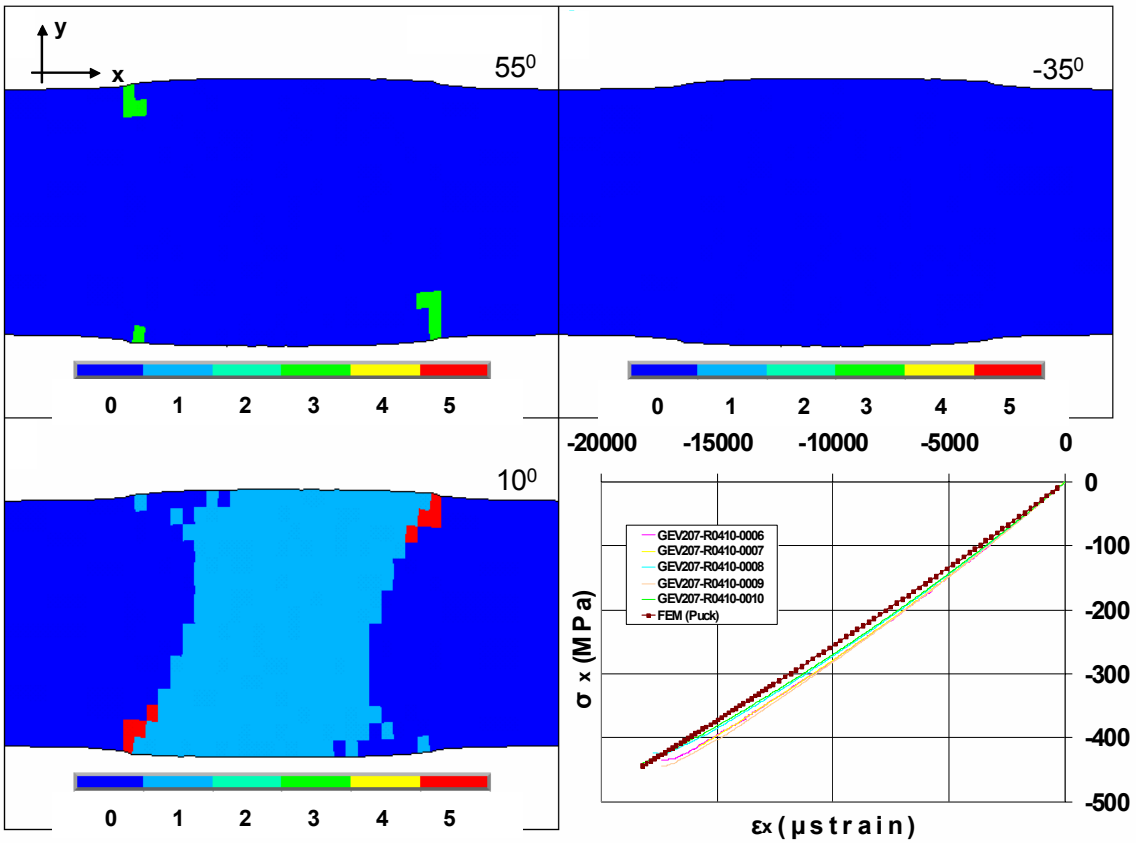
y
x
55⁰
-35⁰
0 1 2 3 4 5
0 1 2 3 4 5
-20000 -15000 -10000 -5000 0
10⁰
0 1 2 3 4 5
GEV207-R0410-0006
GEV207-R0410-0007
GEV207-R0410-0008
GEV207-R0410-0009
GEV207-R0410-0010
FEM (Puck)
σ x (MPa)
0 -100 -200 -300 -400 -500
εx (μstrain)

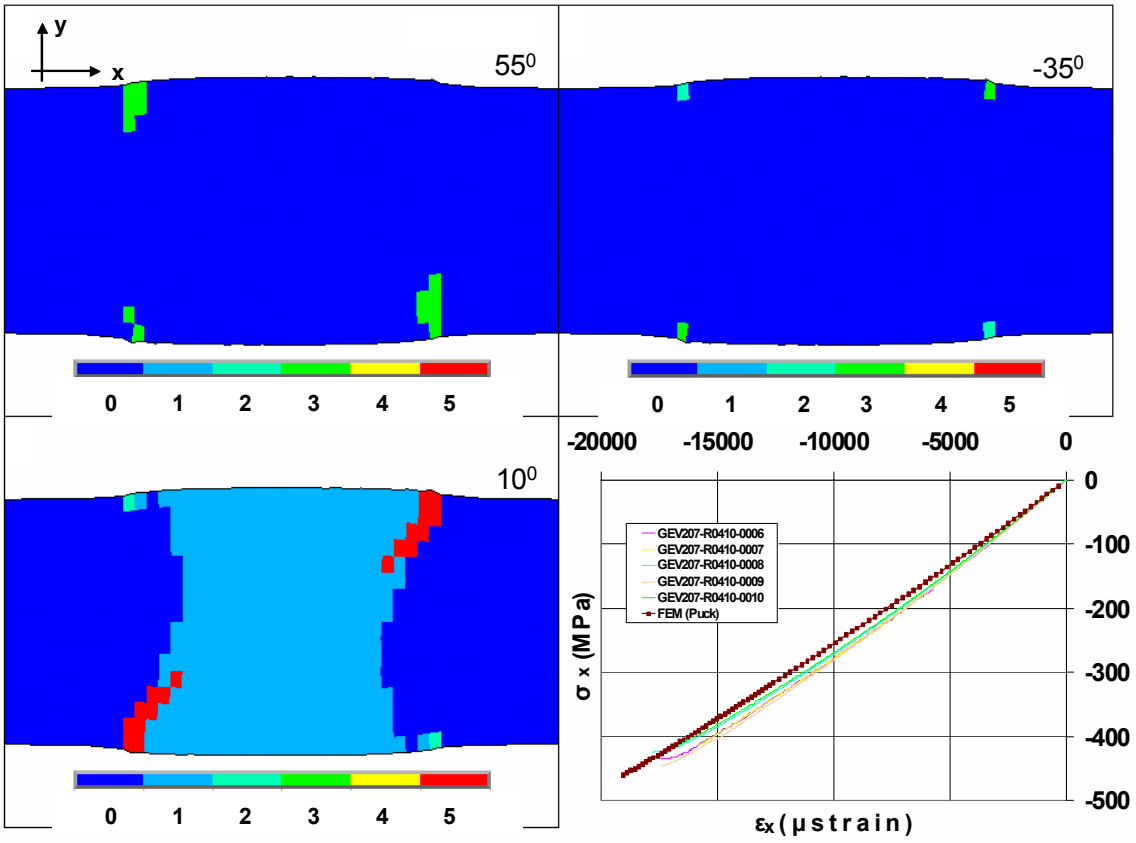
y
x
55⁰
-35⁰
0 1 2 3 4 5
0 1 2 3 4 5
-20000 -15000 -10000 -5000 0
10⁰
0 1 2 3 4 5
GEV207-R0410-0006
GEV207-R0410-0007
GEV207-R0410-0008
GEV207-R0410-0009
GEV207-R0410-0010
FEM (Puck)
σ x (MPa)
0 -100 -200 -300 -400 -500
εx (μstrain)

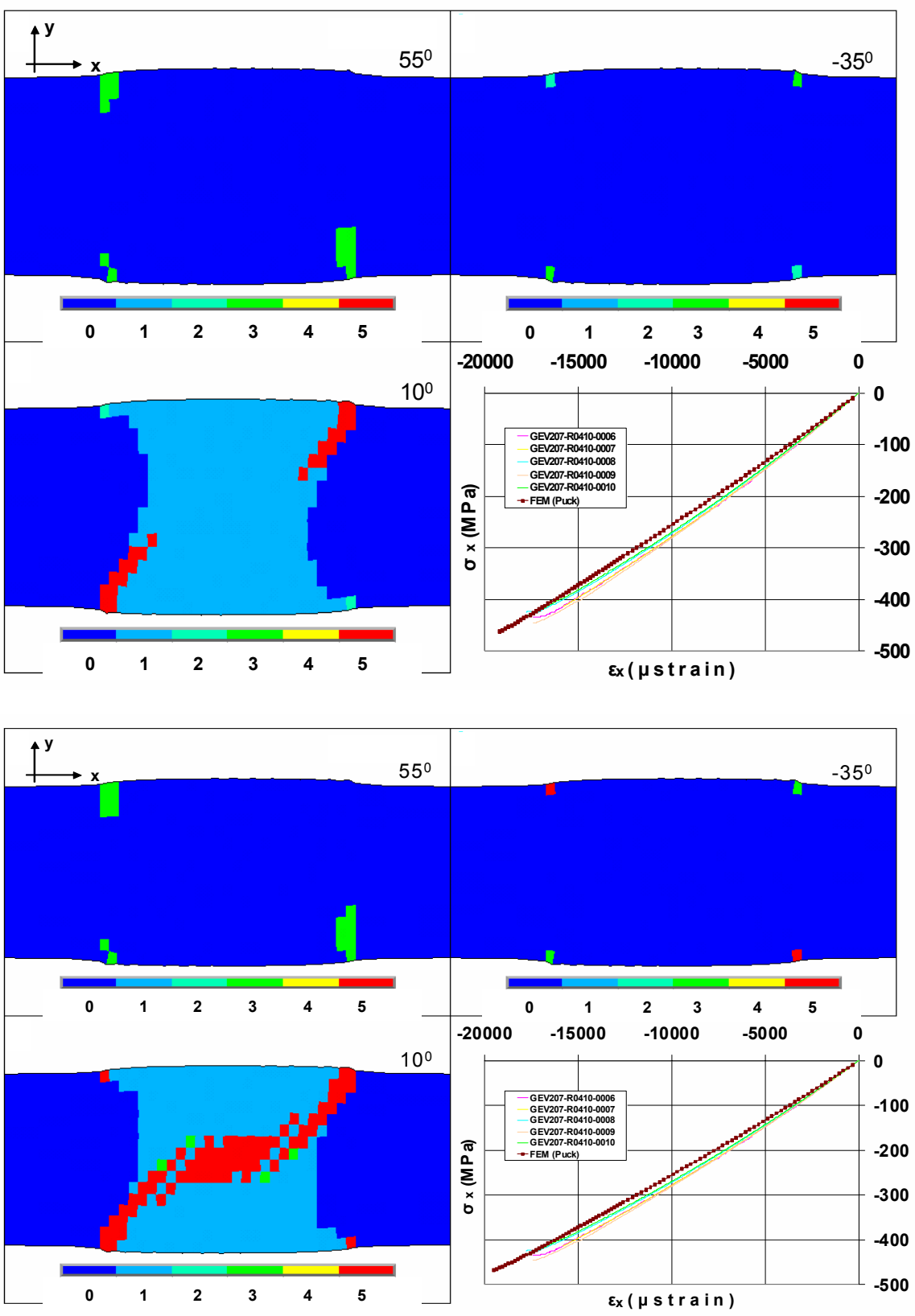

Fig. 55: Stress-Strain behaviour of an MD [10] coupon in compression.

Table 13: Experimental and numerical strength values for MD coupon @ 10 degrees under compression

	Exp.	**FEM**	**%**
MPa	-432.76	-478.15	-10.49

Damage initiates at 80% of the ultimate compressive strength and accumulates in the [10] plies as tensile matrix cracks of type A, indicated with number 1, enhancing fibre kinking. After fibre compressive failure emanates from the tabs area, indicated with number 5, final rupture occurs in an almost abrupt way, Fig. 55. Except the extended damage near the tabs, caused from fibre kinking in the UD [10] layer, a direct comparison cannot be done between the simulated and the experimental failure mode, Fig. 56, but ultrasonic C-scan tests could enhance further assessment.

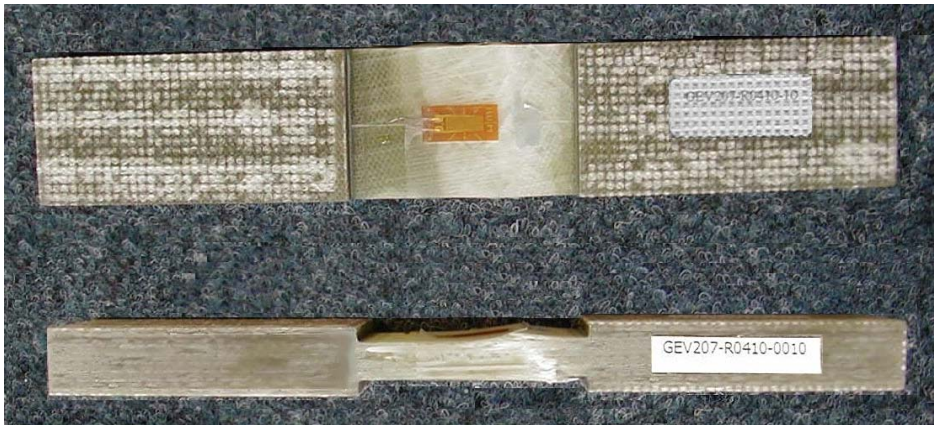

Fig. 56: Failed MD coupon loaded off-axis in compression at 10^{o}

6.1.12 Tension of MD coupon off-axis loaded at 60^{o}

The MD 60 coupon is cut at 60 degrees with respect to the [0] ply and it is composed of [-75], [15] and [60] plies. In these tests matrix non-linear performance dominates the coupon stress-strain behaviour. The numerical simulation predicts satisfactorily material performance up to failure, Fig.57, estimating very well the specimen strength, see Table 14.

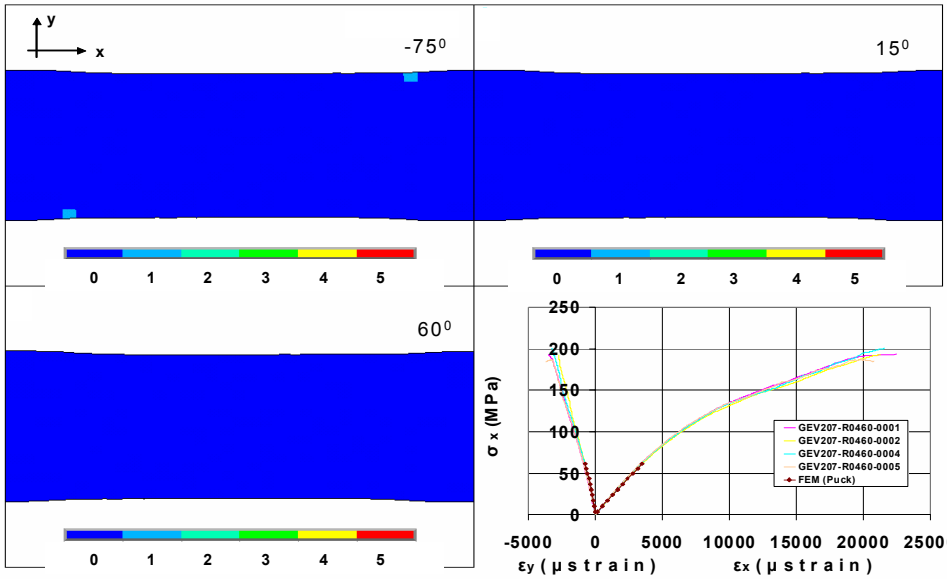
y
x
-75⁰
15⁰
60⁰
0 1 2 3 4 5
σ x (MPa)
250
200
150
100
50
0
-5000 0 5000 10000 15000 20000 25000
εy (μstrain)
εx (μstrain)
GEV207-R0460-0001
GEV207-R0460-0002
GEV207-R0460-0004
GEV207-R0460-0005
FEM (Puck)

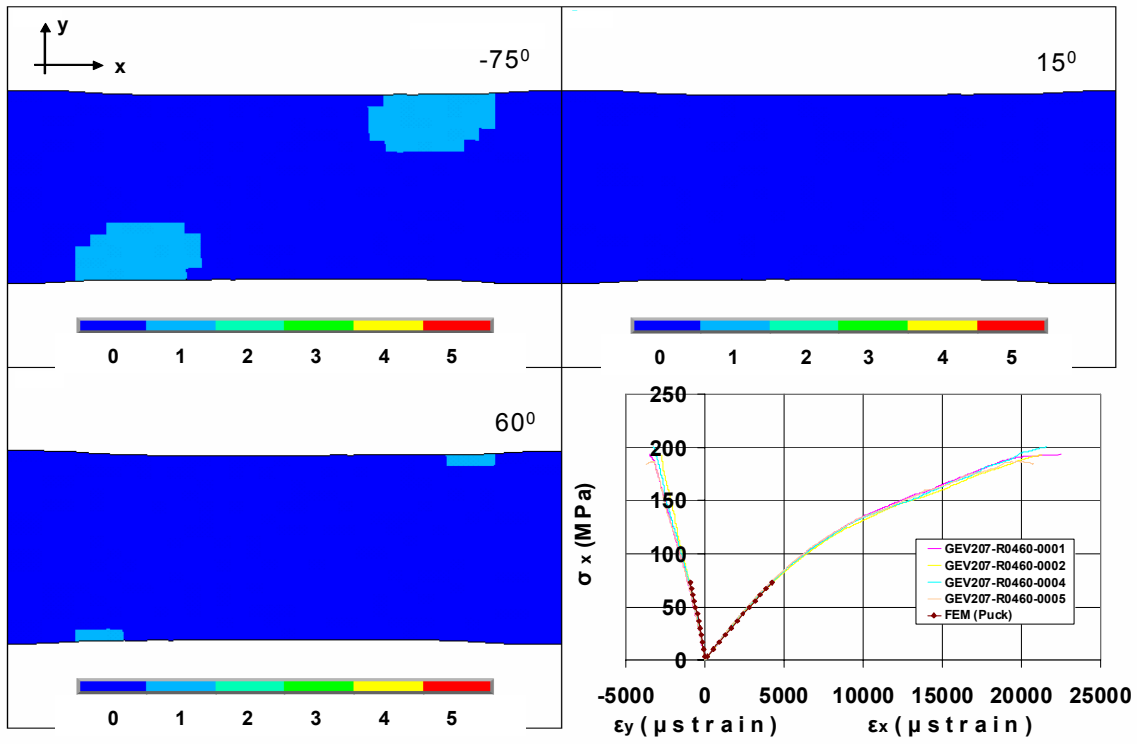
y
x
-75⁰
15⁰
60⁰
0 1 2 3 4 5
σ x (MPa)
250
200
150
100
50
0
-5000 0 5000 10000 15000 20000 25000
εy (μstrain)
εx (μstrain)
GEV207-R0460-0001
GEV207-R0460-0002
GEV207-R0460-0004
GEV207-R0460-0005
FEM (Puck)

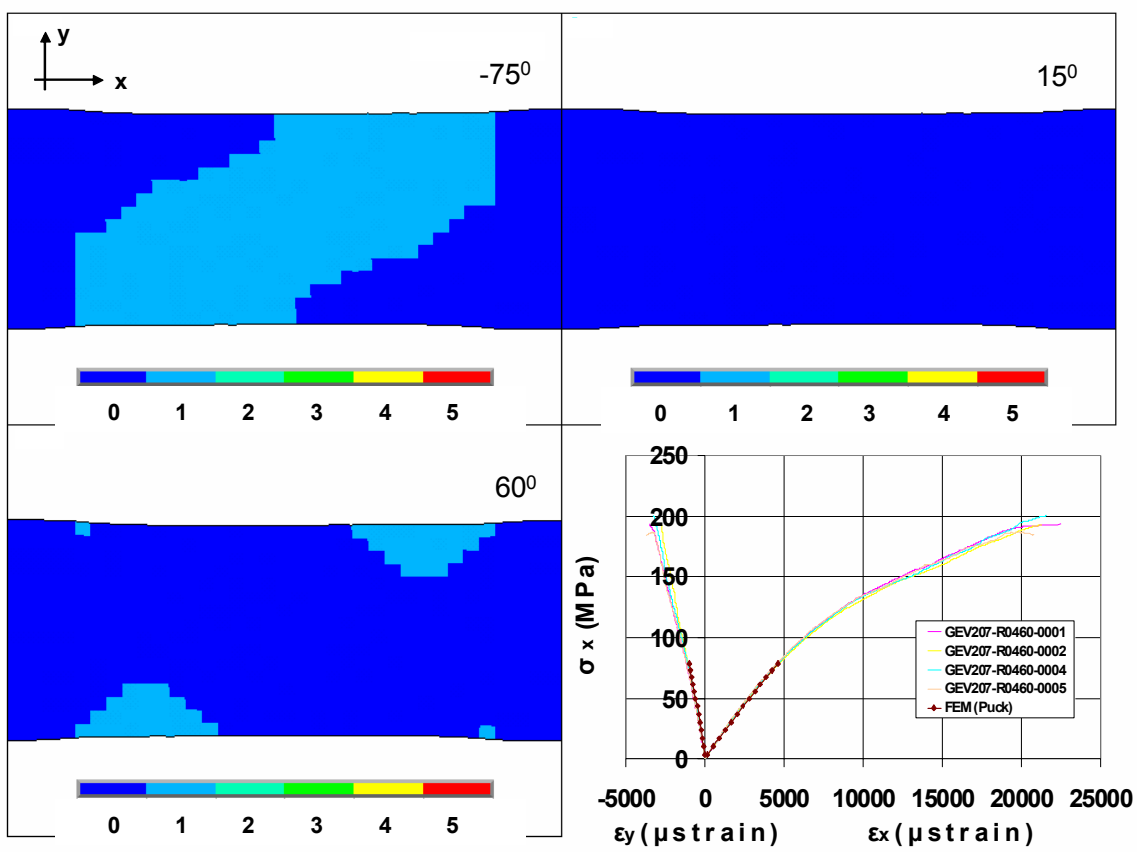
y
x
-75⁰
15⁰
60⁰
0 1 2 3 4 5
σ x (MPa)
250
200
150
100
50
0
-5000 0 5000 10000 15000 20000 25000
εy (μstrain)
εx (μstrain)
GEV207-R0460-0001
GEV207-R0460-0002
GEV207-R0460-0004
GEV207-R0460-0005
FEM (Puck)

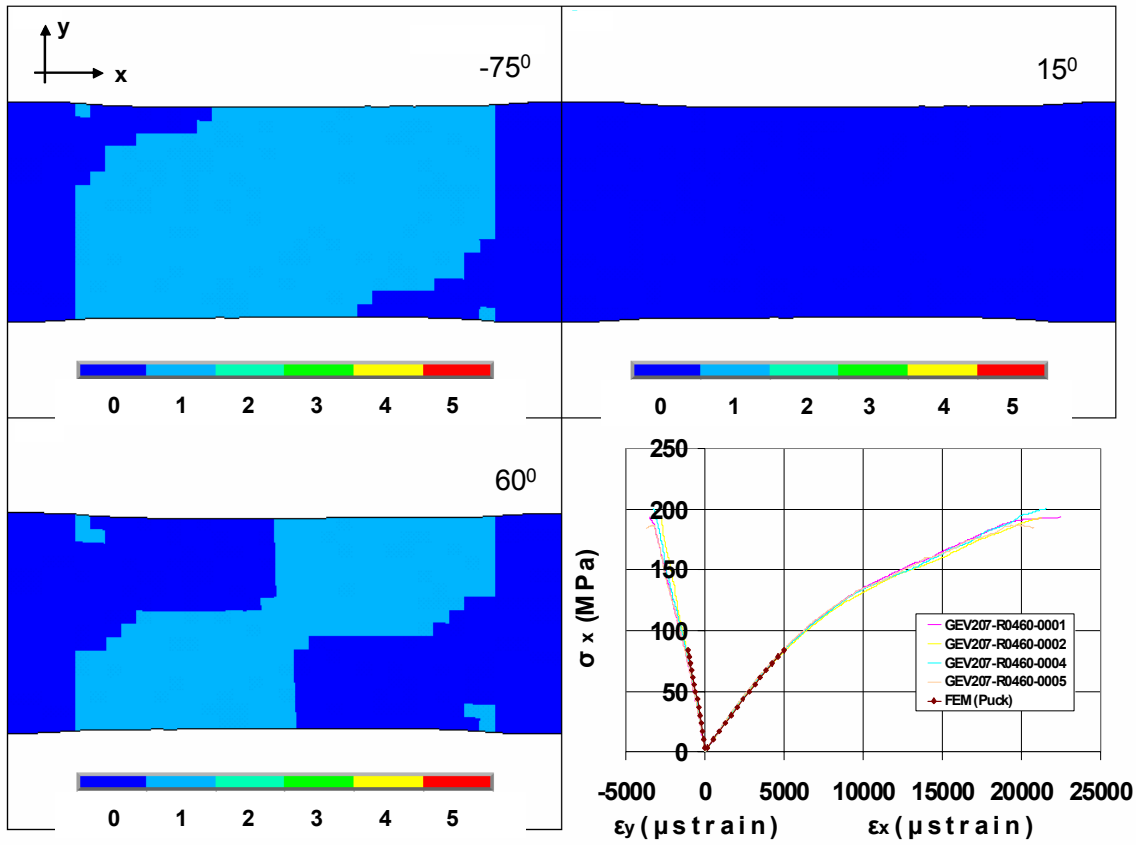
y
x
-75⁰
15⁰
60⁰
0 1 2 3 4 5
σ x (MPa)
250
200
150
100
50
0
-5000 0 5000 10000 15000 20000 25000
εy (μstrain)
εx (μstrain)
GEV207-R0460-0001
GEV207-R0460-0002
GEV207-R0460-0004
GEV207-R0460-0005
FEM (Puck)

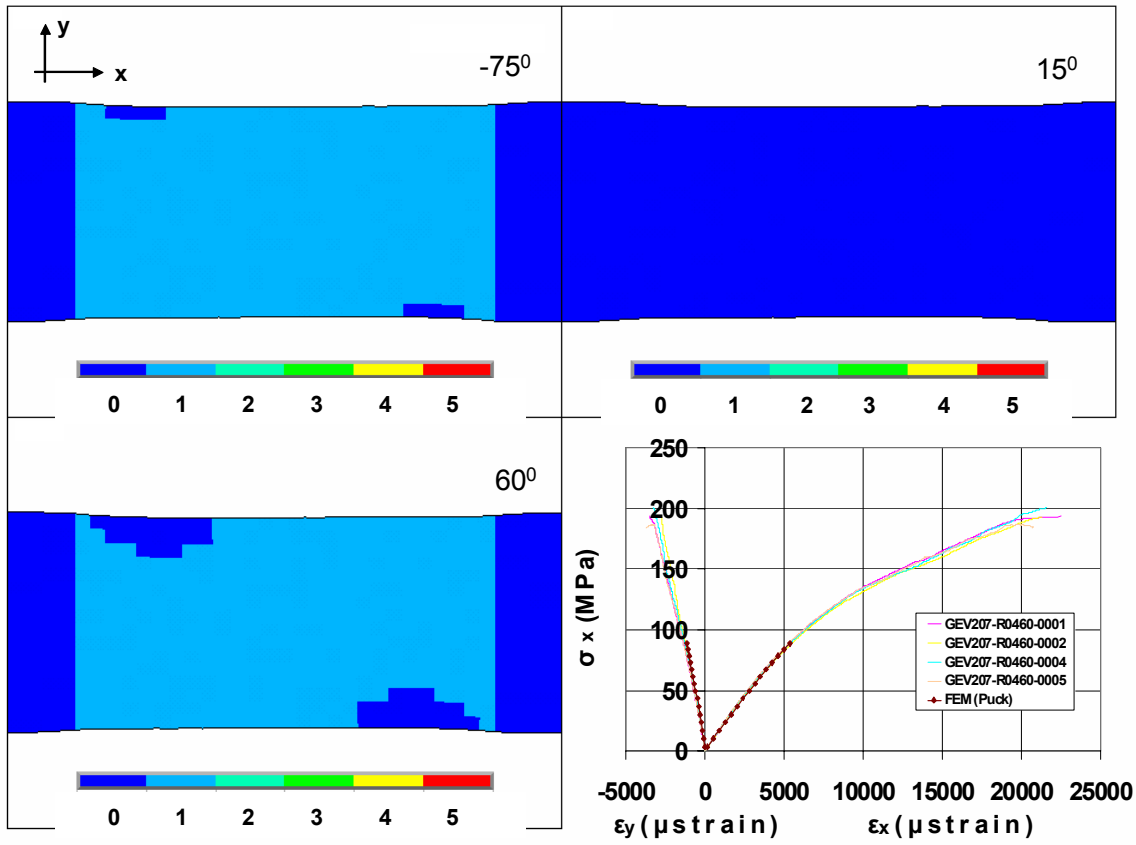
y
x
-75⁰
15⁰
60⁰
0 1 2 3 4 5
σ x (MPa)
250
200
150
100
50
0
-5000 0 5000 10000 15000 20000 25000
εy (μstrain)
εx (μstrain)
GEV207-R0460-0001
GEV207-R0460-0002
GEV207-R0460-0004
GEV207-R0460-0005
FEM (Puck)

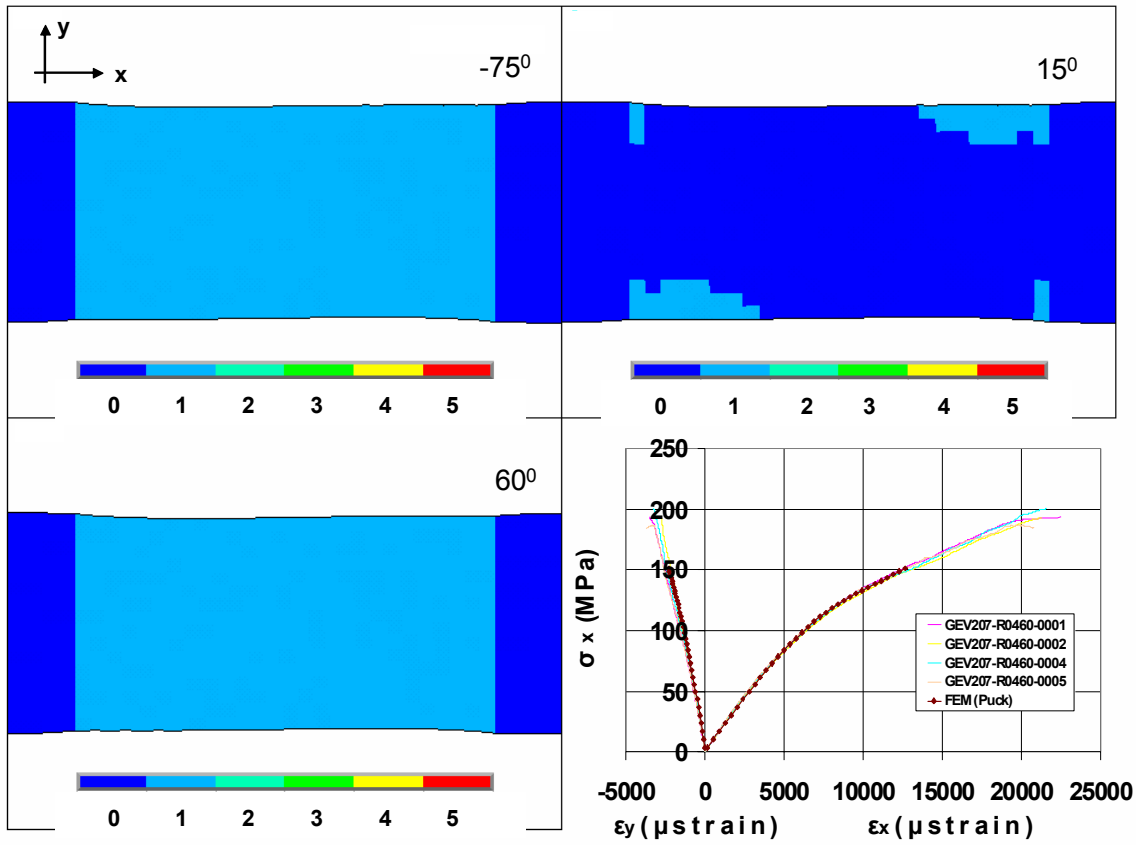
y
x
-75⁰
15⁰
60⁰
0 1 2 3 4 5
σ x (MPa)
250
200
150
100
50
0
-5000 0 5000 10000 15000 20000 25000
εy (μstrain)
εx (μstrain)
GEV207-R0460-0001
GEV207-R0460-0002
GEV207-R0460-0004
GEV207-R0460-0005
FEM (Puck)

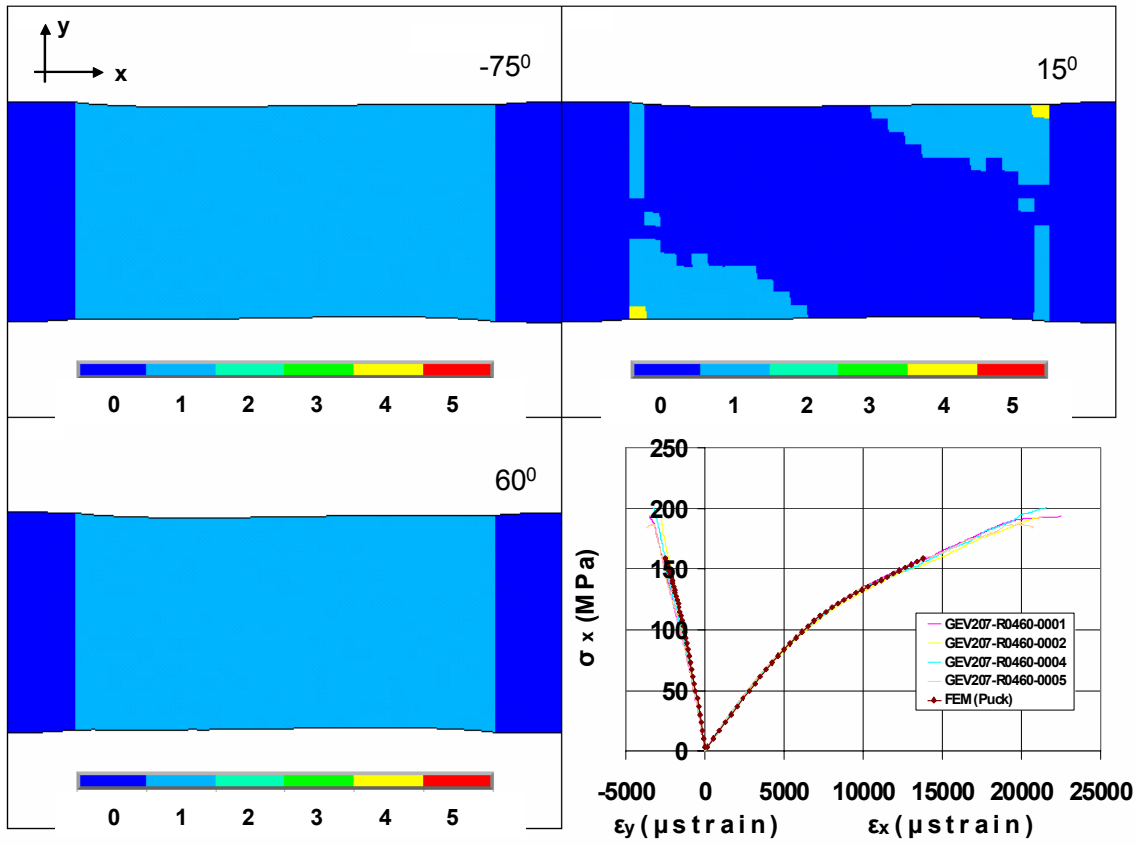
y
x
-75⁰
15⁰
60⁰
0 1 2 3 4 5
σ x (MPa)
250
200
150
100
50
0
-5000 0 5000 10000 15000 20000 25000
εy (μstrain)
εx (μstrain)
GEV207-R0460-0001
GEV207-R0460-0002
GEV207-R0460-0004
GEV207-R0460-0005
FEM (Puck)

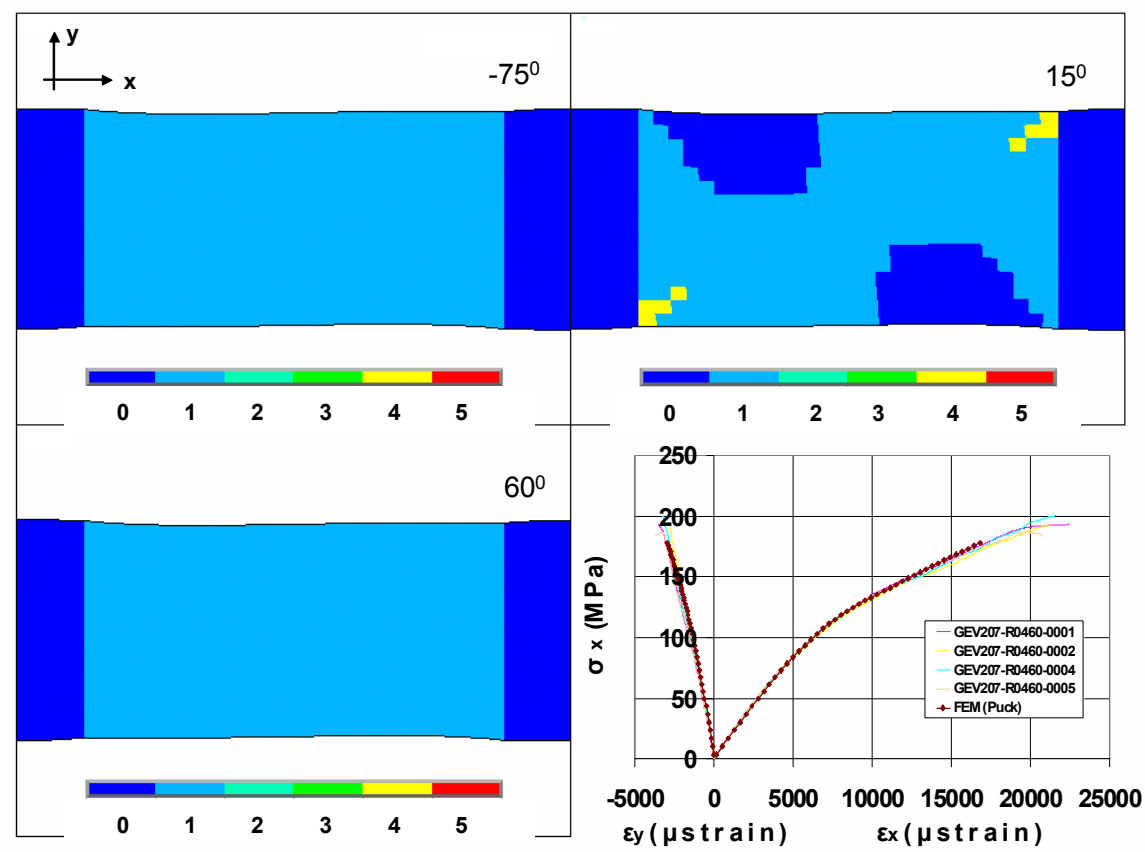
y
x
-75⁰
15⁰
0 1 2 3 4 5
60⁰
σ x (MPa)
250
200
150
100
50
0
-5000 0 5000 10000 15000 20000 25000
εy (μstrain)
εx (μstrain)
GEV207-R0460-0001
GEV207-R0460-0002
GEV207-R0460-0004
GEV207-R0460-0005
FEM (Puck)

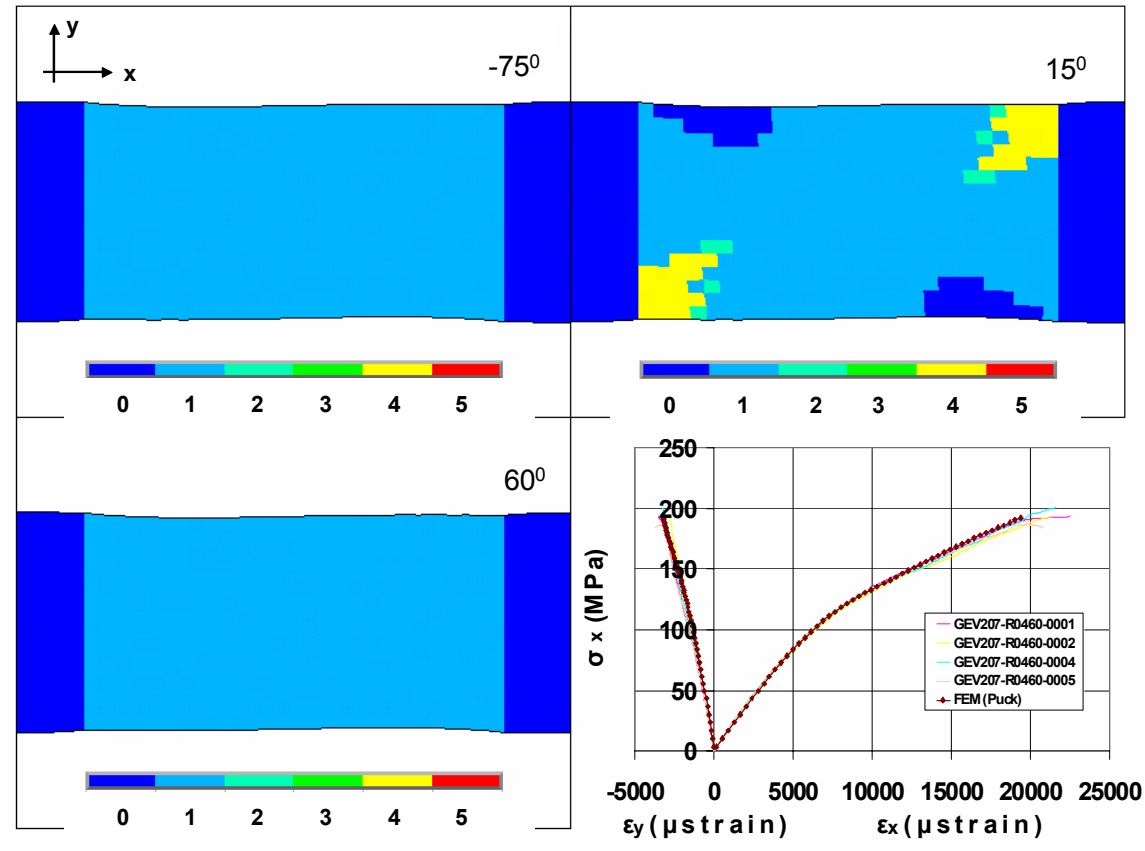
y
x
-75⁰
15⁰
0 1 2 3 4 5
60⁰
σ x (MPa)
250
200
150
100
50
0
-5000 0 5000 10000 15000 20000 25000
εy (μstrain)
εx (μstrain)
GEV207-R0460-0001
GEV207-R0460-0002
GEV207-R0460-0004
GEV207-R0460-0005
FEM (Puck)

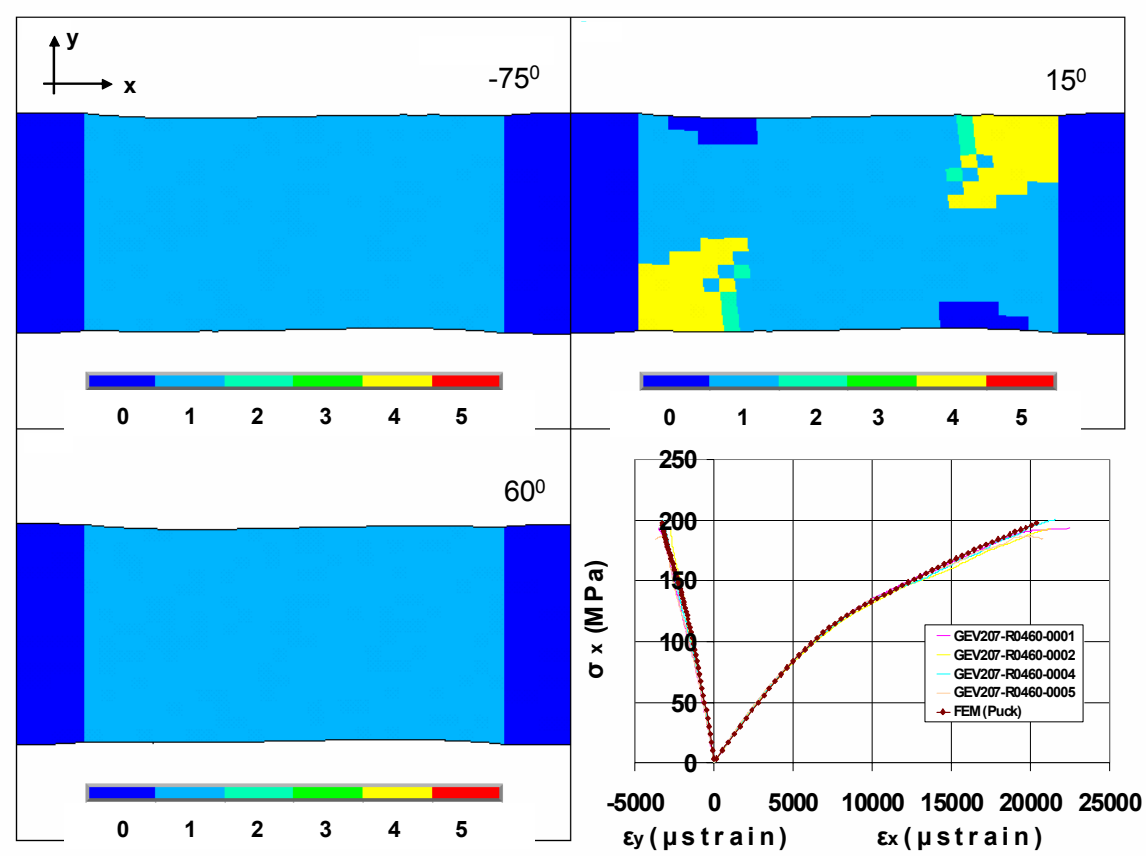
y
x
-75⁰
15⁰
0 1 2 3 4 5
60⁰
σ x (MPa)
250
200
150
100
50
0
-5000 0 5000 10000 15000 20000 25000
εy (μstrain)
εx (μstrain)
GEV207-R0460-0001
GEV207-R0460-0002
GEV207-R0460-0004
GEV207-R0460-0005
FEM (Puck)

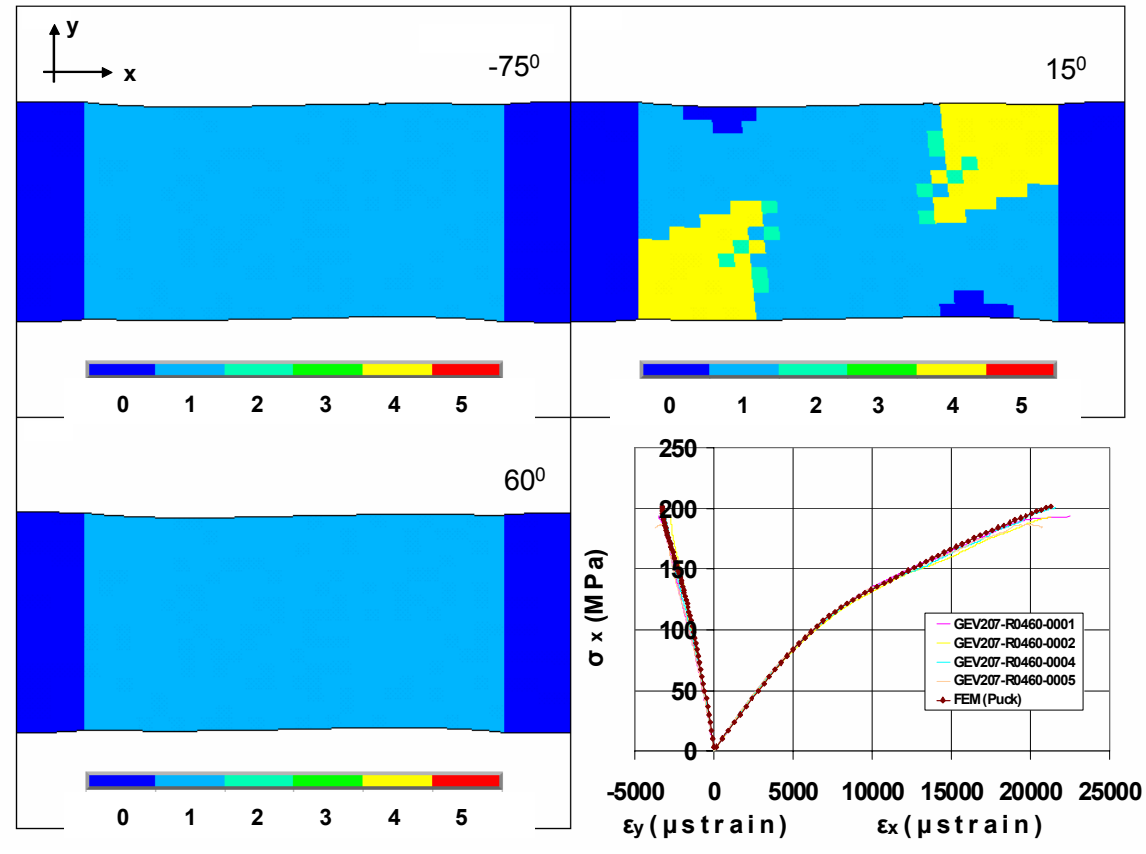
y
x
-75⁰
15⁰
0 1 2 3 4 5
60⁰
σ x (MPa)
250
200
150
100
50
0
-5000 0 5000 10000 15000 20000 25000
εy (μstrain)
εx (μstrain)
GEV207-R0460-0001
GEV207-R0460-0002
GEV207-R0460-0004
GEV207-R0460-0005
FEM (Puck)

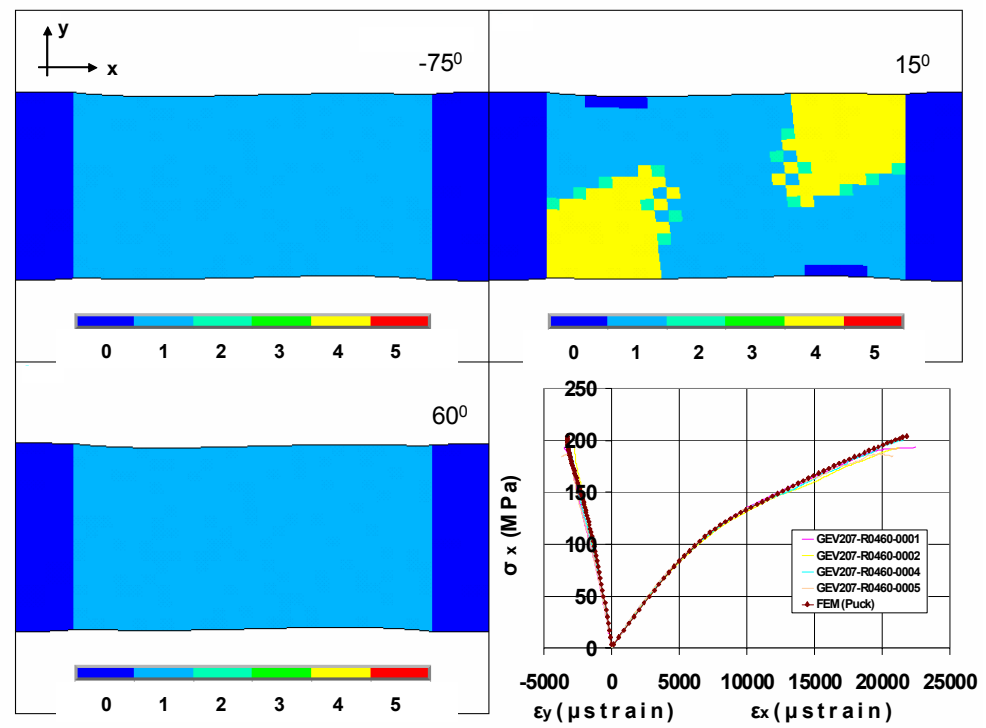

Fig. 57: Stress-Strain behaviour of an MD 60 coupon in tension

Table 14: Experimental and numerical strength values for MD coupon @ 60 degrees under tension

	Exp.	**FEM**	**%**
MPa	196.17	204.08	-4.03

Tensile matrix cracks (mode A), indicated with number 1, are predicted to initiate in the [-75] layers at 30% of the ultimate tensile stress and subsequently in the [60] layers. Well after first ply failure occurs, tensile matrix cracks and fibre breakage arise in the [15] plies. According to the FEM calculations, coupon rupture is caused by fibre failure in the 15° plies. Prediction of damage propagation is presented in Fig. 57. The experimentally observed failure pattern is presented in Fig. 58, and it is not amenable to direct correlation with the numerical model.

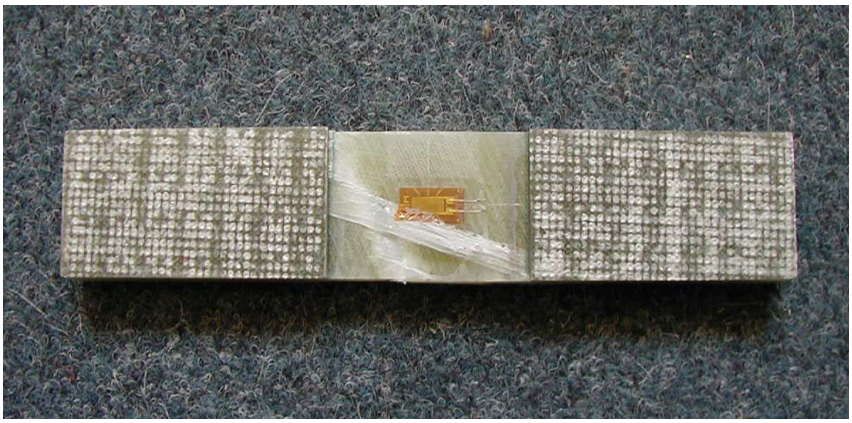

Fig. 58: Failed MD coupon loaded off-axis in tension at 60°.

6.1.13 Compression of MD coupon off-axis loaded at 60°

MD coupon cut @ 60° is simulated under compression. FEM results are in good agreement with the experimental data. Although the numerical model is less stiff than the tested coupons, Fig. 59, it predicts the ultimate compressive stress with fine precision, see Table 15.

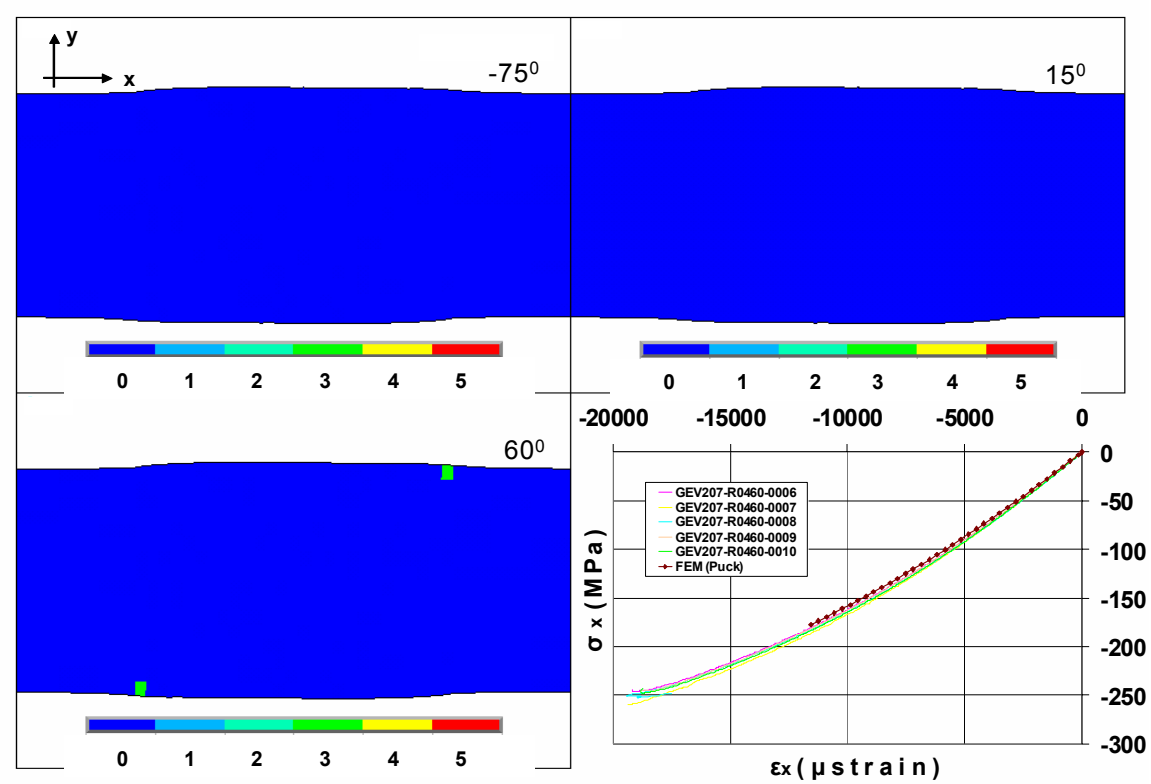

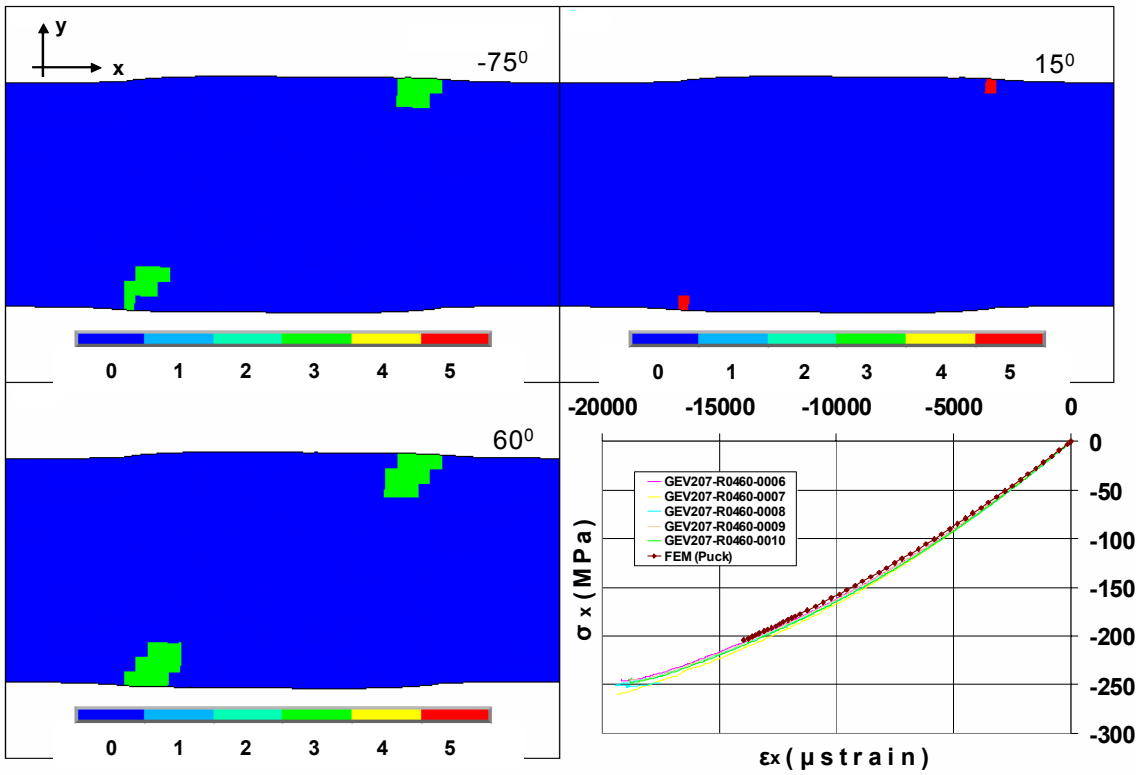
y
x
-75⁰
15⁰
60⁰
0 1 2 3 4 5
-20000 -15000 -10000 -5000 0
0 -50 -100 -150 -200 -250 -300
σx (MPa)
εx (μstrain)
GEV207-R0460-0006
GEV207-R0460-0007
GEV207-R0460-0008
GEV207-R0460-0009
GEV207-R0460-0010
FEM (Puck)

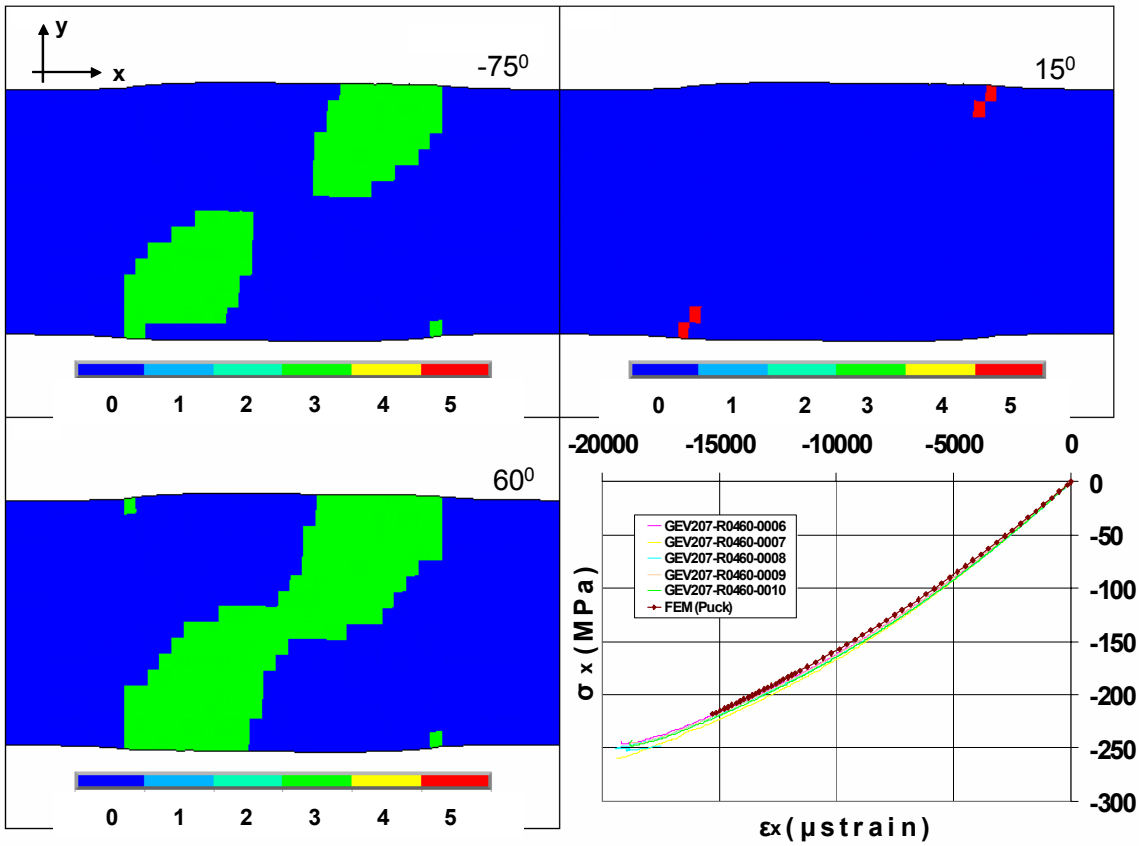
y
x
-75⁰
15⁰
60⁰
0 1 2 3 4 5
-20000 -15000 -10000 -5000 0
0 -50 -100 -150 -200 -250 -300
σx (MPa)
εx (μstrain)
GEV207-R0460-0006
GEV207-R0460-0007
GEV207-R0460-0008
GEV207-R0460-0009
GEV207-R0460-0010
FEM (Puck)

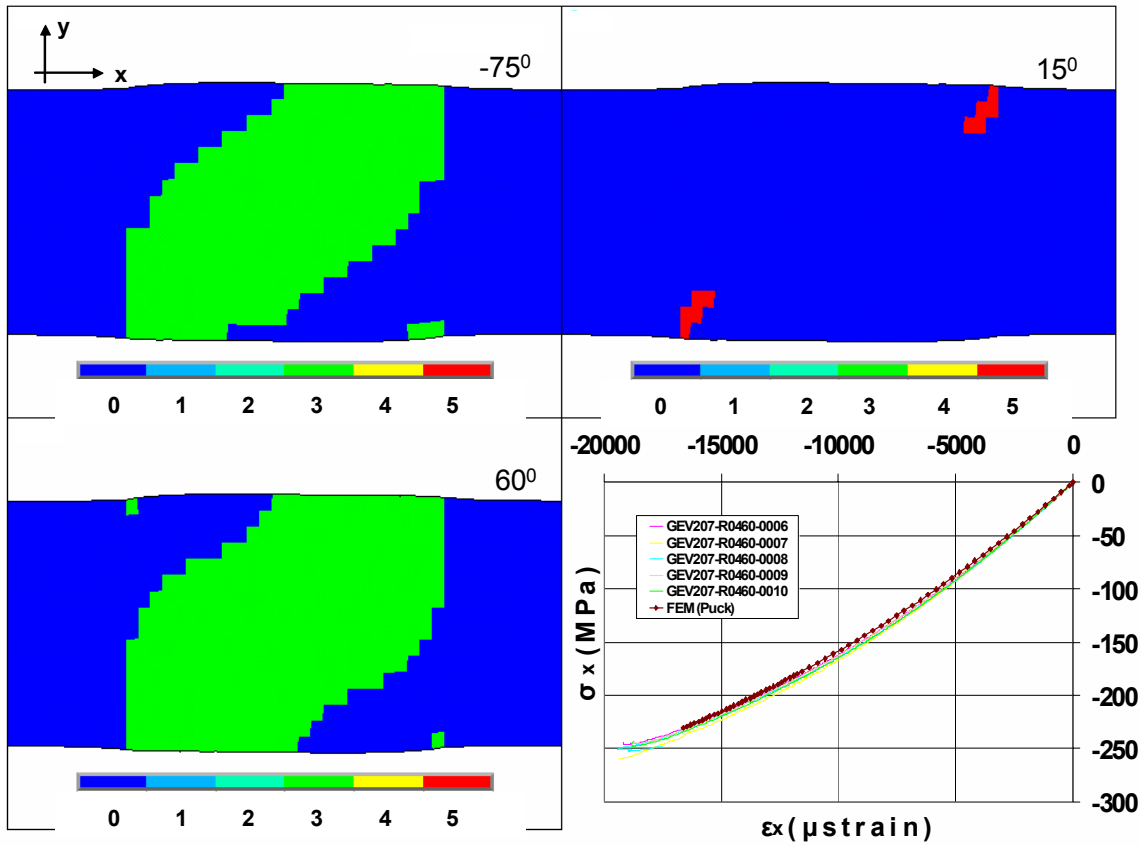
y
x
-75⁰
15⁰
60⁰
0 1 2 3 4 5
-20000 -15000 -10000 -5000 0
0 -50 -100 -150 -200 -250 -300
σx (MPa)
εx (μstrain)
GEV207-R0460-0006
GEV207-R0460-0007
GEV207-R0460-0008
GEV207-R0460-0009
GEV207-R0460-0010
FEM (Puck)

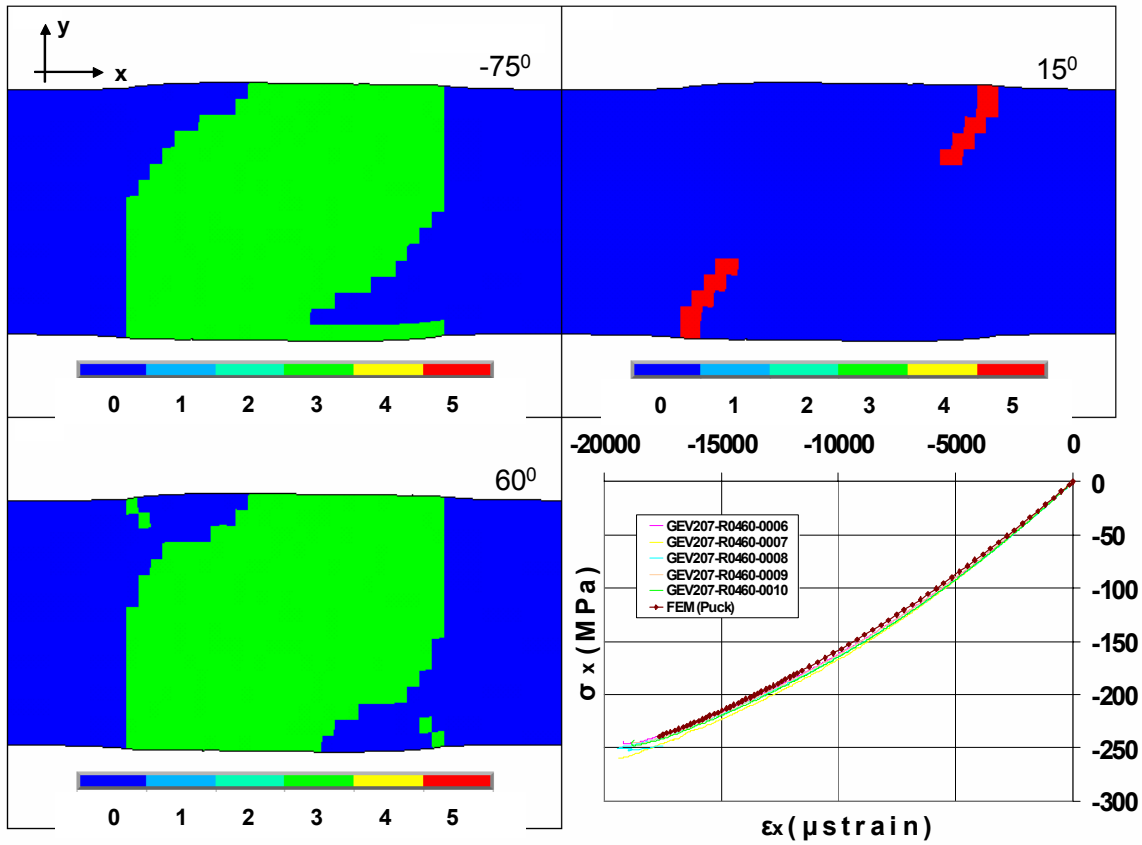
y
x
-75⁰
15⁰
60⁰
0 1 2 3 4 5
-20000 -15000 -10000 -5000 0
0 -50 -100 -150 -200 -250 -300
σx (MPa)
εx (μstrain)
GEV207-R0460-0006
GEV207-R0460-0007
GEV207-R0460-0008
GEV207-R0460-0009
GEV207-R0460-0010
FEM (Puck)

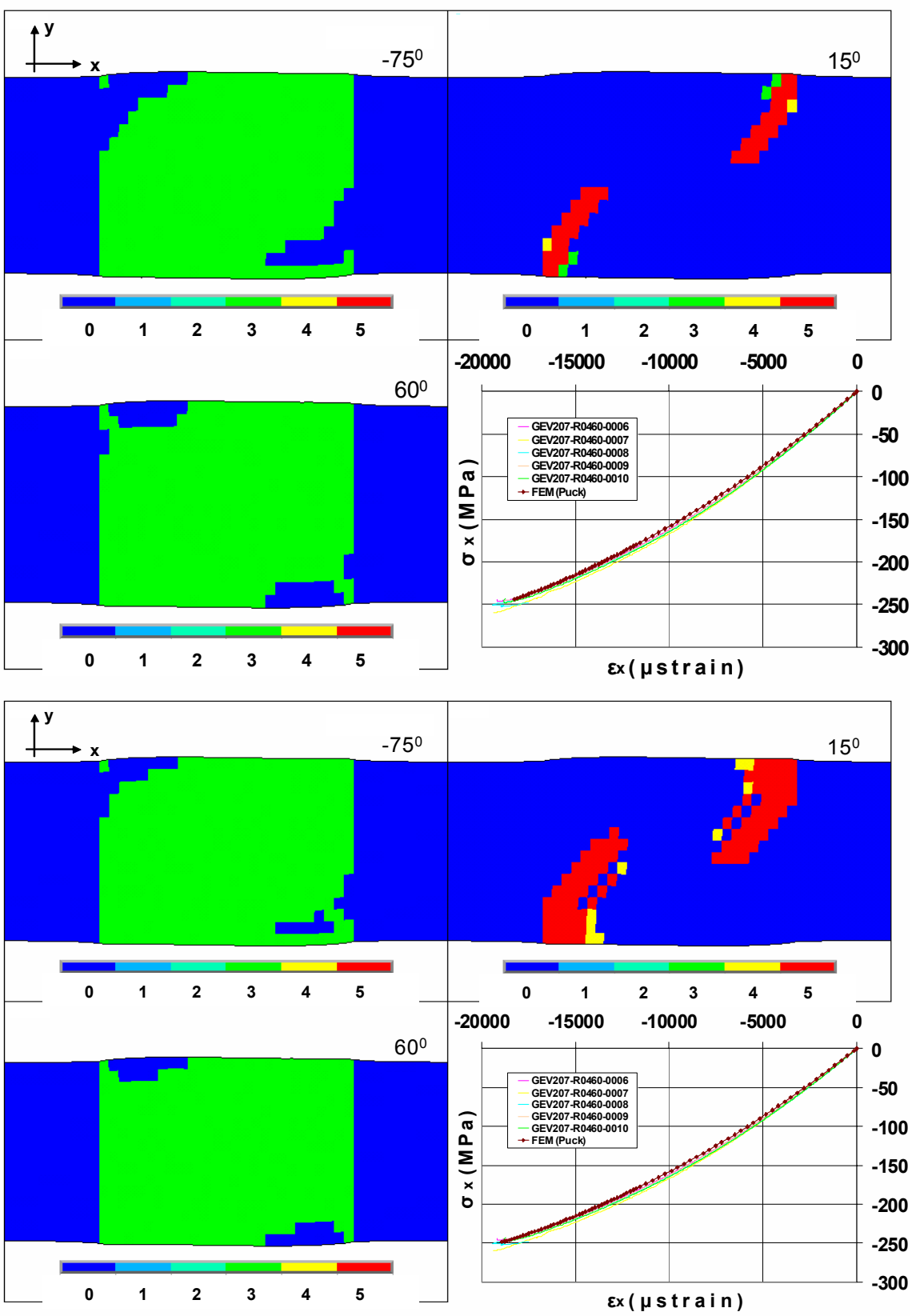

Fig. 59: Stress-Strain behaviour of an MD 60 coupon in tension

Table 15. Experimental and numerical strength values for MD coupon @ 60 degrees under compression

	Exp.	**FEM**	**%**
MPa	-250.77	-249.03	0.69

Matrix cracks of mode C, indicated with number 3 are introduced in [-75] and [60] plies while fibre breakage evolution under compression, pointed out with number 5, takes place in [15] plies. First ply failure occurs at 70% of ultimate compressive stress. The experimental failure pattern presented in Fig. 60 can not be compared with the predicted one since no extensive matrix damage is observed in the coupon faces but a milky zone designating the matrix and the fibre failure.

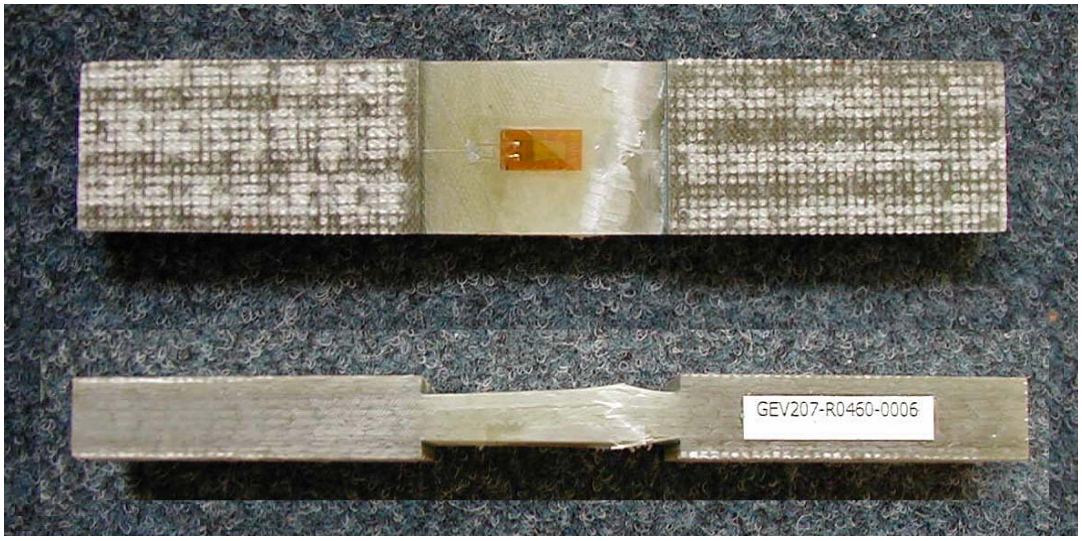

Fig. 60: Failed MD coupon loaded off-axis in compression at 60^{o}

6.1.14 Tension of MD coupon off-axis loaded at 90^{o}

MD coupon cut @ 90^{o} is simulated under tension. The FEM model performs moderately stiffer than the experiment, see Fig. 61, not predicting accurately the experimental stress-strain curve, failing to calculate the coupon ultimate tensile strength, see Table 16.

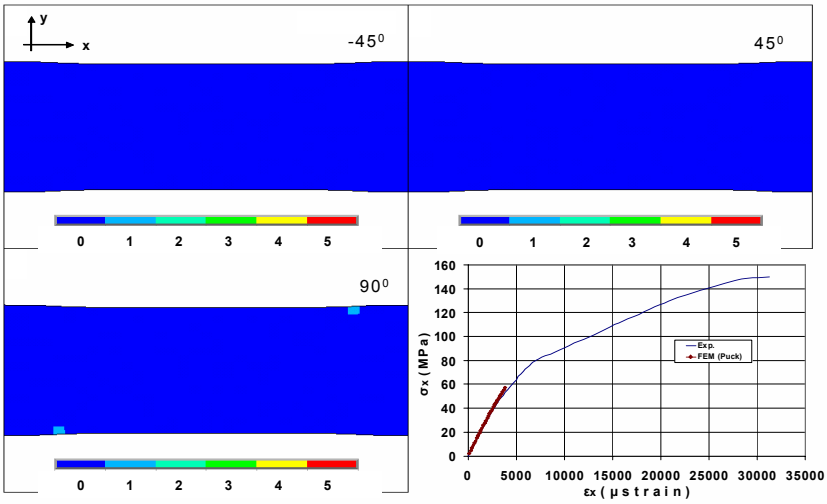
y
x
-45⁰
45⁰
90⁰
0 1 2 3 4 5
σx (MPa)
εx (μstrain)
Exp.
FEM (Puck)

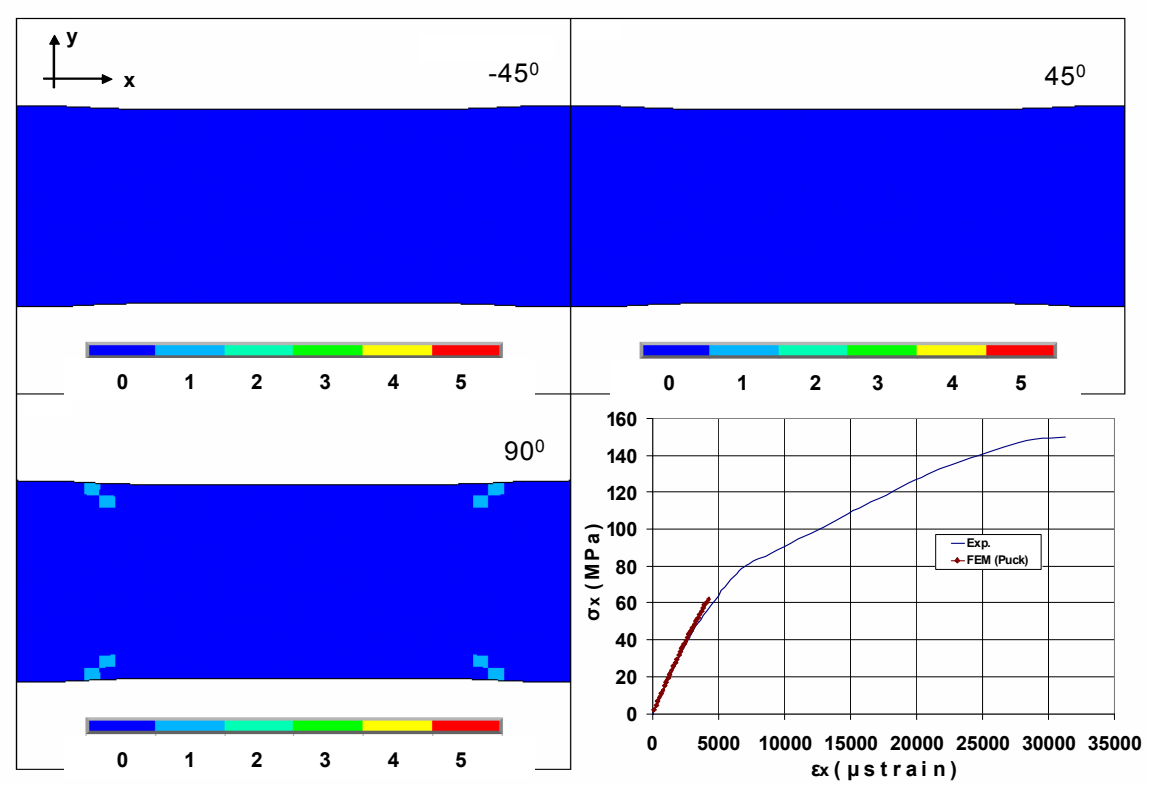
y
x
-45⁰
45⁰
90⁰
0 1 2 3 4 5
σx (MPa)
εx (μstrain)
Exp.
FEM (Puck)

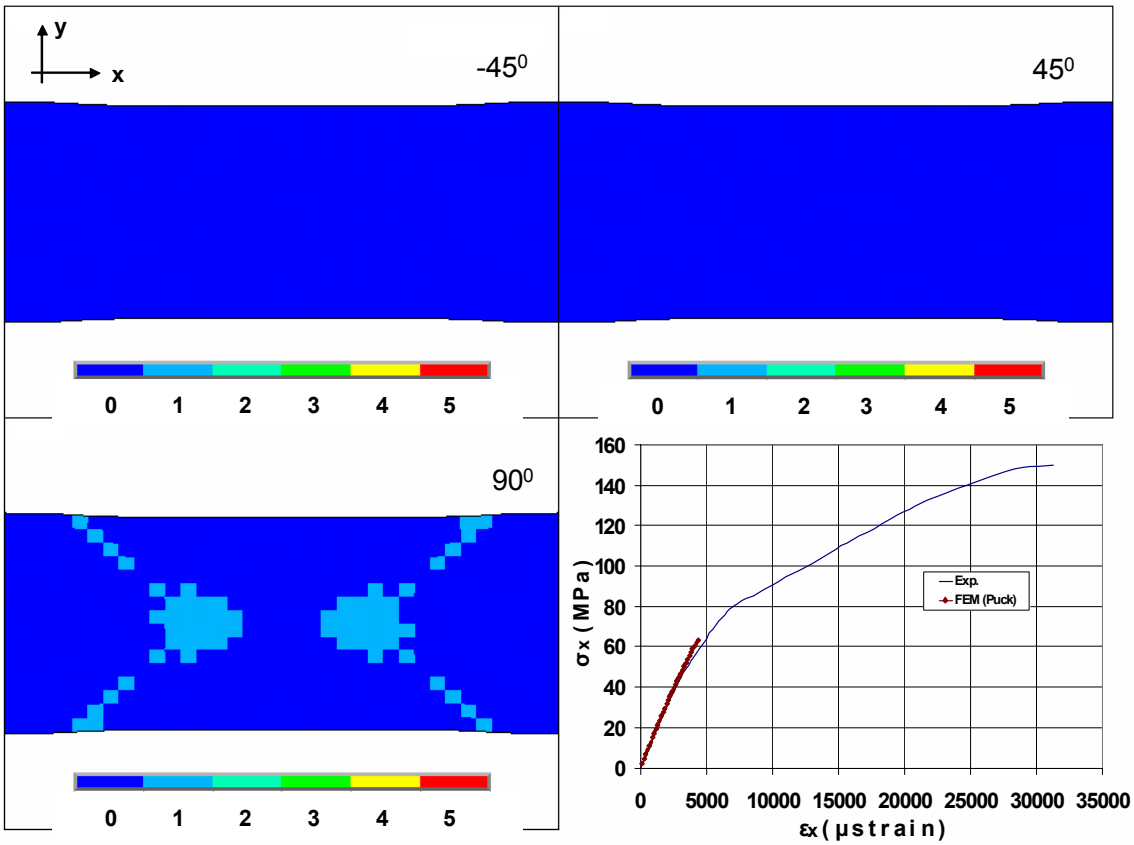
y
x
-45⁰
45⁰
0 1 2 3 4 5
0 1 2 3 4 5
90⁰
0 1 2 3 4 5
160
140
120
100
80
60
40
20
0
σx (MPa)
Exp.
FEM (Puck)
0 5000 10000 15000 20000 25000 30000 35000
εx (μstrain)

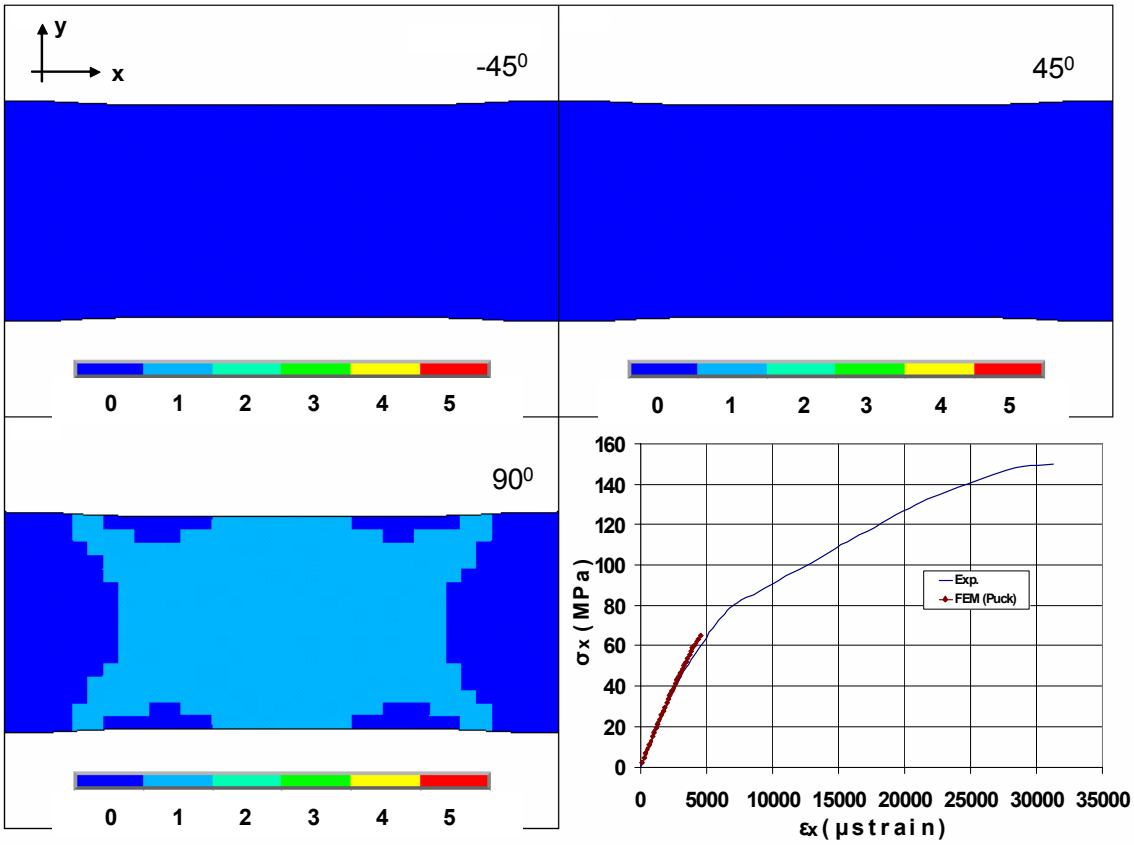
y
x
-45⁰
45⁰
0 1 2 3 4 5
0 1 2 3 4 5
90⁰
0 1 2 3 4 5
160
140
120
100
80
60
40
20
0
σx (MPa)
Exp.
FEM (Puck)
0 5000 10000 15000 20000 25000 30000 35000
εx (μstrain)

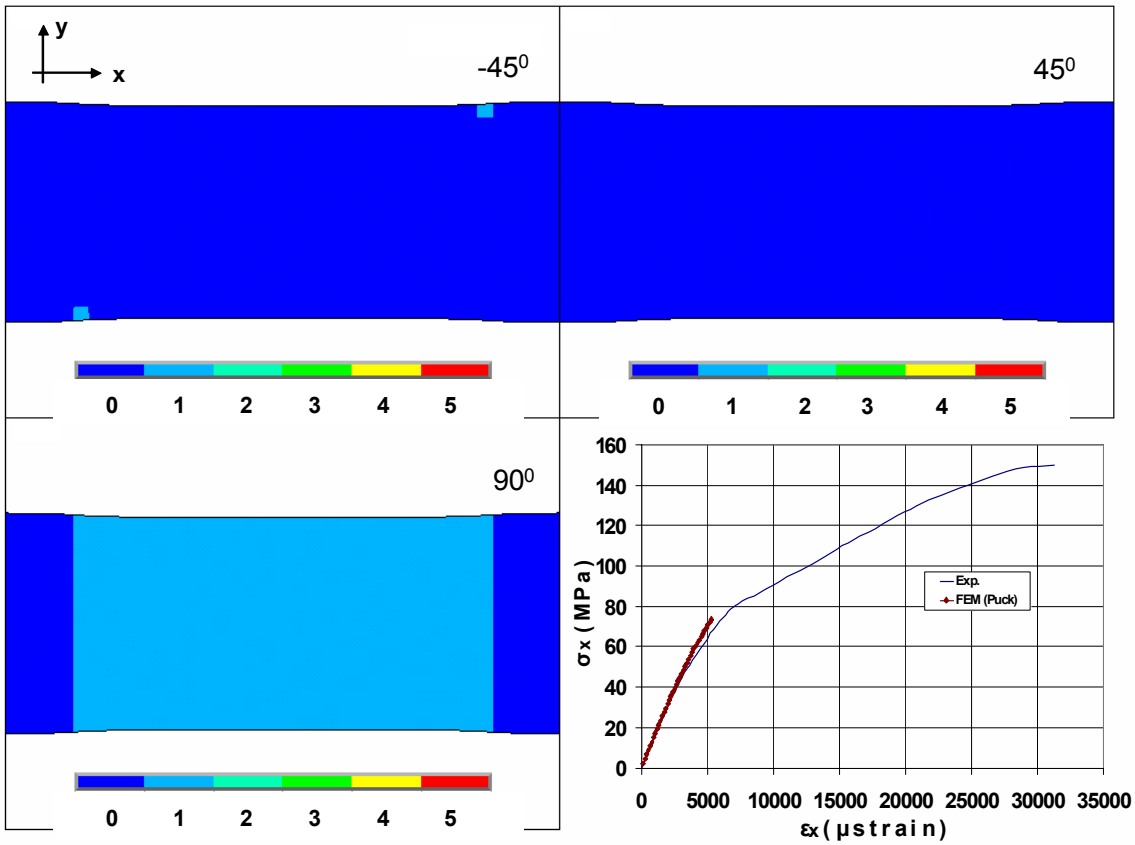
y
x
-45⁰
45⁰
90⁰
0 1 2 3 4 5
σx (MPa)
εx (μstrain)
Exp.
FEM (Puck)

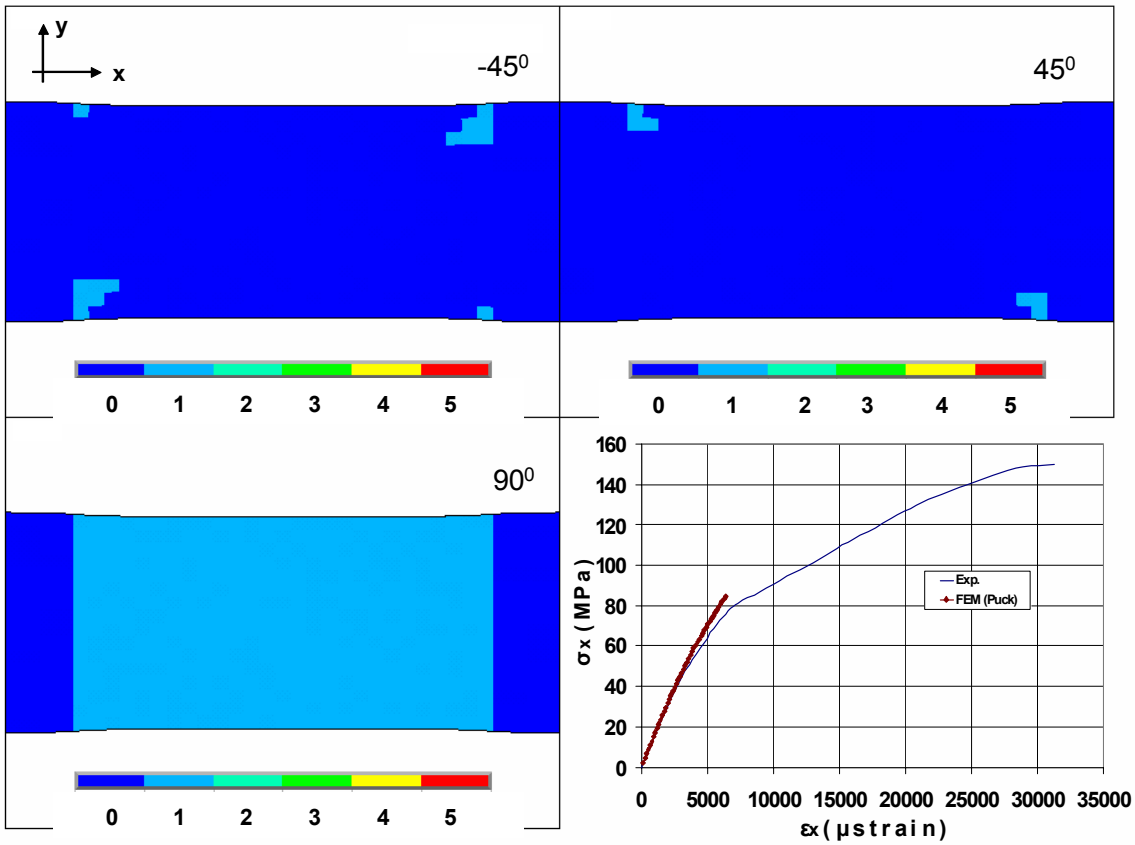
y
x
-45⁰
45⁰
90⁰
0 1 2 3 4 5
σx (MPa)
εx (μstrain)
Exp.
FEM (Puck)

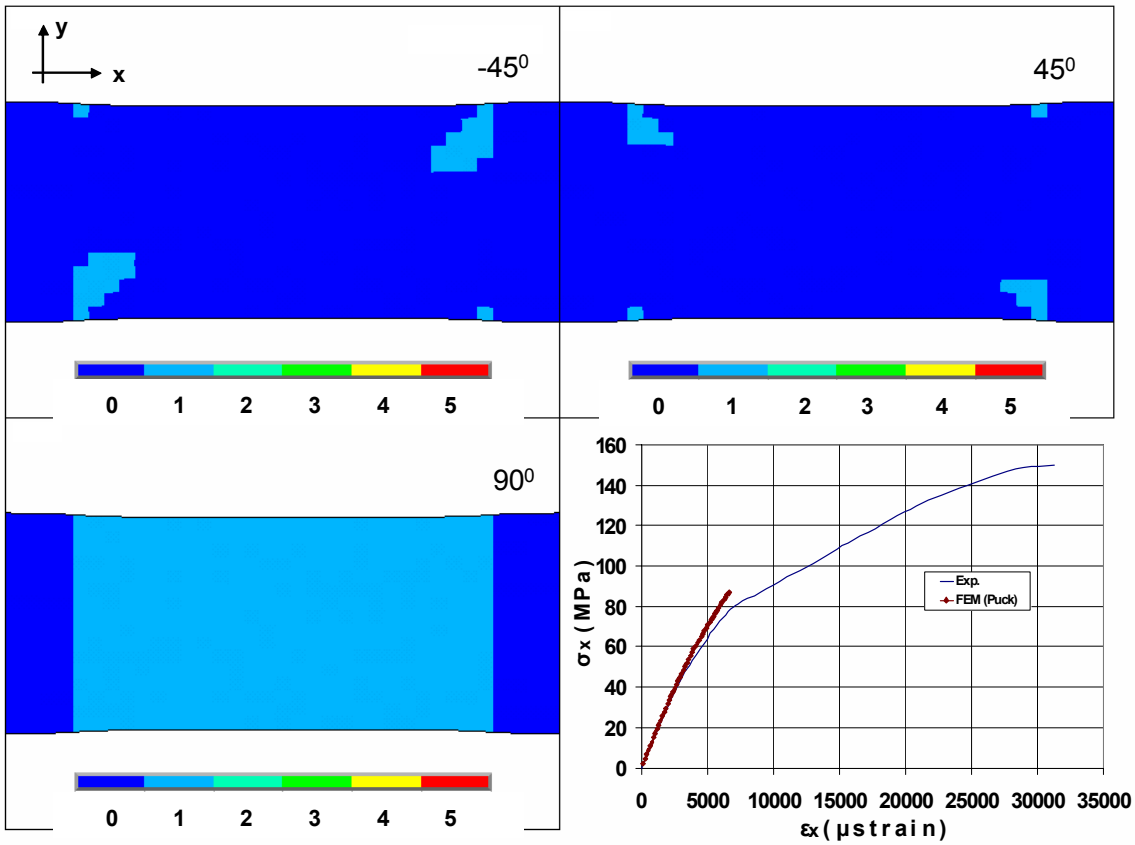
y
x
-45⁰
45⁰
90⁰
0 1 2 3 4 5
σx (MPa)
εx (μstrain)
Exp.
FEM (Puck)

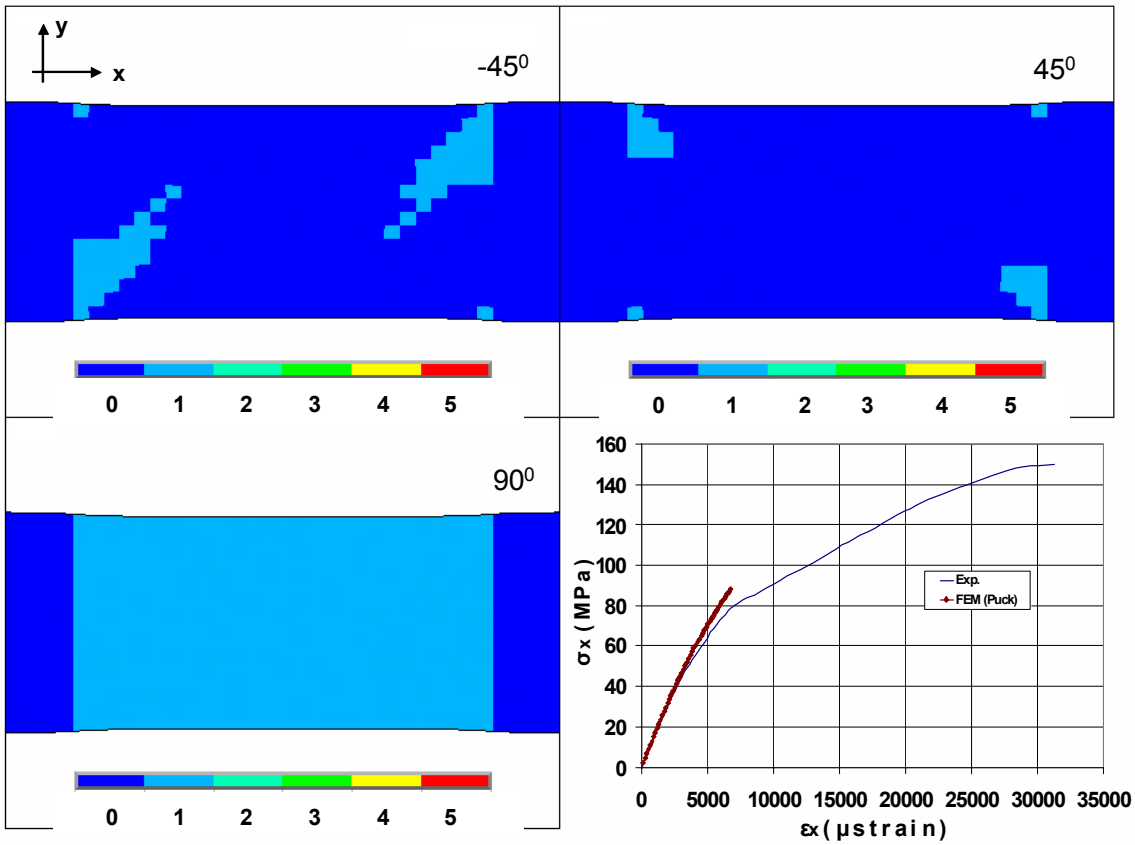
y
x
-45⁰
45⁰
90⁰
0 1 2 3 4 5
σx (MPa)
εx (μstrain)
Exp.
FEM (Puck)

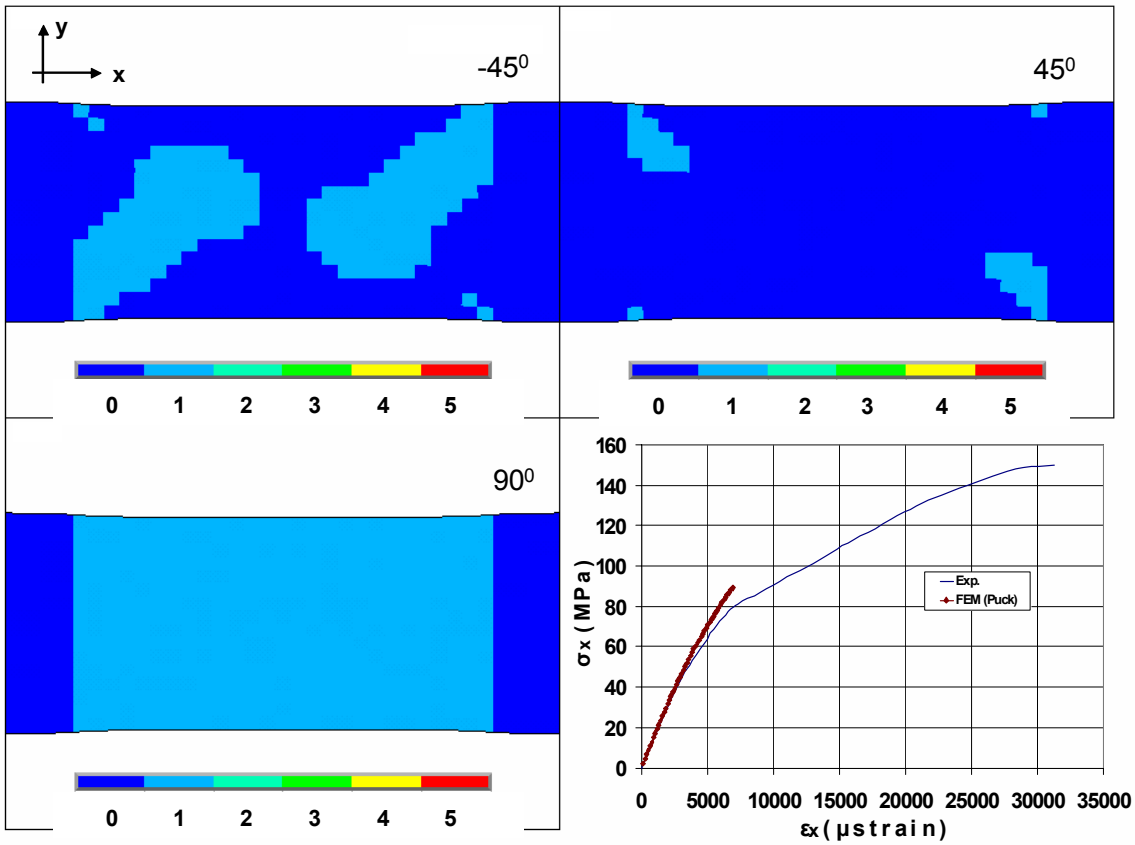
y
x
-45⁰
45⁰
90⁰
0 1 2 3 4 5
σx (MPa)
εx (μstrain)
Exp.
FEM (Puck)

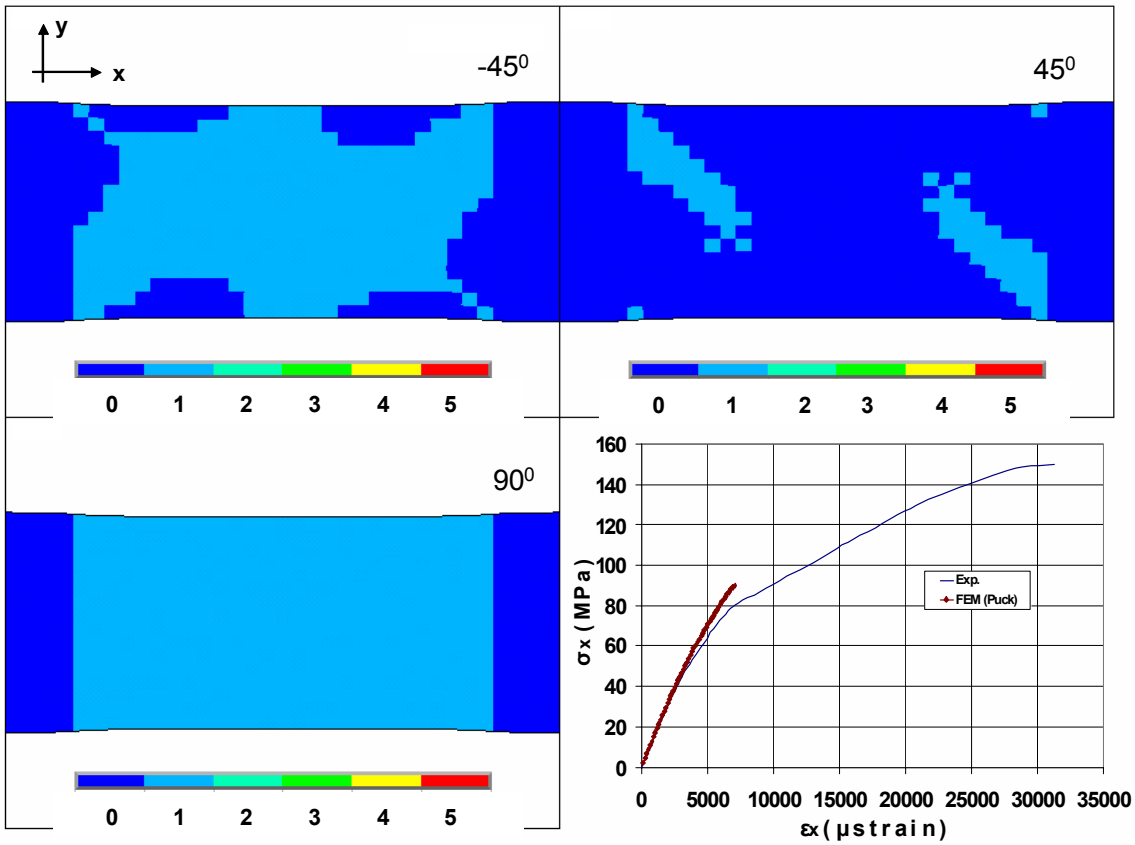
y
x
-45⁰
45⁰
90⁰
0 1 2 3 4 5
σx (MPa)
εx (μstrain)
Exp.
FEM (Puck)

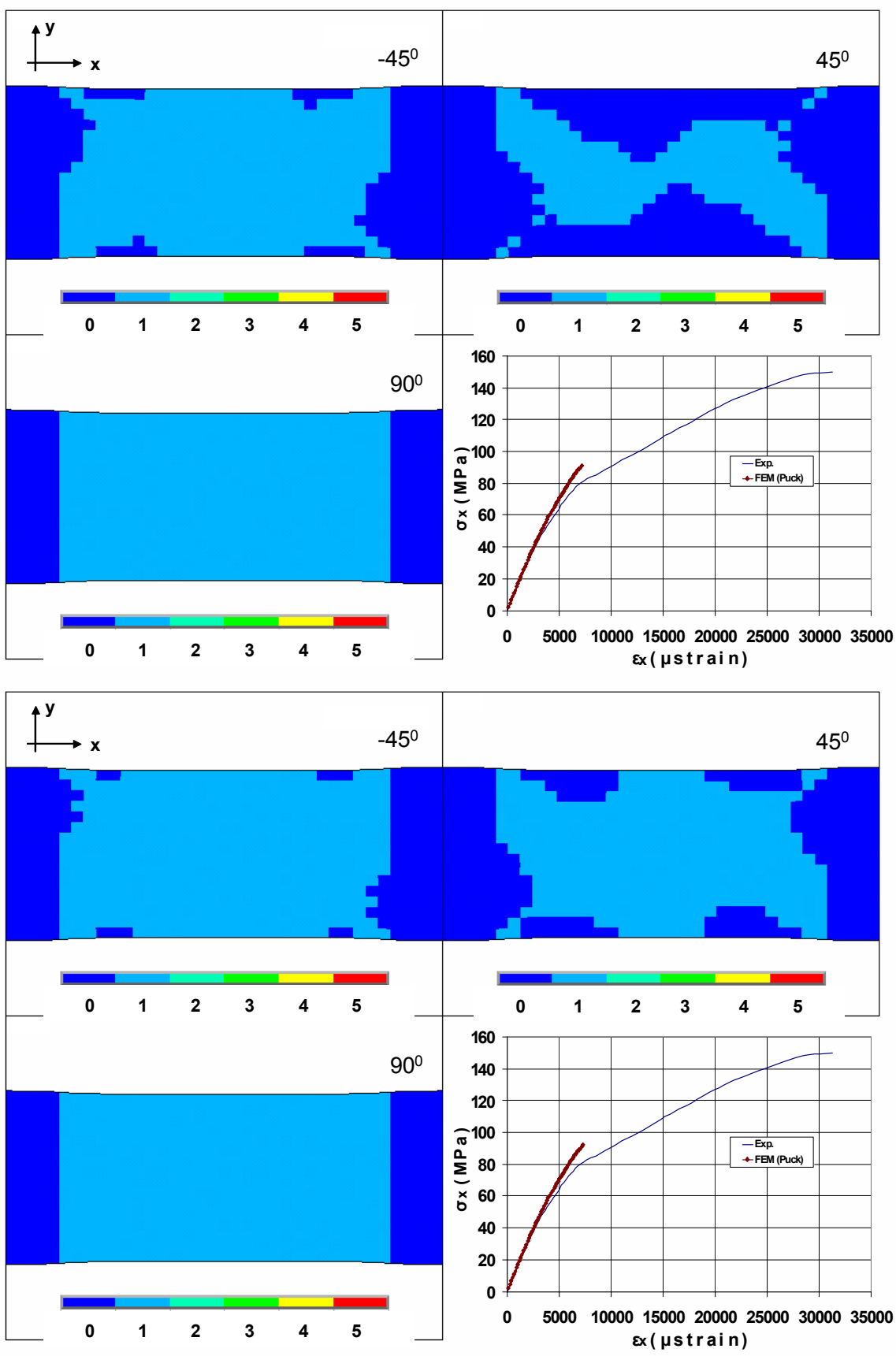

Fig. 61: Stress-Strain behaviour of an MD 90 coupon in tension

Table 16: Experimental and numerical strength values for MD coupon @ 90 degrees under tension

	Exp.	**FEM**	**%**
MPa	143.0	91.95	35.7

Tensile matrix failure is introduced in [90] layers. After saturation point, damage propagates gradually in [±45] layers. The coupon fails when cracks are bridged among gauge length free edges. Stitches that run along [90] and [±45] layers add some stiffness to the laminate and may prevent macroscopic separation. Since these are not simulated, they might produce some discrepancies between the FEM model and the experimental results.

6.1.15 Compression of MD coupon off-axis loaded at 90°

MD coupon cut @ 90° is simulated under compression. The FEM model performs moderately stiffer than the experiment, see Fig.62, not predicting satisfactorily the experimental stress-strain curve neither the coupon ultimate compressive stress with precision, see Table17.

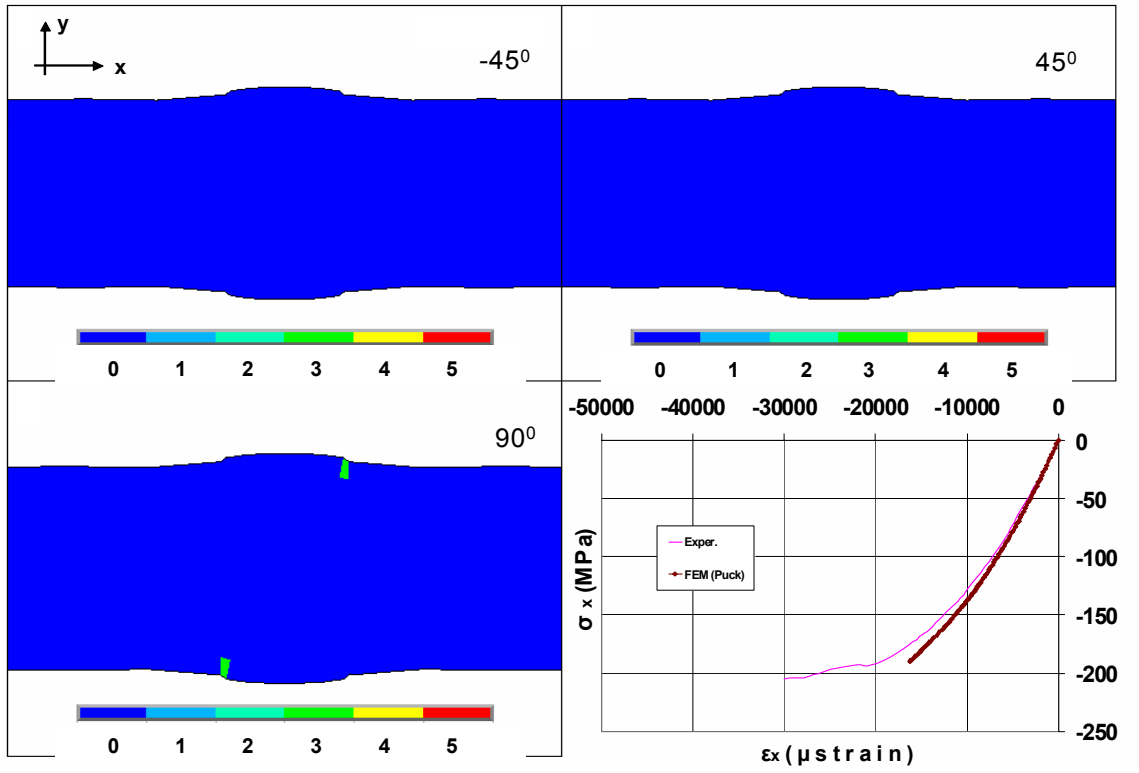

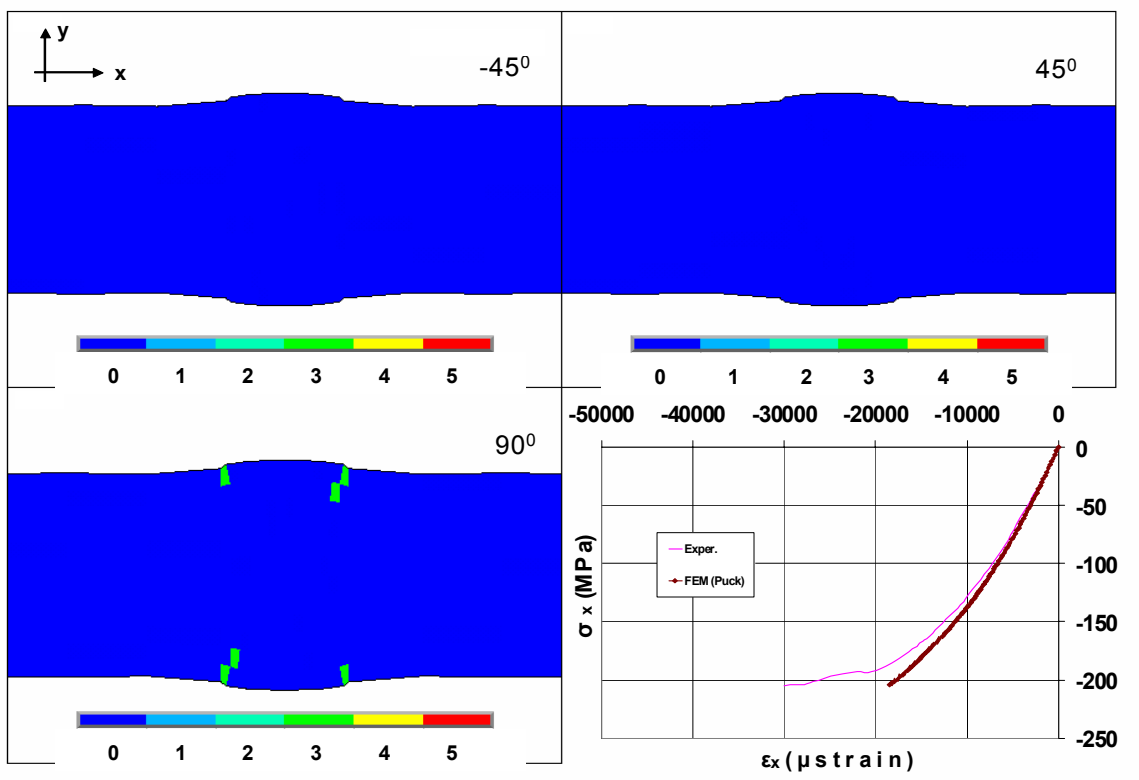
y
x
-45⁰
45⁰
90⁰
0 1 2 3 4 5
-50000 -40000 -30000 -20000 -10000 0
0 -50 -100 -150 -200 -250
σ x (MPa)
εx (μstrain)
Exper.
FEM (Puck)

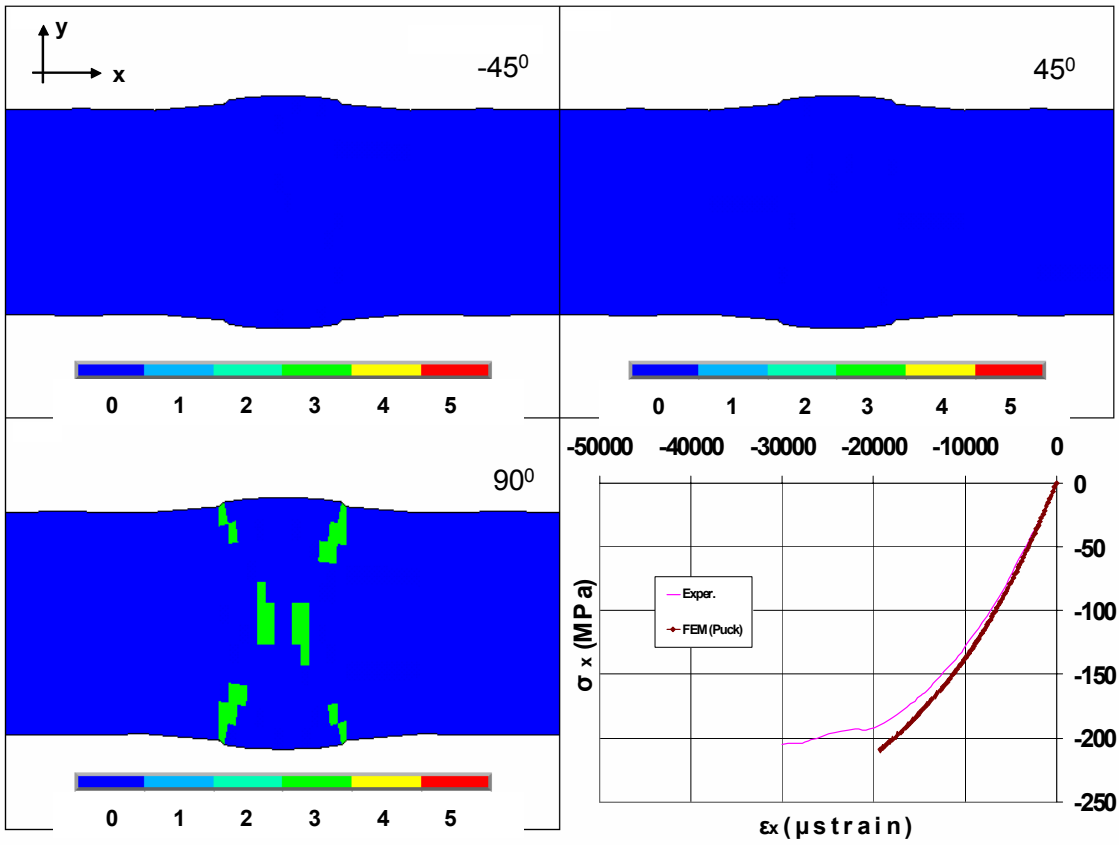
y
x
-45⁰
45⁰
90⁰
0 1 2 3 4 5
-50000 -40000 -30000 -20000 -10000 0
0 -50 -100 -150 -200 -250
σ x (MPa)
εx (μstrain)
Exper.
FEM (Puck)

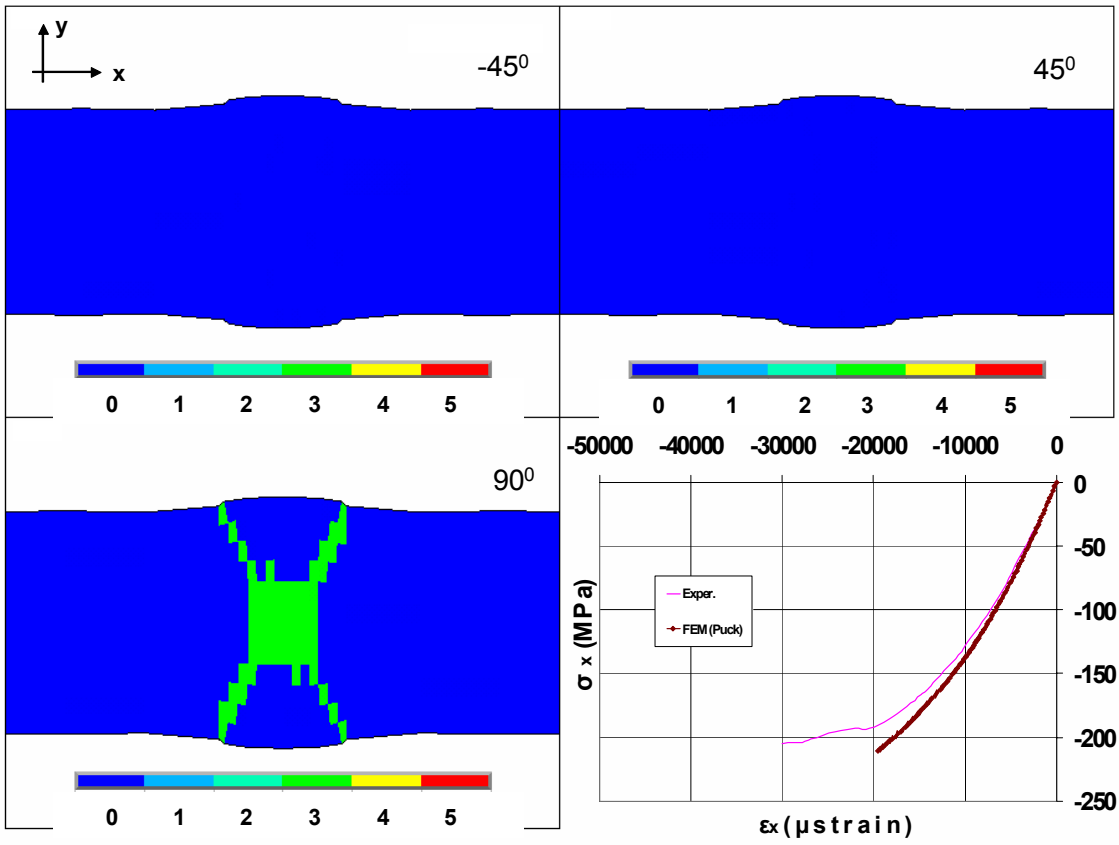
y
x
-45⁰
45⁰
90⁰
0 1 2 3 4 5
-50000 -40000 -30000 -20000 -10000 0
0 -50 -100 -150 -200 -250
σ x (MPa)
εx (μstrain)
Exper.
FEM (Puck)

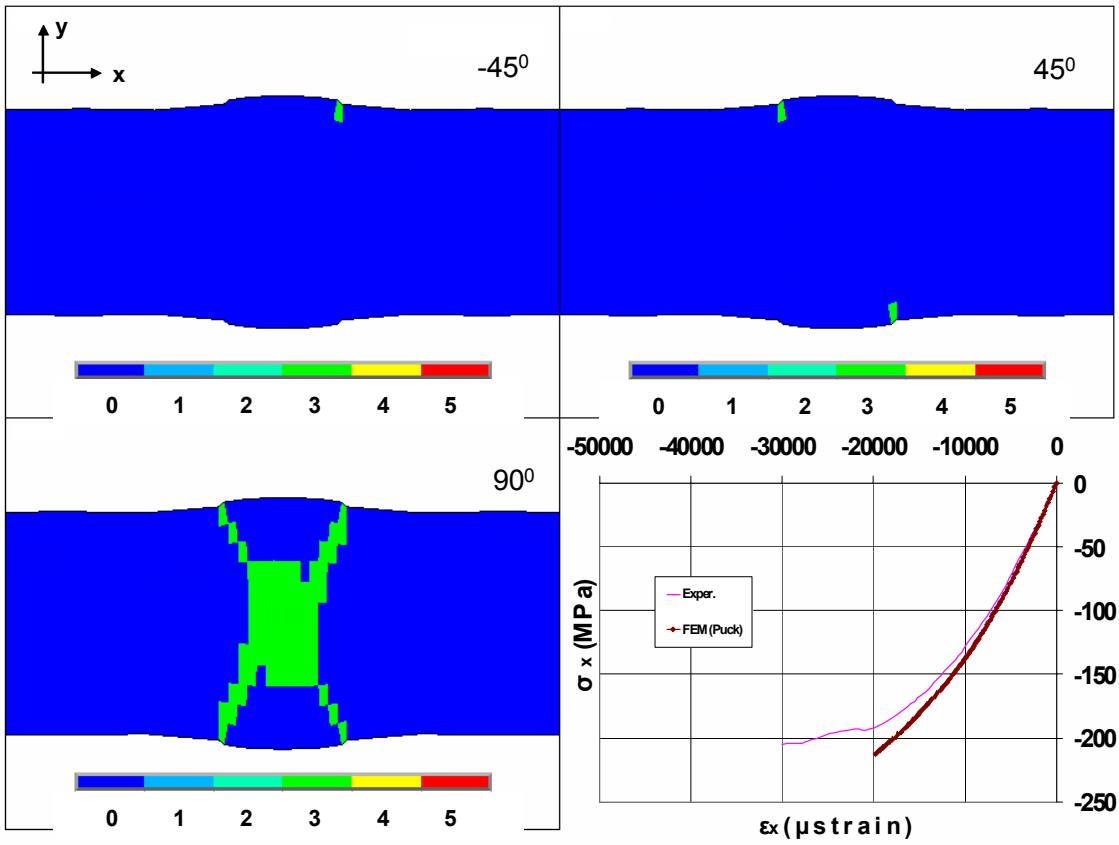
y
x
-45⁰
45⁰
90⁰
0 1 2 3 4 5
-50000 -40000 -30000 -20000 -10000 0
0 -50 -100 -150 -200 -250
σ x (MPa)
εx (μstrain)
Exper.
FEM (Puck)

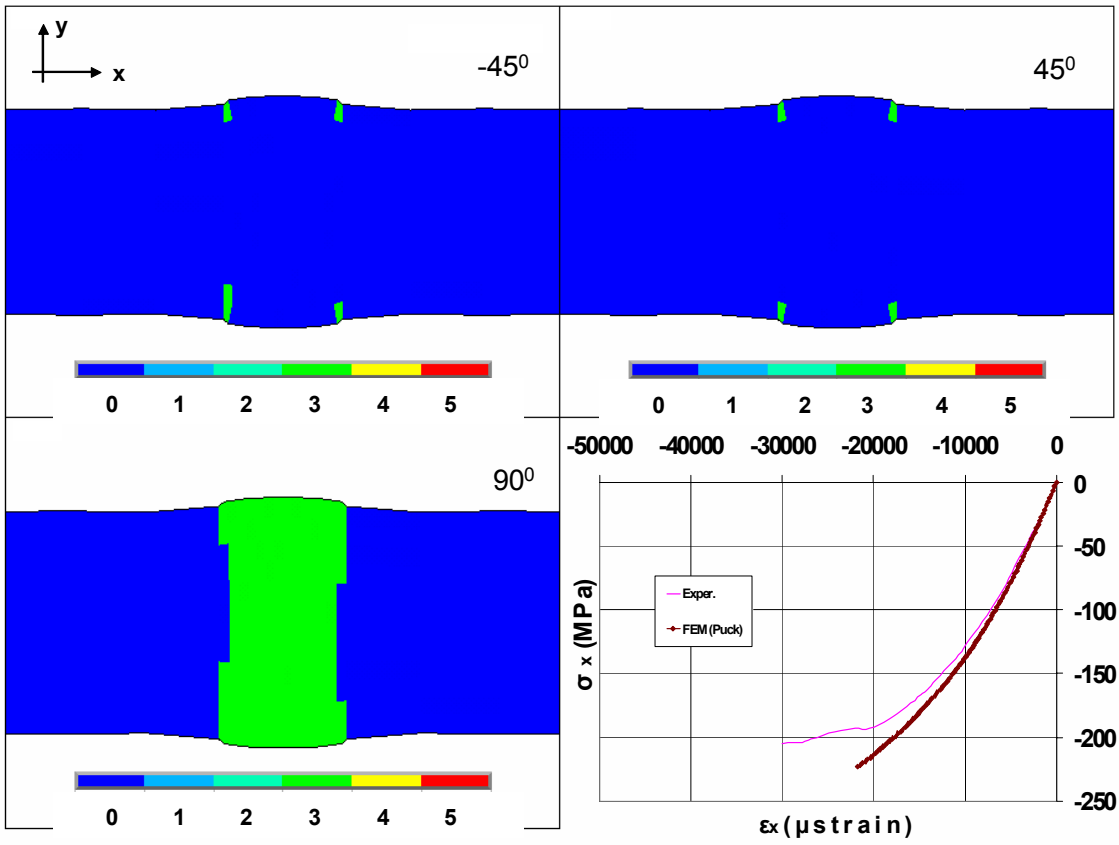
y
x
-45⁰
45⁰
90⁰
0 1 2 3 4 5
-50000 -40000 -30000 -20000 -10000 0
0 -50 -100 -150 -200 -250
σ x (MPa)
εx (μstrain)
Exper.
FEM (Puck)

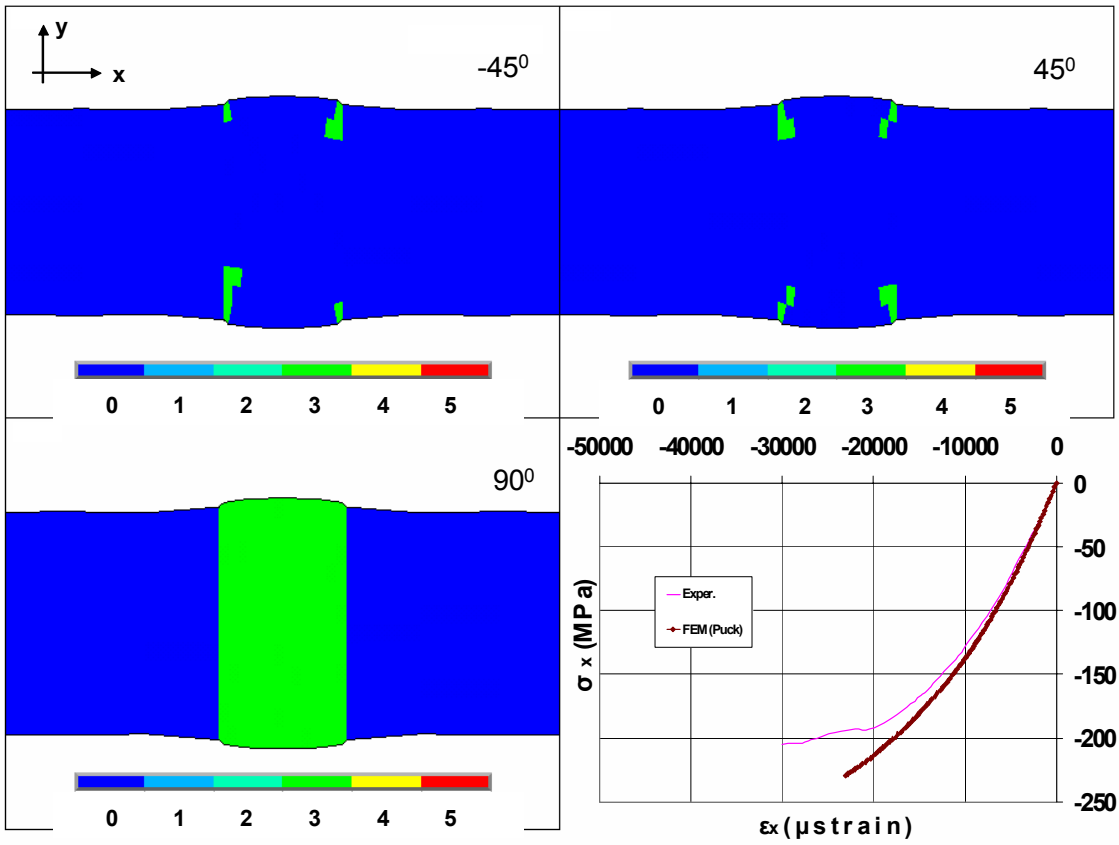
y
x
-45⁰
45⁰
90⁰
0 1 2 3 4 5
-50000 -40000 -30000 -20000 -10000 0
0 -50 -100 -150 -200 -250
σ x (MPa)
εx (μstrain)
Exper.
FEM (Puck)

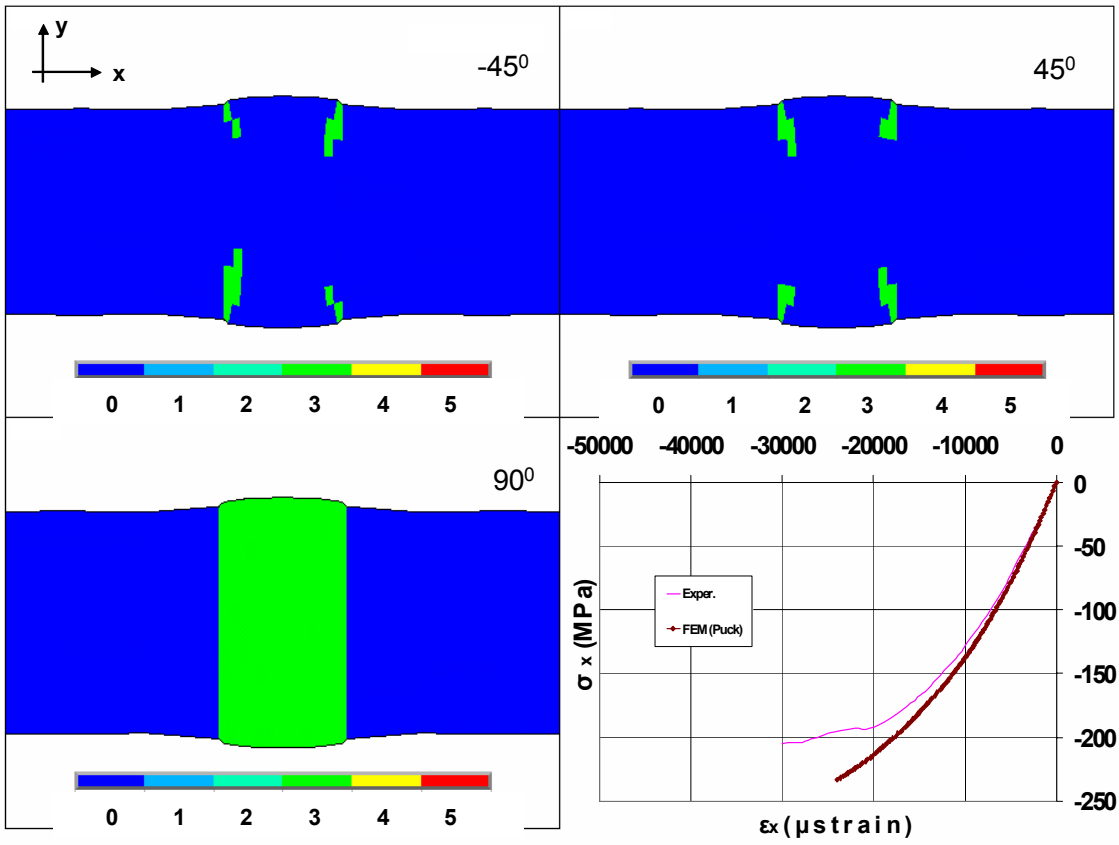
y
x
-45⁰
45⁰
90⁰
0 1 2 3 4 5
-50000 -40000 -30000 -20000 -10000 0
0 -50 -100 -150 -200 -250
σ x (MPa)
εx (μstrain)
Exper.
FEM (Puck)

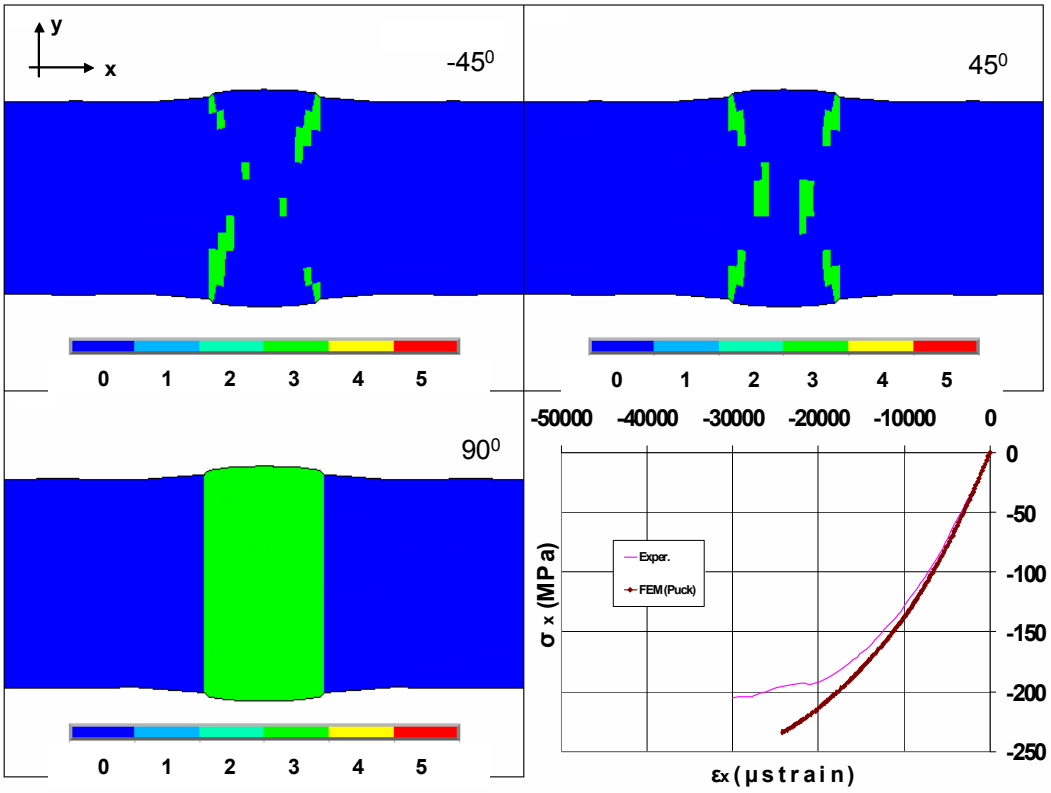

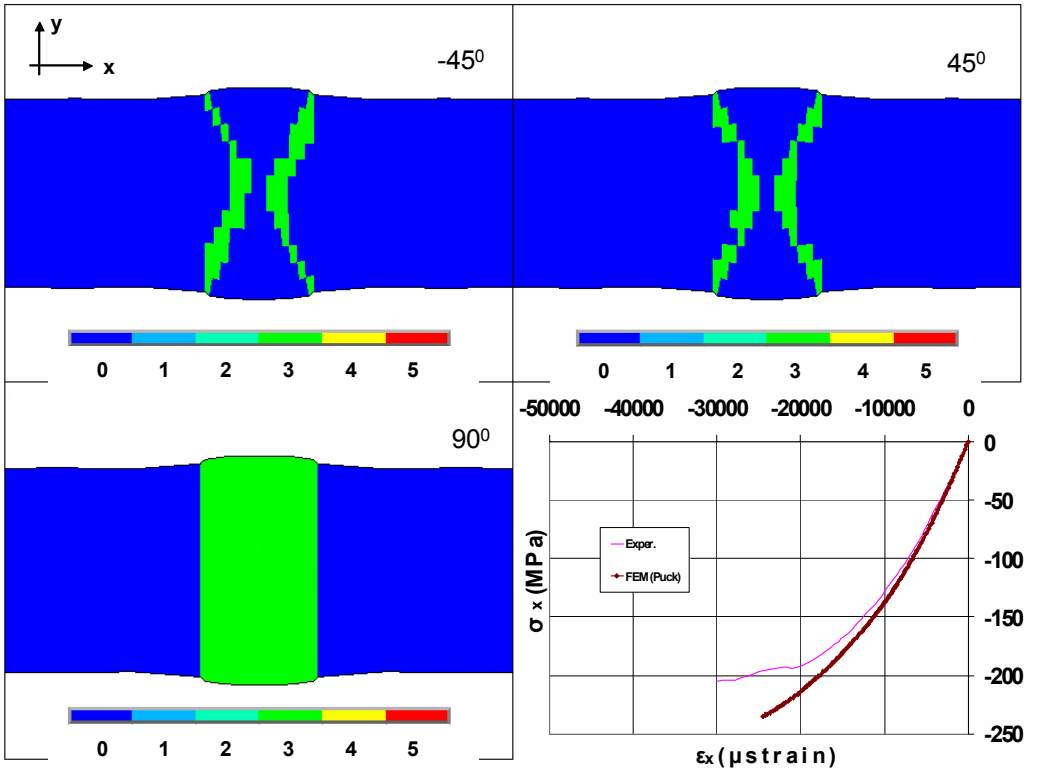

Fig. 62: Stress-Strain behaviour of an MD 90 coupon in compression

Table 17: Experimental and numerical strength values for MD coupon @ 90 degrees under compression

	Exp.	**FEM**	**%**
MPa	-195.0	-235.46	-20.75

Explosive matrix cracks of mode C, indicated with number 3 are emanating in [90] plies. This failure mechanism potentially leads to delamination and final failure. The implemented thick shell element cannot support the modelling of such damage mode. It is expected that the predicted ultimate compressive stress might be in poor agreement with the experiment. Subsequent to [90] plies total failure the damage propagates to [±45] plies. The coupon is considered failed when crack bridges among the two free edges of the gauge length.

6.2 Predictions vs. Experimental data; CA Cyclic Loading

The OB MD laminate of $[(\pm 45/0)_4/\pm 45]_T$ lay-up and the ISO 14129 coupon of $[\pm 45]_S$ stacking sequence are used for preliminary model verification. At this phase, a first data set of CA fatigue tests was used consisting of on-axis MD coupons at R=-1 and ISO coupons at R=0.1. Details on the test data can be found in [30]-[32].

6.2.1 S-N curve for $[(\pm 45/0)_4/\pm 45]_T$ Gl/Ep OB coupon (R=-1)

Calculations are performed for 3 stress levels, namely SL1=230 MPa, SL2=180 MPa and SL3=133 MPa. At SL1 the complete cycle is realized in 60 load steps and this is repeated in blocks of 200 cycles, i.e. a complete cycle calculation procedure is performed every 200 cycles. The complete cycles of SL2 and SL3 are also analyzed in 60 loading steps, however, the respective block sizes are 2000 and 20000 cycles. From a complete cycle set to another it is assumed that strength and stiffness are degraded appropriately, as defined in chapter 2.

Calculated S-N curves, derived by means of linear regression in log-log scale of the three simulated stress levels, are presented in Fig. 63. Max and min prediction values are related to the uncertainty of knowing exactly the number of cycles failure has occurred. This in turn is related to the size of the block of cycles used in the simulation. Coupon failure is indicated by the computational procedure itself; observing damage plots of each ply, coupon failure is considered when fibres are broken in the [0] ply through coupon width. This is also supported by the spread of catastrophic failure modes, e.g. fibre breaks, see Fig. 64, where an example of the sequence of failure events occurring in each ply of the $[(\pm 45/0)_4/\pm 45]_T$ lay-up with respect to the applied number of CA cycles is presented.

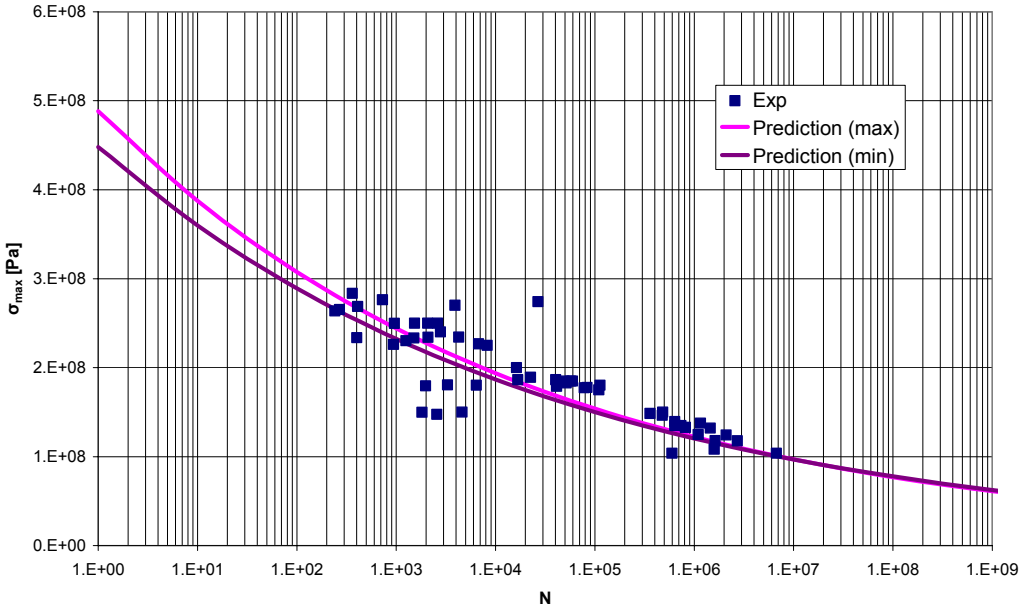

Fig. 63: Comparison of FADAS predictions and exp. Data; OB MD Gl/Ep under R=-1

Simulation results presented in Fig.64 were derived for a coupon cycled at SL2, i.e. at $\sigma_{\max} = 180\ MPa$, R=-1.

In Figs. 65-70, an example of the exact alternating plane stress field developed at each integration point of each ply, at each element with respect to the applied number of cycles is presented and compared with the respective residual strength value for each component of the plane stress tensor. These results are in agreement with those of Fig.64 and also support the designation of coupon global failure.

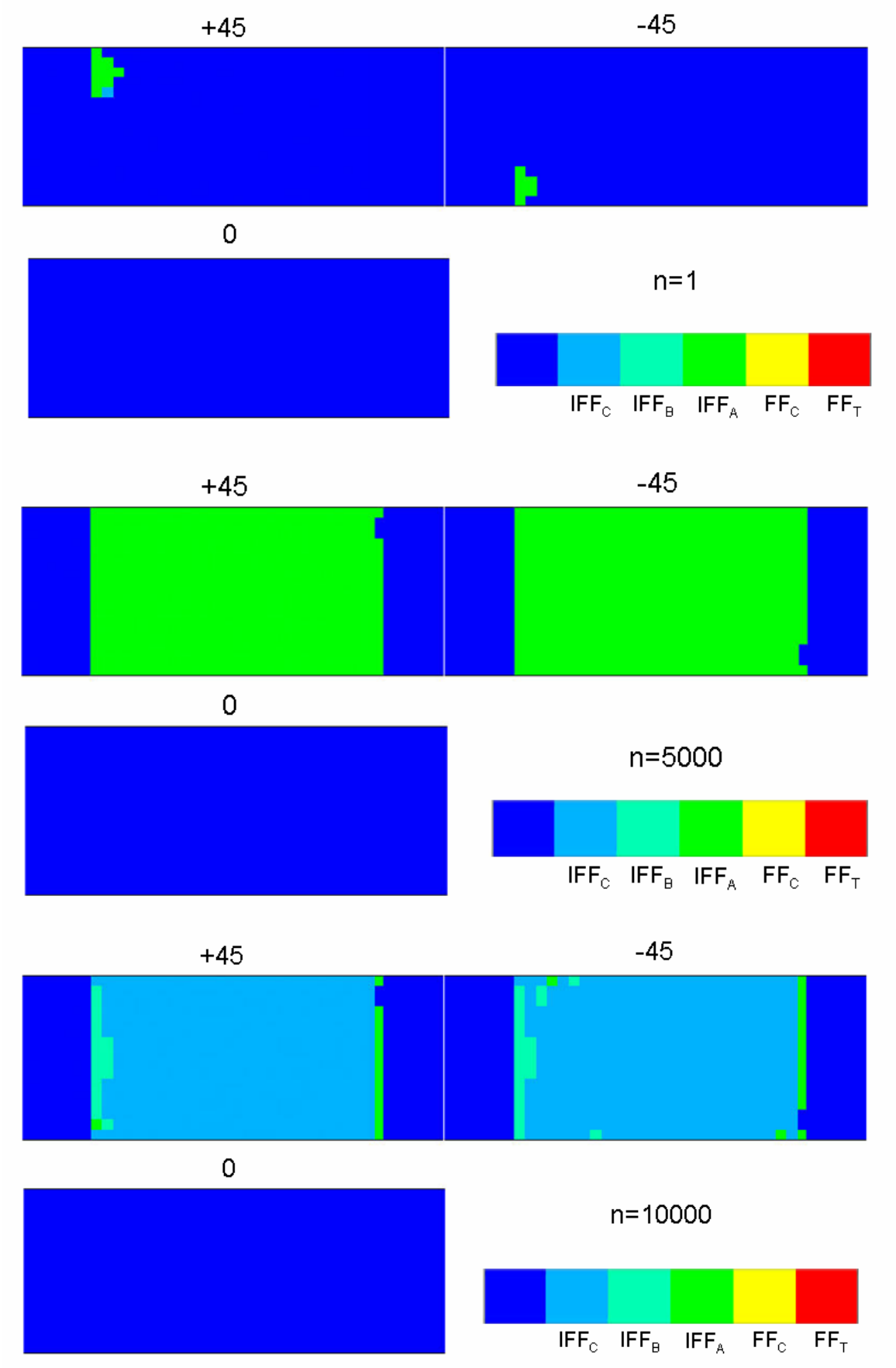
+45
-45
0
n=1
IFF$_C$ IFF$_B$ IFF$_A$ FF$_C$ FF$_T$
+45
-45
0
n=5000
IFF$_C$ IFF$_B$ IFF$_A$ FF$_C$ FF$_T$
+45
-45
0
n=10000
IFF$_C$ IFF$_B$ IFF$_A$ FF$_C$ FF$_T$

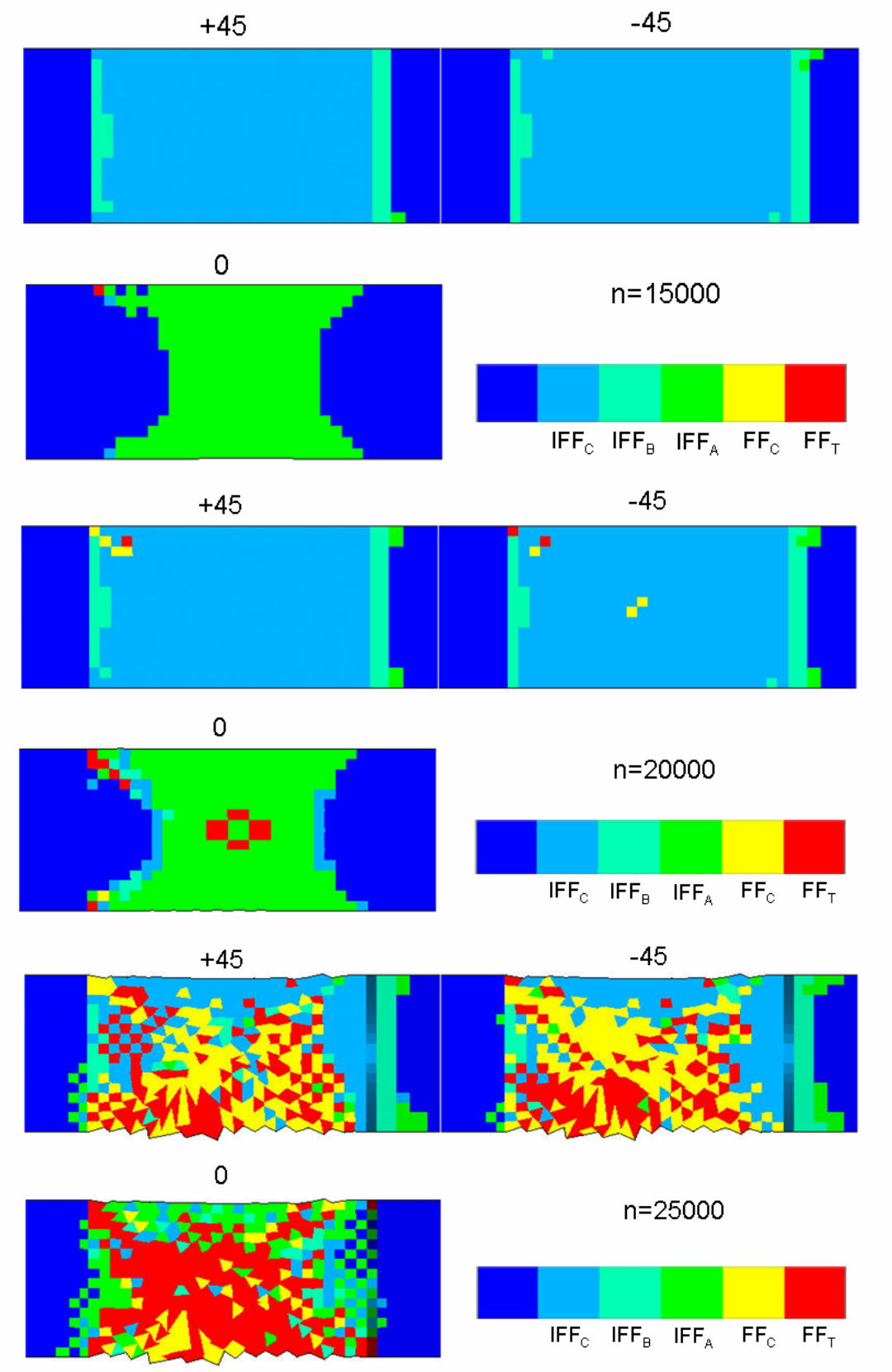

Fig. 64: Failure modes of a $[(\pm 45/0)_4/\pm 45]$ Gl/Ep OB coupon, SL2 σ_{max}=180 [MPa], R=-1

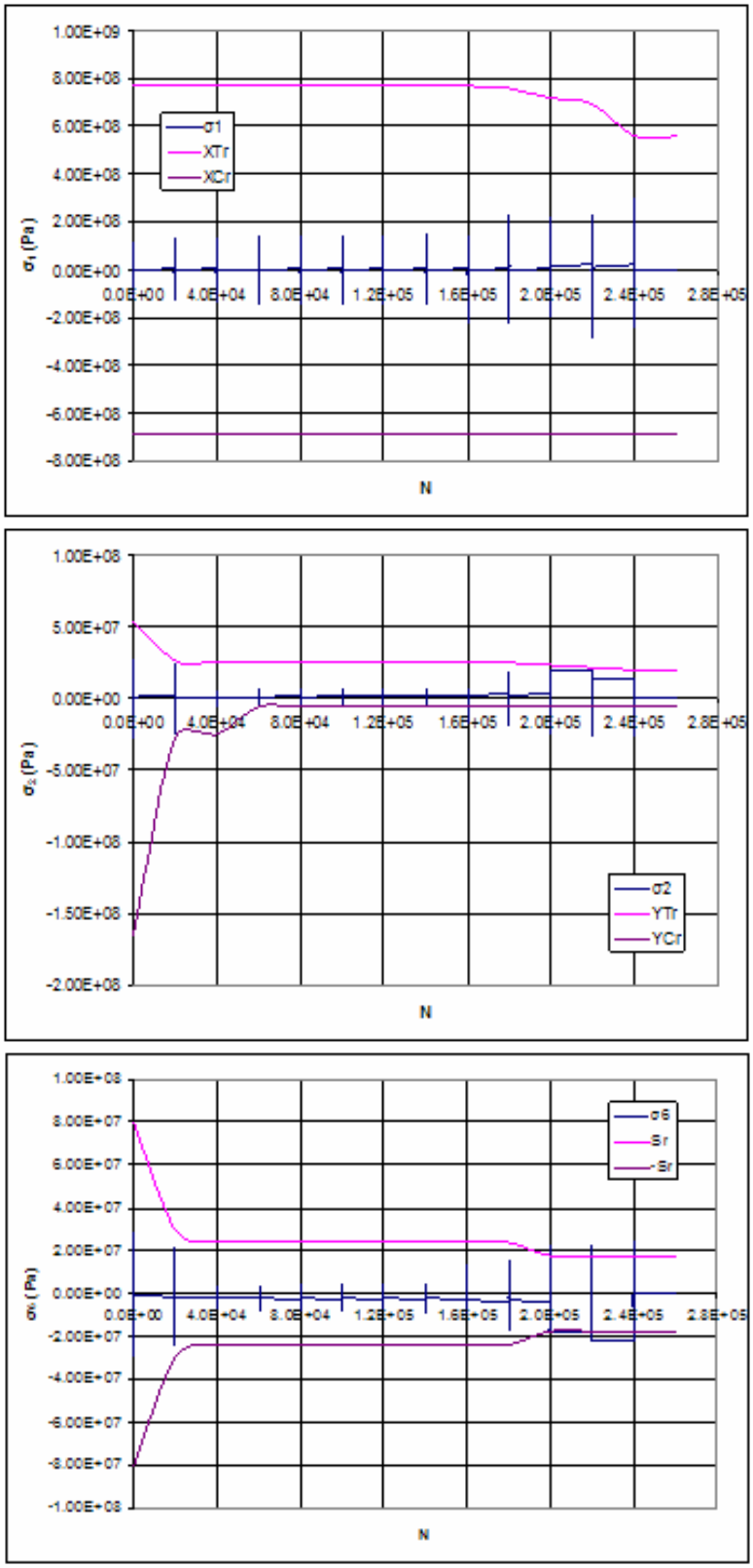

Fig. 65: Alternating plane stress field in the [+45] ply of a $[(\pm 45/0)_4/\pm 45]$ Gl/Ep OB coupon, SL3 σ_{max}=133 [MPa], R=-1. Corner element adjacent to the tab

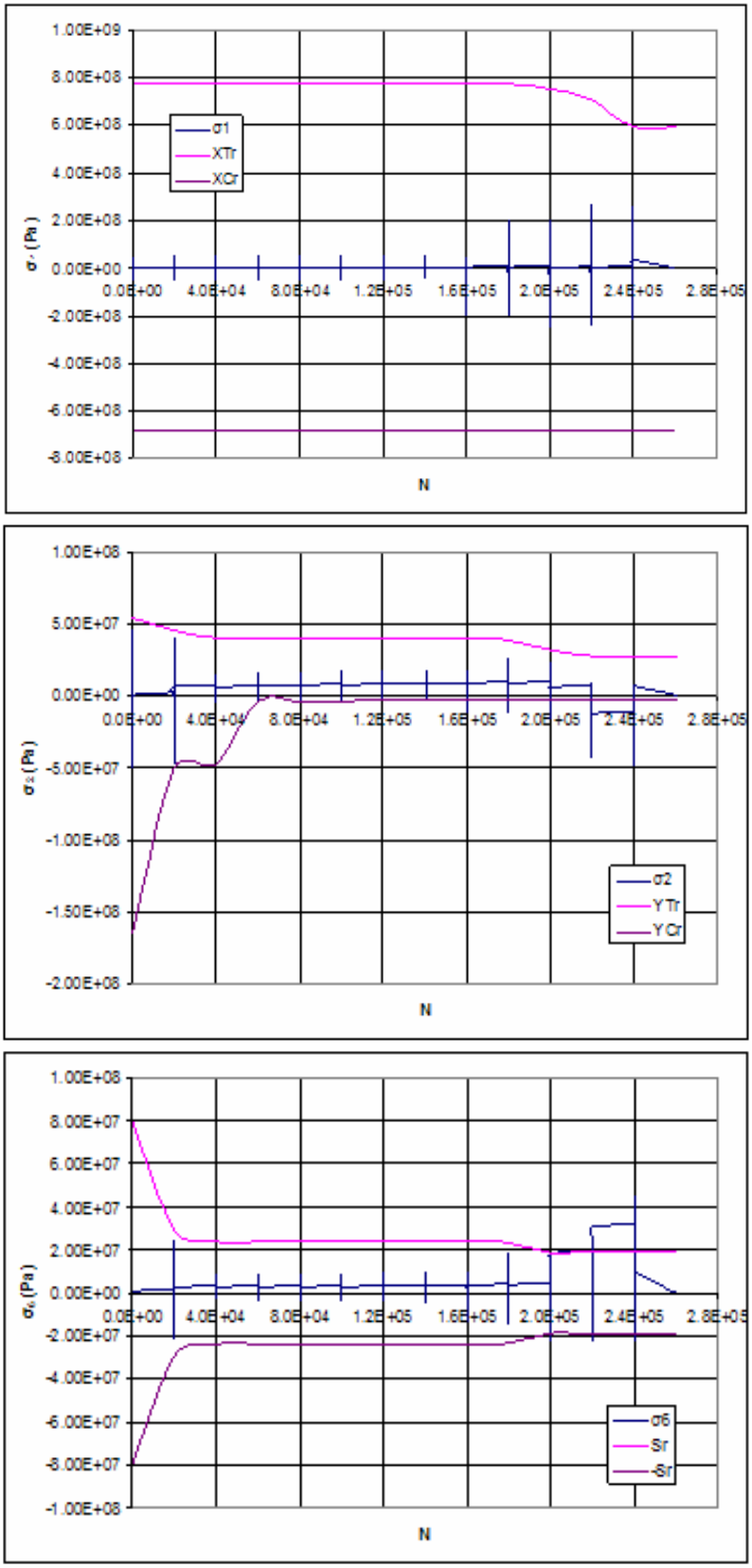

Fig. 66: Alternating plane stress field in the [-45] ply of a $[(\pm 45/0)_4/\pm 45]$ Gl/Ep OB coupon, SL3 σ_{max}=133 [MPa], R=-1. Corner element adjacent to the tab

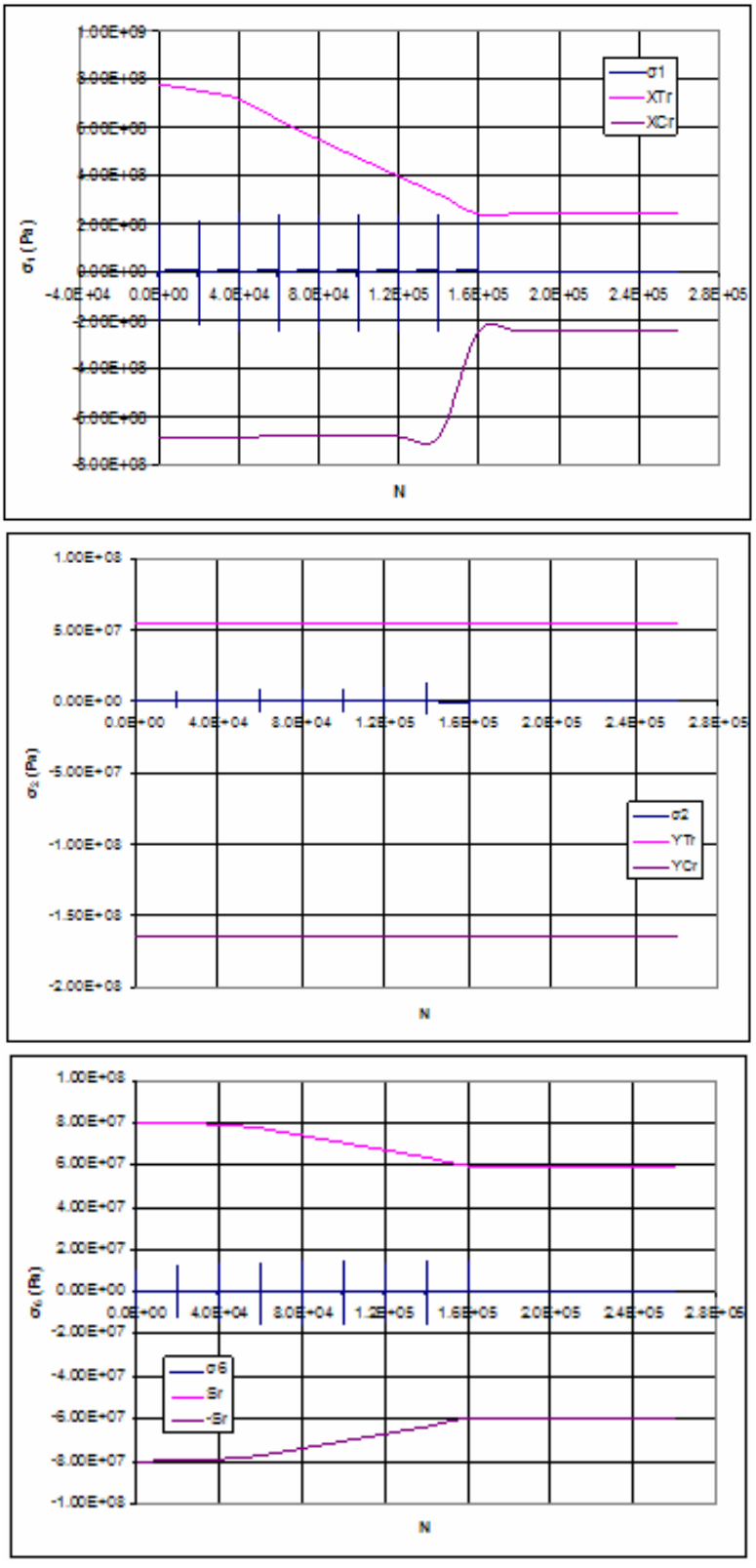

Fig. 67: Alternating plane stress field in the [0] ply of a $[(\pm 45/0)_4/\pm 45]$ Gl/Ep OB coupon, SL3 σ_{max}=133 [MPa], R=-1. Corner element adjacent to the tab

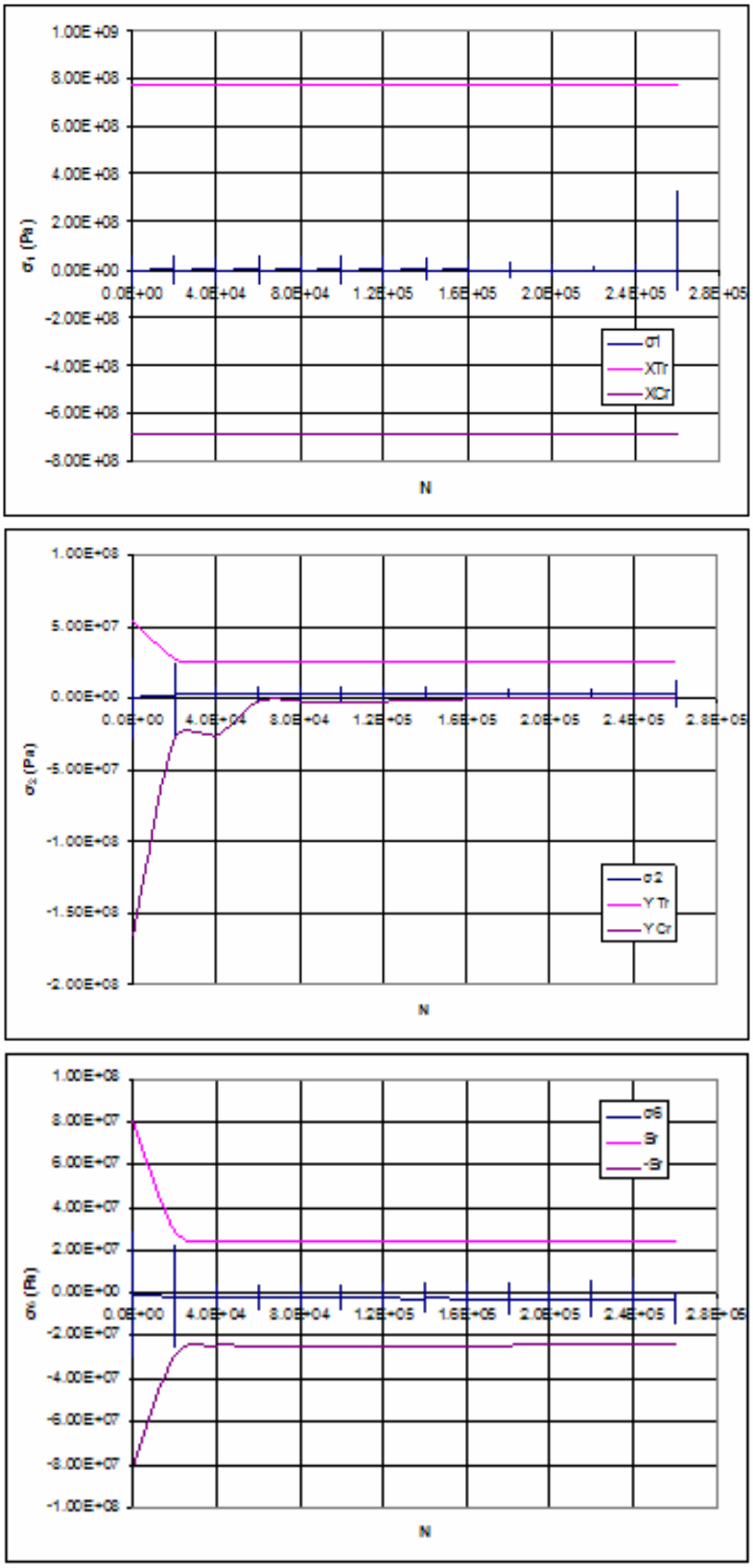

Fig. 68: Alternating plane stress field in the [+45] ply of a $[(\pm 45/0)_4/\pm 45]$ Gl/Ep OB coupon, SL3 σ_{max}=133 [MPa], R=-1. Element in the centre of the coupon

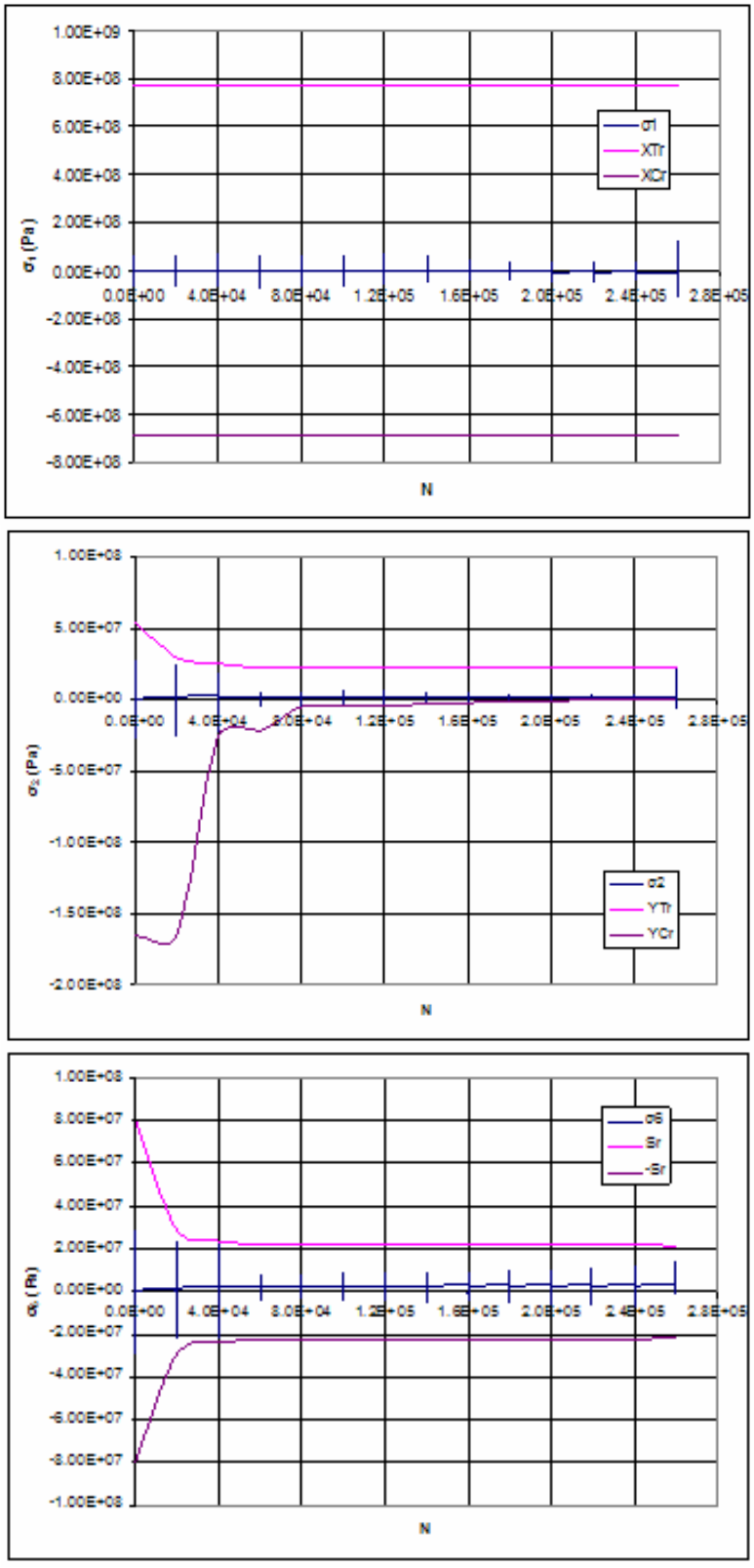

Fig. 69: Alternating plane stress field in the [-45] ply of a $[(\pm 45/0)_4/\pm 45]$ Gl/Ep OB coupon, SL3 σ_{max}=133 [MPa], R=-1. Element in the centre of the coupon

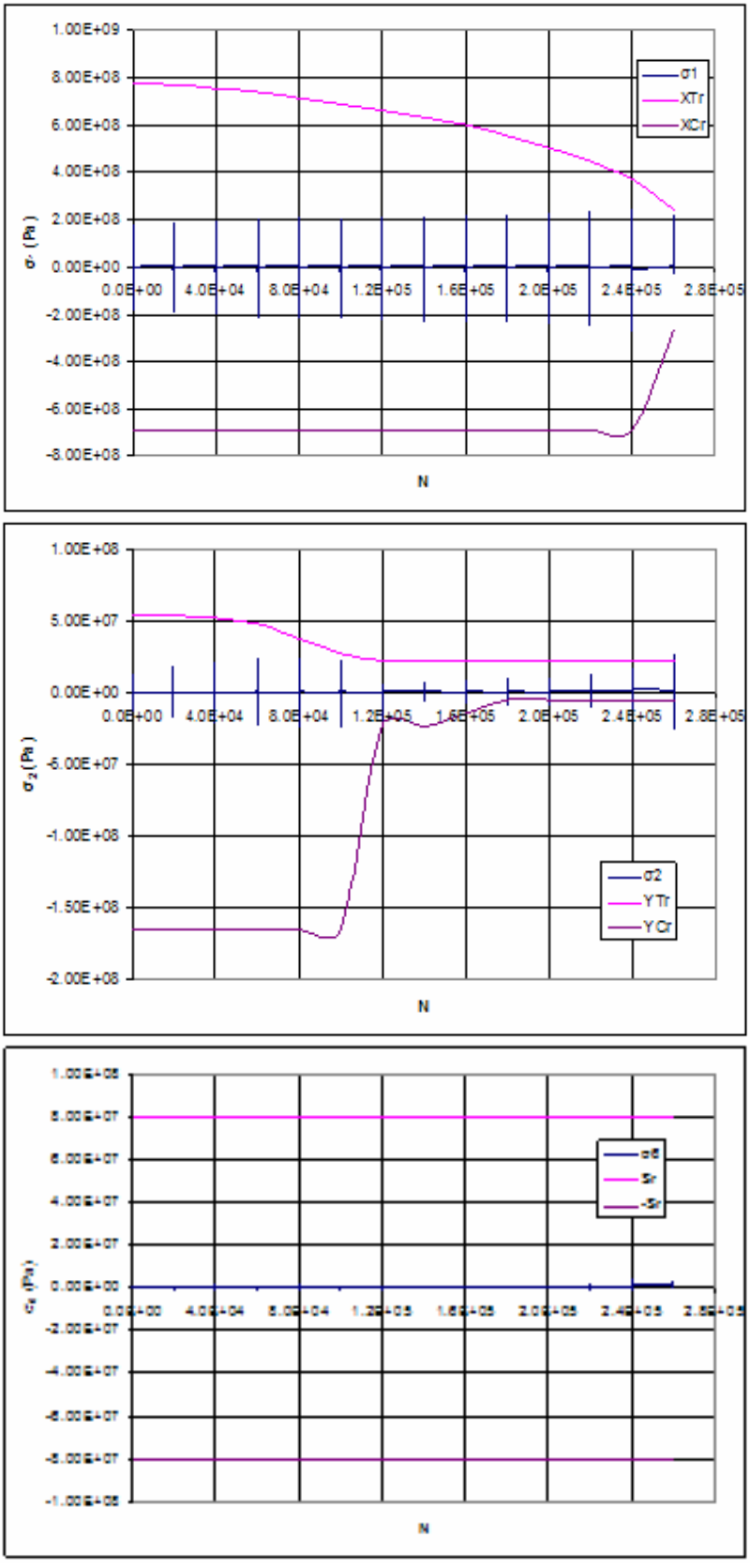

Fig. 70: Alternating plane stress field in the [0] ply of a $[(\pm 45/0)_4/\pm 45]$ Gl/Ep OB coupon, SL3 σ_{max}=133 [MPa], R=-1. Element in the centre of the coupon

6.2.2 S-N curve for $[\pm 45]_S$ Gl/Ep ISO 14129 coupon (R=0.1)

Calculations are performed for 3 stress levels, namely SL1=89.8 MPa, SL2=67.3 MPa and SL3=48.4 MPa. At SL1 the complete cycle is realized in 30 load steps and this is repeated in blocks of 50 cycles. The complete cycles of SL2 and SL3 are also analyzed in 30 loading steps, however, the respective block sizes are 2000 and 50000 cycles.

Calculated S-N curves are presented in Fig. 71. Again, max and min prediction values are related to the uncertainty of knowing exactly the number of cycles failure has occurred. This in turn is related to the size of the block of cycles used in the simulation. Coupon failure is indicated by observing damage plots of either the [+45] or [-45] ply; when matrix damage in the form of failure mode A of Puck criterion is spread along the fibre direction, bridging coupon free edges, the specimen is considered broken. The respective failure patterns per ply and the rate of propagation is shown in Fig. 72.

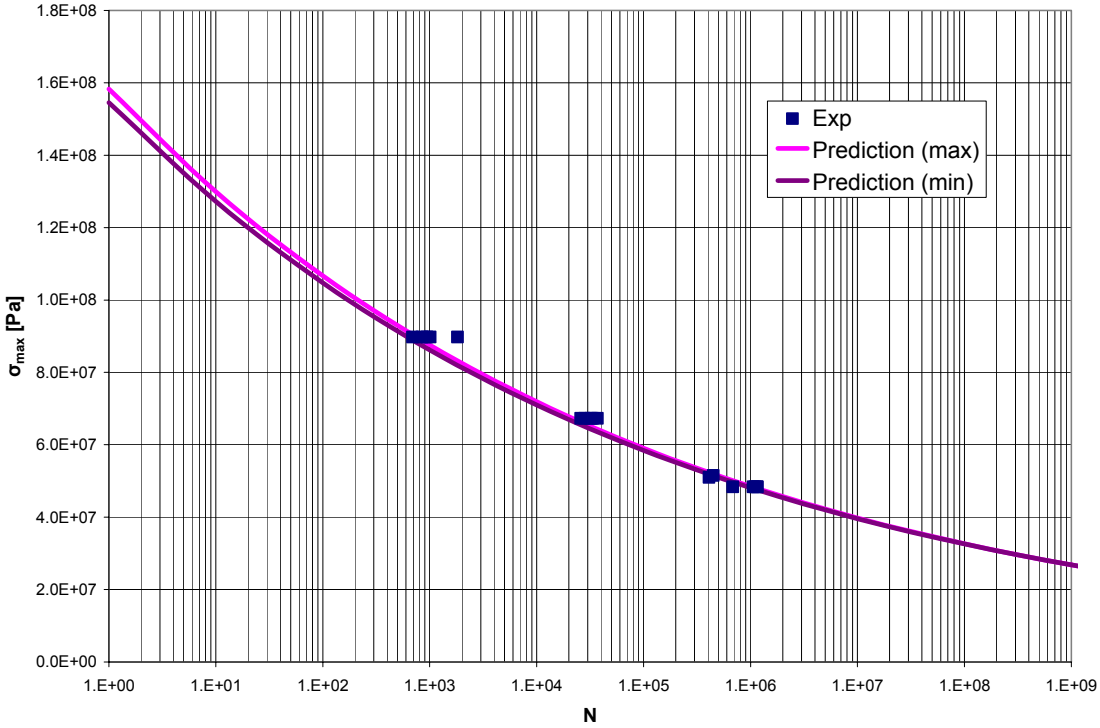

Fig. 71: Comparison of FADAS predictions and exp. Data; $[\pm 45]_S$ coupon, Gl/Ep under R=0.1

Simulation results presented in Fig.72 were derived for a coupon cycled at SL2, i.e. at $\sigma_{\max} = 67.3\ MPa$, R=0.1.

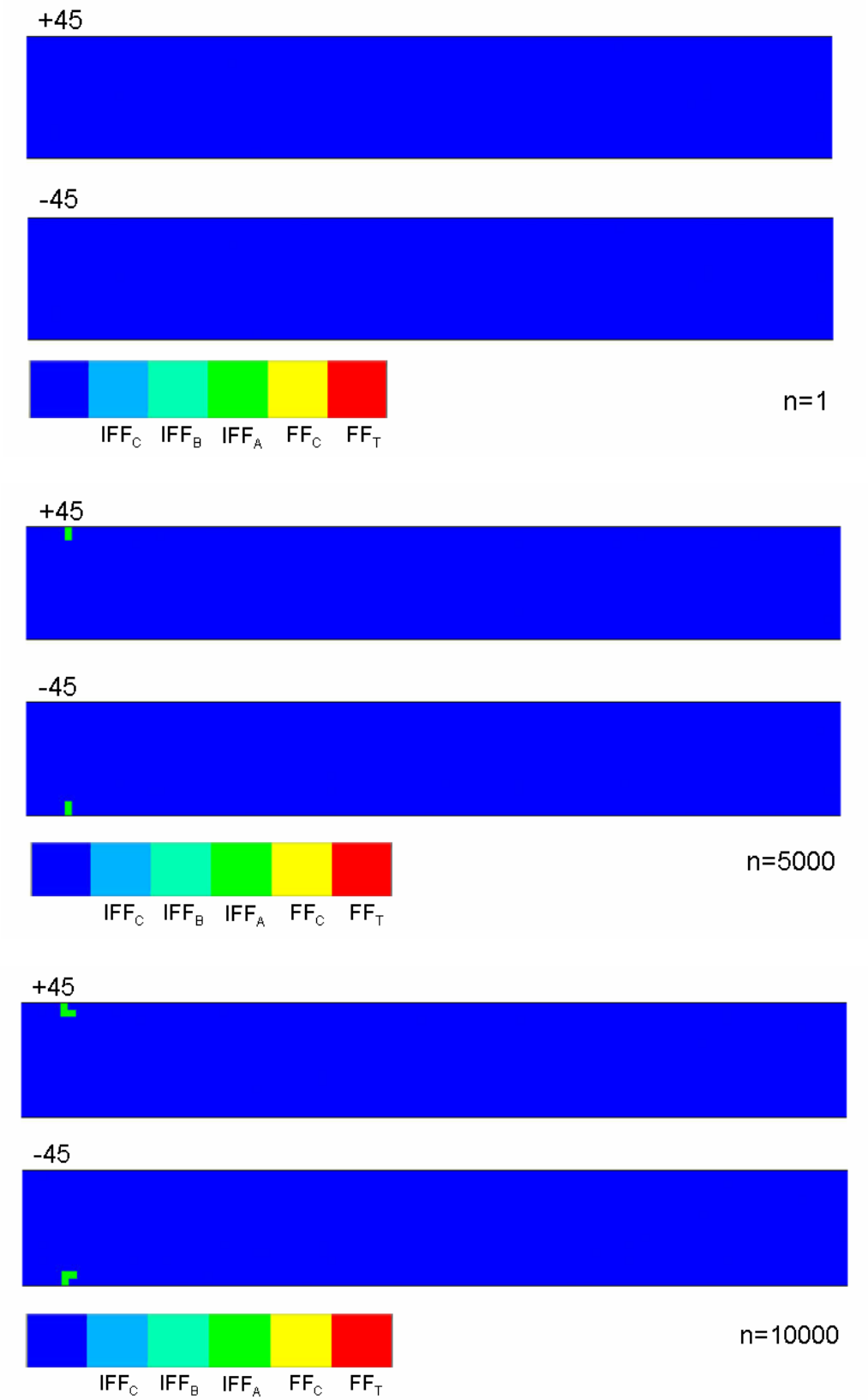
+45
-45
IFF$_C$ IFF$_B$ IFF$_A$ FF$_C$ FF$_T$
n=1
+45
-45
IFF$_C$ IFF$_B$ IFF$_A$ FF$_C$ FF$_T$
n=5000
+45
-45
IFF$_C$ IFF$_B$ IFF$_A$ FF$_C$ FF$_T$
n=10000

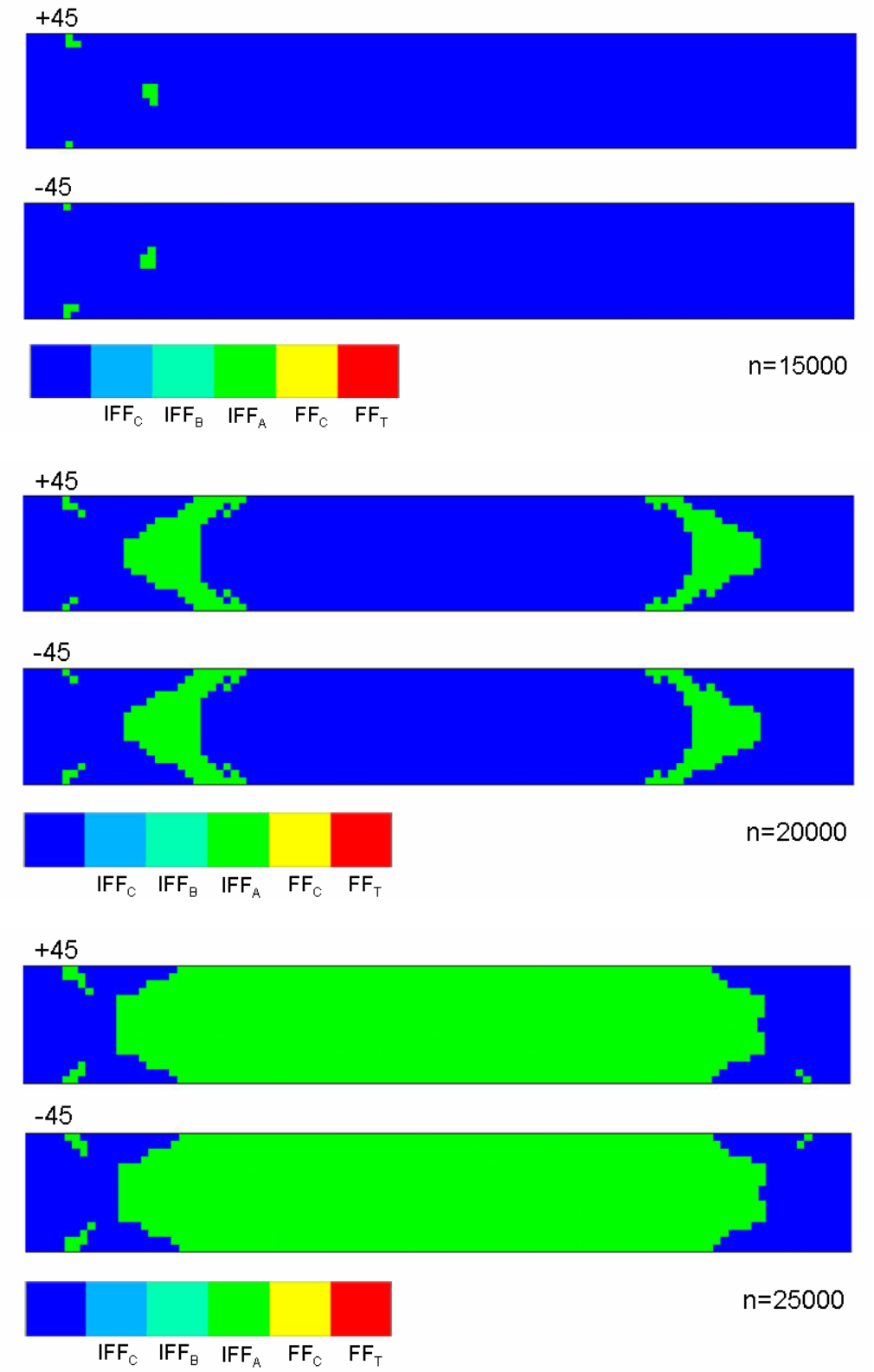

Fig. 72: Failure modes of a $[\pm 45]_S$ Gl/Ep ISO 14129 coupon, SL2 σ_{max}=67.3 MPa, R=0.1

7. Conclusions

In the present work, an anisotropic non-linear material constitutive model is developed along with a thick shell element implementing progressive damage concepts to predict the load bearing capacity and life of composite structures. In-plane mechanical properties of the material are fully characterized for the unidirectional layer; in shear, tension, compression parallel and transverse to the fibres direction.

Having specified the material stress-strain response and strength, numerical simulations of unidirectional and multidirectional laminates are performed under static axial tensile or compressive load. Puck criterion, enhancing failure characterization by distinguishing between different damage modes, is one of several limit criteria available. Different stiffness degradation strategies are utilized depending on the calculated failure mode, providing modelling flexibility.

The plane-stress FEM model is not able to calculate the expected high interlaminar stresses at coupon free edges not either the 3-D stress field developed near the “gripping” area. Still, it predicts very well coupon stress-strain response, even for laminates that behave highly non-linearly as the MD @ 60 degrees, calculating the failure load with fine precision. Discrepancies are expected wherever 3-D effects are present, e.g. delaminations, as probably in the multidirectional laminate @ 90 degrees under compression, but the present model is computationally less expensive than a 3D FEM approximation, allowing simulation of large structures in reasonable time. In most cases where numerical predictions were compared to experimental results, failure patterns were corroborated satisfactorily, especially in the unidirectional coupons. The solution procedure is fast enough allowing simulations of large models in a reasonable computational time. The shell element is incorporated in the ANSYS commercial FEM code and is developed by means of a user FORTRAN routine.

Besides features suitable for static analyses, the FADAS model, simulating fatigue damage progression of a composite laminate by means of ply-by-ply damage modeling, was presented as well. Residual strength and stiffness as fatigue damage metric have been modeled using simple and cost-effective schemes, while the failure criterion of Puck along with post failure behavior of the material, has been implemented. SHELL181 element of ANSYS commercial code has been used for implementing the algorithm. The model has been set up for a Glass/Epoxy material typical of the Wind Turbine Rotor Blade Industry and has been verified through constant amplitude fatigue tests on different lay-ups, simulating a variety of plane stress combinations and failure modes. Preliminary results indicate that the algorithm actually predicts satisfactorily damage and failure. Further improvement of the accuracy of the predictions can be expected through inclusion of more refined material models.

Further development, modifications/debugging of the FE user routines initiated this first 18 month period will continue along with model assessment and validation by comparing theoretical predictions with experimental results either from the OPTIDAT database or from biaxial fatigue tests. Additional coupon testing will be performed to verify and refine theoretical material models implemented in the user routines.

8. References

1. Tsai, S. W. and Wu, E. M., "A general theory of strength for anisotropic materials", *J. Compos. Mater.,* 1971, **5**, 58-80

2. Hashin, Z., "Failure criteria for unidirectional fiber composites", *J. Appl. Mech.*, 1980, **47**, 329-334

3. Puck, A., Schürmann, H., "Failure analysis of FRP laminates by means of physically based phenomenological models", *Compos. Sci. Tech.*, 1998, **58**, 1045-1067

4. Hinton, M. J., Kaddour A. S. and Soden P. D., "A comparison of the predictive capabilities of current failure theories for composite laminates, judged against experimental evidence" *Compos. Sci.Tech.*, 2002, **62**, 1725-1797

5. Chang, K., Liu, S. and Chang, F., "Damage tolerance of laminated composites containing an open hole and subjected to tensile loadings", *J. Compos. Mater.,* 1991, **25**, 274-301

6. Lin, W. and Hu, H., "Nonlinear analysis of fiber-reinforced composite laminates subjected to uniaxial tensile load", *J. Compos. Mater.,* 2002, **36**, 1429-1450

7. Puck, A., Schürmann, H., "Failure analysis of FRP laminates by means of physically based phenomenological models", *Compos. Sci.Tech.*, 2002, **62**, 1633-1662

8. Puck, A., Kopp, J. and Knops, M., "Guidelines for the determination of the parameters in Puck's action plane strength criterion", *Compos. Sci.Tech.*, 2002, **62**, 371-378

9. R. Talreja, *Fatigue of composite materials*, Technomic, Lancaster, Pennsylvania, 1987.

10. I.M. Daniel, 1998 William M. Murray lecture: Experimentation and modeling of composite materials, *Experimental Mechanics*, **39**, 1-19, 1999.

11. J. Varna, R. Joffe, R. Talreja, A synergistic damage-mechanics analysis of transverse cracking in $[\pm\theta/90_4]_S$ laminates, *Composite Science and Technology*, **61**, 657-665, 2001.

12. D.Y. Song, N. Otani, Fatigue life prediction of cross-ply composite laminates, Materials Science & Engineering, **A238**, 329-335, 1997.

13. A. Charewicz, I.M. Daniel, Damage mechanisms and accumulation in Graphite/Epoxy laminates in Composite Materials: *Fatigue and Fracture*, ASTM STP 907, 274-297, 1986.

14. K.L. Reifsnider, S. Case, J. Duthoit, The mechanics of composite strength evolution, *Composite Science and Technology*, **60**, 2539-2546, 2000.

15. T.K. O'Brien, K.L. Reifsnider, Fatigue damage evaluation through stiffness measurements in Boron-Epoxy laminates, *Journal of Composite Materials*, **15**, 55-70, 1981.

16. J.E. Masters, K.L. Reifsnider, An investigation of cumulative damage development in Quasi-Isotropic Graphite/Epoxy laminates, *Damage in Composite Materials*, ASTM STP 775, 40-62, 1982.

17. M.M. Shokrieh, L.B. Lessard, Multiaxial fatigue behaviour of unidirectional plies based on uniaxial fatigue experiments- part I. Modeling, International Journal of Fatigue, **19**, 201-207, 1997.

18. M.M. Shokrieh, L.B. Lessard, Fatigue under Multiaxial stress systems, in *Fatigue in Composites,* Ed. B. Harris, Woodhead Publishing 2003, pp.63-113.

19. Philippidis, T. P., Antoniou, A. E., Assimakopoulou, T. T., Passipoularidis, V. A., "Static tests on the standard OB UD and MD off-axis coupons", OB_TG2_R022_rev.000, report # 10254, OPTIMAT BLADES, 2005

20. Ramberg W., Osgood W. R., "Description of stress-strain curves by three parameters", NACA TN 902, 1943

21. Richard R. M., Blacklock J. R., "Finite element analysis of inelastic structures", AIAA Journal, 1969, **7**(3), 432-438

22. M. Megnis, P. Brondsted, “Static tests of UD and MD specimens using ISO geometries”, OB_TG3_R007, 2003

23. A. Smits, D. van Hemelrijck, “Static tension tests on UD optimat specimens with fibres at 0^{O}, 30^{O} and 90^{O}. Loading-Unloading-Reloading Tests”, OB_TG3_R011, 2003

24. T.P. Philippidis, V.A. Passipoularidis, Validated engineering model for residual strength prediction, OB_TG5_R013_UP, June 2006 (http://www.kc-wmc.nl/optimat blades/Publications)

25. L.J. Broutman, S. Sahu, A new theory to predict cumulative fatigue damage in fibreglass reinforced plastics, *Composite Materials: Testing and Design* (2^{nd} Conference), ASTM STP 497, 170-188, 1972.

26. T.P. Philippidis, V.A. Passipoularidis, Residual Strength After Fatigue in Composites: Theory vs Experiment, International Journal of Fatigue (2007), doi:10.1016/j.ijfatigue .2007.01.019.

27. V.A. Passipoularidis, T.P. Philippidis, Residual strength degradation in the principal directions of a UD Glass/Epoxy laminate, *International Conference on Structures and Advanced Materials*, Patras, Greece, 2-6 September 2007.

28. Modris Megnis, Povl Brøndsted, “Measurement of the in-plane shear properties of GEV206 at ambient room conditions using V-notched beam test specimens”, OB_TG3_R009_rev.001, report # 10146, OPTIMAT BLADES, 2005

29. DNV standard, Design and Manufacture of Wind Turbine Blades, Offshore and Onshore Wind Turbines, Offshore Standard DNV-OS-J102, October 2006

30. OPTIDAT database: http://www.kc-wmc.nl

31. R.P.L. Nijssen, Fatigue life prediction and strength degradation of wind turbine rotor blade composites, PhD thesis, Faculty of Aerospace Engineering, Delft University, 2006

32. T.P. Philippidis, T.T. Assimakopoulou, V.A. Passipoularidis, A.E. Antoniou, Static and Fatigue Tests on ISO Standard $\pm 45^{o}$ Coupons, OB_TG2_R020_UP, August 2004